

A Staggered Scheme
for
Noncomplex Hyperbolic Systems
of
Conservation Laws

Duncan Roy van der Heul



Stellingen

behorende bij het proefschrift

A STAGGERED SCHEME
FOR
NONCONVEX HYPERBOLIC SYSTEMS
OF
CONSERVATION LAWS
van
Duncan Roy van der Heul

1. Als in de ontwikkeling van gestaggerde schema's even veel tijd en geld zou zijn geïnvesteerd als in die van gecoloeerde schema's, zouden eerstgenoemde nu dezelfde *shock capturing ability* hebben als de beste gecoloeerde schema's.
2. De oplossing van het Riemann probleem met een niet-convexe flux functie in voorbeeld 4.5 op bladzijde 60 van C.B. Laney's *Computational Gasdynamics* (referentie [53] uit dit proefschrift) is niet correct. De correcte oplossing volgt de convex omhullende van de fluxfunctie, gegeven door de raaklijnen aan de fluxfunctie door u_R en u_L en het tussenliggende convexe gedeelte van de fluxfunctie (Fig.1).

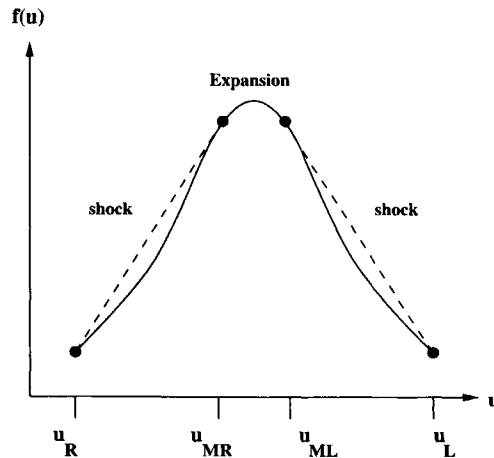


Figure 1: Niet convexe fluxfunctie voor voorbeeld 4.5.

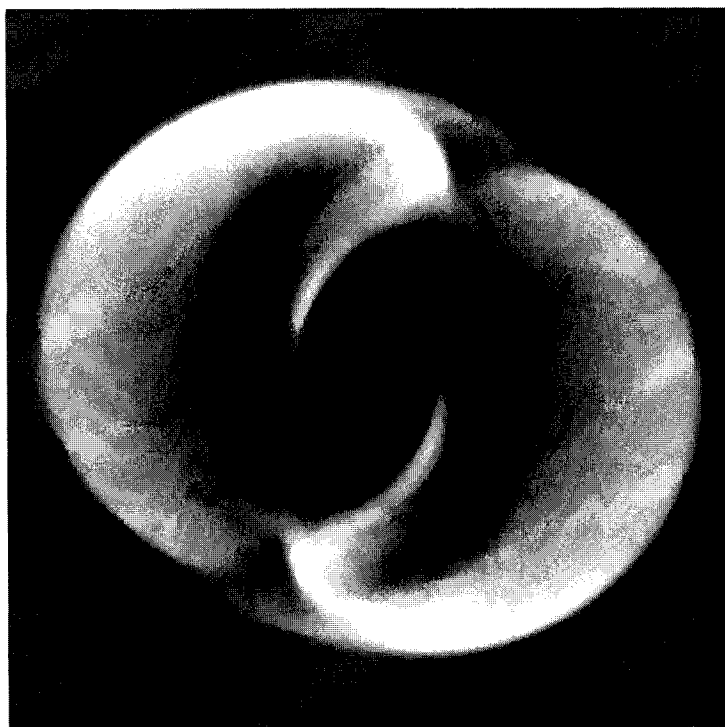
3. De ontwikkeling van nieuwe CFD algorithmes wordt in te sterke mate bepaald door de mogelijkheden van reeds beschikbare computer codes.

4. Zwakke oplossingen berekend met de niet strict conservatieve Mach-uniforme discretisatiemethoden van Bijl en Wesseling (respectievelijk referenties [7] en [108] uit dit proefschrift) voldoen niet exact aan de Rankine-Hugoniot relaties voor de Euler vergelijkingen.
5. De Porsche 924 is evenals de 911 een echte Porsche en in bepaalde opzichten zelfs superieur.
6. Door heffing van accijns op vlees kan de overheid de vleesconsumptie terugdringen. Dit is gerechtvaardigd door de milieubelasting veroorzaakt door de intensieve veehouderij.
7. Televisie kijken is een asociale bezigheid.
8. De uitspraak "Als het een puinhoop is op je bureau, is het ook een puinhoop in je hoofd", is niet noodzakelijk waar.
9. In plaats van een conferentiebijdrage voor toelating te beoordelen op grond van een samenvatting zou het wetenschappelijk comité een beknopte versie van de presentatie (transparanten) moeten bekijken.

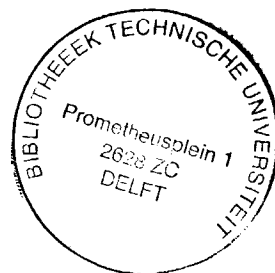
21

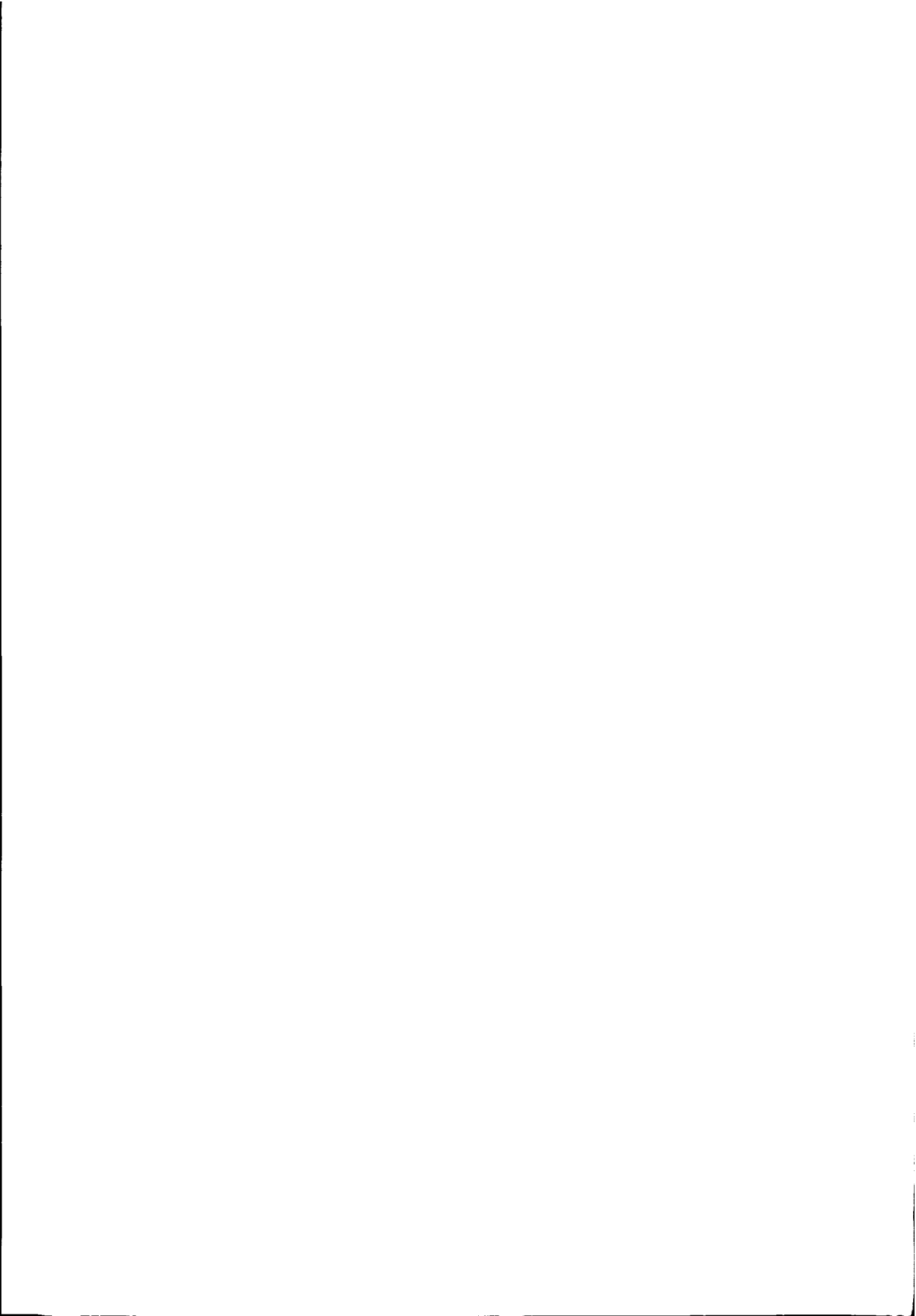
A Staggered Scheme
for
Nonconvex Hyperbolic Systems
of
Conservation Laws

TR 3826



Duncan Roy van der Heul





A Staggered Scheme
for
Nonconvex Hyperbolic Systems
of
Conservation Laws

PROEFSCHRIFT

ter verkrijging van de graad van doctor
aan de Technische Universiteit Delft,
op gezag van de Rector Magnificus prof.dr.ir. J.T. Fokkema,
voorzitter van het College voor Promoties,
in het openbaar te verdedigen
op donderdag 28 februari 2002 te 16:00 uur

door

Duncan Roy VAN DER HEUL
maritiem ingenieur

geboren te Rotterdam

Dit proefschrift is goedgekeurd door de promotor:
Prof.dr.ir. P. Wesseling

Samenstelling promotiecommissie:

Rector Magnificus,	voorzitter
Prof.dr.ir. P. Wesseling,	Technische Universiteit Delft, promotor
Dr.ir. C. Vuik,	Technische Universiteit Delft, toegevoegd promotor
Prof.dr. J.G. Verwer,	Universiteit van Amsterdam
Prof.dr. A.E.P. Veldman,	Rijksuniversiteit Groningen
Prof.dr.ir. J.J.W. van der Vegt,	Universiteit Twente
Prof.dr.ir. G.S. Stelling,	Technische Universiteit Delft
Prof.dr.ir. C.J. van Duijn,	Technische Universiteit Eindhoven

Heul, Duncan Roy van der

A Staggered Scheme for Hyperbolic Systems of Conservation Laws / by Duncan Roy van der Heul

Dissertation at Delft University of Technology. - With ref.- With summary in Dutch

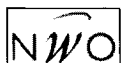
Subject headings: Computer simulations / Staggered Schemes / Cavitation /

Magnetohydrodynamics / Mach-uniform efficiency

COPYRIGHT © 2000 BY D.R. VAN DER HEUL

All rights reserved. No part of the material protected by this copyright notice may be reproduced or utilized in any form or by any means, electronic or mechanical, including photocopying, recording or by any information storage and retrieval system, without permission from the author.

Coverdesign: Ms. ir. J.B. van El



The work described in this thesis was financially supported by the Netherlands Organization for Scientific Research (NWO).



Preface

This dissertation was prepared during my $4\frac{1}{2}$ year appointment at the faculty of Information Technology and Systems of Delft University of Technology in the department of Applied Mathematical Analysis, in the section Numerical Mathematics chaired by Prof.dr.ir. P. Wesseling.

Acknowledgements

First of all I would like to thank my promotor, Piet Wesseling, for his stimulating discussions and his patience for suggesting improvements to my work so a much higher standard of thoroughness has been reached. Furthermore, he has given me many opportunities to contribute to international conferences. I admire his persistent belief in the potential of staggered schemes and the effort he puts in marketing these to the ever sceptical.

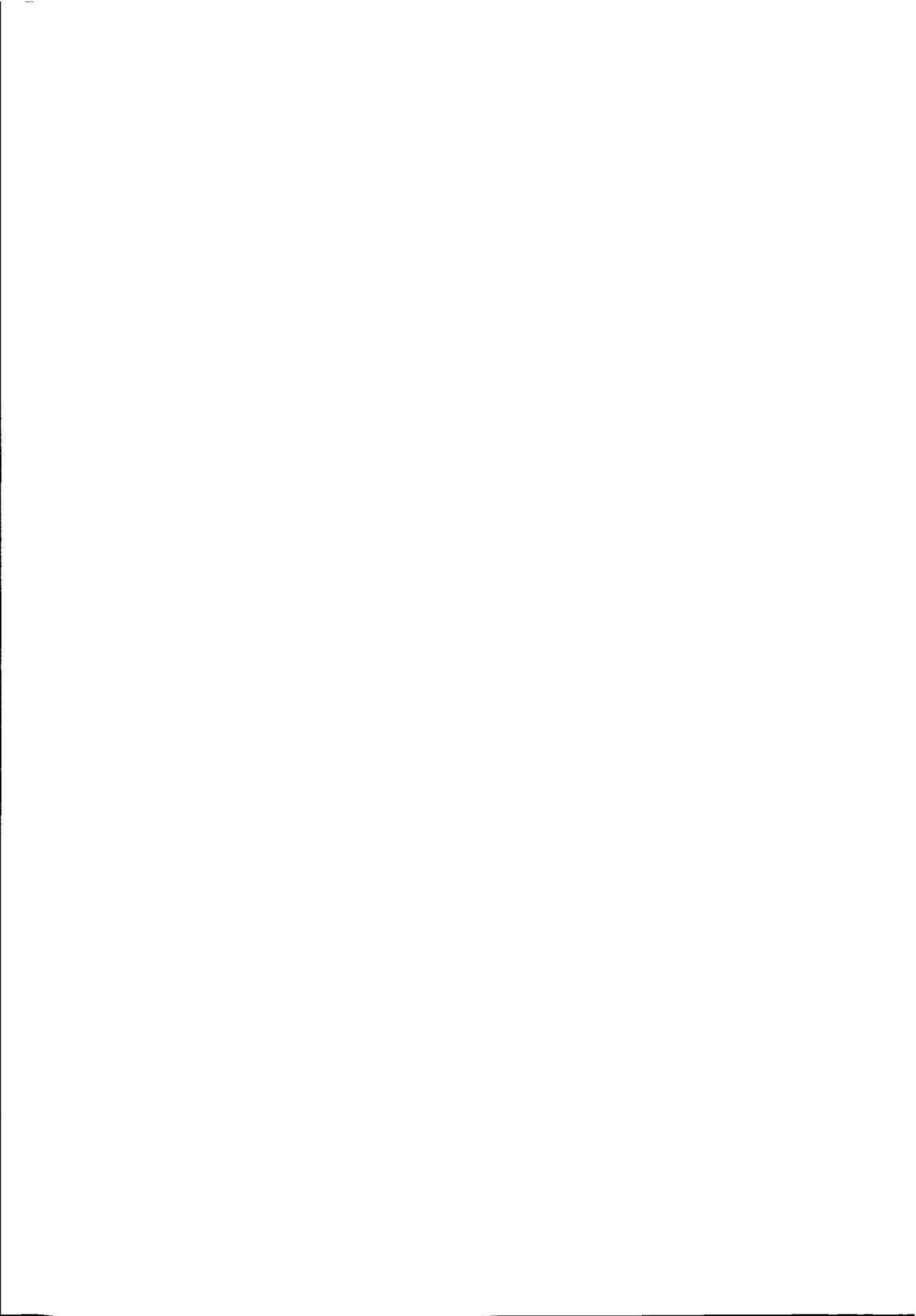
Kees Vuik has provided me with a lot of practical advice, which helped streamline my work. I would like to thank Guus Segal and Kees Kassels for patiently explaining essential details of the ISNAS/DEFT code.

I could not have completed this thesis without all the things I learned from Jason Frank. He helped me transform from the average 'digibeet' into an experienced computer user, constantly improved my English and pointed out the difference between more and less interesting (mathematical) subjects/persons.

Credit is due to my other colleagues at university as well, especially to Fred '*de Lijer*' Vermolen whose company and entertainment, during the final stages of my thesis helped pass the time quickly.

I would like to thank my parents for stimulating me to pursue a scientific career and helping me out many times in stressful periods, when I again had failed to prepare my conference slides in time.

Finally I would like to thank my two sequential house roommates Jurriaan de Bruin and Judith van El for their support and care.



Contents

1	Introduction	1
1.1	Staggered schemes	1
1.2	Nonconvex hyperbolic systems	3
1.3	Outline of this thesis	3
I	Hydrodynamic Cavitation	5
2	Physical background of cavitation	7
2.1	Types of cavitation	8
2.1.1	Bubble cavitation	8
2.1.2	Sheet and cloud cavitation	8
2.1.3	Vortex cavitation	11
2.2	Adverse effects of cavitation	12
2.2.1	Loss of performance	12
2.2.2	Erosion	12
2.2.3	Noise and vibrations	12
2.3	Beneficial effects of cavitation	13
2.4	Concluding remarks	13
3	Review of methods for modeling of cavitation	15
3.1	Introduction	15
3.2	Interface tracking methods	16
3.3	Interface capturing methods	17
3.3.1	The Homogeneous Equilibrium Model	18
3.3.2	Nonequilibrium models	20
3.4	Comparison between interface capturing and fitting	21
3.5	Conclusions	22
4	The interface capturing method of Delannoy	23
4.1	Introduction	23
4.2	Governing equations	23
4.3	Equation of state	24

4.4	Numerical method	24
4.4.1	Staggered placement of the unknowns	26
4.4.2	Discretisation in general coordinates and primitive variables	26
4.4.3	Scaling of the pressure	26
4.4.4	Higher order upwind schemes	27
4.4.5	SIMPLE type solution algorithm	27
4.4.6	Testcases	29
4.5	Conclusions	31
5	Analysis of the equation of state	33
5.1	Introduction	33
5.2	The state diagram of water	33
5.3	The equation of state	36
5.4	Conclusions	37
6	The Riemann problem for a nonconvex hyperbolic system	39
6.1	Introduction	39
6.2	Simple waves	39
6.3	The Riemann problem	46
6.4	Construction of a test case	47
6.4.1	The model equation of state	48
6.4.2	Testcase 1, zero initial velocity	49
6.4.3	Testcase 2, nonzero initial velocity	52
6.5	Conclusions	52
7	Development of a discretisation scheme	57
7.1	Introduction	57
7.2	The notions of target scheme, actual scheme and resolved scheme	57
7.3	The target scheme	58
7.3.1	Spatial discretisation	59
7.3.2	Temporal discretisation	60
7.3.3	Starting point	61
7.4	Actual discretisation	62
7.4.1	The momentum equation	62
7.4.2	The mass conservation equation	64
7.4.3	Starting point	64
7.5	The resolved scheme	65
7.5.1	Starting point: compressible pressure correction	65
7.5.2	Preliminary numerical results	66
7.6	Improvements	67
7.6.1	Nonlinear pressure correction	70
7.7	Conclusions	72

8	Stability analysis of segregated solution methods	75
8.1	Introduction	75
8.2	Fourier stability analysis of schemes for systems.	76
8.3	Derivation of a stability condition	81
8.4	Verification of stability thresholds	87
8.5	Inclusion of solution procedure in stability analysis	93
8.6	Higher order spatial discretisation	96
8.7	Formulation of a discretisation with optimal stability properties	98
	8.7.1 Momentum equation	98
	8.7.2 Mass conservation equation	99
8.8	Conclusions	100
9	Applications	103
9.1	Introduction	103
9.2	Problem specification	103
9.3	Steady cavitation	104
	9.3.1 NACA66 hydrofoil	104
9.4	Unsteady cavitation	105
	9.4.1 Converging/diverging channel.	105
	9.4.2 E.N.-hydrofoil	106
9.5	Concluding remarks	109
II	Magnetohydrodynamics	111
10	Low Mach number ideal magnetohydrodynamics.	113
10.1	Introduction	113
10.2	The equations of ideal magnetohydrodynamics	113
10.3	Analytical aspects	114
10.4	Weakly compressible magnetohydrodynamic flow	116
10.5	A staggered scheme for MHD	116
10.6	Conclusions	119
11	A Mach-uniform scheme for ideal magnetohydrodynamics.	121
11.1	Introduction	121
11.2	A staggered scheme	121
11.3	Pressure based formulation	124
11.4	Mach-uniform formulation	130
11.5	Validation	132
11.6	Conclusions	137

12 A conservative pressure correction scheme for the Euler equations	139
12.1 Introduction	139
12.2 Mach-uniform accuracy and efficiency	140
12.3 Mach-uniform methods	140
12.3.1 Incompressible flow	140
12.3.2 Weakly compressible flow: $0 < M \leq 0.3$	141
12.3.3 Compressible flow: $0.3 < M$	142
12.4 Discretisation and pressure correction method	142
12.5 Validation with Riemann problems	145
12.5.1 The shock tube problem of Sod	145
12.5.2 The shock tube problem of Lax	147
12.5.3 Nonstationary contact discontinuity	147
12.6 Numerical results	149
12.6.1 Channel with bump.	149
12.6.2 NACA0012 airfoil	150
12.7 Conclusions	154
13 A conservative Mach-uniform scheme for ideal magnetohydrodynamics	159
13.1 Introduction	159
13.2 A conservative pressure-correction method for MHD flows	159
13.3 Numerical results	160
13.4 Discussion	168
Bibliography	169
A Some remarks on spatial discretisation in general coordinates	179
A.1 Introduction	179
A.2 Improved discretisation of the convective flux for full upwind scheme.	182
A.3 A higher order limited κ -scheme in general coordinates	183
A.4 Conclusions	186
B Two pressure correction schemes	189
C Conservative pressure correction solution algorithm in general coordinates	193
Summary	195
Samenvatting	197
Curriculum vitae	199
List of publications	201

List of Figures

1.1	The staggered placement of the control volume in the Hansen scheme. . . .	2
2.1	Different types of cavitation on a hydrofoil as a function of the angle of attack	9
2.2	Cyclic behavior of a sheet cavity for small σ	10
2.3	Structure of sheet cavity [88].	11
3.1	Iterative solution of the cavity interface according to [13].	16
3.2	The equation of state in the (P, V) space.	18
3.3	The equation of state for the mixture.	20
4.1	The equation of state according to [20] and [36].	25
4.2	Procedure to treat nonlinear equation of state [20].	28
5.1	Isotherm of H_2O at $20^\circ C$	34
5.2	Detail of isotherm of the vapor phase of H_2O at $20^\circ C$	35
6.1	The model equation of state	42
6.2	Simple wave solution in the nonconvex case, right running.	44
6.3	Simple wave solution in the nonconvex case, left running.	45
6.4	Structure of the Riemann problem for the barotropic Euler equations. . . .	46
6.5	Construction of the isothermal Riemann problem	47
6.6	Testcase I, structure of solution in Lagrangian frame of reference.	50
6.7	Testcase I, construction and solution in Lagrangian frame of reference. . .	51
6.8	Testcase I, solution in Eulerian frame of reference for $t = 0.2$	52
6.9	Testcase II, topology of solution in Lagrangian frame of reference.	53
6.10	Testcase II, solution in Eulerian frame of reference for $t = 0.1$	54
6.11	Testcase II, construction and solution in Lagrangian frame of reference. . .	55
7.1	Staggered placement of unknowns according to Arakawa-C arrangement. . .	60
7.2	Riemann problem 1; 48 cells; $\tau/h = 0.4$, Top: Osher scheme, Bottom: staggered scheme.	68
7.3	Riemann problem 2; 96 cells; $\tau/h = 0.4$, Top: Osher scheme, Bottom: staggered scheme.	69
8.1	Absolute value of eigenvalues as function of θ , case of linear instability. . .	82

8.2	Absolute value of eigenvalues as function of θ , case of linear stability. . . .	83
8.3	Stability conditions for Scheme 2.	87
8.4	Stability conditions for Scheme 2.	88
8.5	Stable integration of $M = 5$ testcase, $CFL = 0.20$	89
8.6	Unstable integration of $M = 5$ testcase, $CFL = 0.25$	89
8.7	Unstable integration with scheme 1, $CFL = 0.430$	90
8.8	Stable integration with scheme 1, $CFL = 0.493$	91
8.9	Unstable integration with scheme 3, $CFL = 0.493$	91
8.10	Stable integration with scheme 4, $CFL = 3.19$	92
8.11	Unstable integration with scheme 4, $CFL = 3.61$	92
8.12	Dependence of $ \lambda_{1,2}(G_2^{-1}G_1) $ on θ , with (<i>resolved</i> discretisation) and without inclusion of the pressure correction algorithm (<i>target</i> discretisation).	95
8.13	Dependence of $ \lambda_{1,2}(G_2^{-1}G_1) $ on θ , for 1st-order upwind scheme with and without higher order upwind deferred correction.	98
8.14	Dependence of the absolute values of eigenvalues of the amplification matrix on wavenumber θ for implicit(left) and semi-implicit(right) discretisation of mass conservation equation.	100
8.15	Dependence of the absolute values of the eigenvalues of the amplification matrix on wavenumber θ for (8.86), $\beta = \frac{1}{2}$	101
9.1	NACA66 hydrofoil, grid with 144×20 cells.	105
9.2	Converging/diverging channel, geometry and mesh.	105
9.3	Converging/diverging channel, time history of pressure, $\sigma = 2.5$	107
9.4	Converging/diverging channel, density levels, $\sigma = 2.5$	108
9.5	E.N.-hydrofoil, geometry and detail of mesh.	108
9.6	EN-wing, density levels, $\alpha = 6.2^\circ$, $\sigma = 1.2$	109
9.7	Steady separation zone at E.N.-hydrofoil	110
10.1	Illustration of the constrained transport approach.	118
11.1	Staggered placement of the unknowns of the equations of ideal MHD (1D).	123
11.2	The Riemann problem of Brio and Wu, staggered scheme, 200 cells, $\lambda = 0.05$, $t_{\text{end}} = 0.14$	133
11.3	The Riemann problem of Brio and Wu, Mach-uniform scheme, 200 cells, $\lambda = 0.05$, $t_{\text{end}} = 0.14$	134
11.4	The Riemann problem of Dai and Woodward, staggered scheme, 200 cells, $\lambda = 0.05$, $t_{\text{end}} = 0.1$	135
11.5	The Riemann problem of Dai and Woodward, Mach-uniform scheme, 200 cells, $\lambda = 0.05$, $t_{\text{end}} = 0.1$	136
12.1	Staggered placement of unknowns.	143
12.2	The stencil of the pressure correction equation.	144
12.3	Sod's Riemann problem, nonconservative Mach-uniform discretisation.	146
12.4	Sod's Riemann problem, conservative Mach-uniform discretisation.	146

12.5 Sod's Riemann problem, Osher scheme.	147
12.6 Lax's Riemann problem, nonconservative Mach-uniform discretisation.	148
12.7 Lax's Riemann problem, conservative Mach-uniform discretisation.	148
12.8 Lax's Riemann problem, Osher scheme.	149
12.9 Nonstationary contact discontinuity, nonconservative Mach-uniform discretisation.	150
12.10 Nonstationary contact discontinuity, conservative Mach-uniform discretisation.	151
12.11 Nonstationary contact discontinuity, Osher scheme.	152
12.12 90×25 mesh for channel with bump.	152
12.13 Iso-lines of density for channel with bump for different Mach numbers.	153
12.14 Mach number distribution on bottom of channel, for the method of [7] (I) and the present method (II).	154
12.15 H-type grid with two blocks of 180×30 cells for NACA0012 airfoil.	155
12.16 Density contours for NACA0012 airfoil for different Mach numbers.	156
12.17 Dimensionless pressure distribution on NACA0012 airfoil, $M = 0.85$, $\alpha = 0^\circ$	157
13.1 The Riemann problem of Brio and Wu, Mach-uniform scheme, 200 cells, $\lambda = 0.05$, $t_{\text{end}} = 0.1$	161
13.2 The Riemann problem of Dai and Woodward, Mach-uniform scheme, 200 cells, $\lambda = 0.05$, $t_{\text{end}} = 0.14$	162
13.3 Thermal pressure p for the rotor problem, 200×200 cells, $t_{\text{end}} = 0.15$	163
13.4 Density ρ for the rotor problem, 200×200 cells, $t_{\text{end}} = 0.15$	164
13.5 Mach number for the rotor problem, 200×200 cells, $t_{\text{end}} = 0.15$	164
13.6 Magnetic energy $ B ^2$ for the rotor problem, 400×400 cells, $t_{\text{end}} = 0.15$	165
13.7 Thermal pressure p for the Orzag-Tang vortex, 200×200 cells, $t_{\text{end}} = 3.14$	166
13.8 Density ρ for the Orzag-Tang vortex, 200×200 cells, $t_{\text{end}} = 3.14$	166
13.9 Mach number for the OT vortex, 200×200 cells, $t_{\text{end}} = 3.14$	167
13.10 Magnetic energy $ B ^2$ for the OT vortex, 200×200 cells, $t_{\text{end}} = 3.14$	167
A.1 The controlvolume for the contravariant velocity V^1	180
A.2 Velocity at the center line, partial upwind discretisation on regular mesh.	181
A.3 Velocity at the center line, full upwind discretisation on regular mesh.	181
A.4 Irregular mesh to test the improved upwind scheme.	183
A.5 Velocity at the center line, original fully upwind discretisation on the mesh of Fig. A.4.	184
A.6 Velocity at the center line, improved fully upwind discretisation on the mesh of Fig. A.4.	184
A.7 Velocity at the center line, classic higher order upwind discretisation on the mesh of Fig. A.4.	187
A.8 Velocity at the center line, improved higher order upwind discretisation on the mesh of Fig. A.4.	187



List of Tables

3.1	Overview of interface capturing methods employing the HEM.	19
8.1	Stability properties of four time integration schemes.	81
8.2	Initial conditions for Riemann problems.	88
8.3	Numerical verification of the stability thresholds (8.64), (8.65) and (8.2) for one-dimensional testcase.	90
8.4	Initial conditions for $M = 4$ Riemann problem.	93
8.5	Numerical verification of the stability thresholds (8.64) and (8.65) for two-dimensional testcase.	93
9.1	Parameter values of physical model and computing method.	104
9.2	NACA66-209 hydrofoil, computed cavity length, $\alpha = 4^\circ$, 144×20 cells. . . .	104
9.3	Converging/diverging channel, comparison of results.	106
9.4	Input parameters for the experiments conducted in [51].	107
9.5	E.N.-hydrofoil, nondimensionalised results compared with [51] and [69]. . .	109
12.1	CPU time for channel with bump for different Mach number.	151



Chapter 1

Introduction

This thesis is devoted to investigation of the application of *staggered* finite volume schemes for the discretisation of more general hyperbolic systems than the Euler equations of gasdynamics. Because state-of-the-art colocated schemes for the Euler equations have reached a state of maturity and sophistication that cannot be matched (yet) by staggered schemes, the former will be more robust and accurate for standard gasdynamic problems. However, for nonstandard conditions, e.g. weakly compressible gasdynamic flow, or more general hyperbolic systems, staggered finite volume schemes can be more efficient, accurate and robust than colocated schemes.

We will consider two different hyperbolic systems:

- The equations of the homogeneous equilibrium model for cavitating hydrodynamic flow,
- The equations of ideal magnetohydrodynamics.

These will be discussed in Part I and Part II of this thesis, respectively.

Both systems share the special property of *nonconvexity*, that will be discussed shortly after, and have a complicated flux function, which is not a homogeneous function of first order. The first system has the additional complication that the equation of state is nonlinear and gives rise to very strong variation in the speed of sound. The successful application of staggered schemes to compute solutions to these very complicated hyperbolic systems with Mach-uniform efficiency and accuracy illustrates the general applicability of the approach.

1.1 Staggered schemes

Staggered schemes are discretisations, either of finite difference, finite volume or finite element type, where variables are not colocated spatially or temporally. A classical example of a staggered finite volume scheme is the Hansen scheme [31]. The Hansen scheme applied

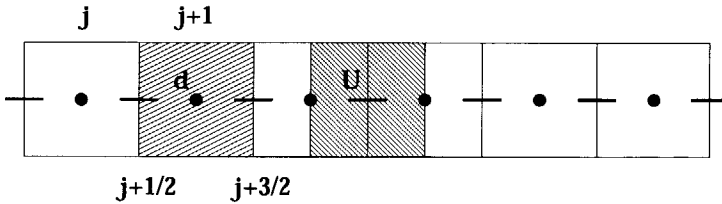


Figure 1.1: The staggered placement of the control volume in the Hansen scheme.

to the linearised shallow-water equations reads:

$$\frac{d_j^{n+1} - d_j^n}{\delta t} + \bar{d} \frac{U_{j+\frac{1}{2}}^{n+\frac{1}{2}} - U_{j-\frac{1}{2}}^{n+\frac{1}{2}}}{\delta x} = 0, \quad (1.1)$$

$$\frac{U_{j+\frac{1}{2}}^{n+\frac{3}{2}} - U_{j+\frac{1}{2}}^{n+\frac{1}{2}}}{\delta t} + g \frac{d_{j+1}^{n+1} - d_j^{n+1}}{\delta x} = 0, \quad (1.2)$$

where d , U , \bar{d} and g are the water depth, velocity, average waterdepth and gravitational acceleration respectively. The equation for d is integrated over the control volume centered around j , whereas the equation for U is integrated over the control volume centered around $j + \frac{1}{2}$ (Fig. 1.1). Note that in this case no interpolations are required to compute the fluxes at the faces of both sets of control volumes. The scheme is second order accurate in space. Furthermore, the temporal staggering of the unknowns raises the accuracy of the time-integration. If d and U would be evaluated at the same discrete time levels, the scheme would be only first order accurate in time (Sielecki scheme [81]). Another property of staggered schemes is that no use is made of information about the characteristics of the flux function, such as the eigensystem of the Jacobian of the flux function; this is a key part of all collocated upwind schemes for hyperbolic systems. Convective terms can be upwind biased easily, because the upwind direction is trivially contrary to the direction of the convective velocity, but all other terms can be discretised centrally.

This type of scheme is fundamentally different from staggered schemes within the context of predictor-corrector methods, e.g. the Richtmyer method (see e.g. [53]). In this case the unknowns are advanced on the *standard* grid in the corrector step, after having been mapped to the *staggered* grid in the predictor step.

Recently pseudo-staggered schemes have been introduced [3], where use is made of a set of help-variables discretised on a staggered grid. The use of the discrete Stokes theorem to update the staggered help-variables with the collocated primary variables enables one to enforce a solenoidality constraint on a subset of the variables, as is encountered for example in incompressible flow ($\nabla \cdot \mathbf{u} = 0$) and in magnetohydrodynamics ($\nabla \cdot \mathbf{B} = 0$). At the end of the time step the help-variables are interpolated to the location of the primary variables.

Because the primary variables are advanced in time in a collocated manner, these schemes are not truly staggered schemes.

1.2 Nonconvex hyperbolic systems

A system is called nonconvex, if one of the characteristic fields is neither genuinely non-linear nor linearly degenerate [30]. The most important differences between convex and nonconvex hyperbolic systems are the possible occurrence of entropy condition satisfying expansion shocks and the fact that simple wave solutions of the equation can be of *composite* type. This means that the simple wave solution can consist of a concatenation of shocks and expansion waves of the same family. Both effects will also occur in the scalar case. A textbook example of a nonconvex hyperbolic equation is the Buckley-Leverett equation, that describes the flow of two immiscible liquids in a porous medium, neglecting capillary effects, see e.g. [59, 105]. We will discuss methods that are accurate and efficient for both the convex and the nonconvex case.

1.3 Outline of this thesis

This thesis is divided into two parts. In Part I the development of a staggered scheme to discretise the equations of the Homogeneous Equilibrium Model (HEM) is discussed. The HEM is a simple model to describe two-phase liquid/vapor flow and is used to model unsteady sheet cavitation on lifting surfaces. The second part is devoted to the formulation of a staggered discretisation of the equations of ideal magnetohydrodynamics, that model the dynamics of an inviscid plasma under the influence of a magnetic field.

We start with a brief discussion of some physical and technical aspects of cavitation. Next an overview is given of the various approaches that are used to model cavitation with the Euler and Navier-Stokes equations. The HEM will turn out to be the most generally applicable model, with modest assumptions. We continue with a review of the method of Delannoy, who was the first to successfully apply the HEM to compute unsteady cavitation. This approach forms the starting point of our method. The discussion will highlight shortcomings in Delannoy's approach and aims to supply some background for some of his sparsely motivated but correct choices.

Before formulating our numerical method we supply information on specific details of the HEM. We proceed with analyzing the nonconvex equation of state of the HEM and then discuss the Riemann problem for a general nonconvex equation of state. The solutions of two Riemann problems will be used as simple testcases for the numerical scheme.

The choice of a suitable time integration method is placed in a formal framework, by distinguishing between the *target*, the *actual* and the *resolved* discretisation. Although a straightforward extension of the method for the Euler equations produces results for Riemann problem test cases with accuracy comparable to a standard collocated scheme, this method has to satisfy a severe stability restriction on the timestep when applied to

the computation of cavitation. Originally this was blamed on the *splitting error* caused by the sequential solution procedure, and a number of ways to reduce the splitting error were devised. One way is to apply the iterative SIMPLE approach. However, stability analysis revealed that the SIMPLE method does not owe its superiority to the absence of the splitting error but to its favorable stability properties for high Mach number flow. Our aim was to formulate a noniterative solution procedure, with stability properties for high Mach number flow, comparable to the SIMPLE method.

To gain insight in the stability properties of these segregated solution procedures we turn to von Neumann stability analysis. The simplicity of linear analysis allows inclusion of details of the segregated solution procedure, e.g. linearisation and deferred/defect correction techniques. This analysis reveals a strong dependence of the maximum allowable dimensionless timestep on the Mach number. It explains the severe restriction on the time step of the original method for the high Mach number flow encountered in cavitation simulations and leads the way to a time integration method with more uniformity of the stability properties in the Mach number. Next we use this time-stepping method to compute a number of applications.

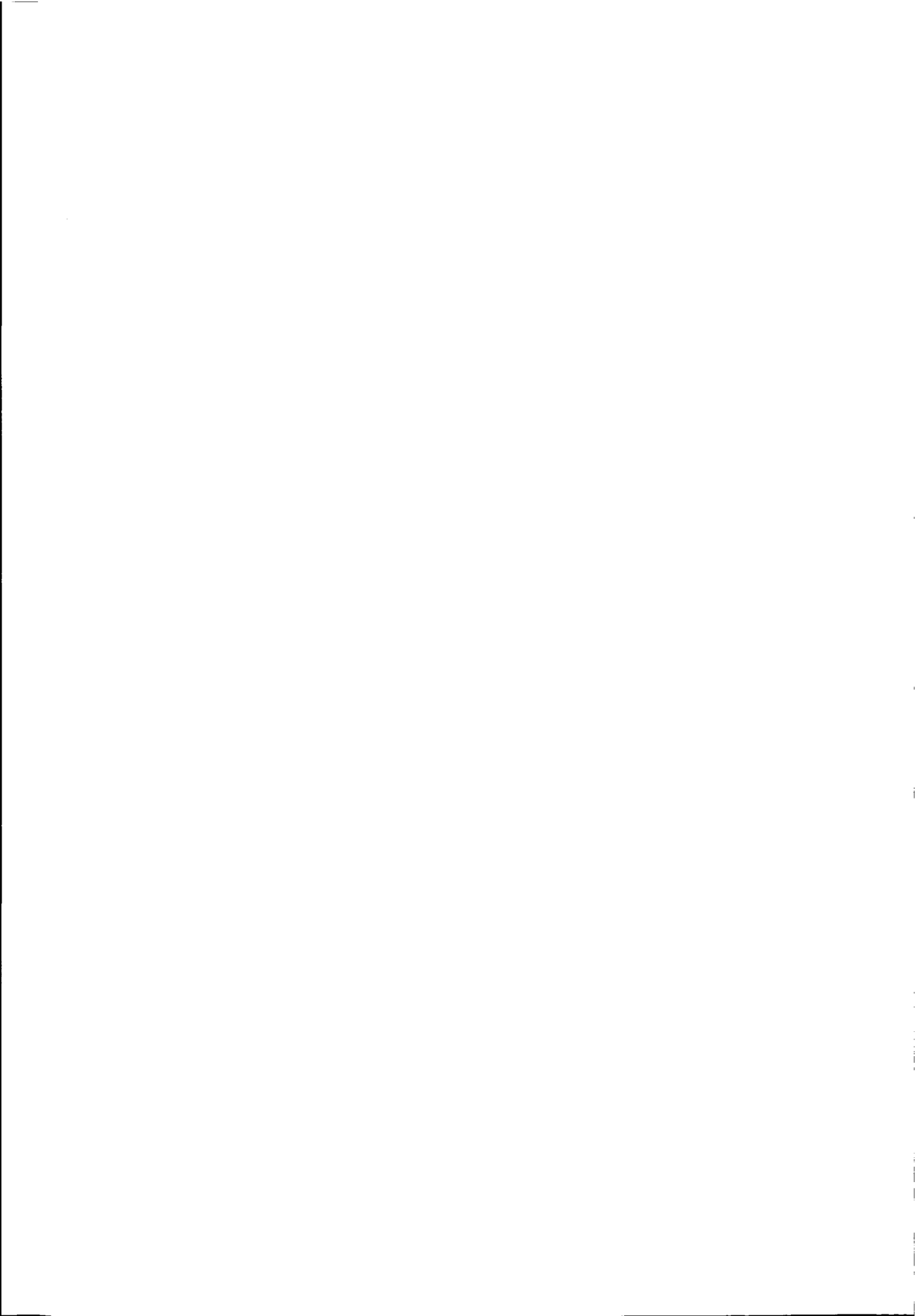
In the second part we direct our attention to the equations of ideal magnetohydrodynamics. A key aspect of the equations of ideal magnetohydrodynamics is that the discrete magnetic field should remain solenoidal to avoid the occurrence of unphysical phenomena, e.g. magnetic monopoles. Furthermore, in some astrophysical applications the plasma flow is weakly compressible, but with physically important density variations. A staggered scheme retains the solenoidality of the discrete magnetic field to machine precision and its efficiency and accuracy in the low Mach number limit. This makes it very suitable for computing weakly compressible MHD flow.

We start with a straightforward extension of a Mach-uniform method for the Euler equations. However, because of the lack of conservation of the discretisation weak solutions are not correctly approximated. For the Euler equations the deviations are very small. But for the equations of ideal magnetohydrodynamic flow they become unacceptable. Therefore we continue with constructing a *conservative* pressure correction method for the Euler equations, that has Mach-uniform behavior similar to earlier nonconservative methods, but produces more accurate approximations to weak solutions. This is illustrated with a number of Riemann problems and with two two-dimensional testcases.

Next, extension of the method to ideal MHD is discussed. Different staggered arrangements of the magnetic field are considered. The new method is shown to be able to produce accurate results for a number of classic Riemann problems for magnetohydrodynamics and for a two-dimensional test case: *the rotor problem*.

Part I

Hydrodynamic Cavitation



Chapter 2

Physical background of cavitation

In this section a brief introduction is given to the phenomenon of cavitation. Cavitation is the phenomenon that when the local pressure in a liquid drops below the (local) vapor pressure, vapor filled bubbles or pockets are formed. We restrict ourselves to *hydrodynamic cavitation*, caused by the kinematics of the fluid, as opposed to *acoustical cavitation*, caused by an externally applied fluctuating pressure field. Furthermore, we restrict our attention to situations, where thermodynamic effects are negligible. This is e.g. the case for the flow of water at room temperature, but not for cavitation in liquefied gases.

Cavitating flow is characterized by the following dimensionless numbers:

- Froude number

$$Fr = \frac{V_\infty}{\sqrt{gL_{\text{ref}}}}$$

- Reynolds number

$$Re = \frac{V_\infty L_{\text{ref}}}{\nu}$$

- Cavitation number

$$\sigma = \frac{p_\infty - p_{\text{vapor}}}{\frac{1}{2}\rho_\infty V_\infty^2}$$

Although the Froude and Reynolds number have some influence on the shape and size of the cavities, it is generally accepted that the influence of the cavitation number is dominant. The cavitation number gives the difference between the ambient pressure and the vapor pressure, nondimensionalised by the density and velocity of the fluid at freestream conditions.

Theoretically, cavitation commences when σ is equal to $-Cp_{\text{min}}$: when the dimension-

less minimal pressure in the flow domain is equal to the dimensionless vapor pressure:

$$Cp_{\min} = \frac{p_{\min} - p_{\infty}}{\frac{1}{2}\rho_{\infty}V_{\infty}^2} = \frac{p_{\text{vapor}} - p_{\infty}}{\frac{1}{2}\rho_{\infty}V_{\infty}^2} = -\frac{p_{\infty} - p_{\text{vapor}}}{\frac{1}{2}\rho_{\infty}V_{\infty}^2} = -\sigma \quad (2.1)$$

Two flow situations, geometrically equivalent and with the same σ , show nearly the same cavitation behavior. This will only hold if the cavitation is fully developed. The conditions for cavitation inception, i.e. the moment at which the liquid flow ruptures, are influenced substantially by the nuclei content of the fluid and the roughness of the surface under consideration. If nuclei to start the vaporization process are nearly absent and the surface of the container of the fluid is extremely smooth, cavitation commences only when $Cp_{\min} \ll -\sigma$.

2.1 Types of cavitation

In this Section we summarize the various forms in which hydrodynamic cavitation appears. The first distinction is made between fixed and traveling cavitation. *Sheet cavitation* and *bubble cavitation* remain stationary and adjacent to the wetted surface and are therefore regarded as fixed cavitation. *Vortex cavitation* and *cloud cavitation* can move freely in the flow domain and are regarded as traveling cavitation. Fig. 2.1 shows the different types of cavitation as they occur on a hydrofoil at different angles of attack.

2.1.1 Bubble cavitation

Bubble cavitation (Fig. 2.1A) occurs when the minimum pressure does not occur in the presence of a steep gradient, e.g. for a hydrofoil or blunt-nosed body at zero angle of attack. As the point of minimum pressure is not sharply defined, the bubbles form randomly around the position of maximum thickness of the hydrofoil.

2.1.2 Sheet and cloud cavitation

Sheet cavitation (Figs. 2.1B & C) is a type of fixed cavitation, which occurs if the minimum pressure is reached after a steep gradient, e.g. for a hydrofoil under an angle of attack. The cavity appears as a transparent sheet starting at the leading edge. If the cavity length is smaller than the chord length, this is referred to as *partial cavitation*. If the length exceeds the chord, we speak of a *supercavitating* hydrofoil.

For large values of σ or small angles of attack the cavity appears to have a steady length (Fig. 2.1B), although the vapor/liquid interface shows small amplitude high frequency oscillations. For small values of σ or large angles of attack the cavity has the following cyclic behavior (Fig. 2.2). First the cavity starts to grow from the leading edge. During this growth phase a reversed flow develops at the lower side of the trailing edge of the growing cavity, called the *reentrant jet*. When this reentrant jet reaches the leading edge of the cavity or when it touches the upper part of the cavity interface, a part of the

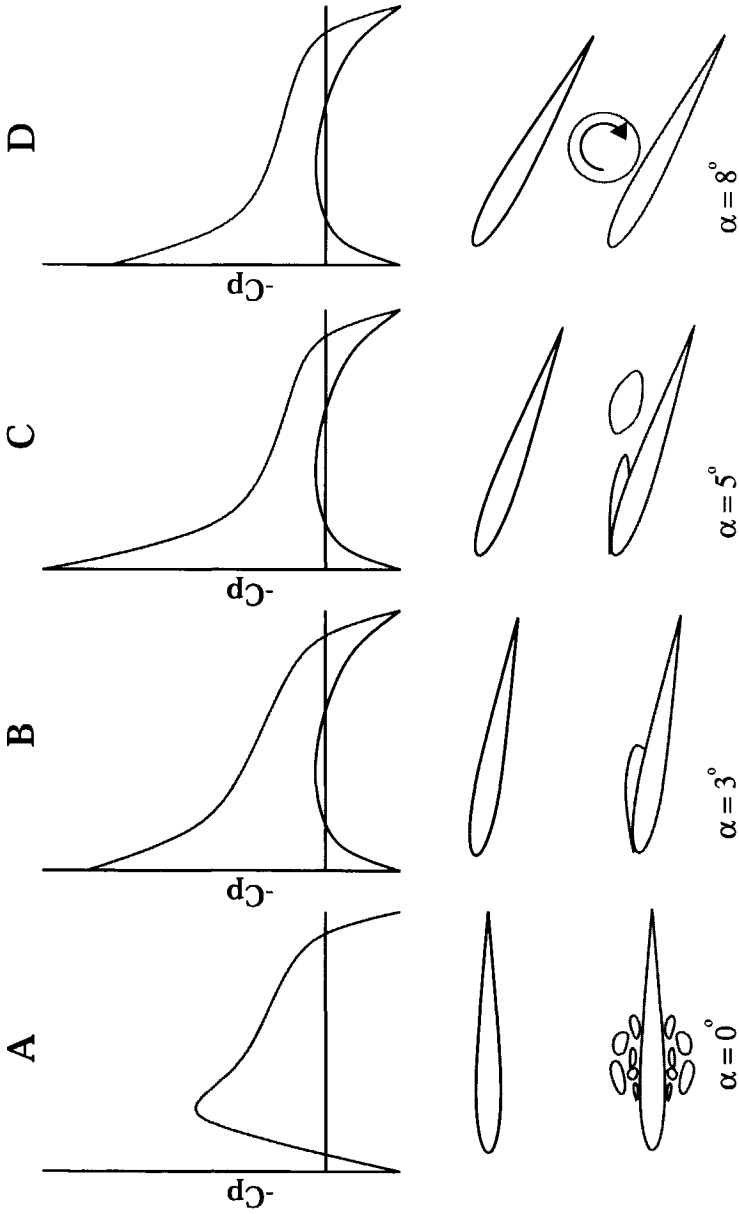


Figure 2.1: Different types of cavitation on a hydrofoil as a function of the angle of attack



Figure 2.2: Cyclic behavior of a sheet cavity for small σ .

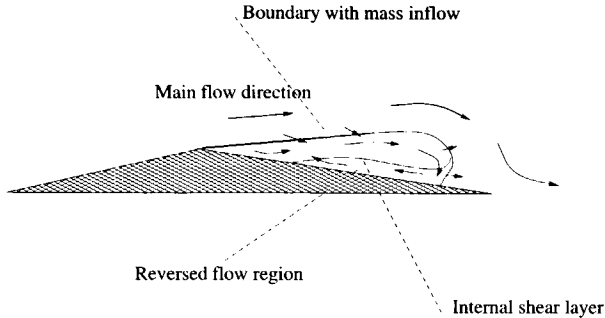


Figure 2.3: Structure of sheet cavity [88].

cavitation bubble detaches and breaks up into a cluster of bubbles, resulting in so-called *cloud cavitation* (Fig. 2.1C). While the detached part of the cavity is in the vicinity of the body surface it will induce a rise of the pressure on the hydrofoil. This will cause the attached part of the cavity to recede. After it has been convected a certain distance from the section leading edge, the pressure recovers its undisturbed value and the cavity will start to grow again. If there is a strong spanwise cross flow, a sheet cavity can be steady. Recently, a number of experiments have been conducted studying the internal flow structure of a sheet cavity [70, 88], for a venturi configuration. Both the velocity and the void fraction inside the cavity were measured, for a number of testcases, including both oscillating and steady cavities. First of all it was found that sheet cavities, independent of the cavitation number, are not filled with pure vapor, because the measured void fraction varies between 80 and 10 percent, from the leading to the trailing edge of the cavity. Furthermore, the flow pattern inside the cavity is found to be as sketched in Fig. 2.3. Even in the steady case there is a considerable region of reversed flow, as opposed to what is stated in [36]. The reversed flow can extend towards the detachment point, which results in the total cavity being shed. It is also possible that due to instabilities in the upper vapor/liquid interface, the reversed flow and the free stream make contact and only the aft part of the cavity is shed. Mass inflow into the cavity takes place across the forward 70 percent of the cavity interface.

2.1.3 Vortex cavitation

In the core of vortices the pressure is much lower than the ambient pressure. If the vortex is sufficiently strong the core will start to cavitate. If the angle of attack of a hydrofoil is beyond the stall angle, cavitation can occur in the separation vortices emanating from the leading edge (Fig. 2.1D). Vortex cavitation often occurs in the strong vortices emanating from the blade tips and hub of a propeller. Also very full-bodied ships, e.g. crude oil tankers

and bulk carriers, can have cavitation in a vortex which results from the interaction between the flow around the stern and the propeller, so called *propeller-hull-vortex-cavitation*.

2.2 Adverse effects of cavitation

The great economic consequences of cavitation motivate the continuing research to improve cavitation models. From a structural point of view the cavitation model can be used in two ways:

- To optimize design and operating conditions of hydraulic machinery to avoid or minimize cavitation.
- If cavitation is unavoidable, to predict the structural damage of the cavitation in time to come to an optimal service/maintenance program.

We list the most important adverse effects of cavitation.

2.2.1 Loss of performance

The most apparent effect of cavitation is loss of performance, encountered in turbomachinery and with ship propellers. In the case of propellers the thrust is only affected if the cavitation is excessive, resulting in thrust breakdown. The most striking example of this effect occurred with the first turbine-driven ship *Turbinia*, which case formed a strong impetus for cavitation research. For pumps the generation of cavitation bubbles affects the mass flow rate.

2.2.2 Erosion

The violent collapse of shed bubbles when they reach a high pressure zone causes erosion and eventually possible breakdown of the surface structure. During collapse of a bubble it loses its spherical shape and a microjet is formed. This microjet causes a pressure pulse of the order of a thousand bar on the surface. The velocities in the neighbourhood of the microjet are so high, that the fluid becomes compressible and shock waves are formed, which also cause excessive pressures on the surface.

2.2.3 Noise and vibrations

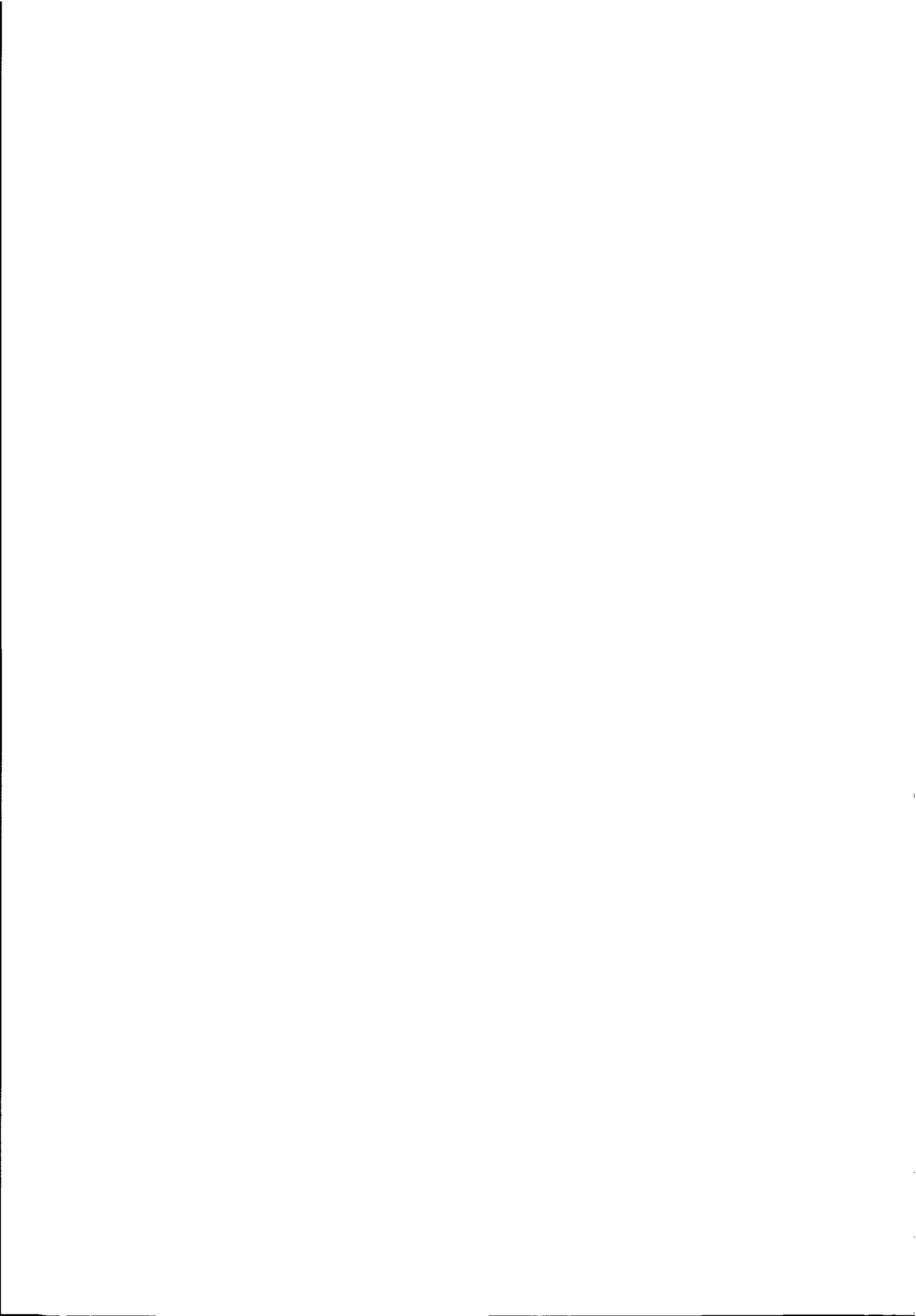
If the cavitation bubbles implode sufficiently close to the wall, the direct impact of the microjet and the resulting shockwaves generate considerable noise. The circumvention of cavitation induced noise is of prime interest in naval ship engineering. The collapse of large detached sheet cavities can cause large pressure variations in the water. These in turn give rise to vibrations of the structure if the collapse occurs sufficiently close to the surface.

2.3 Beneficial effects of cavitation

The pressure on a hydrofoil underneath a steady sheet cavity is constant and equal to the vapor pressure. This pressure distribution can result in an increase in lift, compared to the noncavitating or *fully-wetted* case. Because the main flow is directed along the cavity and the cavity interface acts as a free shear layer, the main flow experiences a freeslip boundary condition and no boundary layer is formed. If this situation is stable, this means that for a cavitating hydrofoil the lift to drag ratio can be higher than for a fully-wetted hydrofoil. Numerical results [55] support this idea.

2.4 Concluding remarks

Hydrodynamic cavitation occurs when due to the flow dynamics the pressure falls below the vapor pressure and a vapor filled bubble is formed. Depending on the cavitation number and the shape of the pressure distribution, cavitation can take different forms. Cavitation can degrade the performance of hydraulic installations and cause structural damage due to erosion and vibration-induced fatigue. Only in very special circumstances cavitation can have a positive effect on the lift to drag ratio of hydrofoils.



Chapter 3

Review of methods for numerical modeling of cavitation with the Euler and Navier-Stokes equations

3.1 Introduction

A brief introduction is given to the plethora of methods currently used to model sheet and cloud cavitation with the Euler and Navier-Stokes equations. For a more elaborate discussion we refer to the review article of Schnerr et al. [76].

Basically, two approaches can be followed. The fundamental distinction between the two methods is similar to the one encountered in supersonic steady flow computations around blunt bodies. First of all one can try to track the position of the shock and then divide the computational domain in an elliptic region and a hyperbolic region, applying boundary conditions and jump conditions on the interface. On the other hand, one can solve the unsteady equations until a steady state has been reached. Then the whole domain is hyperbolic and the shock will develop in a natural way. The first approach is referred to as *interface tracking*, the second one as *interface capturing*.

In the case of cavitation one can try to iteratively find the position of the cavity interface and divide the domain into an incompressible high density part (liquid) and an incompressible low density part (vapor), applying a constant pressure boundary condition on the interface (Section 3.2), or one can use an artificial compressible medium where the cavity interface can develop in a natural way as a shock/shear layer (Section 3.3). To specify the relation between density and pressure/enthalpy in the latter case, one can use steady state thermodynamical relations (Section 3.3.1), or more elaborate models based on bubble dynamics (Section 3.3.2), that try to include the effects of noninstantaneous interfacial mass transfer.

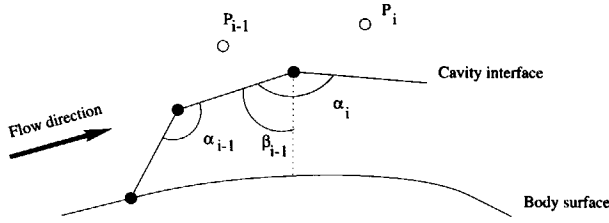


Figure 3.1: Iterative solution of the cavity interface according to [13].

3.2 Interface tracking methods

Interface tracking algorithms are a natural extension of the cavity models used in combination with potential theory, for instance [47, 58], developed in the past and now used in industry.

It is reasoned that due to the fact that the density inside the cavitation bubble is several orders of magnitude smaller than in the liquid state, the influence of the internal flow can be neglected. On the water/vapor interface the following boundary conditions are imposed:

$$\mathbf{V} \cdot \mathbf{n} = 0, \quad (3.1)$$

$$p = p_{\text{vapor, effective}}. \quad (3.2)$$

Here, $p_{\text{vapor, effective}}$ is p_{vapor} , corrected for the nuclei content of the water. The boundary condition (3.1) implies that the flow through the cavity interface is neglected. However, calculations based on interface capturing techniques (Sect. 3.3) indicate there is a substantial mass transfer through the cavity interface. The position of the cavity is found iteratively. The calculation is started assuming the length of the cavity to be equal to the length of the region where $p \leq p_{\text{vapor}}$ and the cavity thickness equal to be zero. Then the cavity interface is shifted in both normal and tangential directions to fulfill the boundary conditions. If, for instance, this boundary is approximated by a sequence of straight line segments, a relation can be derived [13] between an increment in the angle between two consecutive line segments and the pressure increment (Fig. 3.1). After each iteration the geometry of the interface is updated in the following way:

$$\alpha_{i-1}^{n+1} = \alpha_{i-1}^n + C (P_{\text{vapor}} - P_i), \quad (3.3)$$

where C is a small empirically determined constant. The new radial location of the grid points will be:

$$r_i^{n+1} = r_{i-1}^{n+1} - (z_i - z_{i-1}) \times \cot(\alpha_{i-1}^{n+1} - \beta_{i-1}^{n+1}). \quad (3.4)$$

After the boundary location is updated the computational grid is recomputed. More sophisticated models employ a small dense separate grid for the cavity region [55]. Due to the fact that the trailing edge of the cavity interface is not well-defined physically and that in the case of a viscous calculation the free-slip boundary condition on the bubble does not match the no-slip boundary condition on the solid surface, an artificial closure region has to be specified with a spline or a trigonometric function to close the aft part of the cavity.

There is no clear benefit for using an Euler based interface tracking technique over a much less costly potential flow calculation. Use of the Navier-Stokes equations can give a better estimate of the position of the leading edge of the cavity, but viscosity effects can also be included in the value of the effective vapor pressure. The method does not allow for parts of the bubble being shed into the free flow. Potential flow based methods have been developed to allow for the growth of a reentrant jet [19], but the simulation has to be stopped when the reentrant jet separates a part of the cavity. Because in most cases sheet and cloud cavitation occur simultaneously in the flow domain, an interface tracking method can never give a complete picture of the cavitation. Finally, the extension of interface fitting methods to three spatial dimensions is not a trivial task, especially in complex flow geometries encountered in cavitating turbomachinery. Then the evolution of an interface plane, instead of an interface line, has to be computed.

3.3 Interface capturing methods

In interface capturing models, the two-phase flow is modeled as the flow of a homogeneous mixture of liquid and vapor. The density of this artificial medium is equal to the density of the liquid phase when the void fraction α is equal to zero, and the density is equal to the density of the vapor phase when the void fraction is equal to unity. There are two ways to model the evolution of the void fraction.

The first approach is to assume thermodynamic equilibrium and that both phases are at saturation. Then the void fraction is a function of the pressure only. When the pressure is above the vapor pressure the void fraction is equal to zero and the density equal to the liquid density and when the pressure is below the vapor pressure the void fraction is equal to unity and the density equal to the density of the vapor phase. The vapor pressure depends on the local temperature, so that $\alpha = \alpha(p, T)$. Effectively this means that mass transfer between the two phases occurs instantaneously. Although this is only an approximation of the physical situation, in most cases the mass transfer takes place on a time scale orders of magnitude smaller than the shedding period. This model is referred to as the *Homogeneous Equilibrium Model*.

In the second approach the mass transfer between the two phases occurs in finite time. This is the approach that has to be followed to simulate high frequency cavitation phenomena, where the time scale of the mass transfer is of the same order of magnitude as the cavitation cycle. The behavior of the void fraction is governed by a convection equation with a source term, that describes the interfacial mass transfer. The latter is either an empirical expression, or derived from a bubble dynamics model.

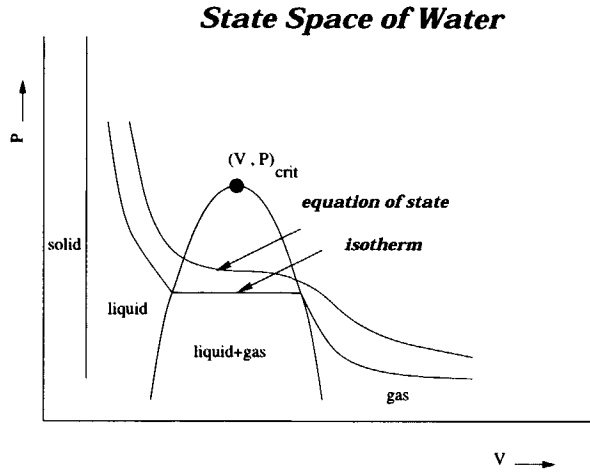


Figure 3.2: The equation of state in the (P, V) space.

Principally, there is no difference in the application of these methods in two or three space dimensions.

3.3.1 The Homogeneous Equilibrium Model

This approach starts with the pioneering work of Delannoy [20]. He chose to follow this approach, because at the time being (1989) no accurate expressions were available to describe the interfacial heat and mass transfer in the case of hydrodynamic cavitation. Because in the case of cavitation of water, the flow can be regarded as isothermal, the void fraction, and therefore the density, is a function of the pressure only. According to the assumptions of the model, the relation between pressure and density should be according to the isotherm shown in Fig. 3.2. This approach is followed in [97]. However, to improve the robustness of the method the isothermal equation of state can be regularized (Fig. 3.2). The slope of the equation of state in the transition region is matched with experimental and theoretical values of the minimal speed of sound in a bubbly mixture. No large variations to the equation of state are found in the literature and the precise specification of the equation of state in the transition region does not seem to influence the solution significantly. The main difference in the methods presented in the literature lies in the treatment of the (nearly) incompressible liquid phase, either with artificial compressibility/preconditioning methods or with projection methods like SIMPLE [66], ICE [32] or PISO [38].

Like in the review article [76] we present the procedures used in tabular form in Tables 1 and 2.

Author	equation of state	solution procedure	time discretisation	space discretisation	Viscous	Turbulence	Application
Delannoy [20, 21, 70]	incompressible+ sine transition	SIMPLE	Euler impl.	HLEPA	yes	$k - \epsilon$	duct hydrofoil
Janssen [43]	incompressible+ sine transition	coupled psd. compr.	BDF2	Jameson	no	no	hydrofoil
Song [85]	compressible+ polyn. transition	coupled	McCormack pred./corr.	central	yes	Smagorinsky	hydrofoil
Shin [79]	empirical relations	coupled	McCormack pred./corr.	TVD	yes	no	duct flat plate
Merkle [63]	incompressible+ spline transition	coupled precond.	Euler impl.	TVD	yes	no	hydrofoil
Ventikos [97]	steam table	iterative PISO	Euler impl.	?	yes	no	hydrofoil

Table 3.1: Overview of interface capturing methods employing the HEM.

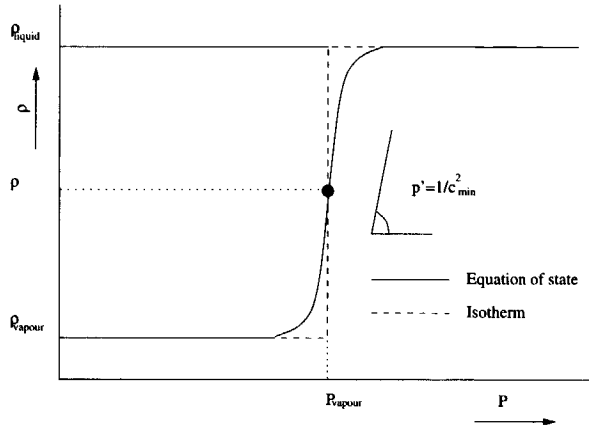


Figure 3.3: The equation of state for the mixture.

3.3.2 Nonequilibrium models

In nonequilibrium models the interfacial mass transfer is explicitly described by an empirical expression [52] or is derived from a bubbly flow model. In the latter approach the flow is regarded at a macroscopic scale and a microscopic scale. In the microscopic model the fluid is a mixture of well separated spherical bubbles filled with incompressible vapor, surrounded by incompressible liquid. In the macroscopic model the density is averaged and the fluidum behaves as a compressible liquid. The evolution of a spherical bubble is described by the Rayleigh-Plesset equation (See for instance [5]). Assuming locally uniformly distributed bubbles, an equation can be derived coupling the evolution of the pressure to the evolution of the void fraction. An additional refinement is the inclusion of the effects of the surface tension and the number of nuclei in the water. This approach started with the work of Kubota [50, 89, 111]. In [82] it is brought forward, that in spite of the fact that the model can predict a number of cavitation phenomena, the assumption of a fluid with locally uniformly distributed bubbles that do not coalesce may not be uniformly valid. This means that high void fraction is described as a situation with a larger number of smaller bubbles than in the physical situation, where coalescence will increase the size but reduce the number of bubbles [14]. In [50, 77, 89, 111] a modified form of the MAC-scheme is applied. In [50, 89, 111] the bubble density n is fixed, whereas the method in [77] includes an additional convection equation for n .

To explain the idea of the incorporation of bubble dynamics we describe the approach of [77]. The semi-discretised momentum equation reads:

$$\frac{\partial(\rho u)}{\partial t} + N((\rho u)^n) = -Gp^{n+1}, \quad (3.5)$$

where N and G are the discrete (nonlinear) convection operator and the discrete gradient operator respectively. By taking the discrete divergence D we get:

$$\begin{aligned} DGp^{n+1} &= -D \left(\frac{\partial(\rho u)}{\partial t} \right) - DN((\rho u)^n) = \\ DGp^{n+1} &= -\frac{\partial}{\partial t} D(\rho u) - DN((\rho u)^n). \end{aligned} \quad (3.6)$$

By substitution of the semi-discretised mass conservation equation we obtain:

$$DGp^{n+1} = \rho_{tt}^n - DN((\rho u)^n). \quad (3.7)$$

Under the assumption of locally uniformly distributed spherical bubbles, ρ_{tt} can be derived from the Rayleigh-Plesset equation for a single bubble, as the bubble density is known.

A very ad hoc method to include nonequilibrium effects is to use the following relation between pressure and density [14]:

$$\frac{D\rho}{Dt} = C_0(p - p_0), \quad (3.8)$$

with $C_0 \gg 1$ and the value of C_0 arbitrary, combined with the constraint:

$$\rho \leq \rho_{\text{vapor}}. \quad (3.9)$$

Small changes of the pressure with respect to the vapor pressure result in large changes of the density, effectively causing a constant pressure in the cavity zone. Chen et al. [14] claim that this formulation is more stable than prescribing the vapor pressure in the cavitating regions directly. Secondly, the solution does not depend on the choice of the parameter C_0 , if it is taken sufficiently large.

3.4 Comparison between interface capturing and fitting

We summarize the differences between the interface fitting and capturing approaches in terms of applicability, accuracy and efficiency.

Applicability

An interface fitting method can only be applied to model isolated cavities. Although in theory cloud cavitation can be modelled by an interface fitting method, in practice tracking all individual bubbles is not feasible. Therefore, an interface fitting method cannot describe all stages in the cavitation cycle described in Section 2.1. Furthermore, extension of interface fitting methods to three spatial dimensions and complex geometries is not straightforward.

Accuracy

Although it seems that the liquid/vapor interface is much more accurately computed with an interface fitting method than with an interface capturing method, the contrary is true. In reality the interface is not well defined and consists of coalescing bubbles. Furthermore, in interface fitting the mass transfer between phases is neglected.

Computational cost

Application of an interface capturing method will require a compressible/incompressible flow solver, whereas an incompressible flow solver will suffice for an interface fitting method. Standard collocated schemes for compressible flow are inefficient and inaccurate for computation of incompressible flow. However, a staggered scheme can be formulated to have efficiency and accuracy uniform in the Mach number. This scheme can nearly match the efficiency of an incompressible flow solver. The development of a Mach-uniform scheme for the HEM is one of the subjects of this thesis.

3.5 Conclusions

We have described the different capabilities and shortcomings of interface capturing and interface fitting methods for the computation of cavitation. Interface capturing methods are more accurate and have broader applicability than interface fitting methods. The application of standard collocated schemes make interface capturing methods less efficient than interface capturing methods. However, it is believed that a Mach-uniform staggered scheme can improve the efficiency of interface capturing; this we will investigate.

Chapter 4

The interface capturing method of Delannoy

4.1 Introduction

As a starting point for further development we choose the method developed by Delannoy [20] for a number of reasons. First of all, it is the most generally applicable model, because it can describe all types of cavitation mentioned in Chapter 2. Despite its simplicity, it retains the key elements of two-phase flow: large variations in density and speed of sound. Furthermore, the method can be readily implemented in the framework of a perfect gas Mach uniform flow solver. Finally, the approach can be extended to incorporate viscous effects and turbulence.

4.2 Governing equations

It is assumed that the flow can be regarded as isothermal and inviscid. Experiments show that the flow at the aft end of the cavitation bubble is highly turbulent. However, well established turbulence models for unsteady two-phase flow are not yet available. Therefore, inviscid flow is assumed. In view of the high value of the Reynolds number (typically 10^{-6} , based on the chordlength of the hydrofoil), this seems more appropriate than to assume laminar viscous flow.

Although it is known that the leading edge position of the cavitation bubble on a smooth body is indeed influenced by the boundary layer, this dependence is circumvented in this study by choosing test cases, where the cavity develops at the downwind side of a sharp corner, that fixes the position of detachment. The assumption of inviscid flow also reduces the computational time with respect to viscous or turbulent computations.

In this study it is shown that cavitation in cold water can be decoupled in a thermodynamic problem and a dynamic problem. Under the assumption of negligible mass transfer between the two phases, the thermodynamic problem is removed and a purely dynamic, isothermal, problem remains. It is argued that neglecting thermodynamics does not influ-

ence the flow outside the cavity, but the flow inside the cavity and through the interface is only roughly approximated.

The main idea is to model the two-phase flow as a homogeneous mixture, by averaging in time and space. Under the assumption of thermodynamic equilibrium and neglecting velocity slip, equations for the conservation of momentum and mass of the mixture are derived, that turn out to be identical to the single phase isothermal Euler equations. Furthermore, mass transfer between the two phases is neglected, and density and pressure are related directly through a barotropic equation of state.

4.3 Equation of state

Starting point for the development of Delannoy's method was assuming an isothermal phase transition between water and vapor. This means that the speed of sound vanishes at the point $p = p_{\text{vapor}}$. This singularity is removed by assuming the fluidum to change continuously from liquid to an intermediate two-phase state to come finally to the pure vapor state. Two different approaches are considered to estimate the speed of sound in this intermediate two-phase state, namely the dynamical approach by Jacobson [42] and the thermal approach of Cooper [15]. The equation of state is chosen in the following way:

- The liquid state is incompressible down to an upper transition pressure.
- The vapor state is incompressible up to a lower transition pressure.
- The intermediate two-phase medium is modeled by the following relation between pressure and density (see Fig. 4.1)

$$\rho = \rho_{\text{vapor}} + \Delta\rho + \Delta\rho \sin\left(\frac{p - p_{\text{vapor}}}{\Delta\rho c_{\text{min}}^2}\right). \quad (4.1)$$

The parameter c_{min} is chosen between the values obtained for the models of Cooper and Jacobsen. The jump in density $\Delta\rho$ and the minimal speed of sound c_{min} , together with the requirement of C^1 continuity dictate the upper and lower transit pressure:

$$\begin{aligned} p_{\text{upp, transit}} &= p_{\text{vapor}} + \Delta p, \\ p_{\text{low, transit}} &= p_{\text{vapor}} - \Delta p, \\ \Delta\rho &= \frac{1}{2}(\rho_{\text{liquid}} - \rho_{\text{vapor}}), \\ \Delta p &= \frac{\pi}{2} c_{\text{min}}^2 \Delta\rho \end{aligned} \quad (4.2)$$

4.4 Numerical method

We summarize the key features of Delannoy's method. This reveals that the method is similar to the Mach-uniform method presented in [7]:

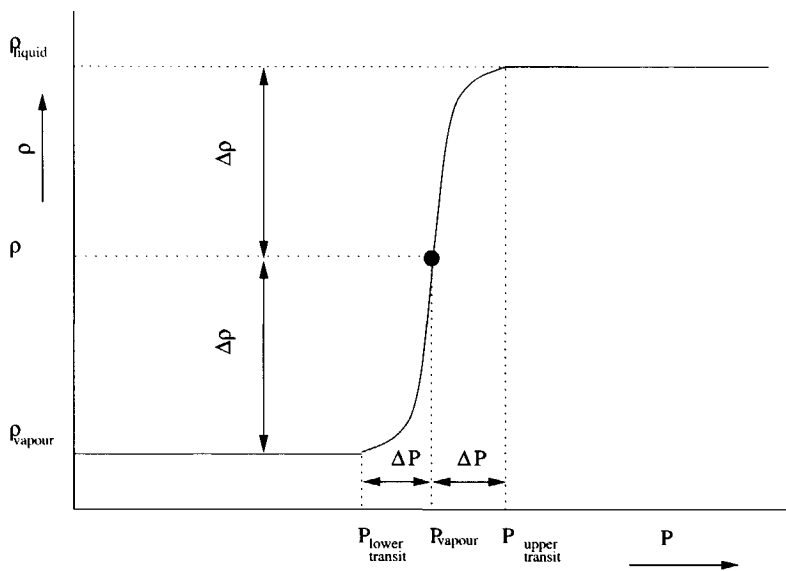


Figure 4.1: The equation of state according to [20] and [36].

- Staggered placement of the unknowns according to ARAKAWA-C arrangement.
- Discretisation in general coordinates and primitive variables.
- Scaling of the pressure, which removes the singularity for $M \downarrow 0$.
- Higher order upwind scheme for both momentum and continuity equation.
- Time stepping with SIMPLE type solution procedure.

These features are more elaborately discussed in the sections below.

4.4.1 Staggered placement of the unknowns

Most of the methods developed for cavitating flow are extensions of existing methods used for incompressible flow. It appears that for cavitating flow the staggered approach is much more commonly used than the collocated approach with Rhie and Chow regularization [72], to treat the incompressible liquid phase.

The application of a staggered scheme by Delannoy to compute solutions of the HEM already showed the capability of staggered schemes for computing highly supersonic flow, although no reference was made to the extreme high Mach number in the computed solution.

4.4.2 Discretisation in general coordinates and primitive variables

In [21] the equations are discretised in the primitive variables u , v , p and ρ in general coordinates, using a conventional approach to approximate the derivatives of the geometric quantities. This means that the method will produce inaccurate results on rough grids, as opposed to the method described in [105, 106, 107].

4.4.3 Scaling of the pressure

To remove the singularity of the compressible Euler equations in the limit $M \downarrow 0$ an appropriate scaling has to be applied to the pressure. In [20] the dimensionless pressure C_p defined as

$$C_p = \frac{p - p_\infty}{\frac{1}{2}\rho U_\infty^2} \quad (4.3)$$

replaces the pressure p as primitive variable. This is equivalent to the approach in [7]. It can be shown that this scaling removes the singularity of the equations and makes the dimensionless density independent of the dimensionless pressure in the limit $M \downarrow 0$. However, Delannoy makes no reference to this fact to motivate his choice.

4.4.4 Higher order upwind schemes

As opposed to the ICE [32] and modified ICE [34] algorithm, which formed the basis of Delannoy's method, use is made of a higher order upwind scheme for both the momentum and the mass conservation equation. This ensures better resolution in the vicinity of discontinuities than the simple first order upwind or central interpolation used in the earlier mentioned methods [32, 34].

4.4.5 SIMPLE type solution algorithm

Both the mass conservation equation and the momentum conservation equation are integrated using the implicit Euler method. This means that a nonlinear system has to be solved, which is accomplished by making use of the compressible form of a SIMPLE/SIMPLER solution procedure. Although not as efficient for perfect gas applications as the ICE or modified ICE method, it is shown in Appendix A that the method has comparable efficiency for the HEM.

Special attention is given to the treatment of the nonlinear equation of state. In the derivation of the pressure correction equation in the ICE-algorithm, all increments in density are replaced by:

$$\delta\rho = \frac{1}{c^2}\delta p \quad (4.4)$$

However, for our strongly nonlinear equation of state this relation is only accurate if the increments in pressure are very small, which implies a very small time step. To overcome this difficulty the relation is underrelaxed: The next iterand for the density is approximated by:

$$\rho^{k+1} = \rho^k + \alpha_\rho (\rho(p^{k+1}) - \rho^k). \quad (4.5)$$

This can be regarded as effectively overrelaxing the speed of sound:

$$\frac{d\rho^{k+1}}{dp} = \alpha_\rho \frac{d\rho}{dp}. \quad (4.6)$$

The solution strategy is most easily explained with an example. Consider a ccl, where the pressure is slightly above the vapor pressure (P1 in Fig. 4.2). This means the density is equal to the liquid density and the speed of sound is infinite, despite the underrelaxation, because the state is regarded as incompressible. The pressure increment following from the pressure correction equation gives a new pressure (P0 in Fig. 4.2), resulting in a state where the fluidum is vapor. Now this pressure is under-relaxed to a new value (P2 in Fig. 4.2) and the density is under-relaxed between the old value and the new value, to give a pressure and density tuplet (ρ_2, P_2) in Fig. 4.2, which does not satisfy the equation of state. Furthermore, when building the pressure correction equation, the effect of the increment in density is disregarded because the speed of sound corresponding to the previous pressure

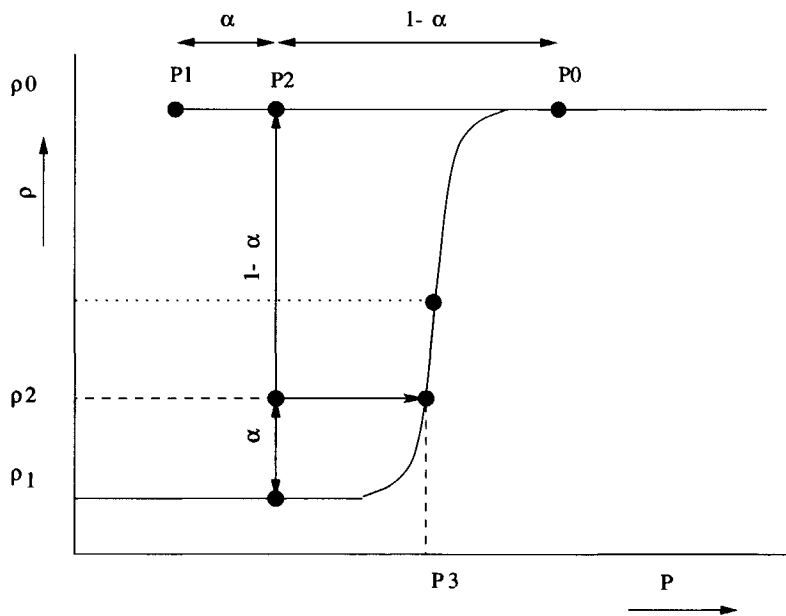


Figure 4.2: Procedure to treat nonlinear equation of state [20].

is infinite. Despite the underrelaxation it is still possible that at certain cells the density will flip between the value of the liquid state and the vapor state.

This is overcome by projecting the under-relaxed density/pressure tuple (ρ_2, P_2) in Fig. 4.2) on the equation of state (ρ_2, P_3) in Fig. 4.2). If the density has an intermediate value, the pressure is calculated by use of the inverse equation of state. The speed of sound corresponding to this latter pressure will indeed have a finite value. This somewhat awkward approach is reported to have a strong positive effect on the speed of convergence of the iterative process within each SIMPLE time step.

4.4.6 Testcases

Apart from standard tests with one-dimensional shocktube problems and a Laval tube simulation, a number of internal cavitating cases are computed in [21]. Cavitating flow is computed in a convergent-divergent channel with a kinked throat. This geometry was experimentally investigated in [61]. As opposed to earlier experiments [28], no reentrant jet is observed but an instability of the liquid/vapor interface that resulted in small parts of the bubble being detached. It was observed that during the cycle of cavity splitting convection of the detached part and collapse and contemporary growth of the new cavity, the sum of the volumes of all bubbles remains constant. Furthermore, the period of the cavity growth/ collapse cycle is proportional to the maximum length of the cavity just prior to the cavity splitting. Both one- and two-dimensional computations have been performed

Start up procedure

All computations are started from the fully wetted condition. This means that the pressure in the flow domain is higher than the vapor pressure. It is noted that the difference between the transit pressures and the vapor pressure (Fig. 4.1) is negligible for an equation of state with physically relevant values of the parameters.

The pressure at the outflow boundary is now lowered until at a certain point in the domain the pressure falls below the vapor pressure and a cavity is formed. It is important to note that, as opposed to [43], the parameters in the equation of state are kept constant.

The rate at which the pressure is lowered is related to the period of the cavity growth/ collapse cycle observed experimentally at the target cavitation number.

One-dimensional cavitation calculation

The geometry of [61] is modeled in one space dimension as a channel with linearly varying cross section. First it is noted that upon decreasing the pressure at the outflow boundary, the pressure will globally decrease in the channel, until the flow starts to cavitate at the throat. Because the flow there is supersonic, further lowering of the outflow pressure will not affect the pressure at the inflow boundary. Delannoy refers to this phenomenon as *sonic blockage*.

The cavity length will grow, even after the outflow pressure has reached its target value, but will converge to a value that depends on the cavitation number. However, if the pressure is lowered very slowly, the converged cavity length is different than when the pressure is lowered more abruptly. This difference in cavity length is identified as a form of quasi-static equilibrium, that can be circumvented if the slow lowering of the pressure is ended with a short but steep decline of the pressure.

In the one-dimensional case it is observed that the length of the cavity does not change when the parameters in the equation of state are altered in the range

$$\begin{aligned} \rho_{\text{vapor}}/\rho_{\text{liquid}} &\in [0.010, 0.10] \\ c_{\text{min}} &\in [0.014, 0.14] \end{aligned} \quad (4.7)$$

However, the time needed for the cavity to converge to steady state depends on the value of c_{min} . This can be explained by the fact that the speed of the shock at the trailing edge of the cavitating zone depends on c_{min} . Buelow [11] observed a similar weak dependence of the solution on the parameters in the equation of state in the two-dimensional case, and explained it by the fact that below a certain threshold value of the density ratio the momentum of the vapor in the bubble is so small that it cannot influence the flow outside the cavity.

By integration of the momentum equation in Lamb-Gromeka form it can be shown that for an inviscid, steady barotropic flow the quantity \mathcal{H} defined as:

$$\mathcal{H} = \int \frac{dp}{\rho} + \frac{1}{2}|u|^2 \quad (4.8)$$

is conserved along streamlines. It is shown that \mathcal{H} is indeed conserved in the whole flow domain, but that \mathcal{H} jumps at the shock at the trailing edge of the cavitating zone. The relation above is obtained from the differential form of the momentum equation and is not valid if the solution only exists in the weak sense.

Due to the effects of sonic blockage, the strong shock at the trailing edge and the discontinuity in \mathcal{H} , Delannoy argues that this one-dimensional case is not representative for the case of two- or three-dimensional cavitating flow.

Two-dimensional cavitation calculation

In the two-dimensional case the same geometry is studied and a qualitative comparison is made with the experimental results of [28, 61]. The same geometry as in the experiments is used, but for the length of the channel, which is increased downstream to reduce the influence of the outflow boundary conditions on the flow near the throat.

The first set of computations was made with a first order upwind scheme. A cavity is formed at the downstream side of the throat. This grows, while at the same time a reentrant jet is formed, that eventually detaches the complete cavity. The cavity contains a vortex generated by the reentrant jet. Finally, the cavity is convected downstream and a new cavity is formed. Due to the strong damping of the time integration scheme the

effects of the initial conditions are damped quickly and the flow becomes periodic. The value of the Strouhal number:

$$S = \frac{L_{\text{cavity,max}}}{U_{\text{throat}} T_{\text{cycle,shedding}}}, \quad (4.9)$$

is over-predicted by a factor of two.

These computations are repeated with a second order limited upwind scheme. The computed velocity and pressure fields show less structure than for the first order scheme. Instead of a reentrant jet, that separates the complete cavity from the channel wall, as observed by [28] experimentally, now the cavity is split in two pieces, of which the aft one is convected as observed in [61]. The reentrant jet moves upward before it has reached the leading edge of the cavity. Furthermore, the forward part recedes and disappears, due to the increase in pressure at the upwind side of the detached part of the cavity. At the location where the bubble is split in two separate bubbles a small vortex, secondary to the vortex contained in the detached part of the bubble, is formed. Delannoy argues this has a purely numerical background. Finally it is mentioned that there is an interaction between the growing, collapsing and shed cavities in the flow domain. This means that the detached bubbles while being convected to the outflow boundary, still influence the pressure field and hence the growth of the new cavity.

4.5 Conclusions

In [20, 21] the author focussed on the feasibility of application of the HEM for the computation of cavitation. We have highlighted the positive aspects of the algorithm utilized, that illustrates the applicability of a staggered scheme for the computation of highly compressible flow. Given the simplicity of the model and the numerical techniques utilized the correlation between the computed results and experiments is acceptable, but for the overprediction of the Strouhal number. Our aim is to improve the efficiency and (temporal) accuracy of the numerical method.



Chapter 5

Analysis of the equation of state

5.1 Introduction

In this chapter we consider isothermal phase transition as a basis for deriving an equation of state for the water/vapor mixture. This basic mixture equation of state has to be formulated in such a way the three laws of thermodynamics are satisfied and thermodynamic stability is maintained.

5.2 The state diagram of water

Phase transition due to *cavitation* is not the same as due to *boiling*. The former is an adiabatic process, while in the latter case the energy needed for the phase transition is supplied by an external heat source and the process is isothermal. However, also for cavitation the assumption of isothermal flow is often made, as the amount of heat transferred is very small at 10 – 15°C. Fig. 5.1 shows an isotherm for 20°C in the pressure/specific volume plane, for values of pressure interesting from an engineering point of view. We distinguish three zones:

1. *The liquid phase:*

$$p > p_{\text{vapor}} \text{ and } V < V_{\text{saturation,liquid}}$$

Here the fluidum is almost incompressible.

2. *The coexistence state:*

$$p = p_{\text{vapor}} \text{ and } V_{\text{saturation,liquid}} < V < V_{\text{saturation,vapor}}$$

The ratio of the water and vapor density is 60000 across the phase change. This number increases with decreasing ambient temperature.

3. *The vapor phase:*

$$p < p_{\text{vapor}} \text{ and } V > V_{\text{saturation,vapor}}$$

For the vapor phase the relation between pressure, temperature and specific volume

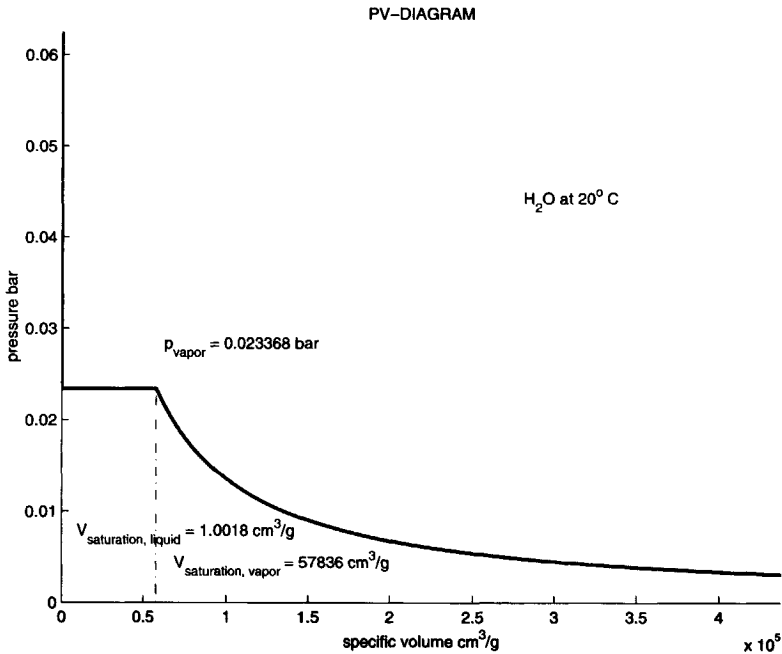


Figure 5.1: Isotherm of H_2O at $20^\circ C$

is given by the following standard form derived in the 1960s [2]. This relation involves small corrections for deviation from behavior of a perfect gas (see Fig. 5.2):

$$v = \frac{RT}{p} + a_0(T) + pa_1(T) + p^4 a_2(T). \quad (5.1)$$

It is clear that in the limit of pressure to zero the vapor will behave like a perfect gas, as opposed to the behavior implied by the equation of state in [20].

Remarks:

- In real flow there will always be an amount of undissolved gas in the form of small bubbles in the water, effectively making the liquid phase more compressible [37].
- The isotherm is not C^1 continuous across the phase transition.

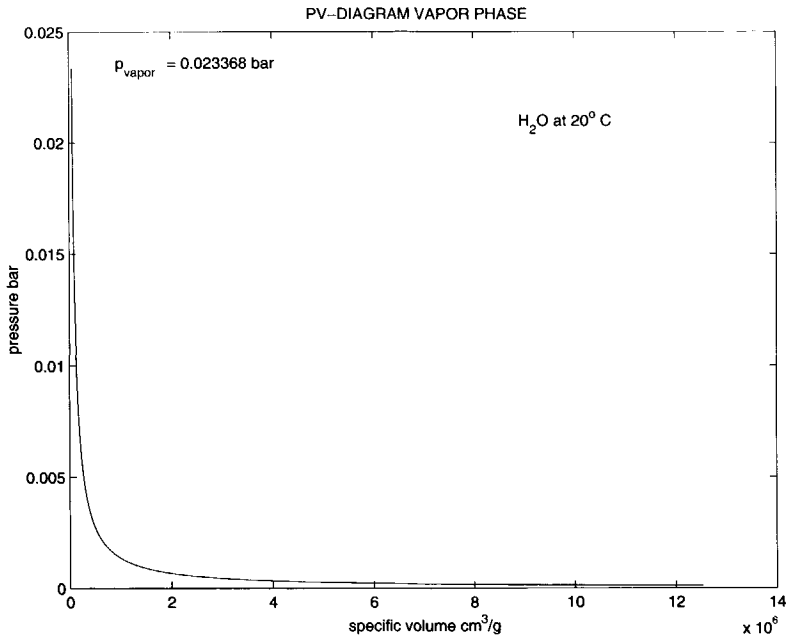


Figure 5.2: Detail of isotherm of the vapor phase of H_2O at 20°C

5.3 The equation of state

The equation of state in [20] and [63] is constructed from an empirical point of view. It is known that the density of the mixture should be the density of the liquid above the vapor pressure and it should be equal to the density of vapor well below the vapor pressure. The transition region is modeled based on empirical knowledge of the speed of sound in a bubbly mixture. As we only need the relation between pressure and density in the computational process, an incomplete equation of state suffices [62]. In theory one should first derive an complete equation of state $E(V, S)$, and therefrom an incomplete equation of state $P(V, E)$. The complete equation of state should obey the three laws of thermodynamics. Completing an incomplete equation of state with an entropy function to obtain a complete equation of state may not be possible or unique. Only if an incomplete equation of state can be completed to a complete equation of state, the former can be regarded as a physical constitutive relation [62]. In the isothermal case, an equation of state $E(S, V)$ can be characterized by the following two quantities: The adiabatic exponent:

$$\gamma = -\frac{V}{P} \frac{\partial P}{\partial V} \Big|_S, \quad (5.2)$$

and the fundamental derivative:

$$\mathcal{G} = -\frac{1}{2} \frac{\partial^3 E / \partial V^3 \Big|_S}{\partial^2 E / \partial V^2 \Big|_S} = \frac{1}{2} \frac{V^2}{\gamma P} \frac{\partial^2 P}{\partial V^2} \Big|_S, \quad (5.3)$$

and by the asymptotic behavior of the equation of state.

Remarks

- Obviously V should be strictly positive, as should P , because the fluidum cannot sustain tension. Thermodynamic stability requires γ to be strictly nonnegative [62]. Therefore the function $P(V)$ should be monotonically decreasing. As a result, a mixture equation of state maintaining isothermal behavior during phase transition will be thermodynamically unstable. This undesirable property can be avoided by keeping a finite speed of sound in the transition region.
- Thermodynamics does not put a requirement on the sign of \mathcal{G} [62]. However, if \mathcal{G} changes sign in the domain, simple wave solutions will have a more complicated, so-called composite, structure, which is more elaborately discussed in chapter 6. Furthermore, if \mathcal{G} does not exist, because there is a kink in the equation of state, discontinuous solutions will no longer be stable against shock-splitting [62]. This means that, as opposed to the strictly convex case, a perturbation can split up a discontinuity into two separate shocks.
- In the limit of vanishing specific volume a natural requirement is [62]:

$$\lim_{V \rightarrow 0} P(V) = \infty. \quad (5.4)$$

- In the limit of vanishing pressure a natural requirement is [62]:

$$\lim_{P \rightarrow 0} V(P) = \infty, \quad (5.5)$$

since this makes $P(V)$ invertible in the presence of thermodynamic stability.

5.4 Conclusions

The structure of the isothermal phase transition and the requirements imposed by thermodynamics, which have to be applied so the mixture equation of state will have thermodynamic stability, have been discussed.



Chapter 6

The Riemann problem for a nonconvex hyperbolic system

6.1 Introduction

To test numerical schemes we will construct two analytical solutions. In one space dimension it is possible to construct exact solutions to a nontrivial initial value problem for the isothermal Euler equations, so-called Riemann problems, comprising two simple wave solutions. First we discuss the structure of the simple waves and then we show how to construct the solution to a nontrivial initial value problem, using the simple wave solutions following the approach of [102].

6.2 Simple waves

By transforming the barotropic Euler equations :

$$\frac{\partial m}{\partial t} + \frac{\partial mu}{\partial x} = -\frac{\partial p}{\partial x}, \quad (6.1)$$

$$\frac{\partial \rho}{\partial t} + \frac{\partial m}{\partial x} = 0, \quad (6.2)$$

to a Lagrangian frame of reference:

$$t' = t, \quad (6.3)$$

$$x' = \int_0^x \rho(\eta, t) d\eta, \quad (6.4)$$

$$v = \frac{1}{\rho}, \quad (6.5)$$

the well-known p -system is obtained:

$$\begin{aligned}\frac{\partial u}{\partial t} + \frac{\partial p}{\partial x} &= 0, \\ \frac{\partial v}{\partial t} - \frac{\partial u}{\partial x} &= 0.\end{aligned}\tag{6.6}$$

Whereas the wave speeds in the Eulerian frame of reference are given by:

$$\lambda = u \pm \sqrt{p'(\rho)},\tag{6.7}$$

in the Lagrangian frame they take the following simple form:

$$\lambda = \pm \sqrt{-p'(v)},\tag{6.8}$$

which makes a geometrical construction of the solution easy.

We will now give a brief overview of the construction of simple wave type solutions, which is elaborately explained in [12]. Simple waves are so-called similarity or scale-invariant solutions, so $u = u(\xi)$, $v = v(\xi)$; $\xi = x/t$. Substitution of this type of solution in (6.7) transforms the system of PDEs to a system of ODEs:

$$-\xi \frac{du}{d\xi} + \frac{dp(v)}{d\xi} = 0,\tag{6.9}$$

$$\xi \frac{dv}{d\xi} + \frac{du}{d\xi} = 0.\tag{6.10}$$

Following [12], any smooth solution to this system will satisfy:

$$\begin{bmatrix} -\xi & p'(v) \\ 1 & \xi \end{bmatrix} \begin{bmatrix} du \\ dv \end{bmatrix} = 0,\tag{6.11}$$

which leads to the right running rarefaction wave

$$\xi = \lambda_1 \equiv -\sqrt{(-p'(v))},\tag{6.12}$$

$$ds \equiv du - \sqrt{(-p'(v))}dv = 0,\tag{6.13}$$

and the left running rarefaction wave

$$\xi = \lambda_2 \equiv \sqrt{(-p'(v))},\tag{6.14}$$

$$dr \equiv du + \sqrt{(-p'(v))}dv = 0.\tag{6.15}$$

The requirement of thermodynamic stability on the adiabatic exponent γ ensures that the two wavespeeds will always be real.

Now the set of all left and right running rarefaction waves is defined by the integral curves of (6.13) and (6.15), the rarefaction curves $u = \mathcal{R}_1(u_0, v_0, v)$ and $u = \mathcal{R}_2(u_0, v_0, v)$

respectively.

Similarly, the structure of discontinuous solutions follows from the Rankine-Hugoniot conditions:

$$\omega[u] = [p], \quad (6.16)$$

$$\omega[v] = -[u]. \quad (6.17)$$

Here ω denotes the speed of the shock, and $[f] \equiv f_{\text{left}} - f_{\text{right}}$ denotes the jump in the quantity f . For the right going shock this is equivalent to

$$\xi = \omega_1 = -\left(-\frac{[p]}{[v]}\right)^{\frac{1}{2}}, \quad (6.18)$$

$$S_2 \equiv [u] - \left(-\frac{[p]}{[v]}\right)^{\frac{1}{2}} [v] = 0, \quad (6.19)$$

and for the left going shock to

$$\xi = \omega_2 = \left(-\frac{[p]}{[v]}\right)^{\frac{1}{2}}, \quad (6.20)$$

$$S_1 \equiv [u] + \left(-\frac{[p]}{[v]}\right)^{\frac{1}{2}} [v] = 0. \quad (6.21)$$

The set of all left and right running shocks is given by the shock relations (6.19) and (6.21), namely the shock curves $u = \mathcal{S}_1(u_0, v_0, v)$ and $u = \mathcal{S}_2(u_0, v_0, v)$ respectively.

The Lax characteristic condition states that characteristics should enter a shock from both sides, if the shock respects the entropy condition. This means that some parts of the shock and expansion curves are not physically realizable. Based on this consideration the wave curves, comprising the entropy condition satisfying parts of the shock and rarefaction curves are given, in the case of a convex equation of state by:

$$u = \mathcal{W}_1(u_0, v_0, v) = \begin{cases} \mathcal{S}_1(u_0, v_0, v), & 0 < v < v_0 \\ \mathcal{R}_1(u_0, v_0, v), & v_0 < v \end{cases} \quad (6.22)$$

for the left going wave curve, and

$$u = \mathcal{W}_2(u_0, v_0, v) = \begin{cases} \mathcal{S}_2(u_0, v_0, v), & v_0 < v \\ \mathcal{R}_2(u_0, v_0, v), & 0 < v < v_0 \end{cases} \quad (6.23)$$

for the right going wave curve. The wave curves define all states lying to the right of the state (u_0, v_0) by a left or right going simple wave, that satisfies the entropy condition. It can be seen that in the convex case a state will always be expanded upon passage of an expansion fan and always compressed upon passage of a shock.

In the case of a nonstrictly convex equation of state, the simple waves will have a

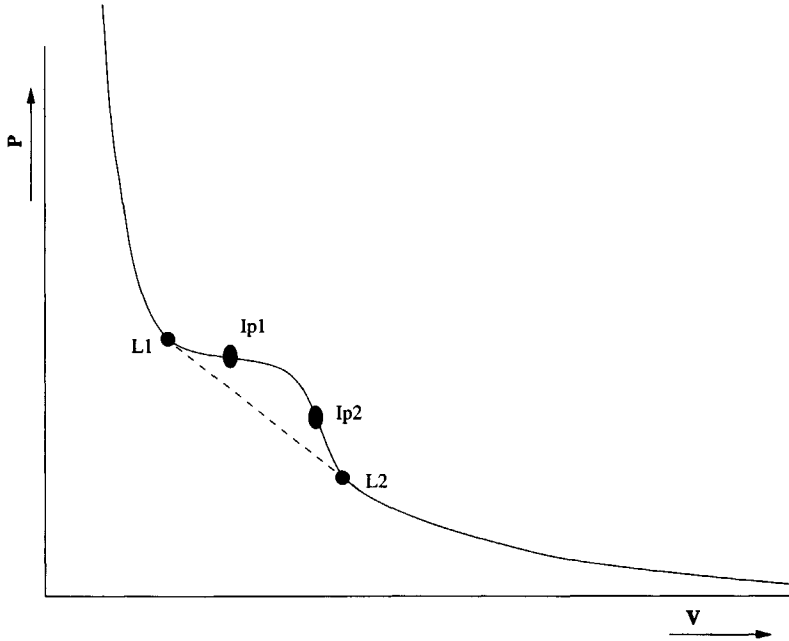


Figure 6.1: The model equation of state

different structure, which is illustrated here with the model equation of state shown in Fig. 6.1. The equation has identical structure to the isotherm discussed in the previous section, but the kinks in the physical case have been removed to avoid shock splitting and enhance numerical stability.

The equation of state is characterized by four values of the specific volume. Two inflection points $ip1$ and $ip2$ mark the beginning and the end of the concave zone and two points denoted by $L1$ and $L2$ help to define the *convex hull* of the equation of state, which plays an important role in defining the structure of the composite waves. First of all, in the concave zones, physical expansion shocks can occur, as is shown by Bethe [62]:

$$\Delta S = -\frac{1}{6} \mathcal{G} \frac{c^2}{T} (\Delta V/V)^3 [1 + \mathcal{O}(\Delta V/V)], \quad (6.24)$$

where ΔS is the jump in entropy across the shock. This means that where \mathcal{G} is positive, an entropy condition satisfying shock is compressive, and when \mathcal{G} is negative the fluid will expand on passage of the discontinuity.

Similarly, the following relation can be derived for an expansion fan [62]

$$d\xi = d(u \pm c) = \mp \rho c \mathcal{G} dV = \pm \mathcal{G} [P/\rho]. \quad (6.25)$$

This means that in the concave case ($\mathcal{G} > 0$) a state will be compressed upon passage of an expansion fan. We will now explain the construction of a composite wave, following the approach of [102].

Right running composite wave Consider the state (v_m, p_m) , which has to be connected to the state $(v_{\text{right}}, p_{\text{right}})$ with a right running wave (cf. Fig. 6.2. In the convex case both states would be connected by a right running shockwave, as indicated by the Rayleigh line 0 in Fig. 6.2. This would, however, in the case of Fig. 6.2 violate the entropy condition, which takes the following form [102]:

$$\lambda(v) < \sigma < \lambda(v_0), \quad (6.26)$$

$$\sigma = \sigma(v, v_0) = \sqrt{\left| \frac{p - p_0}{v - v_0} \right|}, \quad (6.27)$$

which states that in this case the Rayleigh line should lie above the equation of state. Hence, all states between (v_m, p_m) and $(v_{\text{int1}}, p_{\text{int1}})$ can be connected to (v_m, p_m) by a single shock. However for $v > v_{\text{int1}}$ the condition (6.27) is not fulfilled, and we have to continue in another way from the state $(v_{\text{int1}}, p_{\text{int1}})$. Between the state $(v_{\text{int1}}, p_{\text{int1}})$ and the inflection point *ip2* the equation of state is concave. This means that for this right running wave the characteristics are diverging, so state $(v_{\text{int1}}, p_{\text{int1}})$ can be connected to any state between $(v_{\text{int1}}, p_{\text{int1}})$ and the inflection point *ip2* by a right running rarefaction wave. For states with $v > ip2$ this cannot be accomplished because the fundamental derivative cannot change sign within an expansion fan (6.25). States left of the inflection point should be connected to states between the state $(v_{\text{int1}}, p_{\text{int1}})$ and the inflection point by means of a right running shock. This has to be done such that the speed of the shock matches the characteristic speed at the boundary of the expansion fan. This is accomplished, if a Rayleigh line is constructed intersecting the final state $(v_{\text{right}}, p_{\text{right}})$ and being tangent to the equation of state somewhere between the state $(v_{\text{int1}}, p_{\text{int1}})$ and the inflection point (Rayleigh line 2 in Fig. 6.2). Summarizing, the state (v_m, p_m) and the state $(v_{\text{right}}, p_{\text{right}})$ are connected by a shock, followed by an expansion fan and another shock.

Left running composite wave Consider the state $(v_{\text{left}}, p_{\text{left}})$, which has to be connected to the state (v_m, p_m) . If the concave zone between *Ip1* and *Ip2* was not there, the two states would be connected by a single expansion fan. However an expansion fan started at $(v_{\text{left}}, p_{\text{left}})$ can not be extended beyond the inflection point *Ip1*, as otherwise \mathcal{G} would change sign within the expansion fan.

The concave zone has to be bridged by a shock in a way such that the shock speed matches the signal speed at the boundary of the expansion fan. Then another ex-

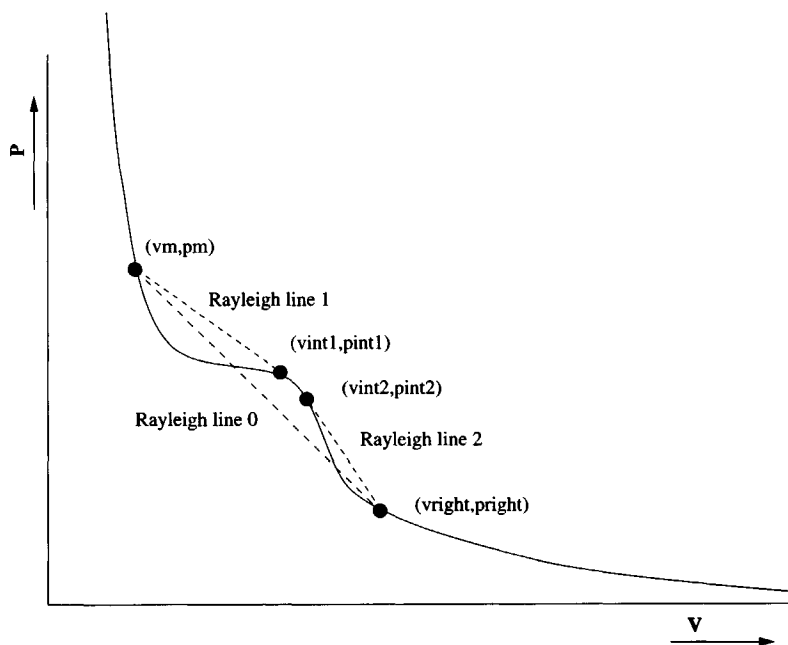


Figure 6.2: Simple wave solution in the nonconvex case, right running.

pansion fan can be followed to reach the final state (v_m, p_m) , as the equation of state is concave there. Also in this case the shock speed has to be in accordance with the signal speed at the boundary of the second expansion fan. This shock is drawn in Fig. 6.3 as the Rayleigh line tangent to the equation of state at both $L1$ and $L2$. This special Rayleigh line belongs to the convex hull of the equation of state.

In the for the HEM relevant case of an equation of state with two points of inflection. The following composite waves are possible:

1. Single shock.
2. Single expansion fan.
3. Shock followed by an expansion fan.
4. Expansion fan followed by a shock.
5. Expansion fan followed by a shock followed by another expansion fan.
6. Shock followed by an expansion fan followed by another shock.

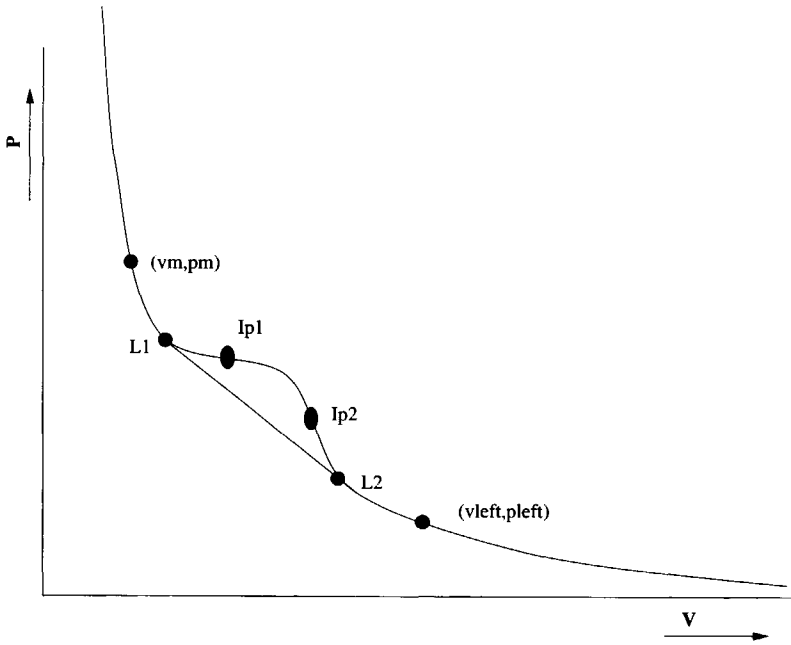


Figure 6.3: Simple wave solution in the nonconvex case, left running.

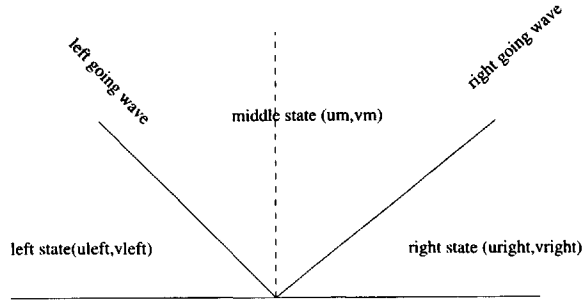


Figure 6.4: Structure of the Riemann problem for the barotropic Euler equations.

If the equation of state is smooth, a composite wave cannot have two neighboring shocks or expansion fans. It is clear from the relations presented in the previous section that in that case, both simple waves can always be regarded as one single wave.

Based on these considerations the *composite* wave curves, comprising the entropy condition satisfying parts of the *composite* shock and *composite* rarefaction curves can be constructed:

$$u = \mathcal{WC}_1(u_0, v_0, v) = \begin{cases} \mathcal{SC}_1(u_0, v_0, v), & 0 < v < v_0 \\ \mathcal{RC}_1(u_0, v_0, v), & v_0 < v \end{cases} \quad (6.28)$$

for the left going composite wave curve, and

$$u = \mathcal{WC}_2(u_0, v_0, v) = \begin{cases} \mathcal{SC}_2(u_0, v_0, v), & v_0 < v \\ \mathcal{RC}_2(u_0, v_0, v), & 0 < v < v_0 \end{cases} \quad (6.29)$$

for the right going composite wave curve.

6.3 The Riemann problem

A Riemann problem is an initial value problem of the following structure:

$$\left. \begin{aligned} u &= u_{\text{left}} \\ v &= v_{\text{left}} \end{aligned} \right\} x < 0 \quad (6.30)$$

$$\left. \begin{aligned} u &= u_{\text{right}} \\ v &= v_{\text{right}} \end{aligned} \right\} x > 0 \quad (6.31)$$

We will consider the convex case, because after construction of the composite wave curves, both cases are completely analogous. The solution will have the structure of Fig. 6.4

Let us choose the left and middle states. Then the right state is found as follows. The

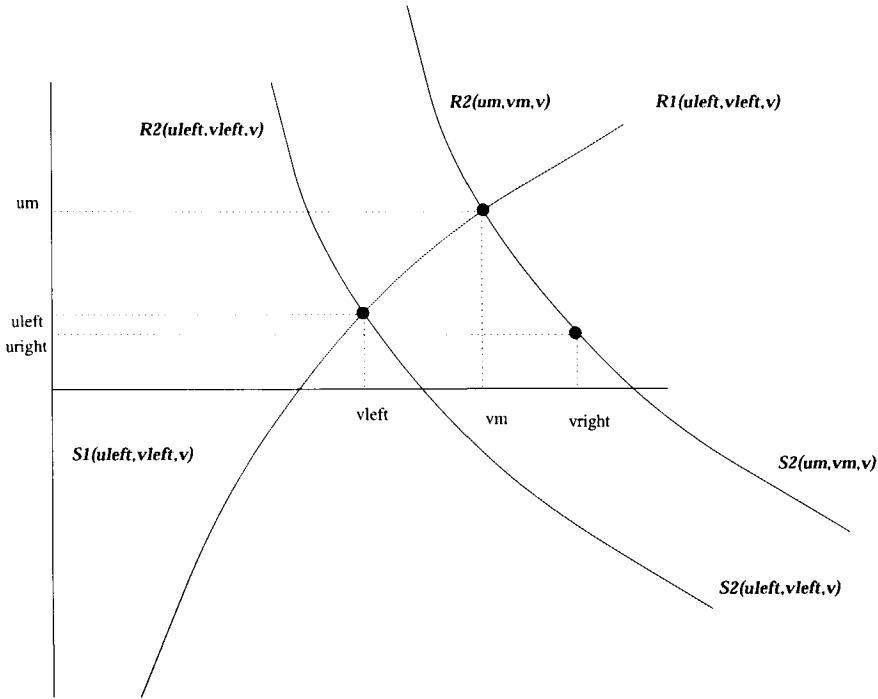


Figure 6.5: Construction of the isothermal Riemann problem

middle state (u_m, v_m) is on the right side of the state $(u_{\text{left}}, v_{\text{left}})$, so we can choose any state on the left going wave curve (either on $\mathcal{R}_1(u_{\text{left}}, v_{\text{left}}, v)$ or on $\mathcal{S}_1(u_{\text{left}}, v_{\text{left}}, v)$) from the left state to define our middle state. Having found the middle state we can proceed with choosing the right state as any state which lies on the right going wave curve of the middle state (u_m, v_m) (either on $\mathcal{R}_2(u_m, v_m, v)$ or on $\mathcal{S}_2(u_m, v_m, v)$). The structure of the left and right running wave is of course dependent on the part of the wave curve where the states are chosen. If we choose a state on the \mathcal{R} part of the wave curve, the states are connected by an expansion fan, otherwise by a shock. This construction is illustrated in the phase plane in Fig. 6.5.

6.4 Construction of a test case

Using the methodology discussed in the previous section two test cases were constructed, using a model equation of state of shape similar to the equation of state of water (two

points of inflection).

6.4.1 The model equation of state

An equation of state has been constructed, which has more parameters to control its properties than the equation of state of [20].

The following properties can be adjusted:

1. Compressibility of the liquid state,
2. Compressibility of the vapor state,
3. The two transition pressures,
4. Continuity from C^1 to C^8 in the transition region.

Although pure water is almost incompressible, a small amount of undissolved gas, that is always present in industrial applications, can change the speed of sound considerably.

As opposed to the equation of state in [20, 63], we treat the vapor phase as compressible, to match the asymptotic behavior of the isotherm, discussed in section 5.2 for the limit of vanishing pressure.

A high degree of smoothness of the equation of state across the transition region diminishes the chance of shock splitting due to numerical accuracies. The latter process may occur only when the wave curves have a kink [62].

The equation of state has the following form:

$$\begin{aligned} \rho &= \rho_0 + c_1 p & ; & \quad p < p_1 \\ \rho &= \rho_0 + c_1 p + c_2 * f(\xi) + c_3 * g(\xi) & ; & \quad p_1 \leq p \leq p_2 \\ \rho &= c_5 + c_4 (p - p_2) & ; & \quad p_2 < p \end{aligned} \quad (6.32)$$

where $f(\xi)$ and $g(\xi)$ are given by:

$$\xi = \frac{p - p_1}{p_2 - p_1} \quad (6.33)$$

$$\begin{aligned} f(\xi) &= \frac{\xi^m (1 - c_6 \xi)}{1 - \frac{(1-\xi)^{c_7} (1 - c_6 (1-\xi))}{c_7}} & ; & \quad \xi < \frac{1}{2} \\ f(\xi) &= \frac{1 - \frac{(1-\xi)^{c_7} (1 - c_6 (1-\xi))}{c_7}}{\frac{1}{8} (2\xi)^{m+1} \left(1 - 2\xi \frac{m-1}{m+2}\right)} & ; & \quad \xi \geq \frac{1}{2} \\ g(\xi) &= \frac{1}{8} (2\xi)^{m+1} \left(1 - 2\xi \frac{m-1}{m+2}\right) & ; & \quad \xi < \frac{1}{2} \\ g(\xi) &= -\frac{1}{2} + \xi - \frac{1}{8} (2 - 2\xi)^{m+1} \left(\frac{(m-1)(2-2\xi)}{m+2} - 1\right) & ; & \quad \xi \geq \frac{1}{2} \end{aligned} \quad (6.34)$$

The following parameters have a direct physical interpretation.

$$c_1 = \frac{1}{c_{\text{vapor}}^2}, \quad (6.35)$$

$$c_4 = \frac{1}{c_{\text{liquid}}^2}, \quad (6.36)$$

$$\Delta\rho = \text{jump in density across the phase transition.} \quad (6.37)$$

$$(6.38)$$

The following parameters can be chosen:

$$p_1 = \text{lower transit pressure,} \quad (6.39)$$

$$p_2 = \text{upper transit pressure,} \quad (6.40)$$

$$m = \text{defines the } C^{m-1} \text{ continuity, } m \leq 9, \quad (6.41)$$

$$\rho_0 = \text{density for } p = 0. \quad (6.42)$$

To simulate the equation of state in [20] [63] it is necessary to incorporate a nonzero ρ for $p = 0$.

The remaining parameters are defined as:

$$c_2 = \Delta\rho - \frac{1}{2}c_3 - c_1(p_2 - p_1), \quad (6.43)$$

$$c_3 = (p_2 - p_1)(c_4 - c_1), \quad (6.44)$$

$$c_5 = \rho_0 + c_1 p_2 + c_2 + \frac{1}{2}c_3, \quad (6.45)$$

$$c_6 = 2\frac{n-1}{n+1}, \quad (6.46)$$

$$c_7 = \frac{2-c_6}{2^n}. \quad (6.47)$$

6.4.2 Testcase 1, zero initial velocity

The following set of parameters was chosen to define the equation of state:

$$\begin{aligned} c_1 &= 4.00 & n &= 9 \\ c_4 &= 0.44 & \Delta\rho &= 4.00 \\ p_1 &= 0.40 & \rho_0 &= 0.10 \\ p_2 &= 0.70 \end{aligned} \quad (6.48)$$

The initial conditions are given by:

$$\begin{aligned} p_{\text{left}} &= 1.1 & u_{\text{left}} &= 0.0 \\ p_{\text{right}} &= 0.1 & u_{\text{right}} &= 0.0 \end{aligned} \quad (6.49)$$

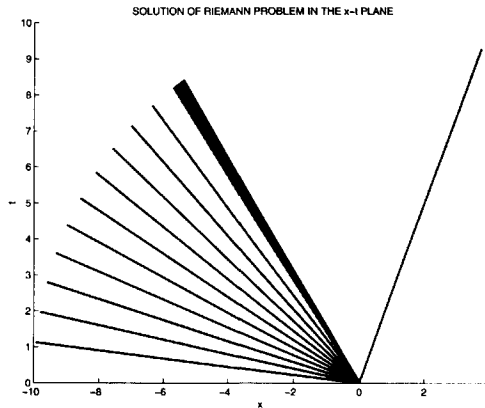


Figure 6.6: Testcase I, structure of solution in Lagrangian frame of reference.

The construction of the solution and its topology are shown in Fig. 6.7. The left going wave curve of the left initial state is plotted together with the inverse right going wave curve for the right state. The inverse wave curve defines all states lying to the right of the initial state, that can be connected to this state by a composite wave. The different symbols indicate different composite waves, that can define the connection between two states.

The intersection point of the left going wave curve and the inverse right going wave curve defines the unknown intermediate state. It is clear that after the wave curves have been constructed the solution can be obtained in exactly the same way as for the strictly convex case. The introduction of the inverse right going wave curve is only necessary to construct a solution where the initial state can be freely chosen, as opposed to the case discussed for the convex case, where we chose to define the left and middle state and then calculate the unknown right state. Note that the wave curves are monotone, thus ensuring uniqueness of the solution.

The topology of the solution is shown in Fig. 6.6. The left state is connected to the middle state by a long expansion fan followed by a shock and another short expansion fan. The middle state is connected to the right state by a single shock.

Fig. 6.8 shows the solution in the Eulerian frame of reference for $t = 0.2$.

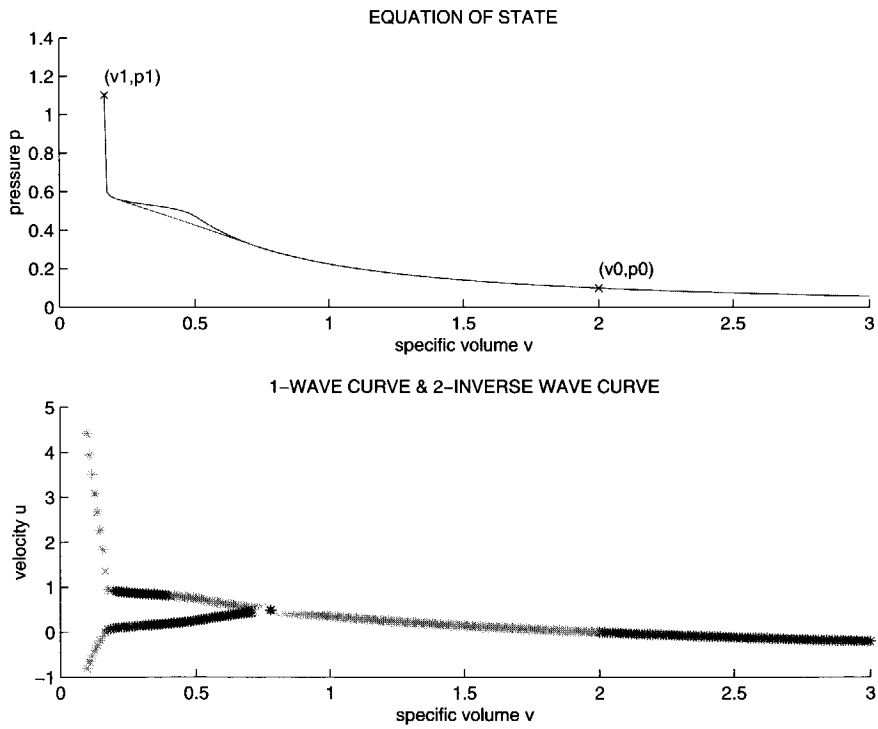


Figure 6.7: Testcase I, construction and solution in Lagrangian frame of reference.

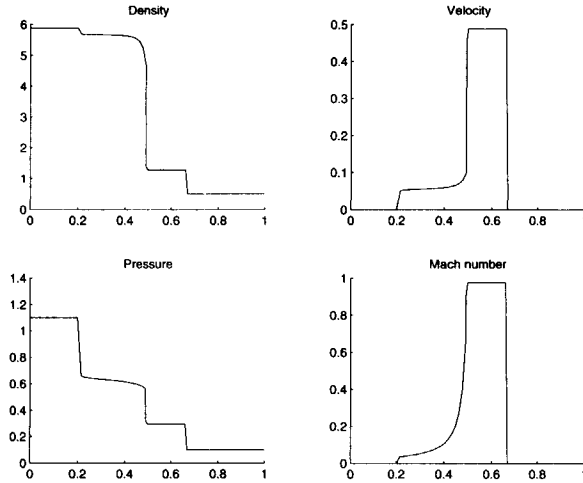


Figure 6.8: Testcase I, solution in Eulerian frame of reference for $t = 0.2$.

6.4.3 Testcase 2, nonzero initial velocity

The second test case uses the same equation of state but has a nonzero initial velocity:

$$\begin{aligned}
 p_{\text{left}} &= 1.1 & u_{\text{left}} &= \frac{1}{\rho(p_{\text{left}})} \\
 p_{\text{right}} &= 0.1 & u_{\text{right}} &= \frac{1}{\rho(p_{\text{right}})}
 \end{aligned}
 \tag{6.50}$$

It is clear that the initial conditions define a continuous initial distribution of the momentum. The structure of the solution is shown in Fig. 6.9. The left state is connected to the intermediate state by a left going expansion fan followed by an expansion shock and another expansion fan. The middle state is connected to the right state by a single expansion fan. Fig. 6.10 shows the solution for $t = 0.2$ in the Eulerian frame of reference. Testcase II is more demanding than testcase I as the two consecutive expansion fans tend to smear out, as opposed to a shock that is "selfsteepening".

Note the small peak in the solution of the Mach number caused by the expansion shock and note the fact that the density in the middle constant state is less than either of the two initial states.

6.5 Conclusions

For the one-dimensional barotropic Euler equations in combination with a strictly convex equation of state solutions to the Riemann problem consist of simple waves, namely

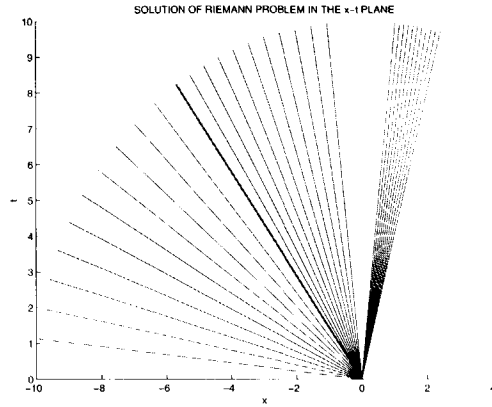


Figure 6.9: Testcase II, topology of solution in Lagrangian frame of reference.

expansion fans and shock discontinuities.

In the case of a nonconvex equation of state solutions to the Riemann problem in general consist of *composite* waves, which may consist of shocks, expansion fans and compression fans. The construction of these composite waves has been discussed following the approach of [102]. To test potential discretisation schemes, two test cases have been constructed, that exhibit the special behavior associated with nonconvex equations of state: composite waves and expansion shocks.

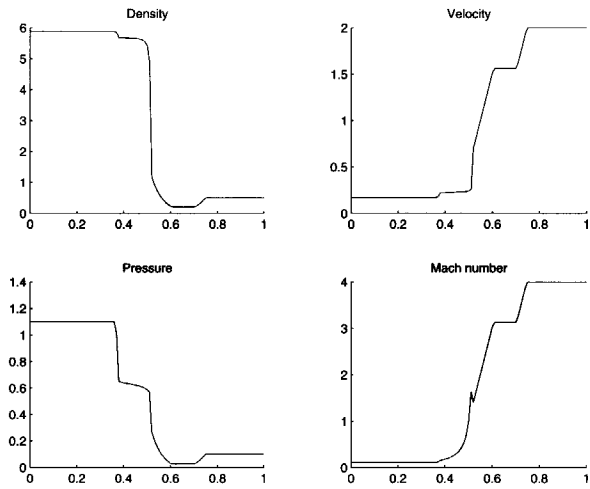


Figure 6.10: Testcase II, solution in Eulerian frame of reference for $t = 0.1$.

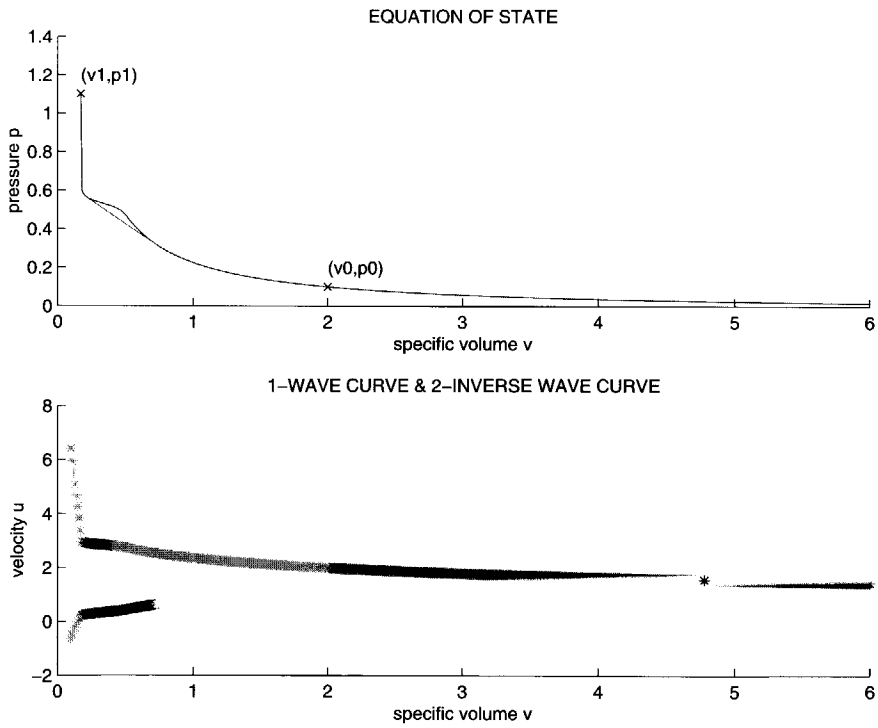
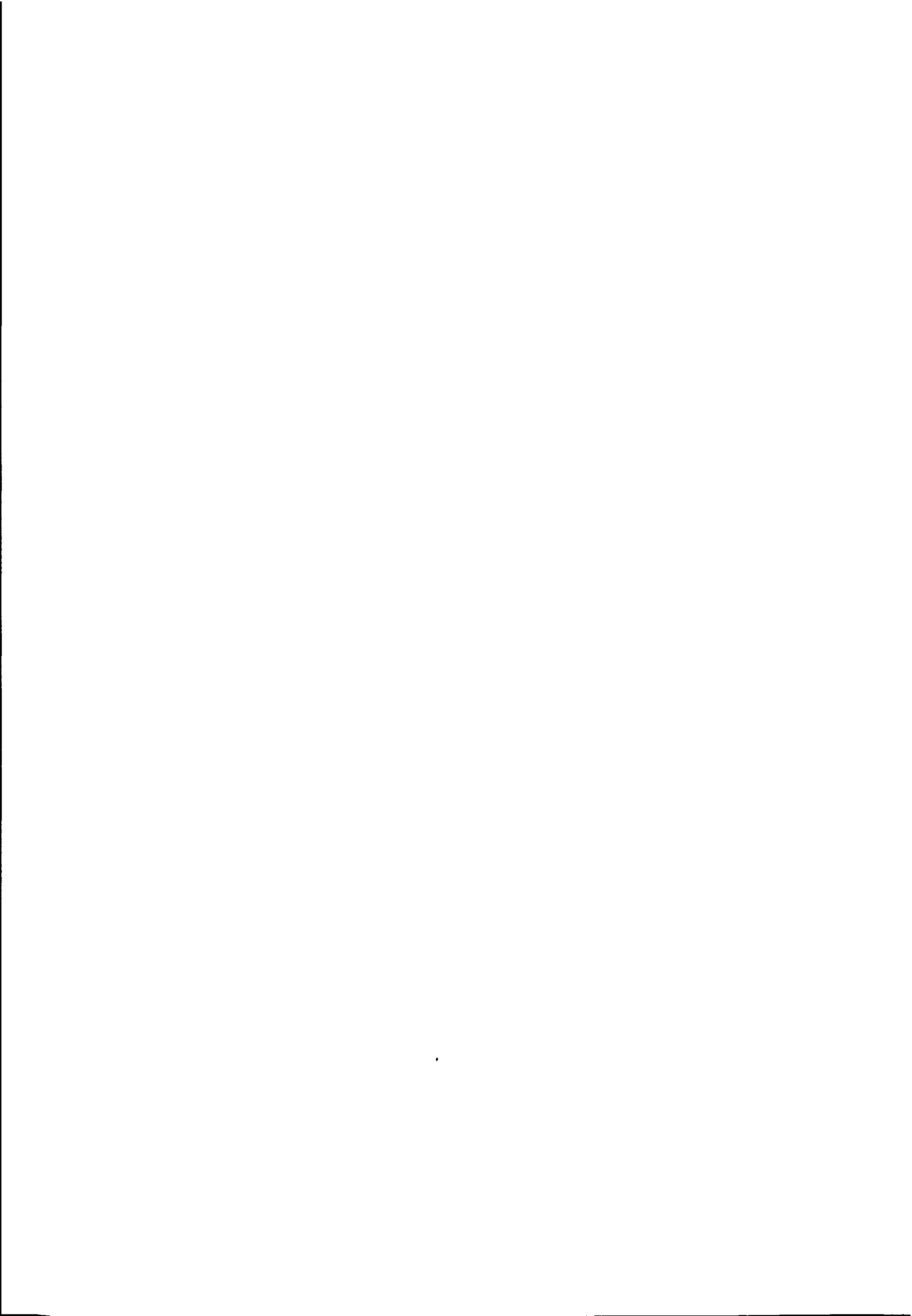


Figure 6.11: Testcase II, construction and solution in Lagrangian frame of reference.



Chapter 7

Development of a discretisation scheme

7.1 Introduction

In this chapter we discuss the development of a suitable discretisation and solution procedure for the HEM. We start with defining three stages of discretisation. Next the requirements imposed by the HEM are listed and a scheme is chosen as starting point for further development. This is applied to two test problems and the results are compared with results obtained with a classic gasdynamic scheme.

From the results presented by Delannoy, we know solutions to the HEM will have the following characteristics:

- Highly unsteady
- Discontinuities two orders of magnitude stronger than in aerospace engineering applications
- Large regions where the flow is nearly incompressible.
- Regions where the flow is highly compressible.

7.2 The notions of target scheme, actual scheme and resolved scheme

For derivation and analysis of our scheme it is convenient to distinguish between the *target*, the *actual* and the *resolved* discretisation.

The *target* discretisation is the discretisation of the given system of nonlinear partial differential equations. The *actual* discretisation is obtained from the target discretisation by linearisation. The *resolved* discretisation is the scheme that is actually solved when a finite number of computing steps is applied to solve the actual scheme approximately.

The difference between target and actual discretisation is due to linearization and other requirements set by the solution method. The difference between actual and resolved scheme results from the segregated solution procedure applied.

Only in the case of an iterative method, e.g. SIMPLE [ref] where the equations are separately solved until the residue due to the splitting and linearization errors present in the actual discretisation has vanished, the target discretisation is solved. Note that this difficulty is only encountered in unsteady problems, because for a steady state solution errors due to the splitting and linearization in time will also vanish.

When results of numerical experiments performed with the actual solution method, here pressure correction, have to be interpreted, it is difficult to distinguish between effects due to the approximations introduced by the solution method and those originating from the numerical approximation of the target discretisation. The best way is to separate these effects by first constructing a target scheme within a framework of a solution method that can exactly (iteratively) solve the discrete equations. Then, after a satisfactory target discretisation has been developed, a solution algorithm with optimal efficiency can be designed that is able to approximate the solution of the target discretisation with satisfactory accuracy. When the target discretisation can only be approximated sufficiently accurate by the actual discretisation through a too expensive solution procedure, a new target discretisation has to be chosen. After this new target scheme has shown its capabilities a new attempt can be made to develop an appropriate actual discretisation.

7.3 The target scheme

Various methods are currently used for discretisation of the HEM equations:

- The MacCormack scheme [74],
- Real gas extensions of flux splitting schemes: AUSM+ [25],
- Real gas extensions of approximate Riemann solvers: Roe [91], Osher [104]
- Jameson type schemes [36],
- Staggered schemes [21, 20, 75], and current approach.

Over the last years a number of approximate Riemann solvers and flux vector splitting schemes, like the Roe and the AUSM+ scheme, have been extended to real gases with a van der Waals equation of state. This equation of state is very similar to the equation of state of the HEM. But the variation of density is much smaller for the van der Waals equation of state. In [104] an extension of the Osher scheme to a general equation of state is presented. In this case the fluxes have to be numerically evaluated from integral relations, rendering the scheme computationally much more expensive than for the perfect gas case.

Schemes of Jameson type can be trivially extended to the HEM, because no use is made of the complicated (due to the nonconvexity of the equation of state) eigen-structure of the

Jacobian of the flux-function. But a difficulty lies in the adjustment of the artificial viscosity parameters for a very large range of Mach numbers and shocks an order of magnitude stronger than generally encountered in aerospace engineering calculations.

Although these schemes are well suited for applications where the Mach number is of order 1 in the whole flow domain, e.g. cavitation in fuel line nozzles [75] or in the wake of detonation driven underwater projectiles [74], a major drawback of these is associated with the behavior for low Mach number flow. To handle the stiffness of the system for $Ma \ll 1$, some form of artificial compressibility/time-derivative preconditioning is needed, that will destroy the temporal accuracy of the scheme. Because in our case the solution is time-dependent, each physical time-step has to be solved for by stepping in pseudo-time until convergence. This makes both types of schemes computationally expensive, the more so because there is still limited knowledge of optimal preconditioners for the HEM.

Unlike the last two schemes, the staggered discretisation of [7] for the Euler equations is a Mach-uniform method. It has computational cost and accuracy uniform in the Mach number. Although this approach may be more costly in an application where the Mach number allows the use of standard compressible schemes, the bulk of the fluid is the liquid phase with a Mach number of the order of 0.001. Therefore, it makes sense to choose a method that treats the large low Mach number region efficiently and the very small high Mach number region a little less efficient, instead of the other way around.

We impose the following requirements on our discretisation to obtain Mach-uniform accuracy and efficiency:

- For $M = 0$ the discretisation reduces to the classic MAC-Scheme of [35].
- The limit $M \downarrow 0$ is regular.
- The discretisation is conservative.

The first requirement is imposed, because the MAC-scheme is a well established, accurate and efficient scheme for computing incompressible flow. The staggered discretisation is the natural discretisation for incompressible flow, because no regularization terms are required to prevent odd-even decoupling. The second requirement is imposed to have a regular transition from the compressible to the incompressible Euler equations. The final requirement is imposed to ensure that weak solutions satisfy the Rankine-Hugoniot conditions.

How these requirements can be met is discussed in the next sections. We conclude with formulating a target discretisation that will form the basis for further development.

7.3.1 Spatial discretisation

To fulfill the first requirement the spatial discretisation is performed on a staggered grid. The placement of the unknowns is chosen according to the Arakawa-C arrangement (Fig. 7.1).

In the case of discontinuities, it is required that the spatial discretisation satisfies both the Rankine-Hugoniot jump conditions and the *entropy* condition. This ensures that only

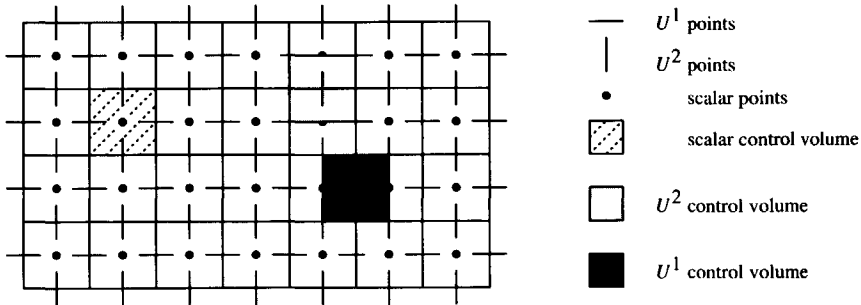


Figure 7.1: Staggered placement of unknowns according to Arakawa-C arrangement.

genuine shocks are resolved. The entropy condition will be fulfilled if a certain amount of numerical viscosity is added to the scheme. This can be accomplished by using a (limited higher order) upwind discretisation. For the staggered discretisation scalar upwind schemes are used. The convected quantity is upwind biased in the flow direction.

7.3.2 Temporal discretisation

As the flow is (nearly) incompressible in large parts of the flow domain, it is essential to require that in the limit $M \downarrow 0$ the discretisation reduces to the incompressible MAC-scheme. This means that the pressure has to be taken implicitly in the momentum equation, so it can act as a Lagrange multiplier to fulfill the solenoidality constraint in the incompressible limit. In this case stability conditions for the (semi-)implicit scheme demand a CFL-like condition based on the flow velocity, instead of on the signal speed. The latter would lead to very small time steps in the incompressible limit.

The cavitating flow has two timescales:

- The large timescale T_l , which is the characteristic timescale of the period of the cycle of cavity growth, detachment and collapse for small σ and the time to reach a quasi-steady cavity from the fully wetted condition, when σ is large enough. The large timescale is most relevant for industrial applications.
- The small timescale T_s , which is the characteristic timescale of the highly oscillatory behavior of the liquid/vapor interface.

Furthermore, the pressure distribution should be resolved with high accuracy to give the correct position of the cavity leading edge. This is accomplished by using a locally refined grid. As a consequence, an explicit scheme would require a very small timestep for stability. Steady state or periodic behavior of the cavity is only obtained after a large number of cavity cycles has passed from the start with the fully wetted solution. Therefore, the

application of an implicit discretisation of the convective terms is appropriate when studying cavitation phenomena characterized by T_i . However, to study the oscillatory behavior of the interface an explicit discretisation of the convective terms is more efficient.

7.3.3 Starting point

As a starting point the scheme of [7] has been chosen, because it has been shown to fulfill all of the above requirements. A formulation in the primitive variables m , ρ and p is chosen. For brevity, the scheme is formulated for the one-dimensional case, and $u > 0$ is assumed when specifying upwind approximations. The target discretisation is given by:

$$\frac{\rho_j^{n+1} - \rho_j^n}{\delta t} + \frac{1}{\delta x} (\zeta^{n+1} m^{n+1}) \Big|_{j-\frac{1}{2}}^{j+\frac{1}{2}} = 0, \quad (7.1)$$

$$\frac{m_{j+\frac{1}{2}}^{n+1} - m_{j+\frac{1}{2}}^n}{\delta t} + \frac{1}{\delta x} (u^{n+1} m^{n+1}) \Big|_j^{j+1} = -\frac{1}{\delta x} p^{n+1} \Big|_j^{j+1}, \quad (7.2)$$

$$\zeta_{j+\frac{1}{2}} = \frac{\tilde{\rho}_{j+\frac{1}{2}}}{\rho_{j+\frac{1}{2}}}. \quad (7.3)$$

Here ρ and $\tilde{\rho}$ are defined as follows:

$$\rho_{j+\frac{1}{2}} = \frac{1}{2} (\rho_j + \rho_{j+1}), \quad (7.4)$$

$$\tilde{\rho}_{j+\frac{1}{2}} = \begin{cases} \rho_j & : \text{First order upwind discretisation} \\ \frac{1}{2} (\rho_j + \rho_{j+1}) & : \text{Central discretisation} \end{cases}. \quad (7.5)$$

Mass conservation equation

In the limit $M \downarrow 0$ the mass conservation reduces to the solenoidality constraint. On the other end of the Mach spectrum, for supersonic flow and hypersonic flow it is desired the mass conservation equation behaves like a convection equation for the density, as is the case in standard compressible formulations. This is accomplished by the introduction of ζ , the ratio between the density evaluated at the location of m and the value of the density interpolated with a directional bias to the location of the cell face.

A first order upwind discretisation is specified in (7.5). For a higher order discretisation a limited κ -scheme is used to interpolate $\tilde{\rho}_{j+\frac{1}{2}}$.

It is observed that it is essential to combine a higher order scheme in the momentum equation with a higher order scheme in the mass conservation equation to avoid wiggles in the velocity distribution. This can be expected, because the velocity is a function of both the momentum and the density distribution.

Momentum equation

In the momentum equation the following first order upwind schemes were studied:

- Scheme 1

$$(um)_{j+1} \approx \frac{1}{2} \left(u_{j+\frac{1}{2}} + u_{j+\frac{3}{2}} \right) m_{j+\frac{1}{2}}, \quad u_{j+\frac{1}{2}} \equiv \frac{2m_{j+\frac{1}{2}}}{\rho_j + \rho_{j+1}}$$

- Scheme 2

$$(um)_{j+1} \approx (um)_{j+\frac{1}{2}}, \quad u_{j+\frac{1}{2}} \equiv \frac{2m_{j+\frac{1}{2}}}{\rho_j + \rho_{j+1}}$$

- Scheme 3

$$(um)_{j+1} \approx \frac{m_{j+\frac{1}{2}}^2}{\rho_{j+1}}$$

Extension of these schemes to higher order can be done in a straightforward way by replacing the zeroth order interpolation by a first order interpolation of the unknowns (κ -scheme).

Scheme 1 produces wiggles in the vicinity of strong discontinuities, but gives more accurate results than Scheme 2 for smooth solutions. Scheme 3, which takes full advantage of the staggering of the unknowns, gives good results for the first order scheme, but fails to give monotone results when a limited higher order upwind scheme is applied. This can be explained by noting that the variation of momentum through a discontinuity is solely due to the speed of the shock, because momentum is conserved through a stationary shock, according to the Rankine-Hugoniot jump conditions:

$$[m] = c_{\text{shock}}[\rho] \quad (7.6)$$

Therefore, the limited version of Scheme 3 does not introduce sufficient hyperviscosity in the vicinity of strong stationary shocks.

We have chosen for Scheme 2.

7.4 Actual discretisation

To design an actual discretisation it is necessary to define certain conditions that the discretisation has to meet. First a number of conditions are set, that have to be met by the discretisation, and the choice of variables. Then it is shown that the actual discretisation chosen fullfills the requirements.

7.4.1 The momentum equation

The following requirements are imposed on the momentum equation:

- linearity,

- compact (3 point) stencil for the implicit part of convection operator,
- implicit discretisation of the pressure gradient in the momentum equation.

To fulfill the first demand, the convective terms have to be linearised. Due to the second one it is only possible to use a higher order limited kappa scheme in a *deferred* or *defect* correction formulation.

Linearisation of the convective terms

In the original formulation in [7] the inertia terms are linearised as

$$u^{n+1} m^{n+1} \approx u^n m^{n+1} \quad (7.7)$$

This linearisation is of first order accuracy in time.

Higher order discretisation by deferred/defect correction

A very simple way to achieve higher order spatial accuracy with a compact stencil is by either deferred or defect correction.

Deferred correction means that the higher order flux is approximated in the following way: Consider the scalar convection equation:

$$\frac{\phi_j^{n+1} - \phi_j^n}{\delta t} + \left(U \phi_{j+\frac{1}{2}}^{n+1} - U \phi_{j-\frac{1}{2}}^{n+1} \right) = 0 \quad (7.8)$$

The value of ϕ at the cell faces is now taken as:

$$\phi_{j+\frac{1}{2}}^{n+1} = \phi_{j+\frac{1}{2}, \text{ first order}}^{n+1} + \left(\phi_{j+\frac{1}{2}, \text{ higher order}}^n - \phi_{j+\frac{1}{2}, \text{ first order}}^n \right) \quad (7.9)$$

It is clear that in the case of a steady calculation the spatial discretisation will indeed be of higher order upon convergence. In the unsteady case this is will only be true for a sufficiently small timestep.

Defect correction is a multistep procedure, but it can be shown that second order accuracy can be obtained in two steps. The first step consists of solution of the first order system to obtain the intermediate value $\hat{\phi}$. Next this value is substituted in the deferred correction scheme to give the value of the flux at the interfaces:

$$\phi_{j+\frac{1}{2}}^{n+1} = \phi_{j+\frac{1}{2}, \text{ first order}}^{n+1} + \left(\hat{\phi}_{j+\frac{1}{2}, \text{ higher order}} - \hat{\phi}_{j+\frac{1}{2}, \text{ first order}} \right) \quad (7.10)$$

Deferred correction has the advantage over defect correction, that it is a single step procedure. Furthermore it is shown in [46] the procedure is unconditionally stable. However defect correction can be shown to attain second order spatial accuracy in only two steps. Deferred correction is currently employed.

In both cases the stencil of the implicit operator for the convective terms is:

$$\begin{aligned} & - \left(\frac{1 + u_j/|u_j|}{2} \right) u_{j-\frac{1}{2}} m_{j-\frac{1}{2}} + \\ & \left(\frac{1 + u_{j+1}/|u_{j+1}|}{2} - \frac{1 - u_j/|u_j|}{2} \right) u_{j+\frac{1}{2}} m_{j+\frac{1}{2}} + \\ & \left(\frac{1 - u_{j+1}/|u_{j+1}|}{2} \right) u_{j+\frac{3}{2}} m_{j+\frac{3}{2}}. \end{aligned} \quad (7.11)$$

Clearly, the second requirement is satisfied.

7.4.2 The mass conservation equation

The demands imposed on the mass conservation equation are:

- linearity
- compact (3 point) stencil for the pressure correction equation for all Mach numbers.
- pressure based upwind biased convection equation for high Mach number flow.

All three demands are related to the high Mach number situation where the mass conservation equation will act as an implicit convection equation for the density. Through the demand of compactness also this convection equation can only be discretised with a higher order limited upwind scheme through the method of deferred or defect correction.

7.4.3 Starting point

With the requirements imposed, the actual discretisation takes the following form:

$$\frac{m_{j+\frac{1}{2}}^{n+1} - m_{j+\frac{1}{2}}^n}{\delta t} + \frac{1}{\delta x} (u^n m^{n+1}) \Big|_{j-\frac{1}{2}}^{j+\frac{1}{2}} = - \frac{1}{\delta x} p^{n+1} \Big|_j^{j+1} + \quad (7.12)$$

$$\left\{ \frac{1}{\delta x} \left((u^n m^n)_{k-\frac{1}{2}} - (\tilde{u}^n \tilde{m}^n)_k \right) \Big|_{k=j}^{k=j+1} \right\},$$

$$\frac{1}{c^2} \frac{\delta p_j}{\delta t} + \frac{1}{\delta x} \left(\zeta_k m_k^{n+1} + \frac{u^n}{c^2} (\delta p_{k+\frac{1}{2}} + \delta p_{k-\frac{1}{2}}) - (\zeta u^n)_k \frac{\delta p_{k-\frac{1}{2}}}{c^2} \right) \Big|_{k=j-\frac{1}{2}}^{k=j+\frac{1}{2}} = \quad (7.13)$$

$$\left\{ \frac{1}{\delta x} \left((\rho_{k-\frac{1}{2}}^n - \tilde{\rho}_k^n) u_k^n \right) \Big|_{k=j-\frac{1}{2}}^{k=j+\frac{1}{2}} \right\},$$

where we have used

$$\frac{d\rho}{dp} = \frac{1}{c^2}. \quad (7.14)$$

The terms between curly braces are the deferred correction terms, that are omitted for the first order scheme. We use the following discretisation for the higher order flux:

$$(\tilde{u}\tilde{m})_{j+1} = (um)_{j+\frac{1}{2}} + \Psi(r_{m\ j+\frac{1}{2}}) \left((um)_{j+\frac{1}{2}} - (um)_{j-\frac{1}{2}} \right), \quad (7.15)$$

$$r_{m\ j+\frac{1}{2}} = \frac{(um)_{j+\frac{3}{2}} - (um)_{j+\frac{1}{2}}}{(um)_{j+\frac{1}{2}} - (um)_{j-\frac{1}{2}}}. \quad (7.16)$$

$$\tilde{\rho}_{j+\frac{1}{2}} = \rho_j + \Psi(r_{\rho\ j+\frac{1}{2}}) (\rho_j - \rho_{j-1}), \quad (7.17)$$

$$r_{\rho\ j+\frac{1}{2}} = \frac{\rho_{j+1} - \rho_j}{\rho_j - \rho_{j-1}}, \quad (7.18)$$

where the limiter function Ψ is chosen as the ISNAS-limiter [116]:

$$\Psi(r) = \frac{r^2 + 3r}{(1+r)^2}. \quad (7.19)$$

7.5 The resolved scheme

For efficiency, equations (7.13, 7.12) are not solved as they stand, but approximately, balancing efficiency, truncation error and stability. In the limit $M \downarrow 0$, the efficiency should not deteriorate, but match the efficiency of standard incompressible schemes. To this end we base ourselves on a pressure correction method.

7.5.1 Starting point: compressible pressure correction

The compressible pressure correction scheme of [7] is a natural extension of the incompressible pressure correction schemes as discussed in [35, 93]. For brevity we will discuss the solution procedure for the one-dimensional case with first order upwind discretisation.

A two step procedure is followed: First a tentative momentum field is calculated using the old pressure:

$$\frac{m_{j+\frac{1}{2}}^* - m_{j+\frac{1}{2}}^n}{\delta t} + \frac{1}{\delta x} (u^n m^*)|_{j-\frac{1}{2}}^{j+\frac{1}{2}} = -\frac{1}{\delta x} p^n|_j^{j+1}. \quad (7.20)$$

This is solved accurately by preconditioned GMRES [99, 100]. The momentum field m^* will not satisfy the mass conservation equation, or be solenoidal in the incompressible case. Therefore, a correction is introduced. This correction is obtained by subtracting the equation for the tentative momentum field from the momentum equation. This gives:

$$\frac{m_{j+\frac{1}{2}}^{n+1} - m_{j+\frac{1}{2}}^*}{\delta t} = - (p^{n+1} - p^n)|_j^{j+1} - (u^n (m^{n+1} - m^*))|_{j-\frac{1}{2}}^{j+\frac{1}{2}}.$$

The last term is neglected, which gives

$$\frac{m_{j+\frac{1}{2}}^{n+1} - m_{j+\frac{1}{2}}^*}{\delta t} = -\delta p|_j^{j+1}, \quad \delta p = p^{n+1} - p^n. \quad (7.21)$$

The resolved scheme consists of (7.20), (7.21) and the mass conservation equation (7.13). It is solved as follows. Substitution of the equation for the momentum correction into the mass conservation equation gives:

$$C_{j-1}\delta p_{j-1} + C_j\delta p_j + C_{j+1}\delta p_{j+1} = f_j, \quad (7.22)$$

where

$$C_{j-1} = -\lambda\zeta_{j-\frac{1}{2}}^n - \frac{1}{c^2} \left(u_{j-\frac{1}{2}}^n + \frac{1}{2} (\zeta u)_{j-\frac{1}{2}}^n \right), \quad (7.23)$$

$$C_j = \lambda \left(\zeta_{j-\frac{1}{2}} + \zeta_{j+\frac{1}{2}} \right) + \frac{1}{c^2} \left\{ \frac{1}{\lambda} + u_{j+\frac{1}{2}}^n - \frac{1}{2} \left((\zeta u)_{j+\frac{1}{2}}^n - (\zeta u)_{j-\frac{1}{2}}^n \right) \right\}, \quad (7.24)$$

$$C_{j+1} = -\lambda\zeta_{j+\frac{1}{2}}^n + \frac{1}{2} \frac{1}{c^2} (\zeta u)_{j+\frac{1}{2}}^n, \quad (7.25)$$

$$f_j = -(\zeta m^*)_{j-\frac{1}{2}}^{j+\frac{1}{2}} \quad (7.26)$$

where ζ is defined in (7.3), and

$$\lambda = \frac{\delta t}{\delta x}, \quad \delta p = (p^{n+1} - p^n). \quad (7.27)$$

After solution of the pressure correction equation the momentum and pressure are updated:

$$m_{j+\frac{1}{2}}^{n+1} = m_{j+\frac{1}{2}}^* - \delta t \delta p|_j^{j+1}, \quad (7.28)$$

$$p_j^{n+1} = p_j^n + \delta p_j. \quad (7.29)$$

Very little is still known about compressible pressure correction. In the incompressible case, where the mass conservation equation reduces to the divergence free constraint, it is known that the pressure correction method will not affect the temporal order of accuracy of the velocity field [93]. The pressure field is only approximated to first order accuracy, irrespective of the temporal accuracy used for the momentum equation.

7.5.2 Preliminary numerical results

Weak solutions of hyperbolic systems are made unique by imposing the requirements, that shocks satisfy the jump condition (Rankine-Hugoniot), and that characteristics converge into and do not emanate from shocks (entropy condition). It is well-known that numerical schemes easily violate one or both of these conditions. Therefore convergence of the

staggered scheme needs to be validated. A theory of convergence is lacking, as for many commonly used schemes for hyperbolic systems. We will carry out validation by comparison with exact solutions and with another scheme. Standard finite volume schemes for the Euler equations are of colocated type and use explicit artificial numerical viscosity or some form of flux-splitting or approximate Riemann solution for the numerical flux at cell boundaries. For two reasons we select the Osher scheme [64] for comparison. First, it applies to general hyperbolic systems and is not restricted to the Euler equations for a perfect gas. Second, there is a proof [64] that it gives numerical solutions that satisfy the jump and entropy conditions, if shocks are sufficiently weak.

We have computed results with the present method for the two Riemann problems described in Section 6.4. For both testcases the two schemes converge to the correct solution with the same accuracy in the eyeball-norm (Figs. 7.2 and 7.3). However, due to the fact that the Osher scheme requires calculation of the eigenvectors and numerical evaluation of integral relations to obtain the Riemann-invariants, it is a few hundred times slower than the staggered scheme. To avoid evaluation of the integral relations, the Riemann invariants could be tabularized, but even then the Osher scheme would still be more costly to apply.

Next, the staggered scheme was applied to compute cavitation with the HEM. The model equation has qualitatively the same behavior as the equation of state of the HEM, but the transition region is narrowed to get good resolution of the cavitation bubbles. The scheme failed to converge.

7.6 Improvements

Principal differences between the equation of state in the Riemann test cases and the HEM application are:

- Much higher curvature close to transition region.
- Much higher compressibility in transition region.

The first means that the linearization of the density is inaccurate. The pressure-based mass conservation equation has to be solved nonlinearly. Therefore, we present an actual discretisation of the mass conservation equation that approximates the target discretisation more closely together with a nonlinear pressure correction algorithm to solve it. The second means that the maximum Mach number encountered in the application is much higher. The nonlinear pressure correction algorithm was successfully applied to compute cavitation. However, the algorithm only converged for very small time step size and lacked general robustness. Initially it was reasoned that this effect could be ascribed to the splitting error of the segregated solution procedure in the high Mach number flow, because the coupling between momentum and mass conservation equation is stronger for highly compressible flow. Therefore, we consider two methods that lack any splitting error (cf. Appendix B. The first one is an adaptation of the SIMPLE-algorithm, the other uses an explicit discretisation of the convective term in the momentum equation. Both methods have

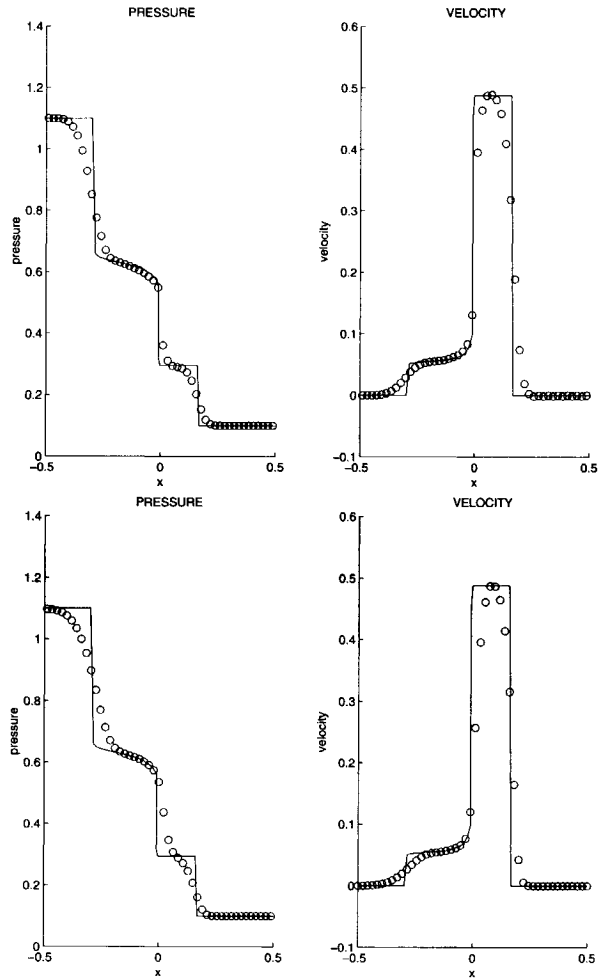


Figure 7.2: Riemann problem 1; 48 cells; $\tau/h = 0.4$, Top: Osher scheme, Bottom: staggered scheme.

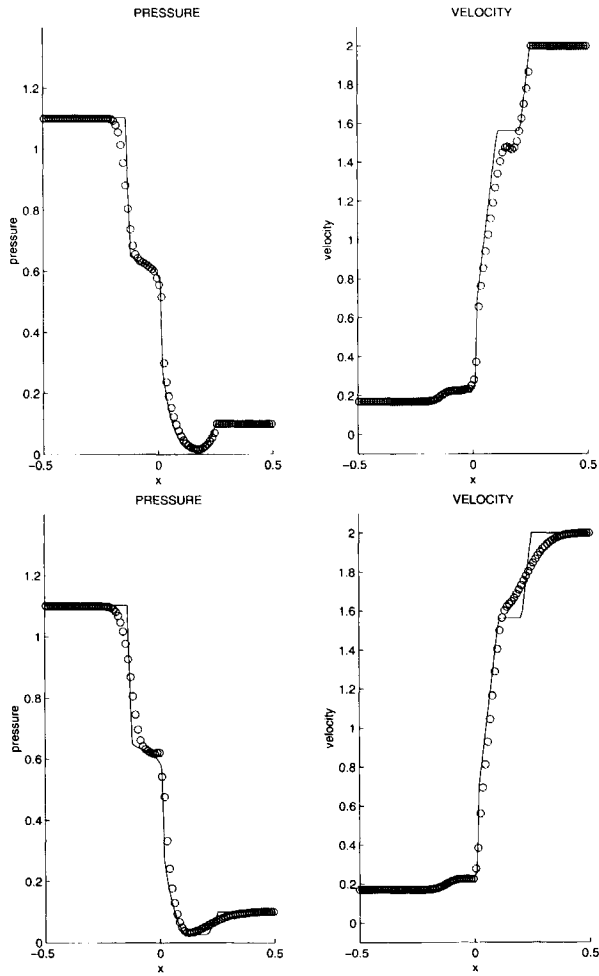


Figure 7.3: Riemann problem 2; 96 cells; $\tau/h = 0.4$, Top: Osher scheme, Bottom: staggered scheme.

been successfully applied to compute solutions to the HEM, but are considered only for development purposes. The SIMPLE-algorithm requires multiple solves of the nonlinear pressure correction equation per timestep, while in the second approach the maximum timestep is severely limited by stability for high Mach number flow. In Chapter 8 we will see that stability of the actual discretisation is the cause of the timestep restriction and not the splitting error.

7.6.1 Nonlinear pressure correction

In the case of a perfect gas, using the relation $\rho(p) = c^{-2}p$ leads to a linear pressure correction equation. It is clear that in the case of the HEM equation of state, the pressure based mass conservation equation:

$$\begin{aligned} & \frac{\rho(p^n + \delta p_j) - \rho_j^n}{\delta t} + \\ & \frac{1}{\delta x} \left(\zeta_k m_k^{n+1} + u^n \left(\rho(\delta p_{k+\frac{1}{2}} + p_{k+\frac{1}{2}}) - \rho_{k+\frac{1}{2}} + \rho(\delta p_{k-\frac{1}{2}} + p_{k-\frac{1}{2}}) - \rho_{k-\frac{1}{2}} \right) \right. \\ & \quad \left. - (\zeta u^n)_k \left(\rho(\delta p_{k-\frac{1}{2}} + p_{k-\frac{1}{2}}) - \rho_{k-\frac{1}{2}} \right) \right) \Big|_{k=j-\frac{1}{2}}^{k=j+\frac{1}{2}} = \\ & \quad \left\{ \frac{1}{\delta x} \left((\rho_{k-\frac{1}{2}}^n - \tilde{\rho}_k^n) u_k^n \right) \Big|_{k=j-\frac{1}{2}}^{k=j+\frac{1}{2}} \right\}, \end{aligned} \quad (7.30)$$

has to be solved nonlinearly due to the strong nonlinearity of the relation $\rho(p)$. After introduction of the pressure correction formulation in (7.30) the nonlinear system

$$\begin{aligned} & \frac{\rho(p^n + \delta p_j) - \rho_j^n}{\delta t} + \\ & \frac{1}{\delta x} \left(\zeta_k \left(m_k^* - \frac{\delta t}{\delta x} (\delta p_{k+\frac{1}{2}} - \delta p_{k-\frac{1}{2}}) \right) \right) + \\ & u^n \left(\left(\rho(\delta p_{k+\frac{1}{2}} + p_{k+\frac{1}{2}}) - \rho_{k+\frac{1}{2}} \right) + \left(\rho(\delta p_{k-\frac{1}{2}} + p_{k-\frac{1}{2}}) - \rho_{k-\frac{1}{2}} \right) \right) \\ & \quad - (\zeta u^n)_k \left(\rho(\delta p_{k-\frac{1}{2}} + p_{k-\frac{1}{2}}) - \rho_{k-\frac{1}{2}} \right) \Big|_{k=j-\frac{1}{2}}^{k=j+\frac{1}{2}} = \\ & \quad \left\{ \left((\rho_{k-\frac{1}{2}}^n - \tilde{\rho}_k^n) u_k^n \right) \Big|_{k=j-\frac{1}{2}}^{k=j+\frac{1}{2}} \right\}, \end{aligned} \quad (7.31)$$

can be represented as:

$$A\delta\mathbf{p} + B\rho(\mathbf{p}^n + \delta\mathbf{p}) = \mathbf{f}, \quad (7.32)$$

with A and B matrices. Although a number of robust methods exist for solving nonlinear scalar equations, most of these are not trivially extended to the case of nonlinear systems. We uncouple the original system by solving it with a nonlinear Gauss-Seidel algorithm,

in which we can choose a very robust method for solving the individual nonlinear scalar equations. Application of Gauss-Seidel gives scalar equations of the following form:

$$F\delta\mathbf{p}^{(k+1)} + K\rho(\mathbf{p}^n + \delta\mathbf{p}^{(k+1)}) = \mathbf{f} - G\delta\mathbf{p}^{(k)} - L\rho(\mathbf{p}^n + \delta\mathbf{p}^{(k)}), \quad (7.33)$$

where $F + G = A$ and $K + L = B$ are Gauss-Seidel splittings of A and B respectively. This system can be solved recursively at a price of one scalar nonlinear solve per step. We choose a Dekker-type algorithm [9], which guarantees convergence if the function values in the end points of the search interval have opposite sign and gives superlinear convergence when the iterate approaches the solution. To improve efficiency, each scalar equation is first linearised, and when both the new and the old pressure are in the same linear branch of the equation of state, the solution is accepted. If either the initial pressure or the newly calculated pressure is in the transition region, the solution of the linearised equation is rejected and use is made of the Dekker-type algorithm to solve the nonlinear scalar equation.

On large multi-dimensional grids the Gauss-Seidel method converges very slowly. To overcome this difficulty we accelerate the algorithm by using intermediate linearized steps, as follows: Define

$$\delta p^{\frac{1}{2}} + \delta p^1 \equiv \delta p^{(k+1)}, \quad (7.34)$$

where $\delta p^{\frac{1}{2}}$ is the solution of one Gauss-Seidel iteration on (7.33). Substitution of (7.34) in (7.33) leads to

$$A(\delta\mathbf{p}^{\frac{1}{2}} + \delta\mathbf{p}^1) + B\rho(\mathbf{p}^n + \delta\mathbf{p}^{\frac{1}{2}} + \delta\mathbf{p}^1) = \mathbf{f} \quad (7.35)$$

Equation (7.35) is linearized to get a linear system for δp^1 :

$$\left(A + B \left(\frac{d\rho}{dp} \right) \Big|_{p=\mathbf{p}^n + \delta\mathbf{p}^{\frac{1}{2}}} \right) \delta\mathbf{p}^1 = \mathbf{f} - \mathbf{A}\delta\mathbf{p}^{\frac{1}{2}} - \mathbf{B}\rho(\mathbf{p}^n + \delta\mathbf{p}^{\frac{1}{2}}) \quad (7.36)$$

To overcome the strong nonlinear behavior of $\rho(p)$ the exact derivative $\frac{d\rho}{dp}$ is replaced by an estimate $\tilde{\rho}'$ according to the secant method:

$$\begin{aligned} \tilde{\rho}' &= \frac{\rho(p + \delta p^{\frac{1}{2}}) - \rho(p^n + \delta p^{(k)})}{\delta p^{\frac{1}{2}} - \delta p^{(k)}}, \\ |\delta p^{\frac{1}{2}} - \delta p^{(k)}| &\geq \mu |p^n + \delta p^{(k)}|; \\ \tilde{\rho}' &= \frac{\rho((1 + \mu)(p^n + \delta p^{(k)})) - \rho(p^n + \delta p^{(k)})}{\mu p^{(k)}}, \\ |\delta p^{\frac{1}{2}} - \delta p^{(k)}| &< \mu |p^n + \delta p^{(k)}|, \end{aligned} \quad (7.37)$$

where μ is chosen in relation to the parameters in the equation of state, $\mu = \nu(p_2 - p_1)$,

typically $\nu = 10^{-6}$. Because the choice of $\tilde{\rho}'$ does not influence the solution, we are free to adapt the value of $\tilde{\rho}'$ to obtain maximum convergence rate. This is done on heuristic arguments in [98]; we believe the use of $\delta\mathbf{p}^{\frac{1}{2}}$ to estimate the speed of sound to be more robust.

The resulting system

$$(A + B\tilde{\rho}') \delta\mathbf{p}^1 = \mathbf{f} - A\delta\mathbf{p}^{\frac{1}{2}} - B\rho(\mathbf{p}^n + \delta\mathbf{p}^{\frac{1}{2}}) \quad (7.38)$$

$$\text{or} \quad H\delta\mathbf{p}^1 = \mathbf{g} \quad (7.39)$$

is solved by GMRES with a multigrid [94] or ILU preconditioner until a relative accuracy of 10^{-1} . Finally the total pressure correction $\delta\mathbf{p}^{(k+1)} = \delta\mathbf{p}^{\frac{1}{2}} + \delta\mathbf{p}^1$ is computed and used as an initial vector for the next iteration step.

The algorithm takes the following form:

while $\|A(\delta\mathbf{p}^{(k)}) + B(\rho(\mathbf{p}^n + \delta\mathbf{p}^{(k)})) - \mathbf{f}\|_{\infty} > \epsilon$

1. update $\delta\mathbf{p}^{\frac{1}{2}} = \delta\mathbf{p}^{(k)}$
2. calculate $\delta\mathbf{p}^{\frac{1}{2}}$ from (7.33) by nonlinear Gauss-Seidel
3. calculate $\delta\mathbf{p}^1$ from (7.38) by preconditioned GMRES
4. calculate the total pressure correction $\delta\mathbf{p}^{(k+1)} = \delta\mathbf{p}^{\frac{1}{2}} + \delta\mathbf{p}^1$

end while

It is clear that upon convergence the right-hand side of the system (7.38) vanishes and $\|\delta\mathbf{p}^1\|_{\infty}$ is zero.

H in (7.39) is the Jacobian of the nonlinear system (7.31). In the case of isothermal perfect gas flow, H will be weakly diagonally dominant, if the variation in speed of sound is relatively small. In the case of the HEM, where the relative variation of the (pseudo) speed of sound is of the order of 1000, the diagonal dominance is lost. This means that the nonlinear Gauss-Seidel algorithm is not guaranteed to converge. In practice we found that if the intermediate linearized steps are omitted, Gauss-Seidel will diverge. However the accelerated algorithm will converge in about 10 global iterations, requiring an equal amount of iterations of GMRES per global iteration.

In each time-step the solution of the nonlinear pressure correction equation is found to take up to 95% of the computational time.

7.7 Conclusions

When developing a discretisation scheme for a particular application, it is helpful to distinguish three different levels of discretisation: The target, the actual and the resolved scheme.

Descending one level introduces additional simplifications that can change the behavior of the scheme with respect to the previous level. When this behavior is unacceptable, and no suitable modification can be found to repair this, one has to go up one level to change the underlying discretisation, until an acceptable resolved scheme can be obtained.

A nonlinear pressure correction algorithm is presented that can accurately solve the nonlinear pressure correction equation of the HEM. The latter algorithm has to respect a severe restriction on the time step. Therefore, two different solution procedures are presented in the next chapter that do not have a splitting error. The actual and resolved discretisation are identical. Both methods were considered too inefficient for practical application, but were used for development purposes.



Chapter 8

Stability analysis of segregated solution methods

8.1 Introduction

The main results of this chapter have appeared in [92]. Because we are not satisfied with the stability properties of the schemes described in the previous chapter, we will investigate the cause of the instabilities in the case of strongly compressible flow.

A frequently used heuristic stability analysis of numerical schemes for hyperbolic systems works as follows. The system is replaced by a simple equation:

$$\psi_t + a\psi_x = 0, \quad (8.1)$$

where the constant a is the maximum signal speed occurring in the system: for the Euler equations, $a = \sup(|u| + c)$. Stability analysis of schemes for (8.1) can be carried out using Schur-Cohn theory or Fourier methods, as in [103]. For the first order upwind scheme, the implicit Euler method is found to be unconditionally stable, and the explicit Euler method is stable under the following condition:

$$a\delta t/\delta x < 1. \quad (8.2)$$

Practical experience shows that this approach gives useful conditions for colocated schemes for systems. But for staggered schemes with pressure correction we found condition (8.2) to be much too weak for high Mach numbers. Therefore, we will analyze our system directly, and not use the drastic simplification given by (8.1). In Section 8.2 we analyze stability of four different discretisations. For two of these a simple necessary, but not sufficient stability condition is derived in Section 8.3. In Section 8.4 the stability conditions are verified by numerical experiments. Although linear stability analysis has only limited applicability, its simplicity allows incorporation of the approximations that are made to derive a resolved discretisation from the target discretisation. In Section 8.5 it is shown that in those cases where the resolved discretisation differs from the target discretisation, it is essential to base

the analysis on the resolved discretisation. Finally, we consider higher order schemes in Section 8.6.

8.2 Fourier stability analysis of schemes for systems.

Because Fourier stability analysis of the systems that we wish to consider is somewhat tedious and involved, we will provide full details. Rather than explain the method in general, we proceed by example, The following schemes will be analyzed:

1. Momentum equation: first order upwind convection explicit,
Continuity equation: no upwind bias.
2. Momentum equation: first order upwind convection implicit
Continuity equation: no upwind bias.
3. Momentum equation: first order upwind convection explicit
Continuity equation: upwind bias.
4. Momentum equation: first order upwind convection implicit
Continuity equation: upwind bias.

No upwind bias for density

Inertia explicit

We start with the following scheme:

$$\rho_j^{n+1} - \rho_j^n + \lambda \left(m_{j+\frac{1}{2}}^{n+1} - m_{j-\frac{1}{2}}^{n+1} \right) = 0, \quad \lambda = \delta t / \delta x, \quad (8.3)$$

$$m_{j+\frac{1}{2}}^{n+1} - m_{j+\frac{1}{2}}^n + \lambda \left[\left(m_{j+\frac{1}{2}}^n \right)^2 / \rho_{j+\frac{1}{2}}^n - \left(m_{j-\frac{1}{2}}^n \right)^2 / \rho_{j-\frac{1}{2}}^n \right] = -\lambda \left(p_{j+1}^{n+1} - p_j^{n+1} \right), \quad (8.4)$$

$$\rho_{j+\frac{1}{2}} = (\rho_{j+1} + \rho_j) / 2.$$

We postulate small perturbations $\delta\rho$, δm and linearize:

$$\delta\rho_j^{n+1} - \delta\rho_j^n + \lambda \delta m \Big|_{j-\frac{1}{2}}^{j+\frac{1}{2}} = 0, \quad (8.5)$$

$$\delta m_{j+\frac{1}{2}}^{n+1} - \delta m_{j+\frac{1}{2}}^n + \lambda \left[2 \left(u^n \delta m^n \right) - \left(u^n \right)^2 \delta\rho^n \Big|_{j-\frac{1}{2}}^{j+\frac{1}{2}} + \lambda \left[\left(c^{n+1} \right)^2 \delta\rho^{n+1} \right] \Big|_j^{j+1} \right] = 0, \quad (8.6)$$

We freeze the coefficients:

$$\delta\rho_j^{n+1} - \delta\rho_j^n + \lambda \delta m^{n+1} \Big|_{j-\frac{1}{2}}^{j+\frac{1}{2}} = 0, \quad (8.7)$$

$$\delta m_{j+\frac{1}{2}}^{n+1} - \delta m_{j+\frac{1}{2}}^n + \lambda \left[2 \left(U \delta m^n \right) - U^2 \delta\rho^n \Big|_{j-\frac{1}{2}}^{j+\frac{1}{2}} + \lambda c^2 \delta\rho^{n+1} \Big|_j^{j+1} \right] = 0. \quad (8.8)$$

Next we postulate a Fourier mode:

$$\delta \rho_j^n = \hat{\rho}^n e^{ij\theta}, \quad \delta m_{j+\frac{1}{2}}^n = \hat{m}^n e^{i(j+\frac{1}{2})\theta} \quad (8.9)$$

This gives:

$$\begin{aligned} \hat{\rho}^{n+1} + \frac{2\delta t}{\delta x} i \sin(\theta/2) \hat{m}^{n+1} &= \hat{\rho}^n, \\ \frac{2c^2\delta t}{\delta x} i \sin(\theta/2) \hat{\rho}^{n+1} + \hat{m}^{n+1} &= \\ \frac{U^2\delta t}{\delta x} i \sin(\theta) e^{-\frac{1}{2}i\theta} \hat{\rho}^n + \left(1 - \frac{4U\delta t}{\delta x} i \sin(\theta/2) e^{-i\theta/2}\right) \hat{m}^n, \end{aligned} \quad (8.10)$$

or in operator form:

$$\begin{aligned} \begin{bmatrix} 1 & \frac{2\delta t}{\delta x} i \sin(\theta/2) \\ \frac{2c^2\delta t}{\delta x} i \sin(\theta/2) & 1 \end{bmatrix} \begin{pmatrix} \hat{\rho}^{n+1} \\ \hat{m}^{n+1} \end{pmatrix} &= \\ \begin{bmatrix} 1 & 0 \\ \frac{U^2\delta t}{\delta x} i \sin(\theta) e^{-\frac{1}{2}i\theta} & 1 - \frac{4U\delta t}{\delta x} i \sin(\theta/2) e^{-i\theta/2} \end{bmatrix} \begin{pmatrix} \hat{\rho}^n \\ \hat{m}^n \end{pmatrix} \end{aligned} \quad (8.11)$$

System (8.11) can be summarized by the relation

$$G_2 \begin{pmatrix} \hat{\rho}^{n+1} \\ \hat{m}^{n+1} \end{pmatrix} = G_1 \begin{pmatrix} \hat{\rho}^n \\ \hat{m}^n \end{pmatrix}, \quad (8.12)$$

where the amplification matrix is $G_2^{-1}G_1$. The scheme is stable in the sense of von Neumann if

$$\|\lambda_{1,2}\|_{G_2^{-1}G_1} \leq 1, \quad (8.13)$$

With the notation:

$$\begin{aligned} a &= \frac{2\delta t}{\delta x} i \sin(\theta/2), \\ g &= U e^{-i\theta/2}, \\ k &= \frac{U^2\delta t}{\delta x} i \sin(\theta) e^{-i\theta/2}, \end{aligned} \quad (8.14)$$

we obtain:

$$\begin{bmatrix} 1 & a \\ ac^2 & 1 \end{bmatrix} \begin{pmatrix} \hat{\rho}^{n+1} \\ \hat{m}^{n+1} \end{pmatrix} = \begin{bmatrix} 1 & 0 \\ k & 1 - 2ag \end{bmatrix} \begin{pmatrix} \hat{\rho}^n \\ \hat{m}^n \end{pmatrix}. \quad (8.15)$$

The determinant of $G_1 - \lambda G_2$ is

$$\det(G_1 - \lambda G_2) = (1 - a^2 c^2) \lambda^2 + \lambda(2ag - 2 + ak) + (1 - 2ag). \quad (8.16)$$

So the eigenvalues are

$$\begin{aligned} \lambda_{1,2} &= \frac{2 - 2ag - ak}{2(1 - a^2 c^2)} \\ &\pm \frac{1}{2(1 - a^2 c^2)} \sqrt{4a^2 g^2 + 4a^2 gk - 4ak + a^2 k^2 + 4a^2 c^2 - 8a^3 g c^2}. \end{aligned} \quad (8.17)$$

These eigenvalues are further analyzed in Section 8.3

No upwind bias for density Inertia implicit

In the next scheme to be analyzed the inertia term is taken implicit. Only the linearisation for the inertia term is presented. The derivation of the amplification matrices proceeds in the same way as above. The only term that differs from the preceding scheme is the inertia term given by:

$$(m^n m^{n+1} / \rho^{n+1}) \Big|_{j-\frac{1}{2}}^{j+\frac{1}{2}} \quad (8.18)$$

Linearization in small perturbations δm , $\delta \rho$ gives:

$$[(m^n \delta m^{n+1} + m^{n+1} \delta m^n) / \rho^n] \Big|_{j-\frac{1}{2}}^{j+\frac{1}{2}} - [m^n m^{n+1} \delta \rho^n / (\rho^n)^2] \Big|_{j-\frac{1}{2}}^{j+\frac{1}{2}} \quad (8.19)$$

Now we can proceed in the same way as in Section 8.2 to find the following system:

$$\begin{bmatrix} 1 & a \\ ac^2 & 1 + ag \end{bmatrix} \begin{pmatrix} \hat{\rho}^{n+1} \\ \hat{m}^{n+1} \end{pmatrix} = \begin{bmatrix} 1 & 0 \\ k & 1 - ag \end{bmatrix} \begin{pmatrix} \hat{\rho}^n \\ \hat{m}^n \end{pmatrix}, \quad (8.20)$$

which leads to the following characteristic polynomial:

$$((1 + ag) - a^2 c^2) \lambda^2 + (ak - 2) \lambda + (1 - ag). \quad (8.21)$$

The roots are

$$\begin{aligned} \lambda_{1,2} &= \frac{2 - ak}{2(1 + ag - a^2 c^2)} \\ &\pm \frac{1}{2(1 + ag - a^2 c^2)} \sqrt{4a^2 g^2 - 4ak + a^2 k^2 + 4a^2 c^2 - 4a^3 c^2 g}. \end{aligned} \quad (8.22)$$

Upwind bias for density Inertia explicit

In the third scheme to be analyzed we apply upwind bias in the mass conservation equation, and take the inertia term explicit.

The mass conservation equation is given by:

$$\frac{\rho_j^{n+1} - \rho_j^n}{\delta t} + \frac{1}{\delta x} \left(\frac{\rho_j^{n+1} m_{j+\frac{1}{2}}^{n+1}}{\rho_{j+\frac{1}{2}}^{n+1}} - \frac{\rho_{j-1}^{n+1} m_{j-\frac{1}{2}}^{n+1}}{\rho_{j-\frac{1}{2}}^{n+1}} \right) = 0, \quad (8.23)$$

$$\rho_{j+\frac{1}{2}} = (\rho_j + \rho_{j+1})/2.$$

The linearized form is:

$$\delta \rho_j^{n+1} - \delta \rho_j^n + \lambda \left[\frac{\rho_j^{n+1} \delta m_{j+\frac{1}{2}}^{n+1} + m_{j+\frac{1}{2}}^{n+1} \delta \rho_j^{n+1}}{\rho_{j+\frac{1}{2}}^{n+1}} - \frac{\rho_j^{n+1} m_{j+\frac{1}{2}}^{n+1}}{(\rho_{j+\frac{1}{2}}^{n+1})^2} \delta \rho_{j+\frac{1}{2}}^{n+1} - \frac{\rho_{j-1}^{n+1} \delta m_{j-\frac{1}{2}}^{n+1} + m_{j-\frac{1}{2}}^{n+1} \delta \rho_{j-1}^{n+1}}{\rho_{j-\frac{1}{2}}^{n+1}} - \frac{\rho_{j-1}^{n+1} m_{j-\frac{1}{2}}^{n+1}}{(\rho_{j-\frac{1}{2}}^{n+1})^2} \delta \rho_{j-\frac{1}{2}}^{n+1} \right] = 0. \quad (8.24)$$

Freezing the coefficients gives:

$$\delta \rho_j^{n+1} - \delta \rho_j^n + \lambda \left[\left(\delta m_{j+\frac{1}{2}}^{n+1} - \delta m_{j-\frac{1}{2}}^{n+1} \right) + \frac{1}{2} U \left(-\delta \rho_{j-1}^{n+1} + 2\delta \rho_j^{n+1} - \delta \rho_{j+1}^{n+1} \right) \right] = 0, \quad (8.25)$$

Postulating a Fourier mode, as before, we obtain:

$$\hat{\rho}^{n+1} e^{ij\theta} = \hat{\rho}^n e^{ij\theta} - \frac{\delta t}{\delta x} \left(\hat{m}^{n+1} e^{ij+\frac{1}{2}\theta} - \hat{m}^{n+1} e^{ij-\frac{1}{2}\theta} \right) - \frac{U\delta t}{2h} \left(-\hat{\rho}^{n+1} e^{ij-1\theta} + 2\hat{\rho}^{n+1} e^{ij\theta} - \hat{\rho}^{n+1} e^{ij+1\theta} \right). \quad (8.26)$$

This is equivalent to:

$$\hat{\rho}^{n+1} \left(1 + \frac{U\delta t}{\delta x} (1 - \cos(\theta)) \right) + \frac{2i\delta t}{\delta x} \sin\left(\frac{1}{2}\theta\right) \hat{m}^{n+1} = 0. \quad (8.27)$$

Define:

$$b = \frac{U\delta t}{\delta x} (1 - \cos(\theta)) \quad (8.28)$$

The system of equations takes the form:

$$\begin{bmatrix} 1+b & a \\ ac^2 & 1 \end{bmatrix} \begin{pmatrix} \hat{\rho}^{n+1} \\ \hat{m}^{n+1} \end{pmatrix} = \begin{bmatrix} 1 & 0 \\ k & 1-2ag \end{bmatrix} \begin{pmatrix} \hat{\rho}^n \\ \hat{m}^n \end{pmatrix}, \quad (8.29)$$

The characteristic polynomial is :

$$\begin{aligned} & (1 - \lambda(1+b))(1 - 2ag - \lambda) - (-a\lambda)(k - \lambda ac^2) = \\ & 1 - 2ag - \lambda - \lambda(1+b) + 2(1+b)ag + (1+b)\lambda^2 + a\lambda c - a^2 c^2 \lambda^2 = \\ & ((1+b) - a^2 c^2)\lambda^2 + \lambda(2(1+b)ag - 2 - b + ak) + (1 - 2ag). \end{aligned} \quad (8.30)$$

The roots are:

$$\begin{aligned} \lambda_{1,2} = & \frac{1}{2((1+b) - a^2 c^2)} \left[2 - 2(1+b)ag - ak + b \pm \right. \\ & \left. \sqrt{4(1+b)^2 a^2 g^2 - 4b(1+b)ag + 4a^2 kg(1+b) - 4ak} \right. \\ & \left. + b^2 - 2abk + a^2 k^2 + 4a^2 c^2 - 8a^3 g c^2 \right]. \end{aligned} \quad (8.31)$$

Upwind bias for density Convection implicit

The fourth scheme to be considered differs from the third, in that the inertia term is taken implicit, as in the second scheme. In the same way as before we have:

$$\begin{bmatrix} 1+b & a \\ ac^2 & 1+ag \end{bmatrix} \begin{pmatrix} \hat{\rho}^{n+1} \\ \hat{m}^{n+1} \end{pmatrix} = \begin{bmatrix} 1 & 0 \\ k & 1-ag \end{bmatrix} \begin{pmatrix} \hat{\rho}^n \\ \hat{m}^n \end{pmatrix} \quad (8.32)$$

which leads to the following characteristic polynomial:

$$\lambda^2 ((1+b)(1+ag) - a^2 c^2) + \lambda(-2 + ak - b(1-ag)) + (1-ag) \quad (8.33)$$

with roots:

$$\begin{aligned} \lambda_{1,2} = & \frac{1}{2((1+b)(1+ag) - a^2 c^2)} \left[2 - ak + b(1-ag) \pm \right. \\ & \left. \sqrt{4a^2 g^2 - 4ak + a^2 k^2 + 4a^2 c^2 - 4a^3 c^2 g +} \right. \\ & \left. 2b((2-ak)(1-ag) - (1+ag) + 2a^2 g^2) \right] \end{aligned} \quad (8.34)$$

Summary of stability properties

Approximate stability properties for the four schemes discussed, obtained by inspection of the plots of $|\lambda_{1,2}(\theta)|$ are summarized in Table 8.1, where $CFL = U\delta t/\delta x$. Note:

scheme	momentum convection	density upwind bias	M = 4	M = 20
1	explicit	no	$0.485 < \text{CFL} < 0.505$	uncond. unstable
2	explicit	yes	$\text{CFL} < 0.253$	$\text{CFL} < 0.068$
3	implicit	no	uncond. unstable	uncond. unstable
4	implicit	yes	$\text{CFL} < 3.315$	$\text{CFL} < 2.1$

Table 8.1: Stability properties of four time integration schemes.

- For scheme 1 and $M = 4$ both an upper and a lower bound on the CFL-number should be satisfied, which is impractical.
- Although scheme 2 is more diffusive than scheme 1, due to the density upwind bias, the former is actually stable for a smaller CFL-number than the latter for $M = 4$.
- Only the schemes with density bias 2 and 4 can be used for practical computations.
- Although scheme 3 is discretised more implicitly than scheme 1, the latter actually has a stability window, whereas the former has not.
- By implicitly discretising the convective terms in the momentum equation, we can raise the stability bound by a factor 10 or more. Moreover, the dependence of the stability on M of the implicit scheme is much weaker than for the explicit case.
- The CFL-number threshold for scheme 4 of $\mathcal{O}(2)$, is what one would expect for an explicit scheme, not for an almost fully implicit scheme.

We will verify the anomalous behavior of schemes 1 and 3, and the stability bound for scheme 4, for the case of $M = 4$ in Section 8.4 by numerical experiments.

8.3 Derivation of a stability condition

From Table 8.1 it is clear that there is a strong relation between the maximum allowable CFL number and the Mach number. Our aim is to provide simple formulas for estimating the maximum allowable CFL number as a function of the Mach number. First of all these can be used as a guideline for choosing the time step for a simulation. Secondly these can help to reflect the essence of the Mach dependent behavior, which can be used to adapt time integration schemes for specific regions of the Mach number.

A necessary and sufficient condition for stability is to require:

$$\forall \theta \text{ such that } \frac{d}{d\theta} |\lambda(\theta)| = 0 : |\lambda(\theta)| \leq 1 \quad (8.35)$$

However, even for these simple schemes, the application of this condition will lead to very complicated expressions. Therefore, a simpler approach is chosen. We will settle for a

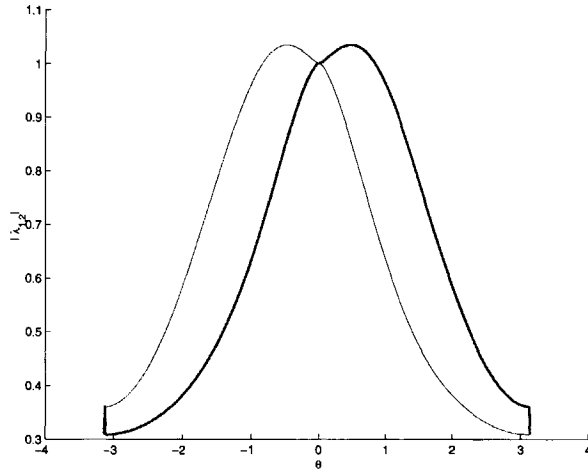


Figure 8.1: Absolute value of eigenvalues as function of θ , case of linear instability.

necessary condition, that is sufficiently close to a sufficient condition to be of practical value. As an example, we will derive a necessary stability condition for Scheme 2. Inspection of the absolute value of the eigenvalues as a function of θ shows that for certain values of velocity and Mach number the absolute value of the eigenvalues has a local minimum at $\theta = 0$ (Figure 8.1) and for other cases a local maximum (Figure 8.2); all four schemes are found to show qualitatively the same behavior. Consistency of the discretisation requires :

$$|\lambda|_{\theta=0} = 1. \quad (8.36)$$

If a local minimum is present for the absolute value of one of eigenvalues at $\theta = 0$, then for this eigen value

$$\left. \frac{d|\lambda|}{d\theta} \right|_{\theta=0} = 0, \quad (8.37)$$

$$\lim_{\theta \rightarrow 0} \frac{d^2|\lambda_{1,2}|}{d\theta^2} > 0, \quad (8.38)$$

because $|\lambda(\theta)| \in C^2$. This means that

$$|\lambda|_{1,2} > 1 | \theta \in \langle -\epsilon, 0 \rangle \cup \langle 0, \epsilon \rangle, \quad (8.39)$$

and the discretisation will be unstable. This gives us the following necessary, but not

and

$$A\sqrt{B} = -\frac{1}{2}\sqrt{2b_2}|\theta| \left(\bar{a}_0 - \frac{\bar{a}_0 b_3}{6b_2}\theta - \bar{a}_1\theta \right) + O(\theta^3). \quad (8.55)$$

so that

$$\bar{A}\sqrt{B} + A\sqrt{B} = \frac{1}{2}\sqrt{2b_2}|\theta| \left(\bar{a}_0 + \frac{\bar{a}_0 b_3}{3b_2}\theta + 2\bar{a}_1\theta \right) + O(\theta^3). \quad (8.56)$$

Finally,

$$\begin{aligned} \sqrt{B\bar{B}} &= \sqrt{\frac{1}{2}b_2\theta^2 + \frac{1}{3}b_3\theta^3 + O(\theta^4)} \sqrt{\frac{1}{2}b_2\theta^2 + \frac{1}{3}b_3\theta^3 + O(\theta^4)} \\ &= \frac{1}{4}|2b_2|\theta^2 + O(\theta^3), \end{aligned} \quad (8.57)$$

and

$$\frac{1}{C^2} = \frac{1}{\left(c_0 + \frac{1}{2}c_2\theta^2 + O(\theta^3)\right)^2} = \frac{1}{c_0^2} \left(1 - \frac{c_2}{c_0}\theta^2 + O(\theta^3) \right). \quad (8.58)$$

Substitution of (8.52)–(8.58) in (8.43) shows that

$$\begin{aligned} \lambda\bar{\lambda} &= \frac{1}{c_0} \left(1 - \frac{c_2}{c_0}\theta^2 + O(\theta^3) \right) \left(a_0^2 + (a_0 a_2 + |a_1|^2)\theta^2 + \right. \\ &\quad \left. \frac{1}{2}\sqrt{2b_2}|\theta| \left(\frac{a_0 b_3}{3b_2}\theta + 2\bar{a}_1\theta \right) + \frac{1}{4}|2b_2|\theta^2 + O(\theta^3) \right). \end{aligned} \quad (8.59)$$

Since

$$\lambda\bar{\lambda}(\theta) \cong 1 + \frac{1}{2} \lim_{\theta \rightarrow 0} \frac{d^2 \lambda\bar{\lambda}}{d\theta^2} \theta^2, \quad (8.60)$$

comparison of (8.59) and (8.60) shows that:

$$\left. \frac{d^2 \lambda\bar{\lambda}}{d\theta^2} \right|_{\theta=0} = \frac{2}{c_0^2} \left((a_0 a_2 + |a_1|^2) \pm \frac{1}{2}\sqrt{2b_2} \left(\frac{\bar{a}_0 b_3}{3b_2} + 2\bar{a}_1 \right) + \frac{1}{2}|b_2| - a_0^2 \frac{c_2}{c_0} \right) \quad (8.61)$$

$$\begin{aligned} &= \left(\left(-\frac{u\tau}{\delta x} + 2\frac{u^2\tau^2}{h^2} \right) + 2\frac{u^2\tau^2}{h^2} \right) \pm 2i \frac{c\tau}{\delta x} \left(\frac{\left(i\frac{\tau^2 u}{h^3} (2u^2\tau - 4c^2\tau) \right)}{\frac{c^2\tau^2}{h^2}} + 4i \frac{u\tau}{\delta x} \right) + \\ &\quad \left(4\frac{c^2\tau^2}{h^2} - 4 \left(\frac{u\tau}{\delta x} + 2\frac{c^2\tau^2}{h^2} \right) \right), \end{aligned} \quad (8.62)$$

which finally gives:

$$\left. \frac{d^2 \lambda \bar{\lambda}}{d\theta^2} \right|_{\theta=0} = \left(-3 \frac{u\tau}{\delta x} + 4 \frac{u^2 \tau^2}{h^2} - 2 \frac{c^2 \tau^2}{h^2} \pm \frac{u^3 \tau^2}{ch^2} \right), \quad (8.63)$$

and substitution of (8.63) in (8.41) gives:

$$\left(4 - \frac{2}{M^2} \pm 2M \right) \frac{U\delta t}{\delta x} \leq 3, \quad (8.64)$$

which should be satisfied for both the + and - sign. For $0.5 < M < 1.5$ we found that, although $|\lambda_{1,2}| \leq 1$ for $|\theta| < \epsilon$, we can have $|\lambda_{1,2}| > 1$ for $\theta = \pm\pi$. Therefore, we add the following constraint:

$$\lambda_i \bar{\lambda}_i \Big|_{\theta=\pm\pi} < 1,$$

which leads to the following conditions:

$$\begin{aligned} \frac{U\delta t}{\delta x} &< \frac{M^2 - M\sqrt{9M^2 - 4}}{1 - 2M^2}, \quad \frac{2}{3} < M, \quad \text{or} \\ \frac{U\delta t}{\delta x} &> \frac{M^2 + M\sqrt{9M^2 - 4}}{1 - 2M^2}, \quad \frac{2}{3} < M. \end{aligned} \quad (8.65)$$

For scheme 1 we can similarly derive from (8.41):

$$\left(4 - \frac{2}{M^2} \pm 2M \right) \frac{U\delta t}{\delta x} \leq 2 \pm M, \quad (8.66)$$

together with:

$$\begin{aligned} \frac{U\delta t}{\delta x} &< M^2 + M\sqrt{M^2 - 1}, \quad 1 < M, \quad \text{or} \\ \frac{U\delta t}{\delta x} &> M^2 - M\sqrt{M^2 - 1}, \quad 1 < M. \end{aligned} \quad (8.67)$$

Taking the limit $M \downarrow 0$ in (8.64) or (8.66), one finds unconditional stability. However, this stability prediction does not carry over to the multi-dimensional case. The one-dimensional case is special, because in the incompressible limit the mass conservation reduces to the solenoidality constraint, which in one space dimension means:

$$\frac{\partial m}{\partial x} = 0 \Rightarrow m = m(t), \quad (8.68)$$

and this means that the momentum field is fully represented by the Fourier mode $\theta = 0$. For a consistent discretisation the amplification factor of the $\theta = 0$ mode is unity by definition, and therefore the scheme is unconditionally stable. However, the multi-

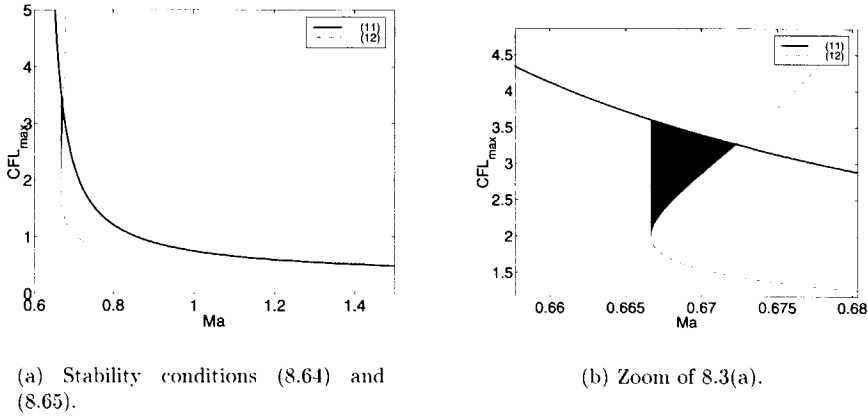


Figure 8.3: Stability conditions for Scheme 2.

dimensional equivalent of (8.68), i.e. $\text{div } \mathbf{m} = 0$, has a nontrivial solution and the previous argument no longer holds. In the multi-dimensional case we find indeed experimentally that for very small Mach numbers the scheme is not unconditionally stable. But practical experience shows that for $M > 0.3$ the above necessary stability conditions give practically useful predictions of the stability properties in the multi-dimensional case, if the above conditions are applied on a component-by-component basis (Section 8.4).

In Figure 8.3(a) the two conditions (8.64) and (8.65) are shown. For stability it is necessary that (M, CFL) is in the intersection of the regions between the axes and the curves.

8.4 Verification of stability thresholds

We will first verify experimentally the stability conditions (8.64) and (8.65) for test cases with increasing Mach number. The test case is a one-dimensional Riemann problem for the isothermal Euler equations, with the left and right states close together, so that we have a small perturbation of homogeneous initial conditions. The solution is computed on a uniform mesh covering $[-L_{\text{left}}, L_{\text{right}}]$, with in the supersonic cases $L_{\text{left}} \ll L_{\text{right}}$. On $[-L_{\text{left}}, 0]$ the initial conditions are $p_{\text{left}}, \rho_{\text{left}}, u_{\text{left}}$ and on $(0, L_{\text{right}}]$ $p_{\text{right}}, \rho_{\text{right}}, u_{\text{right}}$.

The initial conditions and the speed of sound for the various testcases are given in Table 8.2; M is based on u_{right} .

Table 8.3 shows the predicted threshold for the CFL number together with the smallest CFL number tested that induced instability and the largest CFL number tested that preserved stability for a range of Mach numbers. It is clear that the predicted stability threshold is pretty sharp and can be safely used in practice. For the case $M=1$ the

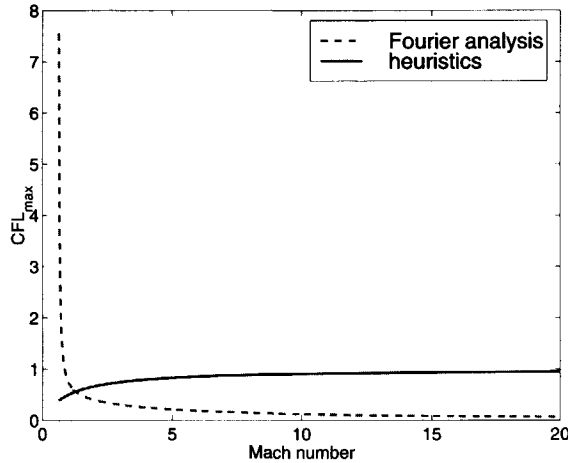


Figure 8.4: Stability conditions for Scheme 2.

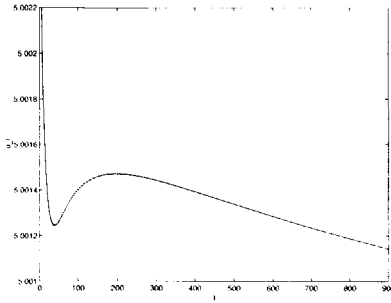
additional condition (8.65) becomes active.

Figs. 8.5 and 8.6 show results for the testcase $M = 5$. At the start of the computation, stability is dominated by nonlinear effects, due to the discontinuous initial condition. An initial overshoot is created, but when the CFL number is chosen within the stability limits, it is eventually damped out.

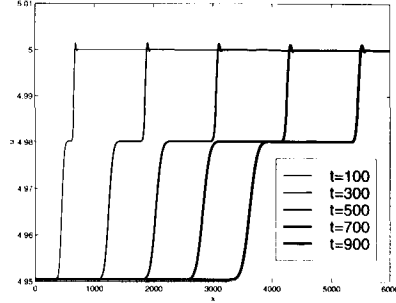
In order to further investigate the predictive capability of Fourier analysis for stability properties of our nonlinear schemes, we will now verify experimentally the stability thresholds obtained in Section 8.2 and listed in Table 8.1 for a testcase with $M \approx 4$, specified in Table 8.4. First we choose scheme 1, for which both an upper and a lower bound on the CFL-number should be fulfilled. Figure 8.7 shows results for $CFL = 0.43$, slightly below the lower bound. The wiggles are clearly amplified. Next we choose $CFL = 0.493$, halfway

M	ρ_{left}	p_{left}	u_{left}	ρ_{right}	p_{right}	u_{right}	c
0.1	1.01	1.1	00.099	1	1.09	0.1	1
1	1.01	1.1	00.990	1	1.09	1	1
5	1.01	1.1	04.950	1	1.09	5	1
10	1.01	1.1	09.901	1	1.09	10	1
15	1.01	1.1	14.851	1	1.09	15	1

Table 8.2: Initial conditions for Riemann problems.

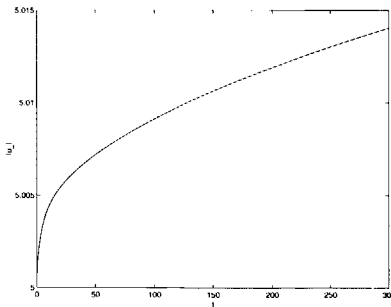


(a) $\|u\|_\infty$ as function of time.

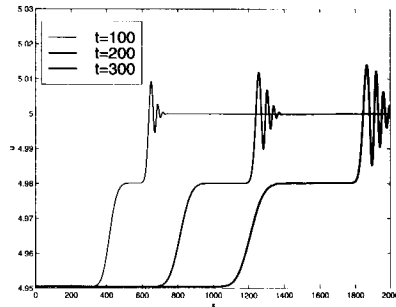


(b) Solution u at $t=100$, $t=300$, $t=500$ and $t=700$.

Figure 8.5: Stable integration of $M = 5$ testcase, $CFL = 0.20$.



(a) $\|u\|_\infty$ as function of time.



(b) Solution u at $t=100$, $t=200$ and $t=300$.

Figure 8.6: Unstable integration of $M = 5$ testcase, $CFL = 0.25$.

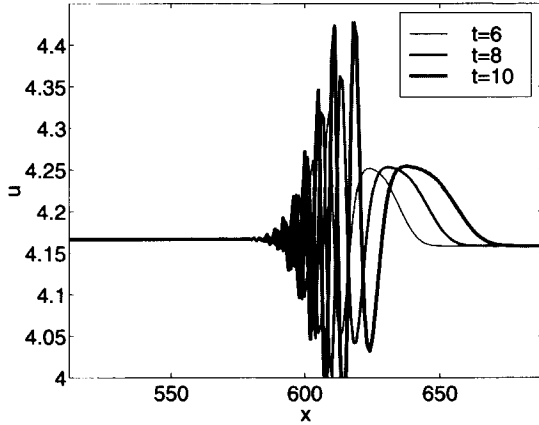


Figure 8.7: Unstable integration with scheme 1, CFL = 0.430.

between the upper and lower bound. Although wiggles occur during the startup phase, they are clearly damped out in time (Figure 8.8). Next scheme 3 is used, again with CFL = 0.493. Although this scheme is more implicit than scheme 1, Figure 8.9 shows that it is unstable, in complete agreement with our analysis! Finally, we will verify the stability threshold for scheme 4. Figure 8.10 shows a computation with CFL = 3.19, and Figure 8.11 with CFL = 3.61. In the first case the solution remains stable, whereas in the second case a smooth wiggle is generated. The smoothness of this overshoot is due to the fact that the absolute value of the eigenvalues of the amplification matrix exceeds unity in the low frequency domain, near $\theta = 0$. We conclude that Fourier stability analysis gives useful

M	CFL-number			
	stable	prediction by (8.64),(8.65) (present approach)	prediction by (8.2) (heuristic approach)	unstable
0.1	4.000	∞	0.009	—
1	0.600	0.618	0.500	0.650
5	0.200	0.215	0.833	0.250
10	0.080	0.125	0.909	0.170
15	0.060	0.088	0.938	0.100

Table 8.3: Numerical verification of the stability thresholds (8.64), (8.65) and (8.2) for one-dimensional testcase.

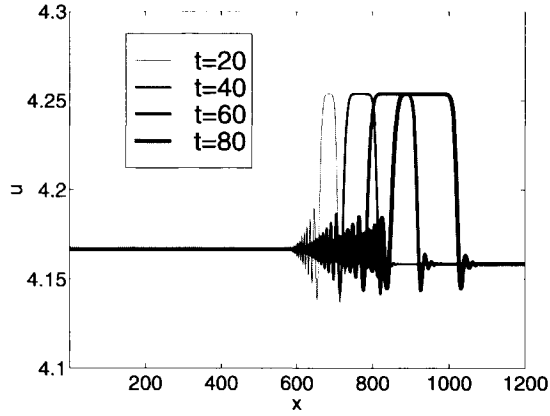


Figure 8.8: Stable integration with scheme 1, CFL = 0.493.

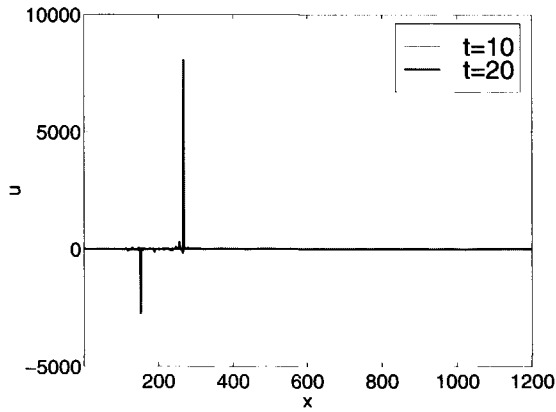


Figure 8.9: Unstable integration with scheme 3, CFL = 0.493.

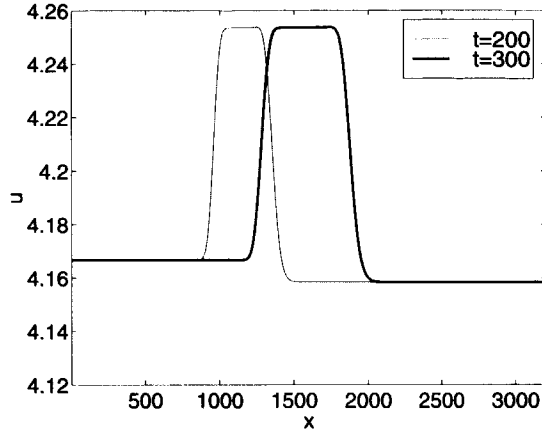


Figure 8.10: Stable integration with scheme 4, CFL = 3.19.

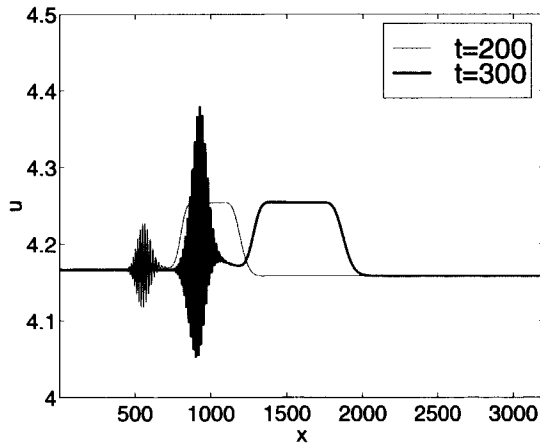


Figure 8.11: Unstable integration with scheme 4, CFL = 3.61.

$u_{\text{left}} = 4.1666$	$u_{\text{right}} = 4.1584$
$\rho_{\text{left}} = 1.2000$	$\rho_{\text{right}} = 1.0000$
$p_{\text{left}} = 1.1000$	$p_{\text{right}} = 0.9000$
$c = 1.0000$	

Table 8.4: Initial conditions for $M = 4$ Riemann problem.

M_{max}	$\text{CFL}_{\text{max,stable}}$	$\text{CFL}_{\text{max,predicted}}$ (8.64) (8.65)
1.1	0.74	0.66
1.8	0.48	0.43
3	0.60	0.37

Table 8.5: Numerical verification of the stability thresholds (8.64) and (8.65) for two-dimensional testcase.

stability predictions for the nonlinear schemes considered here.

Finally we look at a two-dimensional testcase. The inviscid isothermal flow in a two-dimensional channel with a 10% circular bump is computed for a number of inflow Mach numbers. Taking into account that in this testcase the transversal velocity is much smaller than the longitudinal velocity, we impose our one-dimensional stability criterion on the CFL_{max} based on the maximum longitudinal velocity. The predicted one-dimensional stability threshold and the actual stability threshold are listed in Table 8.5. It is clear that the one-dimensional criterion gives a conservative estimate of CFL_{max} . To get a more accurate prediction of the stability threshold, the present analysis can be extended to two dimensions in a straightforward manner, but we will not do this.

8.5 Inclusion of solution procedure in stability analysis

In the pressure correction method, the momentum at the new timestep is calculated as:

$$\begin{aligned}
 m^{n+1} &= m^* - \delta t (p^{n+1} - p^n) \Rightarrow \\
 m^{n+1} &= m^* - \delta t c^2 (\rho^{n+1} - \rho^n).
 \end{aligned}
 \tag{8.69}$$

We introduce this relation in the analysis to make it conform more closely to the actual algorithm. The discrete mass conservation equation can be written as:

$$\rho_j^{n+1} - \rho_j^n + \lambda F|_{j-\frac{1}{2}}^{j+\frac{1}{2}}, \quad \lambda = \delta t / \delta x, \quad (8.70)$$

with

$$F_{j+\frac{1}{2}} = \frac{2\rho_j^{n+1}}{\rho_{j+1}^{n+1} + \rho_j^{n+1}} \left(m_{j+\frac{1}{2}}^* - \frac{\delta t}{\delta x} \left((p_{j+1}^{n+1} - p_{j+1}^n) - (p_j^{n+1} - p_j^n) \right) \right). \quad (8.71)$$

Perturbation with $\delta\rho$, δm and δp gives a linearized perturbation δF with

$$\delta F_{j+\frac{1}{2}} = \delta m_{j+\frac{1}{2}}^* - \left(\lambda c^2 + \frac{1}{2}U \right) \delta \rho^{n+1}|_j^{j+1} + \lambda c^2 \delta \rho^n|_j^{j+1}. \quad (8.72)$$

Substitution of the Fourier modes $\rho_j = \hat{\rho} e^{ij\theta}$, $m_{j+\frac{1}{2}}^* = \hat{m}^* e^{i(j+\frac{1}{2})\theta}$ gives:

$$\begin{aligned} \hat{\rho}^{n+1} - \hat{\rho}^n + \lambda \hat{m}^* \left(e^{\frac{1}{2}i\theta} - e^{-\frac{1}{2}i\theta} \right) + U \lambda \hat{\rho}^{n+1} (1 - e^{-i\theta}) + \\ \frac{1}{2} U \lambda \hat{\rho}^n (e^{-i\theta} - e^{i\theta}) + c^2 \lambda^2 \hat{\rho}^{n+1} (-e^{i\theta} + 2 - e^{-i\theta}) - \\ c^2 \lambda^2 \hat{\rho}^n (-e^{i\theta} + 2 - e^{-i\theta}) = 0, \end{aligned} \quad (8.73)$$

or

$$(1 + ag - l + c^2 s) \hat{\rho}^{n+1} = (1 + c^2 s) \hat{\rho}^n - a \hat{m}^*, \quad (8.74)$$

where

$$s = 1 - 2 \cos(\theta), \quad (8.75)$$

$$p = \frac{1}{4} U \lambda (e^{-2i\theta} - 7e^{-i\theta} + 3 + e^{i\theta}), \quad (8.76)$$

$$a = 2\lambda i \sin(\theta/2), \quad (8.77)$$

$$l = U \lambda i \sin(\theta). \quad (8.78)$$

The Fourier transform of the pressure-correction scheme takes the following form:
Predictor step:

$$\begin{pmatrix} 1 & 0 \\ -k & 1 + 2ag \end{pmatrix} \begin{pmatrix} \hat{\rho}^* \\ \hat{m}^* \end{pmatrix} = \begin{pmatrix} l & 0 \\ -ac^2 & 1 \end{pmatrix} \begin{pmatrix} \hat{\rho}^n \\ \hat{m}^n \end{pmatrix}, \quad (8.79)$$

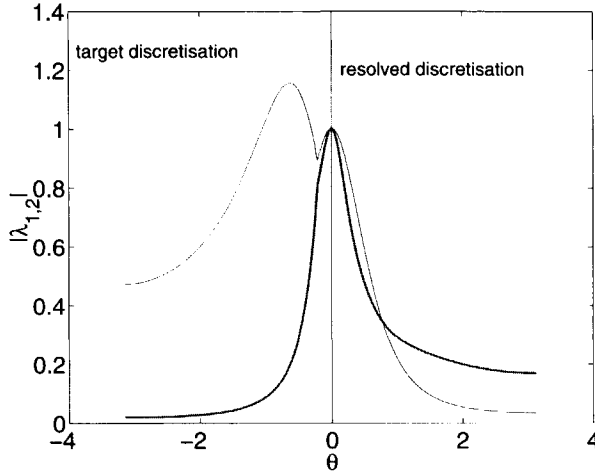


Figure 8.12: Dependence of $|\lambda_{1,2}(G_2^{-1}G_1)|$ on θ , with (*resolved* discretisation) and without inclusion of the pressure correction algorithm (*target* discretisation).

Corrector step:

$$\begin{pmatrix} 1 + ag - l + c^2s & 0 \\ ac^2 & 1 \end{pmatrix} \begin{pmatrix} \hat{\rho}^{n+1} \\ \hat{m}^{n+1} \end{pmatrix} = \begin{pmatrix} 1 + c^2s & 0 \\ ac^2 & 0 \end{pmatrix} \begin{pmatrix} \hat{\rho}^n \\ \hat{m}^n \end{pmatrix} + \begin{pmatrix} 0 & -a \\ 0 & 1 \end{pmatrix} \begin{pmatrix} \hat{\rho}^* \\ \hat{m}^* \end{pmatrix}. \tag{8.80}$$

We write this as follows:

$$\begin{aligned} G_1 \underline{v}^* &= G_0 \underline{v}^n, \\ G_4 \underline{v}^{n+1} &= G_3 \underline{v}^* + G_2 \underline{v}^n. \end{aligned} \tag{8.81}$$

Hence, the amplification matrix is given by:

$$G_4^{-1} (G_3 + G_2 G_1^{-1} G_0).$$

For stability we require that

$$|\lambda_{1,2}(G_4^{-1} (G_3 + G_2 G_1^{-1} G_0))| \leq 1.$$

Fig. 8.12 shows the dependence of $|\lambda_{1,2}(G_2^{-1}G_1)|$ on θ , for a particular case for Scheme

4, both with (*resolved discretisation*) and without (*actual discretisation*) inclusion of the pressure correction algorithm. The different behavior of resolved and target discretisation as observed in Fig. 8.12 shows that it is necessary to study the stability properties of the resolved discretisation to make a correct estimate of the stability thresholds.

8.6 Higher order spatial discretisation

Two different approaches can be followed to choose a suitable time discretisation for a TVD spatial discretisation. The first approach uses the heuristic argument that the stability domain of the time integration method should contain the stability regions of both the first order and higher order method between which the limiter switches. The second approach is to choose a time integration method, which has been proven to be total variation diminishing, since this implies stability. Proofs are available only for (nonlinear) scalar equations [80]. Because for our schemes stability properties have to be analyzed for the coupled system, only the first approach can be followed.

In this example we include the pressure correction method in the stability analysis together with the necessary deferred correction steps, required to obtain a high order spatial discretisation on a compact stencil. The solution procedure is now as follows: First the momentum predictor equation is solved with the κ -scheme in a deferred correction manner:

$$\begin{aligned} \frac{m_{j+\frac{1}{2}}^* - m_{j+\frac{1}{2}}^n}{\delta t} + \frac{1}{\delta x} (F_{j+1} - F_j) &= -\frac{1}{\delta x} (p_{j+1}^n - p_j^n), \\ F_{j+1} &= u_{j+\frac{1}{2}}^n m_{j+\frac{1}{2}}^* - u_{j+\frac{1}{2}}^n m_{j+\frac{1}{2}}^n + \\ &\left(\frac{\kappa - 1}{4} u_{j-\frac{1}{2}}^n m_{j-\frac{1}{2}}^n + \frac{4 - 2\kappa}{4} u_{j+\frac{1}{2}}^n m_{j+\frac{1}{2}}^n + \frac{\kappa + 1}{4} u_{j+\frac{3}{2}}^n m_{j+\frac{3}{2}}^n \right). \end{aligned}$$

Application of the κ -scheme to the mass conservation equation in a deferred correction manner leads, after linearisation, to the following pressure correction equation:

$$\begin{aligned} \frac{\rho_j^{n+1} - \rho_j^n}{\delta t} + \frac{1}{\delta x} (G_{j+\frac{1}{2}} - G_{j-\frac{1}{2}}) &= 0, \\ G_{j+\frac{1}{2}} &= \sigma_{j+1/2,HO}^n m_{j+1/2}^* + \\ &\left(\frac{\delta x}{4\rho^2 c^2} \frac{\partial p}{\partial x} |m^*| \right)_{j+1/2} \left(\left(\frac{dp}{dp} \right)_j \delta p_j + \left(\frac{dp}{dp} \right)_{j+1} \delta p_{j+1} \right) + \\ &\left(-\frac{1}{2\rho} |m^*| \right)_{j+1/2} \left(\left(\frac{dp}{dp} \right)_{j+1} \delta p_{j+1} - \left(\frac{dp}{dp} \right)_j \delta p_j \right) - \sigma_{j+1/2,HO}^n \frac{\delta t}{\Delta x} (\delta p_{j+1} - \delta p_j) \\ &+ \left(\frac{(\sigma_{LO}^n - \sigma_{HO}^n) m^*}{2\rho^n} \right)_{j+1/2} \left(\left(\frac{dp}{dp} \right)_{j+1} \delta p_{j+1} + \left(\frac{dp}{dp} \right)_j \delta p_j \right), \end{aligned}$$

where

$$\sigma_{j+\frac{1}{2},\text{HO}}^n = \frac{2 \left(\frac{\kappa-1}{4} \rho_{j-1}^n + \frac{4-2\kappa}{4} \rho_j^n + \frac{\kappa+1}{4} \rho_{j+1}^n \right)}{\rho_j^n + \rho_{j+1}^n},$$

$$\sigma_{j+\frac{1}{2},\text{LO}}^n = \frac{2\rho_j^n}{\rho_j^n + \rho_{j+1}^n}.$$

Application of the Fourier analysis procedure leads to the following system of equations:
Predictor step

$$\begin{pmatrix} 1 & 0 \\ 0 & 1+ag \end{pmatrix} \begin{pmatrix} \hat{\rho}^* \\ \hat{m}^* \end{pmatrix} = \begin{pmatrix} 1 & 0 \\ -q - ac^2 & 1+ag-p \end{pmatrix} \begin{pmatrix} \hat{\rho}^n \\ \hat{m}^n \end{pmatrix}.$$

Corrector step

$$\begin{pmatrix} 1+ag-l+s & 0 \\ ac^2 & 1 \end{pmatrix} \begin{pmatrix} \hat{\rho}^{n+1} \\ \hat{m}^{n+1} \end{pmatrix} =$$

$$\begin{pmatrix} 1+s & 0 \\ ac^2 & 0 \end{pmatrix} \begin{pmatrix} \hat{\rho}^n \\ \hat{m}^n \end{pmatrix} + \begin{pmatrix} ag - \frac{1}{2}p & -a \\ 0 & 1 \end{pmatrix} \begin{pmatrix} \hat{\rho}^* \\ \hat{m}^* \end{pmatrix},$$

where we have introduced the following abbreviations:

$$s = 1 - 2 \cos(\theta), \quad p = \frac{1}{4} U \lambda (e^{-2i\theta} - 7e^{-i\theta} + 3 + 3e^{i\theta}), \quad l = U \lambda i \sin(\theta),$$

$$q = \frac{1}{16} U^2 \lambda \hat{\rho}^{n+1} \left(-e^{-2\frac{1}{2}i\theta} + 6e^{-1\frac{1}{2}i\theta} + 4e^{-\frac{1}{2}i\theta} - 6e^{\frac{1}{2}i\theta} - 3e^{1\frac{1}{2}i\theta} \right).$$

Or in operator form:

$$G_1 \begin{pmatrix} \tilde{\rho}^* \\ \tilde{m}^* \end{pmatrix} = G_0 \begin{pmatrix} \tilde{\rho}^n \\ \tilde{m}^n \end{pmatrix},$$

$$G_4 \begin{pmatrix} \tilde{\rho}^{n+1} \\ \tilde{m}^{n+1} \end{pmatrix} = G_3 \begin{pmatrix} \tilde{\rho}^n \\ \tilde{m}^n \end{pmatrix} + G_2 \begin{pmatrix} \tilde{\rho}^* \\ \tilde{m}^* \end{pmatrix}.$$

The amplification matrix is now given by:

$$G_4^{-1} (G_3 + G_2 G_1^{-1} G_0).$$

For stability we require that

$$|\lambda_{1,2}(G_4^{-1} (G_3 + G_2 G_1^{-1} G_0))| \leq 1.$$

We have not succeeded yet in deriving from this simple necessary stability conditions, as in the first order case. Instead, we compute $|\lambda_{1,2}(\theta)|$ for a sufficiently fine distribution of $-\pi < \theta < \pi$. For a scalar convection diffusion equation, we know [46] that stability is

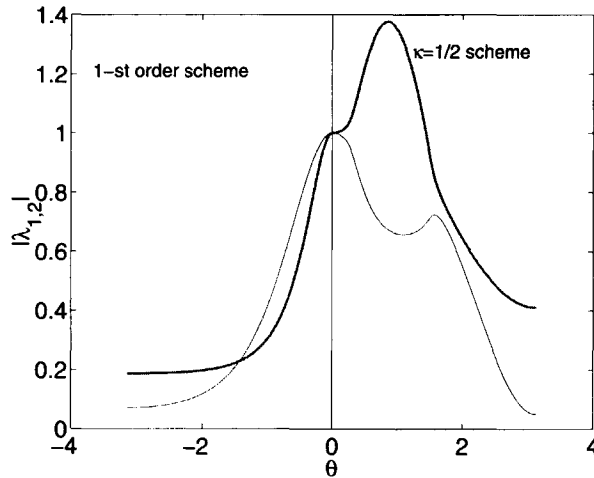


Figure 8.13: Dependence of $|\lambda_{1,2}(G_2^{-1}G_1)|$ on θ , for 1st-order upwind scheme with and without higher order upwind deferred correction.

not affected by a deferred correction step. Figure 8.13 shows, however, that in the case of a system the functional dependence of $|\lambda_{1,2}|$ on θ is qualitatively different from that for the first order upwind scheme. Generally the CFL-number threshold for the higher order upwind scheme is much smaller than for the first order upwind scheme.

8.7 Formulation of a discretisation with optimal stability properties

All schemes that were analysed above have only limited applicability for the HEM, because they all have to respect severe stability restrictions for highly compressible flow $M > 4$. Using the methodology of stability analysis presented before we are able to formulate a time integration scheme that has stability properties nearly uniform in the Mach number for $0 \leq M \leq 20$. This scheme will be used to compute cavitation with the HEM in Chapter 9.

8.7.1 Momentum equation

It is reasoned that the limited stability domain of scheme 4, which is almost fully implicit, is caused by the semi-implicit first order linearized discretisation of the convective terms in the momentum equation: $u_{j+\frac{1}{2}}^n m_{j+\frac{1}{2}}^{n+1}$. This can be avoided by using a Newton linearized fully implicit formulation of the convective terms, where the density at the new time level

is found from a density predictor equation, that is easily solved at low cost. The Newton-linearized convective term takes the following form:

$$\begin{aligned} (u^{n+1}m^{n+1})\Big|_{j-\frac{1}{2}}^{j+\frac{1}{2}} &\approx (u^{n+1}m^n + u^n m^{n+1} - u^n m^n)\Big|_{j-\frac{1}{2}}^{j+\frac{1}{2}} = \quad (8.82) \\ \left(\left(\frac{m^n}{\rho^{n+1}} + u^n\right)m^{n+1} - u^n m^n\right)\Big|_{j-\frac{1}{2}}^{j+\frac{1}{2}} &\approx \left(\left(\frac{m^n}{\rho^*} + u^n\right)m^{n+1} - u^n m^n\right)\Big|_{j-\frac{1}{2}}^{j+\frac{1}{2}}, \end{aligned}$$

where ρ^* is found from the solution of:

$$\frac{\rho^* - \rho^n}{\delta t} + \frac{1}{\delta x} \left(u_{j+\frac{1}{2}}^n \rho_j^* - u_{j-\frac{1}{2}}^n \rho_{j-1}^* \right) = 0 \quad (8.83)$$

8.7.2 Mass conservation equation

In this section the influence of various temporal discretisations for the mass conservation on the stability properties of the coupled system is discussed. Small differences may have a large influence on stability. We will compare two schemes, namely scheme 4 and a modification of scheme 4, consisting in a change of the scheme for the mass conservation equation. To bring out the difference in the two schemes for the mass conservation equation, we rewrite this equation in the following form:

$$\rho_j^{n+1} - \rho_j^n + \lambda \left(u_{k+\frac{1}{2}}^{n+1} \rho_k^{n+1} \right)\Big|_{k=j-1}^{k=j} = 0, \quad \lambda = \delta t / \delta x, \quad (8.84)$$

whereas the modified version of scheme 4 uses

$$\rho_j^{n+1} - \rho_j^n + \lambda \left(u_{k+\frac{1}{2}}^n \rho_k^{n+1} \right)\Big|_{k=j-1}^{k=j} = 0. \quad (8.85)$$

The discretisation (8.85) is not suited for low Mach number flow, because in the limit $M \downarrow 0$ it does not reduce to the zero divergence constraint on u^{n+1} . Fig. 8.14 shows the absolute values of the eigenvalues of the amplification matrix as a function of the wavenumber θ , obtained by Fourier analysis for both schemes for a typical case.

We remark the following:

- The implicit discretisation effectively damps the high frequency modes, $-\pi \leq \theta \leq -\frac{\pi}{2} \cup \frac{\pi}{2} \leq \theta \leq \pi$, but is unstable for low frequency modes in the vicinity of $\theta = 0$.
- The semi-implicit discretisation effectively damps the low frequency modes, $-\frac{\pi}{2} \leq \theta \leq \frac{\pi}{2}$, but is unstable for the high frequency modes $-\pi \leq \theta \leq -\frac{\pi}{2} \cup \frac{\pi}{2} \leq \theta \leq \pi$.

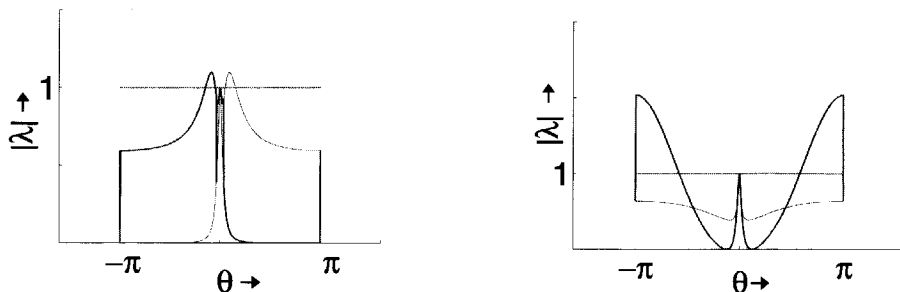


Figure 8.14: Dependence of the absolute values of eigenvalues of the amplification matrix on wavenumber θ for implicit(left) and semi-implicit(right) discretisation of mass conservation equation.

We therefore propose to use the following weighted average of (8.84) and (8.85):

$$\begin{aligned} \frac{\rho_j^{n+1} - \rho_j^n}{\delta t} + \beta \frac{1}{\delta x} \left(u_{j+\frac{1}{2}}^n \rho_j^{n+1} - u_{j-\frac{1}{2}}^n \rho_{j-1}^{n+1} \right) + \\ (1 - \beta) \frac{1}{\delta x} \left(u_{j+\frac{1}{2}}^{n+1} \rho_j^{n+1} - u_{j-\frac{1}{2}}^{n+1} \rho_{j-1}^{n+1} \right) = 0. \end{aligned} \quad (8.86)$$

Figure 8.15 shows the dependence of the absolute values of the eigenvalues of the amplification matrix for this scheme with $\beta = \frac{1}{2}$ and the same case as in Figure 8.14. It is clear that now there is sufficient damping for the whole frequency domain.

The stability analysis for this scheme shows that it is (nearly) unconditionally stable for all Mach numbers for CFL < 30 and beyond.

Based on heuristics we choose the following relation for β :

$$\begin{aligned} \Psi(r_{\rho, j+\frac{1}{2}}) \leq 0 &\Rightarrow \beta = \frac{1}{2}, \\ \Psi(r_{\rho, j+\frac{1}{2}}) > 0 &\Rightarrow \begin{cases} \beta = 1; & 0 < M \leq \frac{1}{2}, \\ \beta = \frac{1}{2}; & \frac{1}{2} < M \leq 8, \\ \beta = \frac{1}{8}; & 8 < M. \end{cases} \end{aligned} \quad (8.87)$$

8.8 Conclusions

We used von Neumann stability analysis to gain insight in the behavior of different time integration schemes. For simple schemes a relation between the Mach number and the maximum allowable CFL-number, following from a necessary stability condition, can be derived, that can be used in practice. The sequential solution procedure and deferred/deferred correction strategies can be included in the analysis in a straightforward manner. The

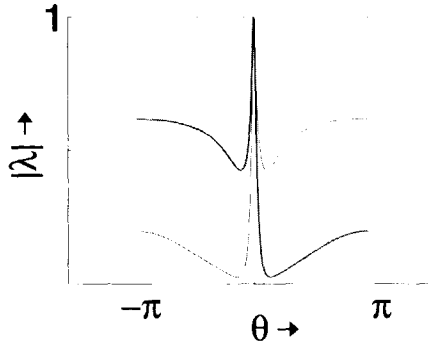


Figure 8.15: Dependence of the absolute values of the eigenvalues of the amplification matrix on wavenumber θ for (8.86), $\beta = \frac{1}{2}$.

linear analysis shows that the stability properties of the resolved discretisation can differ considerably from the properties of the target discretisation. Using the linear stability analysis we were able to formulate a time integration scheme with (nearly) unconditional stability for $0 \leq M < 25$. The latter scheme is used for the computations described in [Chapter 9].



Chapter 9

Applications

9.1 Introduction

We will present results obtained with the modified pressure correction scheme described in Section 8.7 for three different test cases. Use was made of the higher order upwind κ -scheme. First we compute steady sheet cavitation on a NACA66 hydrofoil and compare the obtained cavity length with results obtained with an interface fitting method. Next a comparison is made between computed results for the unsteady cavitation in a channel with the present method and results obtained with a method based on the SIMPLE algorithm. Finally we look at a simulation of unsteady sheet cavitation on the EN-hydrofoil.

9.2 Problem specification

The model has been implemented in the DeFT package [106], which is a structured finite volume code. The code uses discretisation in general (boundary fitted) coordinates and is fully parallelized under MPI [101].

Table 9.1 summarizes the parameter values that have been used to obtain all presented results.

Boundary conditions

At the inflow boundary and at the far-field boundary the two components of momentum m_x , m_y are prescribed. At the outflow boundary the pressure is prescribed. On the hydrofoil and the walls of the channel a nonpermeability condition is imposed. No special measures have been taken to avoid spurious wave reflections from the far field boundary.

Initialisation

Each computation of cavitating flow is started from a steady state solution. The pressure at the outflow boundary is prescribed high enough to ensure that the pressure is well above the vapor pressure in the whole computational domain. At the start of the calculation the

relative tolerance nonlinear Gauss-Seidel	10^{-9}
relative tolerance pressure correction	10^{-6}
relative tolerance momentum equation	10^{-6}

Equation of state		Ambient conditions	
c_1	$2.5 \cdot 10^{-3}$	$U_{\infty, x}$	1
c_4	$2.5 \cdot 10^{-3}$	$U_{\infty, y}$	0
$p_2 - p_1$	0.1	ρ_{∞}	10
ρ_1 / ρ_0	100		
C^n	$n = 9$		

Table 9.1: Parameter values of physical model and computing method.

σ	experiment	current approach	interface fitting approach [23]
1.00	.20	.32	.20
0.91	.36	.40	.32
0.84	.60	.65	.64

Table 9.2: NACA66-209 hydrofoil, computed cavity length, $\alpha = 4^\circ$, 144×20 cells.

pressure is lowered until the desired cavitation number has been reached. As opposed to [36] we maintain the equation of state constant during the startup phase.

9.3 Steady cavitation

9.3.1 NACA66 hydrofoil

We computed steady cavitation on a NACA66-209 hydrofoil [1]. The results were obtained with the first order upwind scheme. The mesh contains 144×20 cells, as shown in Figure 9.1. Table 9.2 compares the length of the computed cavitation region as fraction of chord length with the experimental values of [78], and the results of the interface fitting approach of [23]. In the case of an interface fitting method, the definition of the cavity length is rather arbitrary, because the aft end of the cavity is smoothly connected to the hydrofoil surface by an artificial transition region. Taking into account the simplicity of the HEM, the correlation is satisfactory.

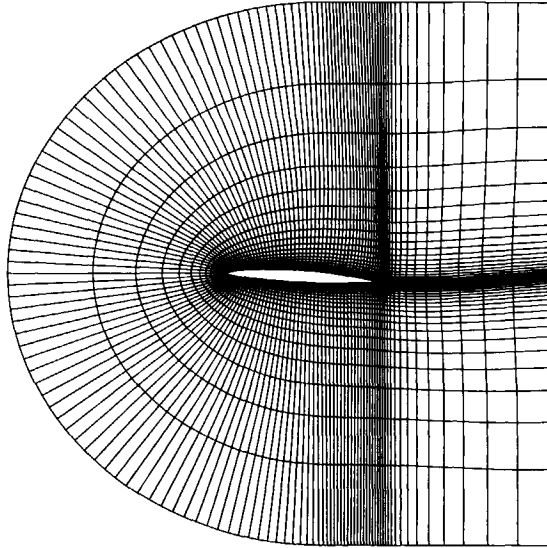


Figure 9.1: NACA66 hydrofoil, grid with 144×20 cells.

9.4 Unsteady cavitation

9.4.1 Converging/diverging channel.

We consider the same geometry as studied experimentally in [61] and numerically in [20, 24]. The geometry consists of a channel with a sharp bump on the bottom and is given in Figure 9.2. The detachment point of the cavity is fixed at the top of the bump. The grid consists of 113×20 cells. In [20] results are presented obtained with a SIMPLE-type

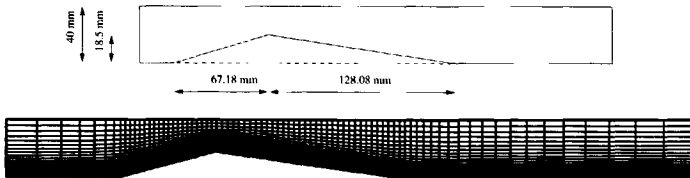


Figure 9.2: Converging/diverging channel, geometry and mesh.

solution procedure. A comparison is made with experimental results of [61]. Delannoy

$L_{cavity, max}/L_{reference}$				
σ	experiment	current approach	Dclannoy [20]	Dieval <i>et al.</i> [24]
2.7	—	2.00	2.0	—
2.5	—	1.75	2.0	—
2.0	—	0.50	1.5	—
Strouhal number				
σ	experiment	current approach	Dclannoy [20]	Dieval <i>et al.</i> [24]
2.7	.28	—	.170	—
2.5	.28	.10	.179	—
2.0	.28	.09	.154	0.235

Table 9.3: Converging/diverging channel, comparison of results.

[20] observed a qualitative difference in the shedding process between the results obtained with a first order upwind and a higher order upwind scheme. With the first order scheme the whole cavitation bubble was detached and convected downstream, whereas with the second order modified SMART-scheme [29] the cavity was cut into two by the re-entrant jet and only the aft part was detached. In the current simulation we observe the latter behavior. The maximum obtained cavity length and the Strouhal number here defined as:

$$S = \frac{L_{cavity,max}}{U_{throat} T_{shedding}}, \quad (9.1)$$

are identical for both schemes and are given in Table 9.3. For $\sigma = 2.7$ the cavity remained very small and highly fluctuating in a nonperiodic manner. Figure 9.3 shows the time-history of the pressure at the top of the channel just aft of the top of the bump. Strong pressure peaks indicating the moment of collapse of the shed part of the cavity are clearly noticeable. The large discrepancy between the experimentally observed and computed Strouhal number, both for the current approach and the method of [20] can be attributed to the use of a first order time-integration method. Future research will focus on the extension of the time-stepping method to second order. Dieval *et al.* [24] studied only the case $\sigma = 2.0$. Their more accurate prediction of the Strouhal number is obtained by using a second order BDF-method for the (physical) time-integration.

9.4.2 E.N.-hydrofoil

The E.N.-hydrofoil is a simple geometry, which has been studied experimentally in [51] and numerically in [69, 110]. The geometry is given by:

$$y = \pm \frac{2}{15} \sqrt{x(0.6-x)}; 0.0000 \leq x \leq 0.4187 \quad (9.2)$$

$$y = \pm (-0.05746x + 0.06079); 0.4187 \leq x \leq 1.0000 \quad (9.3)$$

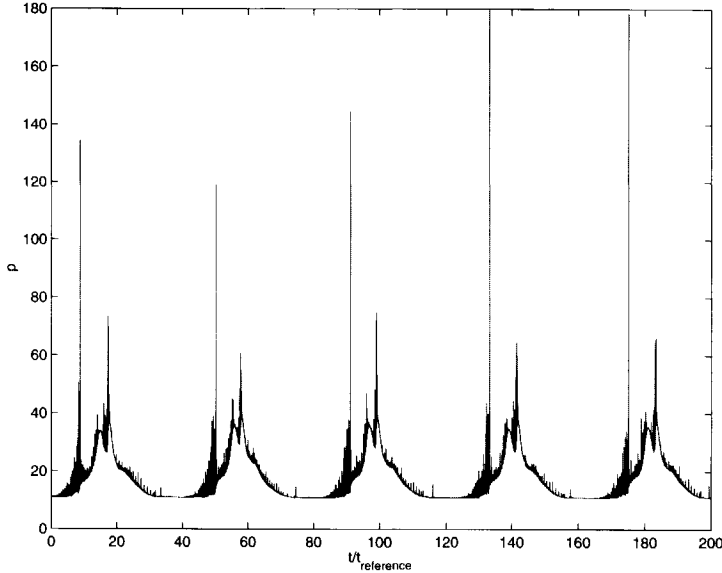


Figure 9.3: Converging/diverging channel, time history of pressure, $\sigma = 2.5$

Because the hydrofoil has a finite trailing edge thickness, we extended the hydrofoil surface linearly to $x = 1.059$, to facilitate generation of the C-type grid. The parameters of the

α_0	6.2°
L_{chord}	150 mm
U_∞	8 m/s
σ	1.2

Table 9.4: Input parameters for the experiments conducted in [51].

experimental setup used in [51] are summarized in Table 9.4. For comparison the resulting cavity length and shedding cycle frequency have been nondimensionalised with U_∞ and L_{chord} . In [69] and the current work the cavitation number is lowered to $\sigma = 1.1$ to obtain the experimentally observed cavity length. This means the model underestimates the experimental cavity extent. Approximately 400 time-steps are required to simulate one cycle (Figure 9.6). The experimentally observed dimensionless period of the cycle is 2.1. In the results we have computed an average dimensionless period of 2.0. To be able to represent the formation of a re-entrant jet, the mesh resolution in radial direction is chosen

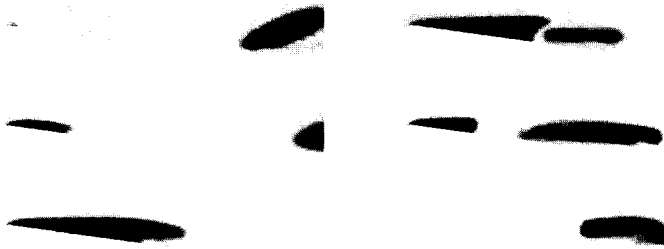


Figure 9.4: Converging/diverging channel, density levels, $\sigma = 2.5$.

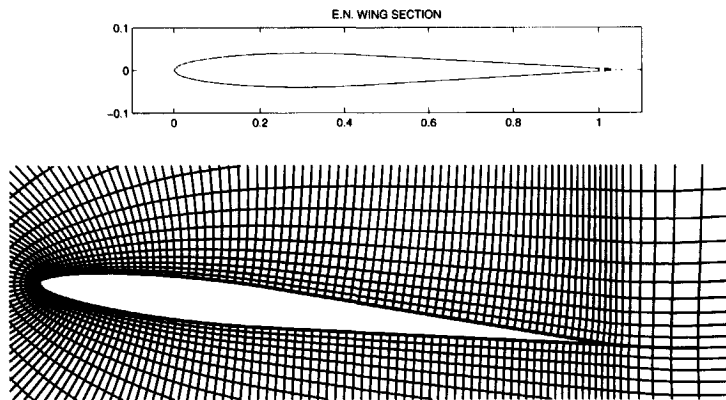


Figure 9.5: E.N.-hydrofoil, geometry and detail of mesh.

much smaller than normally required for inviscid airfoil computations. Furthermore, the grid spacing is increased near the hydrofoil trailing edge. This is done to ensure sufficient damping when a vortex generated by bubble collapse passes near the trailing edge. In this case the Kutta condition is momentarily no longer fulfilled and the fluidum will flow around the sharp trailing edge, introducing high velocities. In [69] artificial viscosity is added near the trailing edge to avoid instability.

In each cycle a part of the cavity is shed. In this detached bubble cloud the fluidum rotates clockwise in a vortex like manner. The vortex is convected downstream to the hydrofoil trailing edge, where it collapses. Zhang *et al.* [115] observed that the detached bubbles indeed collapse close to the attached cavitation region and leave powerful eddies behind. The first shed bubble initiates separation just upstream of the trailing edge and each new bubble causes the separation point to move further upstream. After a large number of cycles has passed a steady massive separation zone has formed behind the hy-

	Experimental [51]	Reboud <i>et al.</i> [69]	DeFT
σ	1.2	1.1	1.1
$U_\infty \Delta t / L_{\text{chord}}$	—	0.005	0.005
$U_\infty L_{\text{chord}} / f_{\text{shedding}}$	2.099	1.75 – 2.00	2.0
$L_{\text{cavity}} / L_{\text{chord}}$	0.4	0.4	0.35

Table 9.5: E.N.-hydrofoil, nondimensionalised results compared with [51] and [69].

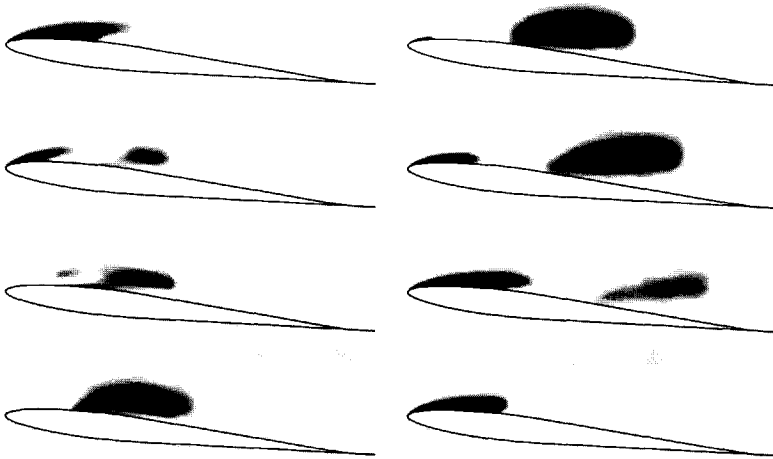


Figure 9.6: EN-wing, density levels, $\alpha = 6.2^\circ$, $\sigma = 1.2$.

drofoil (Figure 9.7). This separation zone decreases circulation and increases the minimum pressure at the leading edge, thus decreasing the size of the cavitation bubble. Both the first order upwind scheme and the third order ISNAS-scheme converge to the stationary solution shown in Figure 9.7. The formation of a steady separation zone was not reported in the numerical work of [69] and in the observations of [51] and [115].

Solutions to the Euler equations are not unique. We believe that in this case the solution is shifted to one of the many nonphysical branches by the vorticity generated by the collapsing bubbles. The incorporation of viscous effects would possibly damp the eddies and prevent the shear layer to arise.

9.5 Concluding remarks

For both the internal and the external flow configuration the agreement between the computed and experimental values of the cavity length is reasonably good. Extension of the first

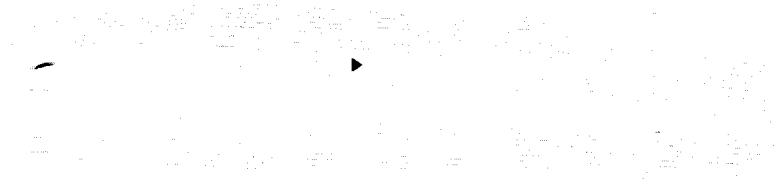


Figure 9.7: Steady separation zone at E.N.-hydrofoil

order time-integration method to higher order will improve the accuracy of the Strouhal number. Although the HEM presents an excellent opportunity to show the Mach uniform accuracy and efficiency of staggered schemes, the accuracy with which the model describes the interphase mass transfer in cavitating flow is, understandably, limited. Recently, more accurate models [52, 63] have appeared, that incorporate explicit expressions for the interfacial mass transfer. These models show more robust behavior and will offer a more fruitful starting point for further development as a method to compute cavitating flow than the HEM. In cases where a nonconvex equation of state corresponds to physical reality (as for nonperfect gases), the method presented here is attractive, cf. [71].

Part II
Magnetohydrodynamics



Chapter 10

Low Mach number ideal magnetohydrodynamics.

10.1 Introduction

The second part of this thesis is devoted to the development of a Mach-uniform method for the equations of ideal magnetohydrodynamics. These share the property of nonconvexity with the equations of the HEM. Although a lot has been written about Mach-uniform schemes for the Euler equations of gasdynamics, this field is more or less untrod. Therefore the methods discussed here have to be considered as a mere start.

10.2 The equations of ideal magnetohydrodynamics

The equations of ideal magnetohydrodynamics describe the dynamics of an inviscid *electrically conducting fluid*, a so-called plasma. The MHD model describes the flow in internal parts of stars, e.g. the sun, the solar wind and the interstellar medium. Numerical simulations of MHD flow are used to gain insight into numerous astrophysical phenomena. The equations are given by:

$$\frac{\partial \rho}{\partial t} + \nabla \cdot (\rho \mathbf{u}) = 0, \quad (10.1)$$

$$\frac{\partial \mathbf{m}}{\partial t} + \left(\nabla \cdot \left(\frac{\mathbf{m} \mathbf{m}^T}{\rho} + \frac{1}{2} |\mathbf{B}|^2 \mathbf{I} - \mathbf{B} \mathbf{B}^T \right) \right)^T = -\nabla p, \quad (10.2)$$

$$\frac{\partial \mathbf{B}}{\partial t} = \nabla \times \left(\frac{\mathbf{m}}{\rho} \times \mathbf{B} \right) = -\nabla \times \mathbf{E}, \quad (10.3)$$

$$\frac{\partial \rho E}{\partial t} + \nabla \cdot \left(\left(\frac{\rho E + p}{\rho} \right) \mathbf{m} + \left(\frac{|\mathbf{B}|^2 \mathbf{I} - 2\mathbf{B} \mathbf{B}^T}{\rho} \right) \mathbf{m} \right) = 0, \quad (10.4)$$

$$\nabla \cdot \mathbf{B} = 0, \quad (10.5)$$

$$p = (\gamma - 1)\rho e. \quad (10.6)$$

Equations (10.1),(10.2),(10.4) are the conservation equations for density ρ , momentum \mathbf{m} and total energy E respectively, while (10.3) is the *induction* equation, relating the evolution of the magnetic field \mathbf{B} to the electric field \mathbf{E} . The magnetic field has to respect the solenoidality constraint (10.5). The system is closed with the equation of state (10.6), relating the thermal pressure p to the density and the internal energy e . The ideal MHD equations reduce to the Euler equations if initial and boundary conditions $\mathbf{B} \equiv \mathbf{0}$ are prescribed.

10.3 Analytical aspects

For brevity we will restrict the analysis to the one-dimensional case. Nondimensionalisation can be done in many different ways [114]. We choose to introduce the following normalization:

$$\rho = \frac{\tilde{\rho}}{\tilde{\rho}_{\text{ref}}}, u = \frac{\tilde{u}}{\tilde{u}_{\text{ref}}}, x = \frac{\tilde{x}}{\tilde{x}_{\text{ref}}}, t = \frac{\tilde{t}}{\tilde{t}_{\text{ref}}}, p = \frac{\tilde{p}}{\tilde{p}_{\text{ref}}}, B = \frac{\tilde{B}}{\tilde{B}_{\text{ref}}}, \quad (10.7)$$

where the dimensional quantities are denoted by a tilde and the reference quantities are chosen in the following way:

$$\begin{aligned} \tilde{\rho}_{\text{ref}} &= \rho_{\text{inflow}} \\ \tilde{u}_{\text{ref}} &= u_{x,\text{inflow}} \\ \tilde{x}_{\text{ref}} &= L_{\text{max}} \\ \tilde{t}_{\text{ref}} &= \frac{\tilde{x}_{\text{ref}}}{\tilde{u}_{\text{ref}}} \\ \tilde{p}_{\text{ref}} &= p_{\text{out}} \\ \tilde{B}_{\text{ref}} &= B_{x,\text{out}} \end{aligned} \quad (10.8)$$

With this scaling the equations take the following form:

$$\frac{\partial \rho}{\partial t} + \frac{\partial m}{\partial x} = 0, \quad (10.9)$$

$$\frac{\partial m_x}{\partial t} + \frac{\partial}{\partial x} \left(\frac{m_x^2}{\rho} + \frac{1}{M_r^2} \left(\frac{1}{\beta} \Lambda_x + p \right) \right) = 0, \quad (10.10)$$

$$\frac{\partial m_y}{\partial t} + \frac{\partial}{\partial x} \left(\frac{m_x m_y}{\rho} + \frac{1}{\beta M_r^2} \Lambda_y \right) = 0, \quad (10.11)$$

$$\frac{\partial m_z}{\partial t} + \frac{\partial}{\partial x} \left(\frac{m_x m_z}{\rho} + \frac{1}{\beta M_r^2} \Lambda_z \right) = 0, \quad (10.12)$$

$$M_r^2 \left(\frac{\partial \rho E}{\partial t} + \frac{\partial}{\partial x} (u(\rho E + p)) \right) + \frac{1}{\beta} \frac{\partial}{\partial x} (\Lambda \cdot \mathbf{u}) + \frac{\partial u}{\partial x} = 0, \quad (10.13)$$

$$\frac{\partial B_x}{\partial t} = 0, \quad (10.14)$$

$$\frac{\partial B_y}{\partial t} + \frac{\partial}{\partial x} (u B_y - v B_x) = 0, \quad (10.15)$$

$$\frac{\partial B_z}{\partial t} + \frac{\partial}{\partial x} (u B_z - w B_x) = 0, \quad (10.16)$$

where

$$\Lambda_x = \frac{1}{8\pi} (B_y^2 + B_z^2 - B_x^2), \quad (10.17)$$

$$\Lambda_y = -\frac{1}{4\pi} B_x B_y, \quad \Lambda_z = -\frac{1}{4\pi} B_x B_z. \quad (10.18)$$

$$M_{Ar} = \sqrt{\rho_{\text{ref}} u_{\text{ref}}^2 / B_{\text{ref}}^2}, \quad (10.19)$$

$$\beta = \frac{M_{Ar}}{M_r}, \quad (10.20)$$

are the *Alfvén number* and the *plasma β* respectively. The plasma β expresses the balance between the thermal pressure and the components of the magnetic stress tensor as driving force. A distinction is made (See e.g. [114]) between the three cases $\beta \ll 1$, $\beta \approx 1$ and $\beta \gg 1$. Note that with the introduction of the scaling the relation between the total energy E and the thermal pressure p has changed accordingly.

Diagonalisation of the dimensional system of equations gives the following signal speeds for the different characteristic fields, (following the notation of [10]) in nonascending order:

$$u + c_f, \quad u + c_a, \quad u + c_s, \quad u, \quad u - c_s, \quad u - c_a, \quad u - c_f, \quad (10.21)$$

where c_f , c_a , c_s are the *fast*, *Alfvén* and the *slow* characteristic speeds respectively, given by:

$$c_a^2 = B_x^2 / \rho, \quad (10.22)$$

$$c_{f,s}^2 = \frac{1}{2} \left((c^*)^2 \pm \sqrt{(c^*)^4 - 4c^2 c_a^2} \right), \quad (10.23)$$

where $c^* = (\gamma p + |\mathbf{B}|^2) / \rho$. For the special case $B_y \ll B_x$, $B_z \ll B_x$, described in [10], the *scaled* characteristic speeds take the form:

$$c_f^2 = \max(M_r^{-2}, \beta^{-1}M_r^{-2}), \quad c_s^2 = \min(M_r^{-2}, \beta^{-1}M_r^{-2}). \quad (10.24)$$

In [10] it is shown that the hyperbolic system of the equations of ideal magnetohydrodynamics is nonconvex. Similar to the equations of the HEM, compound waves can occur.

10.4 Weakly compressible magnetohydrodynamic flow

In many astrophysical applications, weakly compressible magnetohydrodynamic flow is encountered. Because of the stiffness of the equations in the low Mach number limit, standard (explicit) magnetogasdynamics schemes become very inefficient [54]. To circumvent this a number of approximate models have been developed to incorporate compressibility effects in an 'incompressible' formulation. These are, among others:

- The anelastic approach [54]
- The 4-equation weakly compressible model [6]
- The equations of reduced magnetohydrodynamics [112, 113, 114]

Most of these are restricted to low Mach number flow only and/or to a certain β -regime. Furthermore, additional conditions are imposed e.g. on the structure of the magnetic field.

Instead of adapting the model, our approach will be to develop a numerical scheme with Mach-uniform behavior for the equations of ideal MHD. Eq. (10.24) shows that in the case of low acoustic Mach number MHD flow, $\max|\lambda| \approx M_r^{-2}$ for the case $\beta \gg 1$, but that for the cases $\beta \approx 1$, $\beta \ll 1$, $\max|\lambda| \approx \beta^{-1}M_r^{-2}$. This means that in the first case it suffices to take all terms related to the thermal pressure implicitly to handle the low Mach number stiffness of the equations, while in the latter case all terms related to the magnetic field should be taken implicitly as well. We will start with the development of a Mach-uniform scheme for the case $\beta \gg 1$. Unfortunately, this β -regime is of only limited physical importance: inappropriate for the description of the heliosphere, with the possible exception of the polar regions above and below the sun [114].

10.5 A staggered scheme for MHD

There are three reasons that make staggered schemes attractive to compute weakly compressible magnetohydrodynamic flow:

- Simple flux function, irrespective of the complexity of the hyperbolic system to be solved.

- Mach-uniform properties, that retain efficiency and accuracy in the weakly compressible case.
- Very efficient and accurate handling of the solenoidality of the discrete magnetic field.

The flux function

A key feature of the staggered scheme is that no use is made of the eigensystem of the Jacobian of the flux function. This results in very simple expressions for the flux, even for a rather complicated hyperbolic system like the equations of magnetohydrodynamics. The convective terms are upwind interpolated in the direction of the fluid velocity, while nonconvective terms are centrally discretised. Like in the case of the HEM discussed in the first part, extensions of classic schemes to the MHD-system, e.g. the Roe scheme [10], are much more complicated than their gasdynamic counterparts. The application of staggered schemes for the computation of MHD flow is discussed in [27, 86, 87].

Mach-uniform properties

The main reason for the application of staggered schemes in [27, 86, 87], was their straightforwardness, and their possibility to retain solenoidality of the discrete magnetic field. We believe that the Mach-uniform staggered schemes for the Euler equations presented in [7, 109] can be extended to the MHD equations and be a more efficient alternative to classic gasdynamic schemes and a more versatile alternative to the approximate models discussed above.

The solenoidality constraint

Different techniques to impose the solenoidality constraint are extensively discussed in [90]. Although the use of a staggered discretisation is crucial for Mach-uniformity, staggered placement of the components of the magnetic field has an extra advantage, namely accurate and efficient treatment of the solenoidality constraint on the magnetic field \mathbf{B} . If solenoidality of the magnetic field is not guaranteed, unphysical effects, e.g. magnetic monopoles [4], will arise. The *constrained transport* method of [27] uses a discrete version of the Stokes theorem to discretise the induction equation on a staggered grid in a way that guarantees solenoidality of a staggered magnetic field to machine precision. For simplicity we illustrate the approach for a coplanar problem discretised on a uniform Cartesian mesh (Fig. 10.1). Under the condition that $\nabla \cdot \mathbf{B}^n = 0$, straightforward finite difference discretisation of (10.3) and summation leads to:

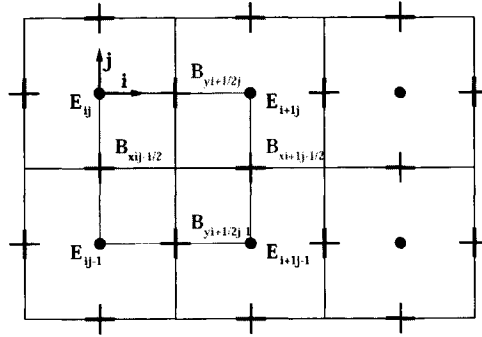


Figure 10.1: Illustration of the constrained transport approach.

$$\begin{aligned}
 - \left(B_{xij-\frac{1}{2}}^{n+1} - B_{xij-\frac{1}{2}}^n \right) &= \frac{\tau}{h} (E_{zij} - E_{zij-1}) \\
 \left(B_{xi+1j-\frac{1}{2}}^{n+1} - B_{xi+1j-\frac{1}{2}}^n \right) &= -\frac{\tau}{h} (E_{zi+1j} - E_{zi+1j-1}) \\
 - \left(B_{yi+\frac{1}{2}j-1}^{n+1} - B_{yi+\frac{1}{2}j-1}^n \right) &= -\frac{\tau}{h} (E_{zi+1j-1} - E_{zij-1}) \\
 \left(B_{yi+\frac{1}{2}j}^{n+1} - B_{yi+\frac{1}{2}j}^n \right) &= \frac{\tau}{h} (E_{zi+1j} - E_{zij}) + \\
 \nabla \cdot \mathbf{B}^{n+1} &= 0
 \end{aligned} \tag{10.25}$$

To impose the solenoidality constraint, two other ways can be followed: an advanced form of the Hodge projection [8] or the nonconservative approach of Powell [68]. The first approach will substantially increase the computational cost, because an additional Poisson equation has to be solved, while the second approach is reported to give unsatisfactory results for strong shocks [90].

Because the constrained transport method is so attractive this has led to the development of algorithms that combine extensions of popular collocated schemes for the Euler equations as base schemes with a constrained transport method to update the staggered help variable \mathbf{b} , using the discrete Stokes theorem [4, 18]. To compute the fluxes for the base scheme the help variable \mathbf{b} is interpolated to the cell centers. In the review paper [90], a variation to this approach is described that circumvents the explicit use of the staggered help variable \mathbf{b} altogether.

The aim of these methods is clearly to mimic the advantageous behavior of staggered schemes, while using the proven technology of standard characteristic based collocated schemes. This is based on the general (mis)conception that staggered schemes are inherently less accurate and robust for fully compressible flow than collocated schemes and that staggered discretisation in general coordinates is inaccurate. However, in [7, 105, 106, 107] a staggered scheme for the Euler and Navier-Stokes equations is presented that is accurate

on nonsmooth nonorthogonal grids.

10.6 Conclusions

Staggered schemes are highly suitable for the computation of magnetohydrodynamic flow, because of their ability to retain solenoidality of the discrete magnetic field and their straightforward flux function. Moreover, we believe the Mach-uniform formulation of staggered schemes can be useful for efficient and accurate computing of weakly compressible magnetohydrodynamic flow, commonly encountered in astrophysical applications.



Chapter 11

A Mach-uniform scheme for ideal magnetohydrodynamics.

11.1 Introduction

Our starting point will be the method of Wesseling [109]. As opposed to the method presented in [7], a pressure based formulation of the energy equation is used. For two reasons, this method is preferred over the method in [7]. First of all, the formulation of the Mach-uniform method is simpler and more elegant than the formulation of [7]. Furthermore, the solenoidality constraint follows from the energy equation instead of the mass conservation equation, in accordance with the small Mach number asymptotic expansion of the equations, see e.g. [48]. However, both methods lack conservation. It will turn out in Section 11.5 that a direct extension of the method produces inaccurate numerical approximations of weak solutions. The deviations are small for the Euler equations but become unacceptable for the strong shocks encountered for the equations of ideal magnetohydrodynamics. The fact that these discrepancies are masked by numerical viscosity and only manifest themselves on a sufficiently fine mesh has left the consequences of this lack of conservativity unnoticed in earlier publications. In Chapter 12 we will present a conservative Mach-uniform pressure based formulation.

11.2 A staggered scheme

The equations of ideal MHD in conservative variables are:

$$\frac{\partial \rho}{\partial t} + \frac{\partial}{\partial x} (m_x) = 0, \quad (11.1)$$

$$\frac{\partial m_x}{\partial t} + \frac{\partial}{\partial x} \left(\frac{m_x^2}{\rho} + P \right) = 0, \quad (11.2)$$

$$\frac{\partial m_y}{\partial t} + \frac{\partial}{\partial x} \left(\frac{m_x m_y}{\rho} + \Lambda_y \right) = 0, \quad (11.3)$$

$$\frac{\partial m_z}{\partial t} + \frac{\partial}{\partial x} \left(\frac{m_x m_z}{\rho} + \Lambda_z \right) = 0, \quad (11.4)$$

$$\frac{\partial \rho E}{\partial t} + \frac{\partial}{\partial x} (u_x \rho E + u_x P + u_y \Lambda_y + u_z \Lambda_z) = 0, \quad (11.5)$$

$$\frac{\partial B_x}{\partial t} = 0, \quad (11.6)$$

$$\frac{\partial B_y}{\partial t} + \frac{\partial}{\partial x} (u_x B_y - u_y B_x) = 0, \quad (11.7)$$

$$\frac{\partial B_z}{\partial t} + \frac{\partial}{\partial x} (u_x B_z - u_z B_x) = 0, \quad (11.8)$$

where

$$E = e + \frac{1}{2} (u_x^2 + u_y^2 + u_z^2) + \frac{1}{8\pi\rho} (B_x^2 + B_y^2 + B_z^2), \quad (11.9)$$

$$P = p + \frac{1}{8\pi} (B_y^2 + B_z^2 - B_x^2), \quad (11.10)$$

$$\Lambda_y = -\frac{1}{4\pi} B_x B_y, \quad \Lambda_z = -\frac{1}{4\pi} B_x B_z. \quad (11.11)$$

Here E is the total energy of the fluid and \mathbf{B} is the magnetic flux vector. We have used the fact that $\nabla \cdot \mathbf{B} = 0$.

We use a staggered placement of the unknowns: ρ , p , m_y , m_z , B_y , B_z are placed at point j , whereas m_x , B_x are placed at point $j + \frac{1}{2}$, cf. Fig. 11.1. Straightforward discretization of (11.1- 11.8) on the staggered mesh using an upwind scheme for the inertial terms and central discretisation for all nonconvective terms gives a scheme that we will refer to as the *fully conservative scheme*. The discretisation corresponds to:

$$\rho_j^{n+1} - \rho_j^n + \lambda \left(u_{k+\frac{1}{2}} \rho_k \right) \Big|_{k=j-1}^{k=j}, \quad (11.12)$$

$$m_x^{n+1} \Big|_{j+\frac{1}{2}} - m_x^n \Big|_{j+\frac{1}{2}} + \lambda (u_x m_x) \Big|_{j-\frac{1}{2}}^{j+\frac{1}{2}} = -\lambda P \Big|_j^{j+1}, \quad (11.13)$$

$$m_y^{n+1} - m_y^n + \lambda \left(u_x \left. m_y \right|_{k=j-1}^{k=j} \right) = -\lambda \Lambda_y |j^{j+1}, \tag{11.14}$$

$$m_z^{n+1} - m_z^n + \lambda \left(u_x \left. m_z \right|_{k=j-1}^{k=j} \right) = -\lambda \Lambda_z |j^{j+1}, \tag{11.15}$$

$$B_y^{n+1} - B_y^n + \lambda \left(u_x \left. B_y \right|_{k=j-1}^{k=j} - u_y \left. B_x \right|_{k=j-1}^{k=j} \right) = 0, \tag{11.16}$$

$$B_z^{n+1} - B_z^n + \lambda \left(u_x \left. B_z \right|_{k=j-1}^{k=j} - u_z \left. B_x \right|_{k=j-1}^{k=j} \right) = 0, \tag{11.17}$$

$$\rho E_j^{n+1} - \rho E_j^n + \lambda \left(u_x \left. \rho E \right|_{k=j-1}^{k=j} + u_x \left. P \right|_{k=j-1}^{k=j} + u_y \left. \Lambda_y \right|_{k=j-1}^{k=j} + u_z \left. \Lambda_z \right|_{k=j-1}^{k=j} \right) = 0, \tag{11.18}$$

where $\lambda = \delta t / \delta x$, and

$$\Lambda_{y,z} |j^{j+1} = 1/2 (\Lambda_{y,z} |j+1 + \Lambda_{y,z} |j), \tag{11.19}$$

$$u_{y,z} |j^{j+1} = 1/2 (u_{y,z} |j+1 + u_{y,z} |j). \tag{11.20}$$

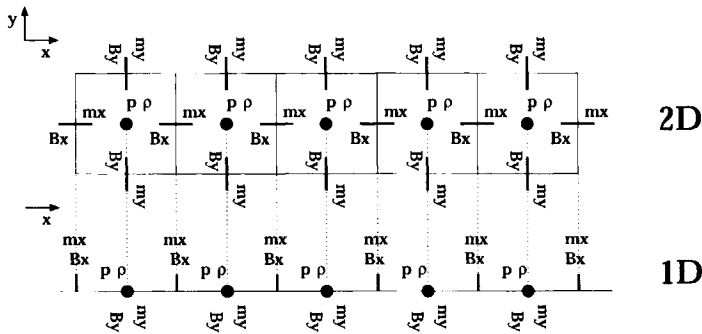


Figure 11.1: Staggered placement of the unknowns of the equations of ideal MHD (1D).

We use the following 4-stage fourth order explicit Runge-Kutta method [84] to advance in time:

$$\phi^* = \phi^n - 1/4\tau L_h \phi^n, \quad (11.21)$$

$$\phi^{**} = \phi^n - 1/3\tau L_h \phi^*, \quad (11.22)$$

$$\phi^{***} = \phi^n - 1/2\tau L_h \phi^{**}, \quad (11.23)$$

$$\phi^{n+1} = \phi^n - \tau L_h \phi^{***}, \quad (11.24)$$

$$(11.25)$$

This scheme will be used to compute reference solutions for validation of the Mach-uniform discretisation because, as opposed to the Euler equations, no analytical solution can be derived for the Riemann problem.

11.3 Pressure based formulation

To obtain a Mach-uniform pressure based formulation we start from the equations of ideal magnetohydrodynamics formulated in conservative variables (11.1, 11.2, 11.3, 11.4, 11.6, 11.7, 11.8). For brevity we discuss the case where the solution depends only on x and t . Formulating the equations in flux form gives:

$$\frac{\partial \mathbf{u}}{\partial t} + \frac{\partial \mathbf{f}(\mathbf{u})}{\partial x} = 0, \quad (11.26)$$

where

$$\mathbf{u} = [U_1 \quad U_2 \quad U_3 \quad U_4 \quad U_5 \quad U_6 \quad U_7 \quad U_8]^T = \quad (11.27)$$

$$[\rho \quad m_x \quad m_y \quad m_z \quad \rho E \quad B_x \quad B_y \quad B_z]^T,$$

$$\mathbf{f}(\mathbf{u}) = \quad (11.28)$$

$$\left[\begin{array}{c} m_x \\ \frac{m_x^2}{\rho} + (\gamma - 1) \rho e + \frac{1}{8\pi} (B_y^2 + B_z^2 - B_x^2) \\ \frac{m_x m_y}{\rho} - \frac{1}{4\pi} (B_x B_y) \\ \frac{m_x m_z}{\rho} - \frac{1}{4\pi} (B_x B_z) \\ \left(\frac{m_x}{\rho}\right) \rho E + \left(\frac{m_x}{\rho}\right) \left((\gamma - 1) \rho e + \frac{1}{8\pi} (B_y^2 + B_z^2 - B_x^2) \right) - \frac{m_y}{4\pi\rho} B_x B_y - \frac{m_z}{4\pi\rho} B_x B_z \\ 0 \\ \frac{m_x}{\rho} B_y - \frac{m_y}{\rho} B_x \\ \frac{m_x}{\rho} B_z - \frac{m_z}{\rho} B_x \end{array} \right],$$

where

$$\rho e = \left(\rho E - \frac{1}{2} \rho |\mathbf{v}|^2 - \frac{1}{8\pi} |\mathbf{B}|^2 \right) \quad (11.29)$$

Rewritten in the components of \mathbf{u} this gives:

$$\left[\begin{array}{c} U_2 \\ \frac{U_2^2}{U_1} + (\gamma - 1)q + \frac{1}{8\pi} (U_7^2 + U_8^2 - U_6^2) \\ \frac{U_2 U_3}{U_1} - \frac{1}{4\pi} U_6 U_7 \\ \frac{U_2 U_4}{U_1} - \frac{1}{4\pi} U_6 U_8 \\ \frac{U_2 U_5}{U_1} + \frac{U_2}{U_1} \left((\gamma - 1)q + \frac{1}{8\pi} (U_7^2 + U_8^2 - U_6^2) \right) - \frac{U_3 U_6 U_7}{4\pi U_1} - \frac{U_3 U_6 U_8}{4\pi U_1} \\ 0 \\ \frac{U_2 U_7}{U_1} - \frac{U_3 U_6}{U_1} \\ \frac{U_2 U_8}{U_1} - \frac{U_4 U_6}{U_1} \end{array} \right], \quad (11.30)$$

where

$$q = \left(U_5 - \frac{1}{2} \frac{U_2^2 + U_3^2 + U_4^2}{U_1} - \frac{1}{8\pi} (U_6^2 + U_7^2 + U_8^2) \right). \quad (11.31)$$

The Jacobian $\mathbf{f}(\mathbf{u})'$ is given by:

Row 1:

$$[0 \ 1 \ 0 \ 0 \ 0 \ 0 \ 0 \ 0], \quad (11.32)$$

Row 2:

$$\left[-\frac{U_2^2}{U_1^2} - \frac{(\gamma-1)(U_2^2+U_3^2+U_4^2)}{2U_1^2} \quad (3-\gamma)\frac{U_2}{U_1} \quad -(\gamma-1)\frac{U_3}{U_1} \right] \quad (11.33)$$

$$-(\gamma-1)\frac{U_4}{U_1} \quad (\gamma-1) \quad -\frac{\gamma}{4\pi}U_6 \quad -\frac{\gamma-2}{4\pi}U_7 \quad -\frac{\gamma-2}{4\pi}U_8], \quad (11.34)$$

Row 3:

$$\left[-\frac{U_2 U_3}{U_1^2} \quad \frac{U_3}{U_1} \quad \frac{U_2}{U_1} \quad 0 \quad 0 \quad -\frac{U_7}{4\pi} \quad -\frac{U_8}{4\pi} \quad 0 \right], \quad (11.35)$$

Row 4:

$$\left[-\frac{U_2 U_4}{U_1^2} \quad \frac{U_4}{U_1} \quad 0 \quad \frac{U_2}{U_1} \quad 0 \quad -\frac{U_8}{4\pi} \quad 0 \quad -\frac{U_6}{4\pi} \right], \quad (11.36)$$

Row 5:

$$\begin{aligned}
 & \left[-\frac{U_2 U_5}{U_1^2} - \frac{(\gamma-1)U_2 U_5}{U_1^2} + \frac{(\gamma-1)U_2(U_2^2 + U_3^2 + U_4^2)}{U_1^3} + \frac{(\gamma-1)U_2(U_6^2 + U_7^2 + U_8^2)}{8\pi U_1^2} \right. \\
 & \qquad \qquad \qquad - \frac{U_2(U_7^2 + U_8^2 - U_6^2)}{8\pi U_1^2} + \frac{U_3 U_6 U_7}{4\pi U_1^2} + \frac{U_4 U_6 U_8}{4\pi U_1^2} \\
 & \frac{\gamma U_5}{U_1} - \frac{(\gamma-1)(3U_2^2 + U_3^2 + U_4^2)}{2U_1^2} - \frac{(\gamma-1)(U_6^2 + U_7^2 + U_8^2)}{8\pi U_1} + \frac{U_7^2 + U_8^2 - U_6^2}{U_1^2} - \frac{(\gamma-1)U_2 U_3}{U_1} - \frac{U_6 U_7}{4\pi U_1} \\
 & \left. - \frac{(\gamma-1)U_2 U_4}{U_1} - \frac{U_6 U_8}{4\pi U_1} \quad (\gamma-1)\frac{U_2}{U_1} + \frac{U_2}{U_1} - \frac{(\gamma-1)U_6 U_2}{4\pi U_1} - \frac{U_6 U_2}{4\pi U_1} - \frac{U_3 U_7}{4\pi U_1} - \frac{U_4 U_8}{4\pi U_1} \right. \\
 & \left. - \frac{(\gamma-1)U_2 U_7}{4\pi U_1} + \frac{U_2 U_7}{4\pi U_1} - \frac{U_3 U_6}{4\pi U_1} - \frac{(\gamma-1)U_2 U_8}{4\pi U_1} + \frac{U_2 U_8}{4\pi U_1} - \frac{U_4 U_6}{4\pi U_1} \right], \tag{11.37}
 \end{aligned}$$

Row 6:

$$[0 \ 0 \ 0 \ 0 \ 0 \ 0 \ 0 \ 0 \ 0], \tag{11.38}$$

Row 7:

$$\left[-\frac{U_2 U_7 - U_3 U_6}{U_1^2} \quad \frac{U_7}{U_1} \quad -\frac{U_6}{U_1} \quad 0 \quad -\frac{U_3}{U_1} \quad \frac{U_2}{U_1} \quad 0 \right], \tag{11.39}$$

Row 8:

$$\left[-\frac{U_2 U_8 - U_4 U_6}{U_1^2} \quad \frac{U_8}{U_1} \quad 0 \quad -\frac{U_6}{U_1} \quad 0 \quad -\frac{U_4}{U_1} \quad 0 \quad \frac{U_2}{U_1} \right]. \tag{11.40}$$

In order to obtain a pressure based formulation, we transform from \mathbf{u} to \mathbf{W} , given by:

$$\mathbf{W} = \begin{bmatrix} W_1 \\ W_2 \\ W_3 \\ W_4 \\ W_5 \\ W_6 \\ W_7 \\ W_8 \end{bmatrix} = \begin{bmatrix} \rho \\ m_x \\ m_y \\ m_z \\ p \\ B_x \\ B_y \\ B_z \end{bmatrix} \tag{11.41}$$

We have $du = \frac{du}{d\mathbf{W}} d\mathbf{W}$, with the transformation matrix $\frac{du}{d\mathbf{W}}$ given by:

$$\begin{bmatrix} 1 & 0 & 0 & 0 & 0 & 0 & 0 & 0 \\ 0 & 1 & 0 & 0 & 0 & 0 & 0 & 0 \\ 0 & 0 & 1 & 0 & 0 & 0 & 0 & 0 \\ 0 & 0 & 0 & 1 & 0 & 0 & 0 & 0 \\ -\frac{w_2^2 + w_3^2 + w_4^2}{2w_1^2} & \frac{w_2}{w_1} & \frac{w_3}{w_1} & \frac{w_4}{w_1} & \frac{1}{\gamma-1} & \frac{w_6}{4\pi} & \frac{w_7}{4\pi} & \frac{w_8}{4\pi} \\ 0 & 0 & 0 & 0 & 0 & 1 & 0 & 0 \\ 0 & 0 & 0 & 0 & 0 & 0 & 1 & 0 \\ 0 & 0 & 0 & 0 & 0 & 0 & 0 & 1 \end{bmatrix} \quad (11.42)$$

The inverse $\frac{d\mathbf{W}}{du}$ is given by

$$\begin{bmatrix} 1 & 0 & 0 & 0 \\ 0 & 1 & 0 & 0 \\ 0 & 0 & 1 & 0 \\ 0 & 0 & 0 & 1 \\ (\gamma-1)\frac{w_2^2 + w_3^2 + w_4^2}{2w_1^2} & -(\gamma-1)\frac{w_2}{w_1} & -(\gamma-1)\frac{w_3}{w_1} & -(\gamma-1)\frac{w_4}{w_1} \\ 0 & 0 & 0 & 0 \\ 0 & 0 & 0 & 0 \\ 0 & 0 & 0 & 0 \\ 0 & 0 & 0 & 0 \\ (\gamma-1) & -\frac{(\gamma-1)w_6}{4\pi} & -\frac{(\gamma-1)w_7}{4\pi} & -\frac{(\gamma-1)w_8}{4\pi} \\ 0 & 1 & 0 & 0 \\ 0 & 0 & 1 & 0 \\ 0 & 0 & 0 & 1 \end{bmatrix} \quad (11.43)$$

With the primitive variables \mathbf{W} the system is given by:

$$\frac{\partial \mathbf{W}}{\partial t} + \tilde{\mathbf{f}}(\mathbf{u})' \frac{\partial \mathbf{W}}{\partial x} = 0, \quad (11.44)$$

where

$$\tilde{\mathbf{f}}(\mathbf{u})' = \frac{d\mathbf{W}}{du} \mathbf{f}(\mathbf{u})' \frac{du}{d\mathbf{W}} \quad (11.45)$$

We find

$$\tilde{\mathbf{f}}(\mathbf{u})' = \begin{pmatrix} 0 & 1 & 0 & 0 & 0 & 0 & 0 & 0 \\ -u^2 & 2u & 0 & 0 & 1 & -\frac{B_x}{4\pi} & \frac{B_y}{4\pi} & \frac{B_z}{4\pi} \\ -uv & v & u & 0 & 0 & -\frac{B_y}{4\pi} & -\frac{B_x}{4\pi} & 0 \\ -uw & w & 0 & u & 0 & -\frac{B_z}{4\pi} & 0 & -\frac{B_x}{4\pi} \\ (\gamma-1)\gamma u D & -(\gamma-1)\gamma D & 0 & 0 & u & (\gamma-1)\frac{uB_x+vB_y+wB_z}{4\pi} & 0 & 0 \\ 0 & 0 & 0 & 0 & 0 & 0 & 0 & 0 \\ \frac{-uB_y+vB_x}{\rho} & \frac{B_y}{\rho} & -\frac{B_x}{\rho} & 0 & 0 & -v & u & 0 \\ \frac{-uB_z+wB_x}{\rho} & \frac{B_z}{\rho} & 0 & -\frac{B_x}{\rho} & 0 & -w & 0 & u \end{pmatrix}, \quad (11.46)$$

where

$$D = \frac{-8\rho E\pi + 4\rho\pi(u^2 + v^2 + w^2) + B_x^2 + B_y^2 + B_z^2}{8\rho\pi} = \quad (11.47)$$

$$\frac{p}{\rho(\gamma-1)}. \quad (11.48)$$

With

$$\gamma \frac{p}{\rho} = c^2, \quad (11.49)$$

the Jacobian of the flux function $\tilde{\mathbf{f}}(\mathbf{u})'$ can be rewritten as follows:

$$\begin{pmatrix} 0 & 1 & 0 & 0 & 0 & 0 & 0 & 0 \\ -u^2 & 2u & 0 & 0 & 1 & -\frac{B_x}{4\pi} & \frac{B_y}{4\pi} & \frac{B_z}{4\pi} \\ -uv & v & u & 0 & 0 & -\frac{B_y}{4\pi} & -\frac{B_x}{4\pi} & 0 \\ -uw & w & 0 & u & 0 & -\frac{B_z}{4\pi} & 0 & -\frac{B_x}{4\pi} \\ -uc^2 & c^2 & 0 & 0 & u & (\gamma-1)\frac{uB_x+vB_y+wB_z}{4\pi} & 0 & 0 \\ 0 & 0 & 0 & 0 & 0 & 0 & 0 & 0 \\ \frac{-uB_y+vB_x}{\rho} & \frac{B_y}{\rho} & -\frac{B_x}{\rho} & 0 & 0 & -v & u & 0 \\ \frac{-uB_z+wB_x}{\rho} & \frac{B_z}{\rho} & 0 & -\frac{B_x}{\rho} & 0 & -w & 0 & u \end{pmatrix} \quad (11.50)$$

Using (11.50), we find that (11.44) can be written in the following form:

$$\frac{\partial \rho}{\partial t} + \frac{\partial m}{\partial x} = 0, \quad (11.51)$$

$$\frac{\partial m_x}{\partial t} + \frac{\partial}{\partial x} \left(\frac{m_x^2}{\rho} + P \right) = 0, \quad (11.52)$$

$$\frac{\partial m_y}{\partial t} + \frac{\partial}{\partial x} \left(\frac{m_x m_y}{\rho} + \Lambda_y \right) = 0, \quad (11.53)$$

$$\frac{\partial m_z}{\partial t} + \frac{\partial}{\partial x} \left(\frac{m_x m_z}{\rho} + \Lambda_z \right) = 0, \quad (11.54)$$

$$\frac{\partial p}{\partial t} + u \frac{\partial p}{\partial x} + \rho c^2 \frac{\partial u}{\partial x} + (\gamma - 1) \frac{u B_x + v B_y + w B_z}{\pi} \frac{\partial B_x}{\partial x} = 0, \quad (11.55)$$

$$\frac{\partial B_x}{\partial t} = 0, \quad (11.56)$$

$$\frac{\partial B_y}{\partial t} + \frac{\partial}{\partial x} (u B_y - v B_x) = 0, \quad (11.57)$$

$$\frac{\partial B_z}{\partial t} + \frac{\partial}{\partial x} (u B_z - w B_x) = 0. \quad (11.58)$$

Taking into account that:

$$\nabla \cdot \mathbf{B} = 0 \quad (11.59)$$

and

$$\rho c^2 = \gamma p \quad (11.60)$$

these equations can be rewritten as:

$$\frac{\partial \rho}{\partial t} + \frac{\partial m}{\partial x} = 0, \quad (11.61)$$

$$\frac{\partial m_x}{\partial t} + \frac{\partial}{\partial x} \left(\frac{m_x^2}{\rho} + P \right) = 0, \quad (11.62)$$

$$\frac{\partial m_y}{\partial t} + \frac{\partial}{\partial x} \left(\frac{m_x m_y}{\rho} + \Lambda_y \right) = 0, \quad (11.63)$$

$$\frac{\partial m_z}{\partial t} + \frac{\partial}{\partial x} \left(\frac{m_x m_z}{\rho} + \Lambda_z \right) = 0, \quad (11.64)$$

$$\frac{\partial p}{\partial t} + \frac{\partial}{\partial x}(up) + (\gamma - 1)p \frac{\partial u}{\partial x} = 0, \quad (11.65)$$

$$\frac{\partial B_x}{\partial t} = 0, \quad (11.66)$$

$$\frac{\partial B_y}{\partial t} + \frac{\partial}{\partial x}(uB_y - vB_x) = 0, \quad (11.67)$$

$$\frac{\partial B_z}{\partial t} + \frac{\partial}{\partial x}(uB_z - wB_x) = 0. \quad (11.68)$$

In this pressure based formulation the energy equation is identical to the energy equation for the Euler equations. This makes this approach very attractive for the extension of a Mach-uniform equation for the Euler equations. Note that also in the multidimensional case solenoidality of the discrete \mathbf{B} field in the pressure points is guaranteed due to the staggering of the components of \mathbf{B} , and therefore the accuracy of the scheme is not jeopardized by explicitly using (11.59) in the derivation.

11.4 Mach-uniform formulation

We apply the following Mach-uniform scaling to the equations:

$$\rho = \frac{\tilde{\rho}}{\tilde{\rho}_{\text{ref}}}, u = \frac{\tilde{u}}{\tilde{u}_{\text{ref}}}, x = \frac{\tilde{x}}{\tilde{x}_{\text{ref}}}, t = \frac{\tilde{t}}{\tilde{t}_{\text{ref}}}, p = \frac{\tilde{p} - \tilde{p}_{\text{ref}}}{\tilde{\rho}_{\text{ref}}\tilde{u}_{\text{ref}}}, B^2 = \frac{\tilde{B}^2}{\tilde{\rho}_{\text{ref}}\tilde{u}_{\text{ref}}^2}, \quad (11.69)$$

where the dimensional quantities are denoted by a tilde and the reference quantities are chosen in the following way:

$$\begin{aligned} \tilde{\rho}_{\text{ref}} &= \rho_{\text{inflow}} & \tilde{t}_{\text{ref}} &= \frac{\tilde{x}_{\text{ref}}}{\tilde{u}_{\text{ref}}} \\ \tilde{u}_{\text{ref}} &= u_{x,\text{inflow}} & \tilde{p}_{\text{ref}} &= p_{\text{out}} \\ \tilde{x}_{\text{ref}} &= L_{\text{max}} \end{aligned} \quad (11.70)$$

With this scaling the equations take the following form:

$$\frac{\partial \rho}{\partial t} + \frac{\partial m}{\partial x} = 0, \quad (11.71)$$

$$\frac{\partial m_x}{\partial t} + \frac{\partial}{\partial x} \left(\frac{m_x^2}{\rho} + P \right) = 0, \quad (11.72)$$

$$\frac{\partial m_y}{\partial t} + \frac{\partial}{\partial x} \left(\frac{m_x m_y}{\rho} + \Lambda_y \right) = 0, \quad (11.73)$$

$$\frac{\partial m_z}{\partial t} + \frac{\partial}{\partial x} \left(\frac{m_x m_z}{\rho} + \Lambda_z \right) = 0, \quad (11.74)$$

$$\frac{\partial B_x}{\partial t} = 0, \quad (11.75)$$

$$\frac{\partial B_y}{\partial t} + \frac{\partial}{\partial x} (u B_y - v B_x) = 0. \quad (11.76)$$

$$\frac{\partial B_z}{\partial t} + \frac{\partial}{\partial x} (u B_z - w B_x) = 0. \quad (11.77)$$

$$M_{\text{ref}}^2 \left(\frac{\partial p}{\partial t} + \frac{\partial}{\partial x} (u p) + (\gamma - 1) p \frac{\partial u}{\partial x} \right) + \frac{\partial u}{\partial x} = 0, \quad (11.78)$$

Eqs. (11.71)–(11.77) are discretized identically to (11.12)–(11.17). The pressure-correction equation (11.78) is discretised in the following way (assuming $u_{j+\frac{1}{2}} > 0$ for brevity):

$$\begin{aligned} & M_{\text{ref}}^2 \left(\delta p_j + \lambda \left(u_{j+\frac{1}{2}}^{n+1} p_j^n - u_{j-\frac{1}{2}}^{n+1} p_{j-1}^n \right) + \right. \\ & \left. \lambda (\gamma - 1) p_j^n \left(u_{j+\frac{1}{2}}^{n+1} - u_{j-\frac{1}{2}}^{n+1} \right) \right) + \lambda \left(u_{j+\frac{1}{2}}^{n+1} - u_{j-\frac{1}{2}}^{n+1} \right) = 0, \end{aligned} \quad (11.79)$$

which can be rewritten as

$$\begin{aligned} & M_{\text{ref}}^2 \delta p_j + \lambda \left([M_{\text{ref}}^2 (p_j^n + (\gamma - 1) p_j^n) + 1] u_{j+\frac{1}{2}}^{n+1} - \right. \\ & \left. [M_{\text{ref}}^2 (p_{j-1}^n + (\gamma - 1) p_j^n) + 1] u_{j-\frac{1}{2}}^{n+1} \right) = 0. \end{aligned} \quad (11.80)$$

Substitution of the pressure correction postulate:

$$u_{j+\frac{1}{2}}^{n+1} = \frac{1}{\rho_j^{n+1}} \left(m_{xj+\frac{1}{2}}^* - \lambda (\delta p_{j+1} - \delta p_j) \right), \quad (11.81)$$

gives:

$$M_{\text{ref}}^2 \delta p_j + \lambda \left([M_{\text{ref}}^2 (p_j^n + (\gamma - 1)p_j^n) + 1] \frac{1}{\rho_j^{n+1}} (m_{x_{j+\frac{1}{2}}}^* - \lambda (\delta p_{j+1} - \delta p_j)) - \right. \quad (11.82)$$

$$\left. [M_{\text{ref}}^2 (p_{j-1}^n + (\gamma - 1)p_j^n) + 1] \frac{1}{\rho_{j-1}^{n+1}} (m_{x_{j-\frac{1}{2}}}^* - \lambda (\delta p_j - \delta p_{j-1})) \right) = 0,$$

or rearranged:

$$\left[M_{\text{ref}}^2 \left(1 + \frac{\lambda^2}{\rho_{j-1}^{n+1} \rho_j^{n+1}} ((\rho_{j-1}^{n+1} p_j^n + \rho_j^{n+1} p_{j-1}^n) + (\rho_{j-1}^{n+1} + \rho_j^{n+1}) (\gamma - 1) p_j^n) \right) + \right. \quad (11.83)$$

$$\left. \frac{\rho_{j-1}^{n+1} + \rho_j^{n+1}}{\rho_{j-1}^{n+1} \rho_j^{n+1}} \lambda^2 \right] \delta p_j +$$

$$\left[-\frac{\lambda^2}{\rho_j^{n+1}} (M_{\text{ref}}^2 (p_j^n + (\gamma - 1)p_j^n) + 1) \right] \delta p_{j+1} +$$

$$\left[-\frac{\lambda^2}{\rho_{j-1}^{n+1}} (M_{\text{ref}}^2 (p_{j-1}^n + (\gamma - 1)p_j^n) + 1) \right] \delta p_{j-1} =$$

$$- \left[\frac{\lambda}{\rho_j^{n+1}} (M_{\text{ref}}^2 (p_j^n + (\gamma - 1)p_j^n) + 1) \right] u_{j+\frac{1}{2}}^* + \left[\frac{\lambda}{\rho_{j-1}^{n+1}} (M_{\text{ref}}^2 (p_{j-1}^n + (\gamma - 1)p_j^n) + 1) \right] u_{j-\frac{1}{2}}^*.$$

The solution procedure consists of the following steps:

- Advance Eqs. (11.71)–(11.77) with the Runge-Kutta method (11.21–11.24).
- Solve the pressure correction equation (11.83).
- Update momentum and pressure.

Note that because no special measures are taken for the contribution of the magnetic field, this formulation can only be expected to have Mach-uniform behavior for the case $\beta \gg 1$, as discussed in Sect. 10.4.

11.5 Validation

To validate the scheme we consider two classic Riemann problems for the equations of ideal MHD: The Riemann problem of Brio & Wu [10] and the one of Dai & Woodward [17]. Figs. 11.2 and 11.3 show results for the Brio & Wu testcase on a grid with 200 cells on the unit interval, obtained with the conservative staggered scheme (Sect. 11.2) and the Mach-uniform staggered scheme respectively. The full line is not the exact solution, but a high-resolution reference solution obtained with the conservative scheme. The results

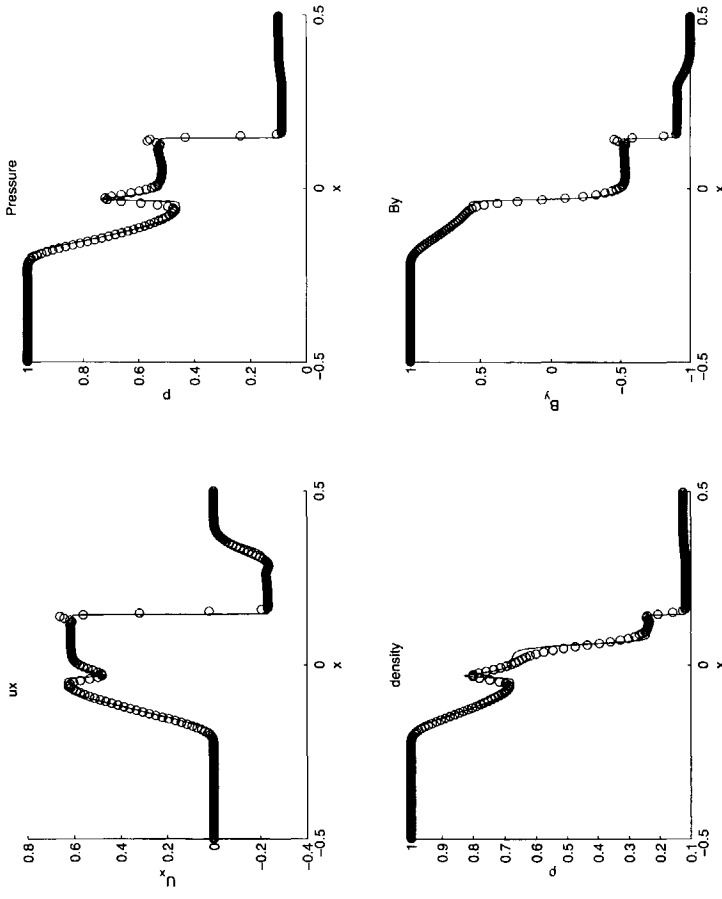


Figure 11.2: The Riemann problem of Brio and Wu, staggered scheme, 200 cells, $\lambda = 0.05$, $t_{end} = 0.14$.

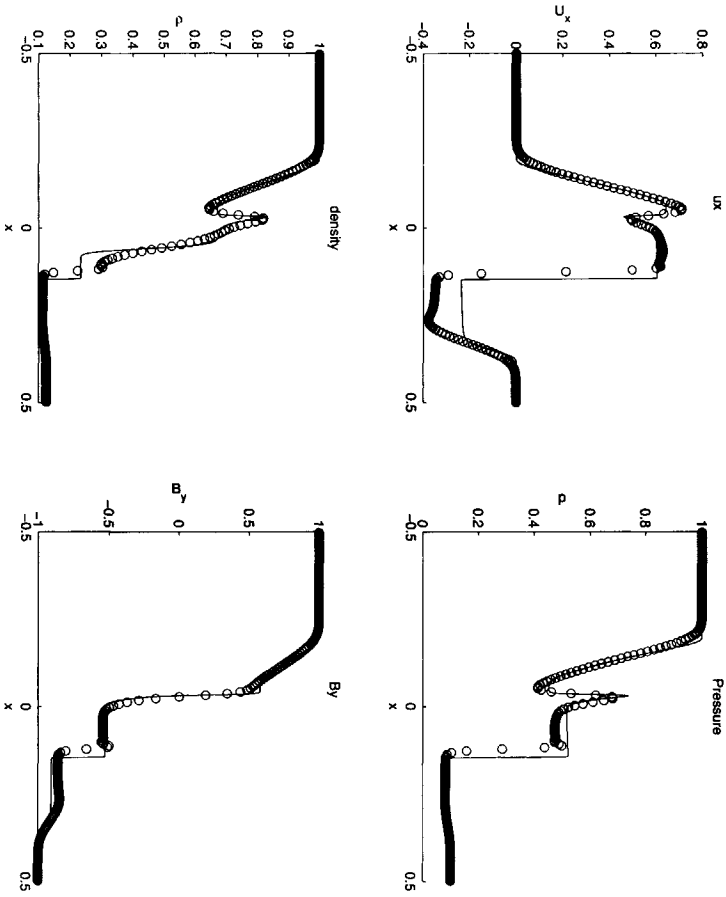


Figure 11.3: The Riemann problem of Brio and Wu, Mach-uniform scheme, 200 cells, $\lambda = 0.05$, $t_{\text{end}} = 0.14$.

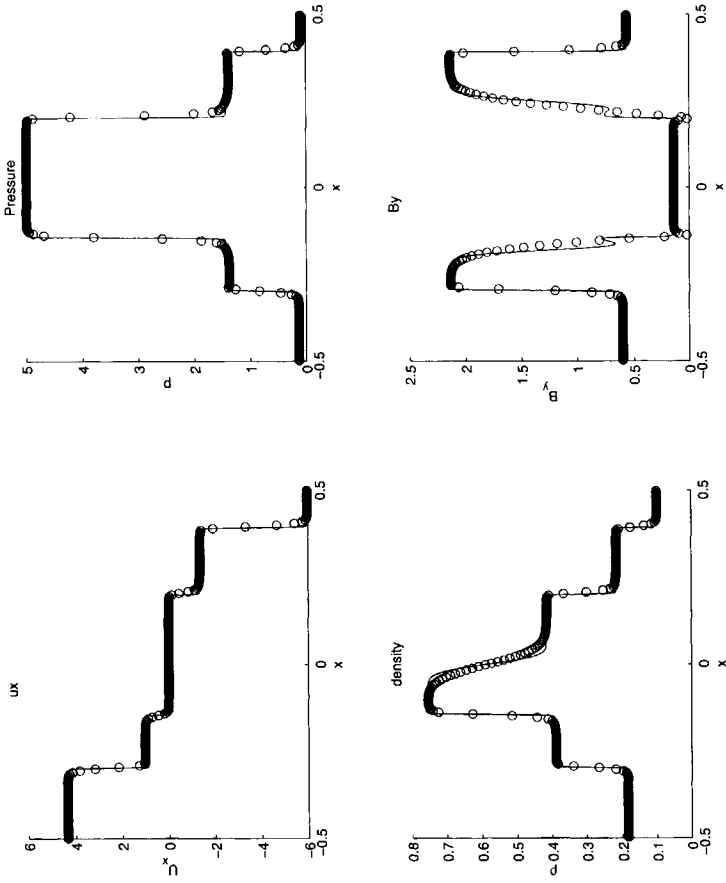


Figure 11.4: The Riemann problem of Dai and Woodward, staggered scheme, 200 cells, $\lambda = 0.05$, $t_{\text{end}} = 0.1$.

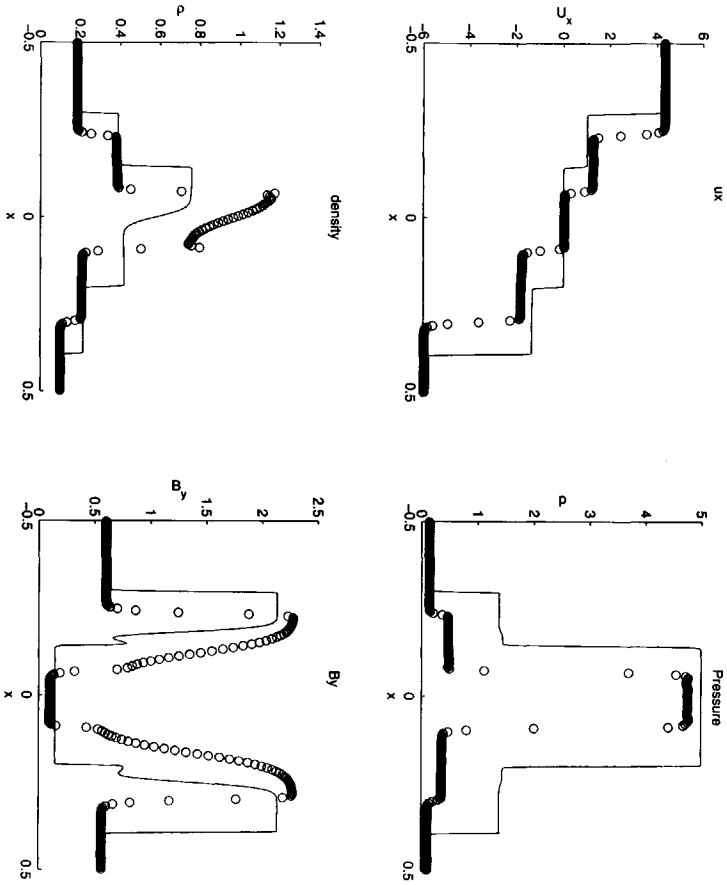


Figure 11.5: The Riemann problem of Dai and Woodward, Mach-uniform scheme, 200 cells, $\lambda = 0.05$, $t_{end} = 0.1$.

obtained with the Mach-uniform method show a small deviation of the shockspeed and hence an incorrect jump at the discontinuity.

Figs. 11.4 and 11.5 show results for the Dai & Woodward testcase on a grid with 200 cells on the unit interval, obtained with a staggered scheme and the Mach-uniform staggered scheme respectively. In both cases an artificial viscosity was added to stabilize the solution in the region where $u_x \approx 0$. A future improvement will be to utilize a RK-method that more effectively dampens the high frequency modes, e.g. one used in dual time-stepping methods. In this case the nonconservative Mach-uniform method produces completely erroneous results.

Because the nonconservative energy equation is identical to the energy equation for the Euler equations, we made a close inspection of results for various Riemann problems for the latter equations. It was found that the methods of [7] and [109] produce inaccurate results for strong discontinuities for the Euler equations as well. These discrepancies had been earlier wrongly identified as the result of numerical diffusion.

These results show, that to guarantee that numerical solutions converge to the correct weak solution, strict conservation has to be maintained in accordance with the Lax-theorem. However, the simplicity of this pressure based formulation makes it very attractive for the computation of smooth MHD flow.

In the next chapter we present a conservative pressure-correction scheme for the Euler equations. In Chapter 13 we present the extension of that method to MHD.

11.6 Conclusions

We have presented a Mach-uniform pressure based formulation of the equations of ideal MHD. However, due to lack of conservation the scheme produces inaccurate approximations to weak solutions. Close inspection of earlier results obtained with the Mach-uniform method for the Euler equations that forms the basis of the method discussed revealed that that method suffers from the same deficiency.



Chapter 12

A conservative pressure correction scheme for the Euler equations

12.1 Introduction

We discuss extension and improvement of the schemes proposed in [7, 108] for computing flows at all Mach number, with accuracy and efficiency uniform in the Mach number. These methods use a staggered scheme and a pressure correction solution procedure, similar to the classic ICE method [33]. To facilitate application of the pressure correction method, use is made of a nonconservative discretisation of the energy equation. Extending the method of [7, 108] to ideal magnetohydrodynamics we found that the nonconservative discretisation of the energy equation leads to a discrepancy in the shock speed. This effect is more pronounced in ideal magnetohydrodynamics than in gasdynamics, because the shocks encountered are much stronger. Furthermore, both methods proposed in [7, 108] suffer from small wiggles in the presence of a moving contact discontinuity. We believe these are also caused by a lack of conservation. Here we discuss a Mach-uniform scheme, that incorporates two improvements with respect to the methods of [7, 108]:

1. The method is derived from the Euler equations in conservation form. Numerical experiments show that solutions converge to genuine weak solutions.
2. The method gives monotone solutions for moving contact discontinuities.

The outline of the paper is as follows. In Section 12.2 the need for conservative Mach-uniform discretisations is briefly discussed. In Section 12.3 the requirements we impose on a Mach-uniform method are presented. A dimensionless pressure-based formulation is discussed, that forms the basis of the conservative Mach-uniform pressure correction scheme presented in Section 12.4. In Section 12.5 we show by numerical experiments, that solutions to a number of Riemann problems obtained with the present method converge to genuine weak solutions for the Euler equations. In Section 12.6 we consider two-dimensional test cases, to demonstrate the Mach-uniform behaviour of the present method.

12.2 Mach-uniform accuracy and efficiency

Mach-uniform methods are required when in one flow domain weakly compressible and compressible regions occur simultaneously, as for instance in flow inside internal combustion engines and in the flow around aircraft in take-off or landing conditions. Computation of weakly compressible flow in a standard density-based compressible formulation gives rise to loss of accuracy due to weak coupling between pressure and density and loss of efficiency due to the stiffness of the system of equations, when the Mach number is below 0.3. Furthermore, in the incompressible limit $M \downarrow 0$ the coupling between density and pressure vanishes, and leaves the pressure undetermined. Although both effects can be neutralised to some degree by time-derivative preconditioning/pseudo-compressibility techniques, this gives a significant increase in computing time, and choosing an effective preconditioner remains something of an art and has to be reconsidered for each new physical situation (e.g. different geometry, nonconvex equation of state, magnetohydrodynamics). For a survey of the state-of-the-art, see Chap. 14 of [105].

On the other hand, incompressible methods can be extended to incorporate compressibility following the approach of Harlow and Amsden [33]. Intended originally for the computation of weakly compressible flow, these methods show remarkable capability for efficient computation of compressible flow as well. However, to correctly compute shocks the discretisation has to be conservative [56].

Although a Mach-uniform conservative formulation can be easily obtained for an iterative method, e.g. SIMPLE [67], or a semi-iterative method e.g. PISO [39, 40], this is not trivially achieved for an efficient time-accurate single step sequential solution procedure. Either a nonconservative formulation is adopted [7, 108], or the special case of isothermal flow is assumed [33] in the formulation of the pressure correction equation.

12.3 Mach-uniform methods

In formulating the requirements for a Mach-uniform method we distinguish between three flow regimes:

1. $M = 0$: incompressible flow, but with variable density.
2. $0 < M \leq 0.3$: weakly compressible flow.
3. $0.3 < M$: fully compressible flow.

$M = 0.3$ is generally accepted as a threshold, below which the flow can be regarded as incompressible, because the density variations are less than 5% of the freestream value [44]. We will now formulate requirements for a Mach-uniform method for each regime.

12.3.1 Incompressible flow

For incompressible flow we require that the discretisation reduces to the well-known MAC-scheme of Harlow and Welch [35]. Therefore, a pressure-based formulation and a staggered

scheme are required. The MAC-scheme is accurate and efficient for incompressible nonstationary flows. The staggered scheme is the natural discretisation for incompressible flow, in the sense that it does not require regularization to prevent odd-even decoupling.

12.3.2 Weakly compressible flow: $0 < M \leq 0.3$

To make the Euler equations dimensionless we choose units u_{ref} , L_{ref} , ρ_{ref} and T_{ref} for velocity, length, density and temperature, respectively. If we take p_{ref} from the equation of state of a perfect gas:

$$p_{\text{ref}} = \rho_{\text{ref}} R T_{\text{ref}}, \quad (12.1)$$

and choose the unit of time as $t_{\text{ref}} = L_{\text{ref}}/u_{\text{ref}}$, then the dimensionless momentum equation is found to be, in Cartesian tensor notation,

$$\frac{\partial(\rho u_\alpha)}{\partial t} + (\rho u_\alpha u_\beta)_{,\beta} = -\frac{1}{\gamma M_{\text{ref}}^2} p_{,\alpha}, \quad M_{\text{ref}} = \frac{u_{\text{ref}}}{\sqrt{\gamma R T_{\text{ref}}}}, \quad (12.2)$$

where $\gamma = c_p/c_v$ is the ratio of specific heats. Of course, the reference quantities are chosen equal to values representative of the flow under consideration, for example equal to conditions at infinity, so that $M_{\text{ref}} \downarrow 0$ for weakly compressible flow. For a Mach-uniform method this limit must be regular, so that a different nondimensionalisation is required. If acoustic effects are not present, the asymptotic behaviour of p^* (dimensional nonreference quantities are denoted by an asterisk) is given by:

$$p^*(t^*, \mathbf{x}) = p_0^*(t^*) + \epsilon p_1^*(t^*, \mathbf{x}) + \mathcal{O}(\epsilon^2), \quad \epsilon = \gamma M_{\text{ref}}^2, \quad (12.3)$$

cf. Sect. 14.4 of [105] and [48]. If there is no global compression or expansion, as for the flow around a body, $p_0^*(t^*) = \text{constant} = p_{\text{ref}}$, which is assumed here. By postulating a similar asymptotic expansion for ρ^* and u_α^* it is easily seen that p_1^* is of the same order as $\rho_0^* \mathbf{u}_0 \cdot \mathbf{u}_0$. We therefore define a dimensionless pressure variable as follows:

$$p = \frac{p^* - p_{\text{ref}}}{\rho_{\text{ref}} u_{\text{ref}}^2}. \quad (12.4)$$

This makes the singular factor $1/\gamma M_{\text{ref}}^2$ disappear from the dimensionless momentum equation. Noting that for a perfect gas we have for the internal energy $\rho^* e^* = p^*/(\gamma - 1)$, we find that the dimensionless conservative pressure-based form of the Euler equations is given by:

$$\frac{\partial \rho}{\partial t} + (\rho u_\alpha)_{,\alpha} = 0, \quad (12.5)$$

$$\frac{\partial \rho u_\alpha}{\partial t} + (\rho u_\alpha u_\beta)_{,\beta} = -p_{,\alpha}, \quad (12.6)$$

$$M_{\text{ref}}^2 \left(\frac{\partial}{\partial t} \left(p + \frac{1}{2} \rho |\mathbf{u}|^2 \right) + \left(\gamma p u_\alpha + \frac{\gamma - 1}{2} \rho |\mathbf{u}|^2 u_\alpha \right)_{,\alpha} \right) + u_{\alpha,\alpha} = 0. \quad (12.7)$$

Note that as $M_{\text{ref}} \downarrow 0$ the solenoidality condition on the velocity field for incompressible flow follows from the energy equation. The dimensionless equation of state for a perfect gas can be written as

$$\rho(p, T) = \gamma M_{\text{ref}}^2 \frac{p}{T} + \frac{1}{T}. \quad (12.8)$$

We see that density becomes independent of pressure in the limit $M_{\text{ref}} \downarrow 0$, as expected for incompressible flow without acoustics.

12.3.3 Compressible flow: $0.3 < M$

For compressible flow we require that the scheme is conservative. This ensures that if the discrete solutions converge, they converge to a genuine weak solution that satisfies the jump condition, according to the well known Lax-Wendroff theorem [56]. The Mach-uniform methods of [7] and [108] are not in conservation form. This lack of conservation is found to only manifest itself when shocks are sufficiently strong and the mesh sufficiently fine, otherwise numerical diffusion will mask the small discrepancy between exact and computed shock speed (Section 12.5).

12.4 Discretisation and pressure correction method

For brevity and clarity we will discuss the solution procedure for a discretisation in Cartesian coordinates. Appendix C lists the equations discretised in general coordinates, used for the two-dimensional test cases in Section 12.6. Equations (12.5–12.7) are discretised on the staggered grid shown in Fig. 12.1. Convective terms are discretised with a first order upwind scheme, whereas the pressure gradient is discretised with a central scheme. Higher order upwind discretisation of the convective terms can be obtained with the MUSCL strategy [95, 96], using deferred correction in a straightforward way. The time-stepping method takes the following form: First the mass conservation equation is solved:

$$\frac{\rho^{n+1} - \rho^n}{\delta t} + (\rho^{n+1} u_\alpha^n)_{,\alpha} = 0. \quad (12.9)$$

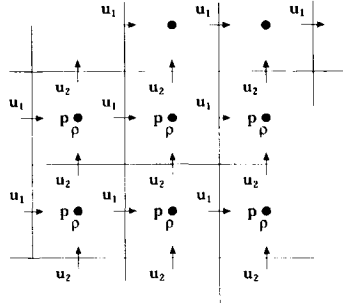


Figure 12.1: Staggered placement of unknowns.

Next, a prediction of the momentum field $m_\alpha^* = \rho^{n+1} u_\alpha^*$ is computed using the pressure at the previous time level:

$$\frac{m_\alpha^* - m_\alpha^n}{\delta t} + (m_\alpha^* u_\beta^n)_{,\beta} = -p_{,\alpha}^n. \tag{12.10}$$

The following pressure correction is postulated:

$$u_\alpha^{n+1} = u_\alpha^* - \frac{\delta t}{\rho^{n+1}} (p^{n+1} - p^n)_{,\alpha}. \tag{12.11}$$

The postulate is substituted in the energy equation:

$$M_{\text{ref}}^2 (\gamma - 1) \left\{ \frac{1}{\gamma - 1} \frac{\delta p}{\delta t} + \frac{\frac{1}{2} \rho^{n+1} |\mathbf{u}^* - \frac{\delta t}{\rho} \nabla \delta p|^2 - \frac{1}{2} \rho^n |\mathbf{u}^n|^2}{\delta t} + \right. \tag{12.12}$$

$$\left. \left[\left(\frac{\gamma}{\gamma - 1} (p^n + \delta p) + \frac{1}{2} \rho^{n+1} |\mathbf{u}^* - \frac{\delta t}{\rho} \nabla \delta p|^2 \right) \left(u_\alpha^* - \frac{\delta t}{\rho} \delta p_{,\alpha} \right) \right]_{,\alpha} \right\}$$

$$+ \left(u_\alpha^* - \frac{\delta t}{\rho} \delta p_{,\alpha} \right)_{,\alpha} = 0.$$

We use central interpolation of the velocity (12.11) at the cell faces to obtain the kinetic energy in the cell centers. Newton linearisation in δp leads to a linear equation for the pressure correction. However, the resulting stencil (Fig. 12.2 Version A) for the pressure equation is larger than the stencil for the classic MAC-scheme (Fig. 12.2 Version B), which is not efficient. It is clear that the $u_{\alpha,\alpha}$ term has to be discretised implicitly, to have the scheme reduce to the classic MAC-scheme. Close inspection of the scaled energy equation (12.7) shows that the $u_{\alpha,\alpha}$ term stems from the convection velocity of the pressure. We require that the unscaled and scaled equations give identical results for moderate Mach

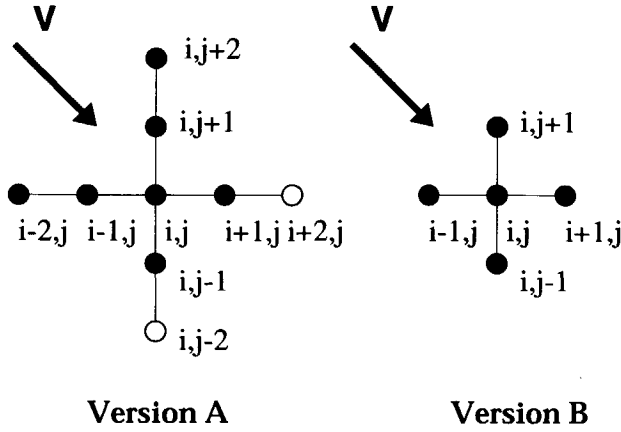


Figure 12.2: The stencil of the pressure correction equation.

number. This means that we have to discretise the convection velocity in the pressure equation at the new time level. If the kinetic energy is discretised at the predictor $*$ level, the resulting pressure correction equation has the standard 5-point stencil of the classic MAC-scheme in Cartesian coordinates (Fig. 12.2 Version B). Taking the kinetic energy at the $*$ level instead of the new time level will not affect the scheme in the limit $M_{\text{ref}} \downarrow 0$. Neither does it reduce the temporal order of accuracy. The pressure correction equation now takes the following form:

$$M_{\text{ref}}^2 \left\{ \frac{\delta p}{\delta t} + \frac{(\gamma - 1)\rho^{n+1}|\mathbf{u}^* - \frac{\delta t}{\rho}\delta\nabla p|^2 - \rho^n|\mathbf{u}^n|^2}{2\delta t} + \left[\left(\gamma(p^n + \delta p) + \frac{\gamma - 1}{2}\rho^{n+1}|\mathbf{u}^*|^2 \right) \left(u_{\alpha}^* - \frac{\delta t}{\rho}\delta p_{,\alpha} \right) \right]_{,\alpha} \right\} + \left(u_{\alpha}^* - \frac{\delta t}{\rho}\delta p_{,\alpha} \right)_{,\alpha} = 0. \quad (12.13)$$

The linearised pressure correction equation is solved by GMRES, preconditioned with ILU [99, 100]. Finally, pressure and momentum are updated:

$$p^{n+1} = p^n + \delta p, \quad (12.14)$$

$$m_{\alpha}^{n+1} = m_{\alpha}^* - \delta t \delta p_{,\alpha}. \quad (12.15)$$

12.5 Validation with Riemann problems

We will compare the conservative Mach-uniform method with the nonconservative method of [108] and with the classic Osher scheme [65] for a number of Riemann problems. The method of [7] shows behavior very similar to the method of [108]. To exhibit the difference between the various methods use is made of a relatively fine mesh of 400 cells on the unit interval. The following test cases are discussed:

1. The shock tube problem of Sod [83],
2. The shock tube problem of Lax [57],
3. Nonstationary contact discontinuity.

For both Sod's and Lax's Riemann problem the Mach-uniform method of [7] and [108] do not give exactly the correct shock speed. Differences between solutions of the conservative and nonconservative method manifest themselves most clearly for different quantities in the various shock tube problems.

The definition of the initial condition for a Riemann problem on the staggered grid is as follows: The discontinuity is defined on the common face of two adjacent control volumes for the pressure. Variables at the location of the discontinuity are defined as:

$$u_{\text{disc}} = u_{\text{left}}, \quad m_{\text{disc}} = \frac{1}{2} (m_{\text{left}} + m_{\text{right}}). \quad (12.16)$$

The convection velocity u_{center} takes the upwind value, whereas the momentum is centrally interpolated to the interface. This apparently arbitrary specification has been designed to propagate a contact discontinuity exactly with our first order upwind scheme during the first time step. We emphasise that our goal here is to show that the conservative Mach-uniform method converges to the genuine weak solution.

12.5.1 The shock tube problem of Sod

Figures 12.3, 12.4 and 12.5 show results obtained with the three methods for Sod's shock tube problem. The dimensionless time step in each case is chosen to ensure stability of the explicit Osher scheme, resulting in $\delta t/\delta x = 0.45$ (how to find stable values for $\delta t/\delta x$ is discussed in Sect. 10.6 of [105]). In Sod's shock tube problem the improvement with respect to the nonconservative method is most clear for the enthalpy. Although the staggered scheme shows more smearing at the discontinuities than the Osher scheme, this can be overcome in a straightforward manner by using a higher order interpolation for the fluxes (MUSCL), instead of the first order upwind scheme used in these experiments. The small overshoot in the entropy is associated with the staggering of the jump in velocity and the scalar quantities at the location of the shock.

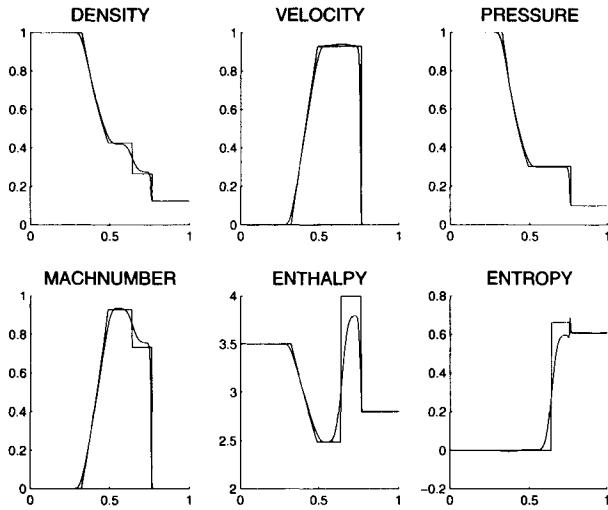


Figure 12.3: Sod's Riemann problem, nonconservative Mach-uniform discretisation.

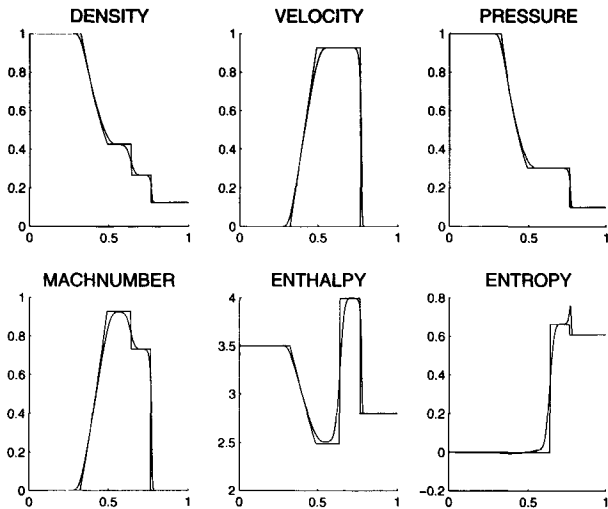


Figure 12.4: Sod's Riemann problem, conservative Mach-uniform discretisation.

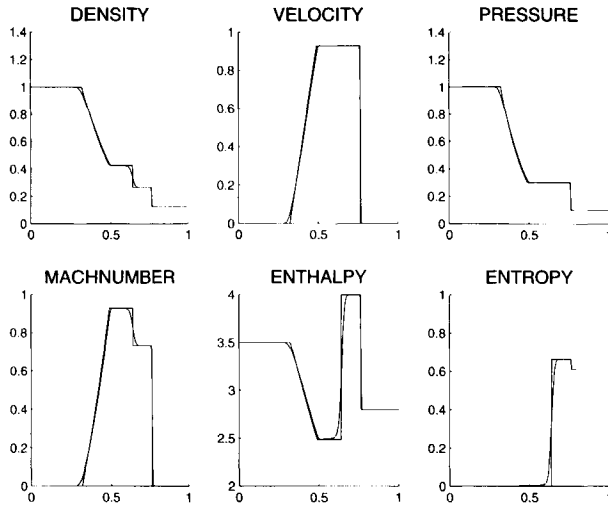


Figure 12.5: Sod's Riemann problem, Osher scheme.

12.5.2 The shock tube problem of Lax

Figures 12.6, 12.7 and 12.8 show results obtained with the three methods for Lax's shock tube problem. The dimensionless timestep in each case is chosen to ensure stability of the explicit Osher scheme, resulting in $\delta t/\delta x = 0.25$. In Lax's shock tube problem the improvement with respect to the nonconservative method is most clear for the density.

12.5.3 Nonstationary contact discontinuity

Figures 12.9, 12.10 and 12.11 show results obtained with the three methods for a nonstationary contact discontinuity. The dimensionless timestep in each case is chosen to ensure stability of the explicit Osher scheme, resulting in $\delta t/\delta x = 0.4$.

In [7] and [108] two different Mach-uniform discretisations were presented. With both schemes oscillations arose in pressure and velocity close to the contact discontinuity. Clearly, in the conservative method the wiggles have disappeared. The staggered scheme shows more smearing of the contact discontinuity than the Osher scheme, but requires considerably less computational cost.

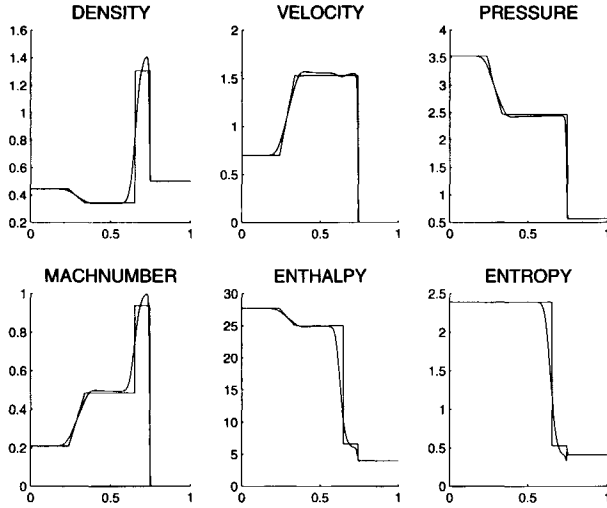


Figure 12.6: Lax's Riemann problem, nonconservative Mach-uniform discretisation.

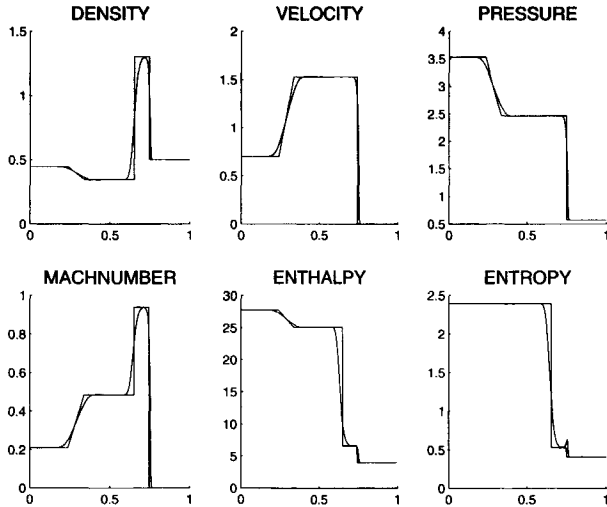


Figure 12.7: Lax's Riemann problem, conservative Mach-uniform discretisation.

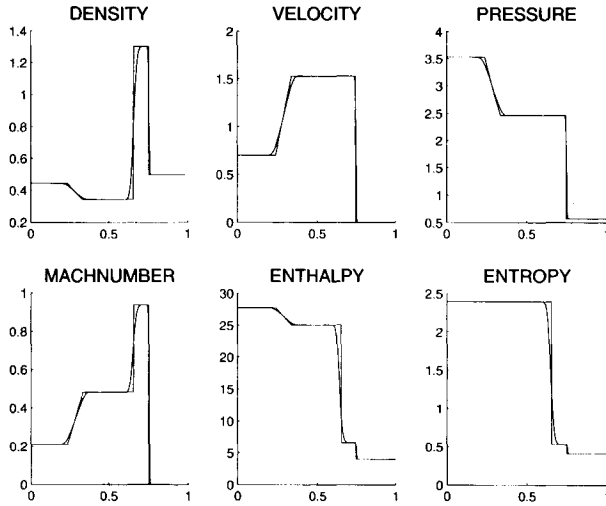


Figure 12.8: Lax's Riemann problem, Osher scheme.

12.6 Numerical results

We present two test cases to show the ability of the present method to compute flow at all speeds. The first is the standard test case of a two-dimensional channel with a bump, for a range of Mach numbers. This case is discussed in e.g. [7, 26, 41, 45, 49]. The second test case is the flow around a NACA0012 airfoil for a range of Mach numbers, from incompressible flow to transonic flow.

12.6.1 Channel with bump.

We look at a channel with a 10% circular bump for different inflow Mach numbers ranging from the incompressible to the supersonic case. The mesh with 90×25 cells is shown in Fig. 12.12. In the case of supersonic inflow it is necessary to apply a Dirichlet boundary condition for the pressure at the inflow boundary. For all Mach numbers the numerical scheme is identical. Table 12.1 lists the computing time on a 500 MHz, Pentium III processor to reach a steady state solution within 1% accuracy. The timestep in the subsonic test cases was chosen to achieve fast convergence to steady state. For the supersonic test case, the timestep was limited by the stability of the time-stepping method. It is clear that the computing cost is nearly independent of the Mach number, except for the supersonic test case, which is due to the decrease in timestep.

Because the density variations are of the order of the reference Mach number, the

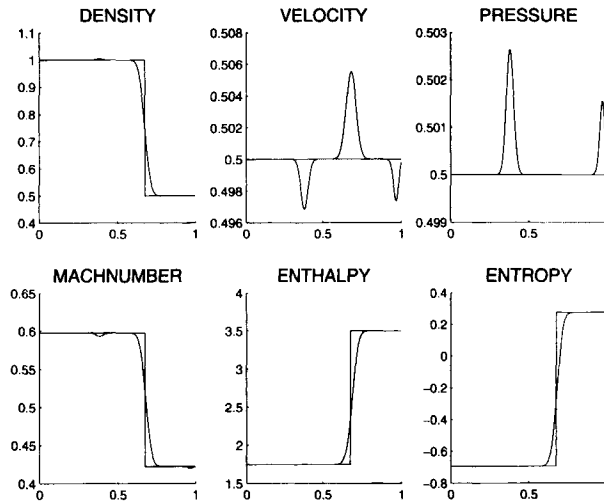


Figure 12.9: Nonstationary contact discontinuity, nonconservative Mach-uniform discretisation.

accuracy of the iterative linear solver has to be chosen much smaller than the reference Mach number to resolve the density distribution. In practice, this is not necessary, because the almost constant density will be satisfactorily obtained when the iterative solver is only partially converged. To show the capability of the method to accurately compute this low Mach number density field we have computed the cases listed in the table to convergence up to machine accuracy in the time-stepping algorithm. The resulting contour plots for the density are shown in Fig. 12.13. Note there is no visible difference between the density distributions at $M = 0.0001$ and $M = 0.01$, as it should be. We have compared our results for the case $M = 0.675$ with those presented in [22]. For this case [22] reports a maximum Mach number of 1.43, with the shock located at 75% of the length of the bump. Fig. 12.14 shows the Mach number distribution at the lower side of the channel computed with the present method and with the nonconservative method of [7] for a mesh with 270×75 cells. We find the shock to be positioned at 75% of the length of the bump and a maximum Mach number of 1.40, in good agreement with [22]. Note that the nonconservative method of [7] produces a small discrepancy in the position of the shock.

12.6.2 NACA0012 airfoil

The present method is used to compute the flow on a NACA 0012 airfoil under an angle of attack of 2° . The H-type grid with two blocks of 180×30 cells is shown in Fig. 12.15. The

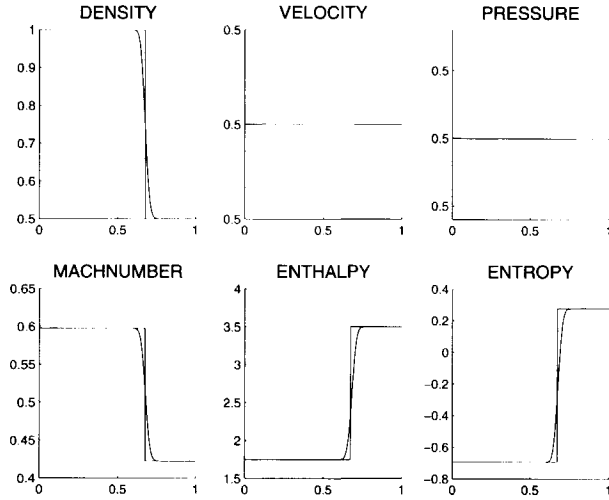


Figure 12.10: Nonstationary contact discontinuity, conservative Mach-uniform discretisation.

Mach	CPU-time s	number of time steps	timestep
0	17s	51	0.5
10^{-4}	17s	51	0.5
0.01	20s	62	0.5
0.5	18s	61	0.5
0.675	20s	73	0.5
1.65	36s	130	0.1

Table 12.1: CPU time for channel with bump for different Mach number.

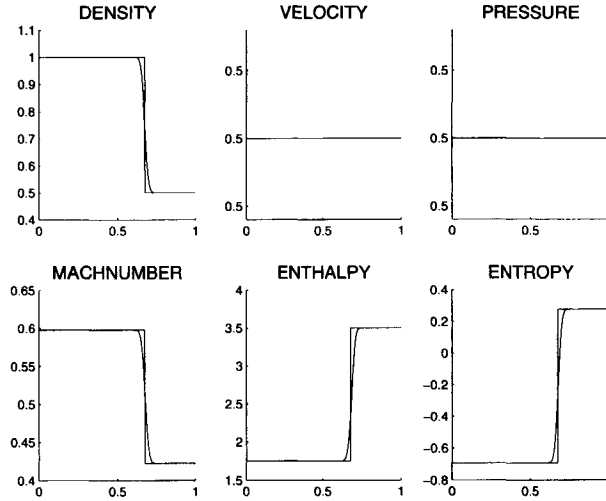


Figure 12.11: Nonstationary contact discontinuity, Osher scheme.

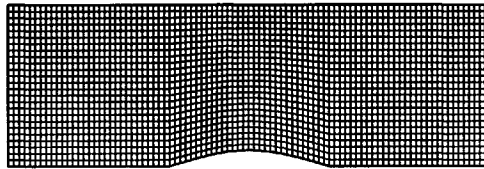
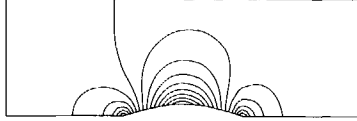


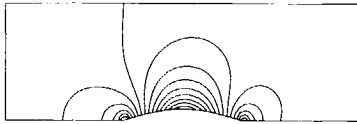
Figure 12.12: 90×25 mesh for channel with bump.

total number of cells on the section is 120. For this application use was made of the third order ISNAS-scheme [116], by means of a deferred correction strategy. Results are shown in Fig. 12.16. Computing work per timestep was found to depend only weakly on the Mach number. To confirm the conservativity of the method, we computed the flow around the NACA 0012 airfoil at zero angle of attack and for an inflow Mach number of 0.85. This is one of the testcases considered at a GAMM Workshop on the computation of inviscid transonic flow [73]. The dimensionless pressure distribution, computed on a mesh with 120 cells on the upper side of the airfoil, is shown in Fig. 12.17. We found the shock to be located at 73% of the chord length, in close resemblance with the average value reported in [73]. However, a value of 0.84 was found for $-C_{p_{\max}}$, which is smaller than the average value of 0.90 reported in [73]. We believe that this pressure loss is a result of the meagre quality of the H-type grid in the vicinity of the leading edge of the airfoil.

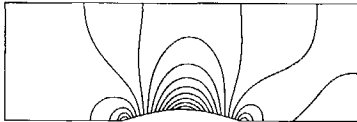
Mach=0.0001



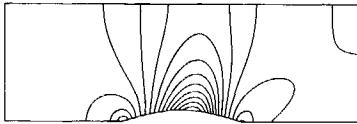
Mach=0.01



Mach=0.5



Mach=0.675



Mach=1.65

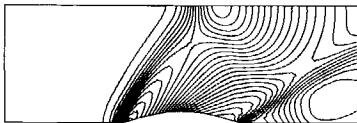


Figure 12.13: Iso-lines of density for channel with bump for different Mach numbers.

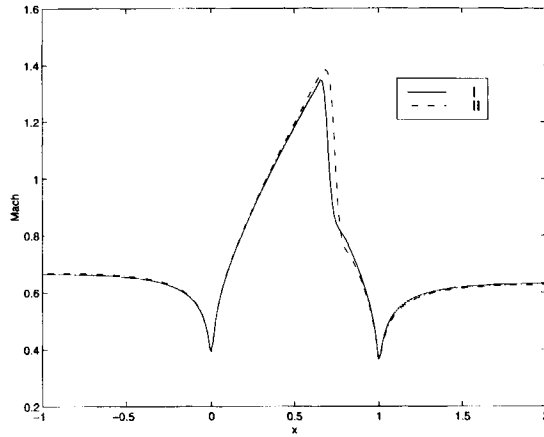


Figure 12.14: Mach number distribution on bottom of channel, for the method of [7] (I) and the present method (II).

12.7 Conclusions

With a Mach-uniform method one is able to compute flow with a Mach number ranging from the incompressible flow to the supersonic regime with nearly uniform accuracy and efficiency. To correctly compute weak solutions to the Euler equations, the scheme has to be in conservation form, in accordance with the theorem of Lax and Wendroff [56].

We have presented a conservative staggered pressure correction scheme, that has Mach-uniform properties similar to earlier nonconservative methods. Furthermore, weak solutions computed with the present method are found to converge to the correct weak solutions for a number of Riemann problems. Two-dimensional applications show that the computing work is nearly independent of the Mach number.

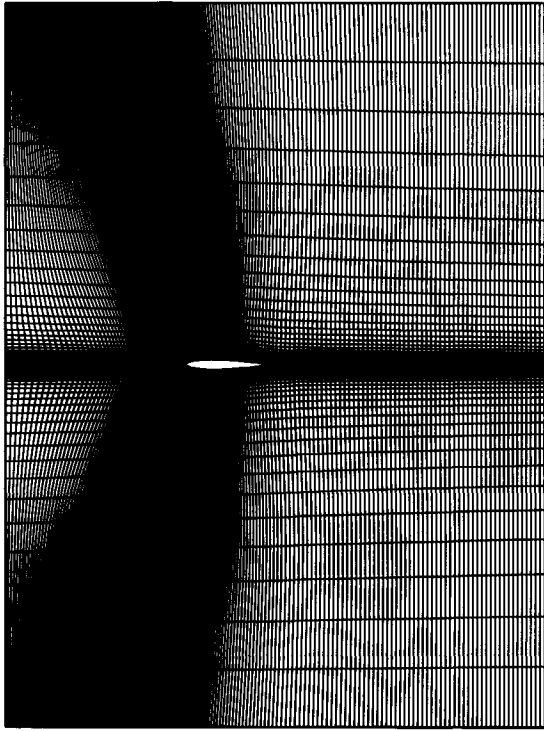
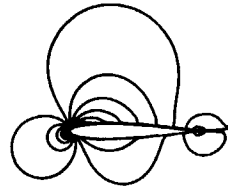
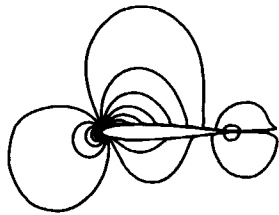


Figure 12.15: H-type grid with two blocks of 180×30 cells for NACA0012 airfoil.

Mach=0.0001

Mach=0.01



Mach=0.5

Mach=0.75

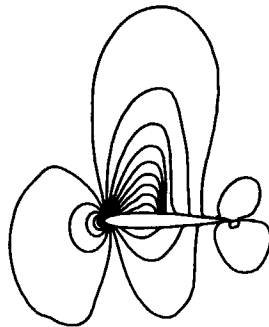
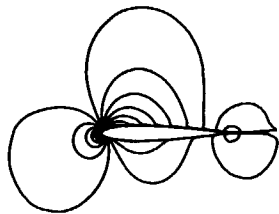


Figure 12.16: Density contours for NACA0012 airfoil for different Mach numbers.

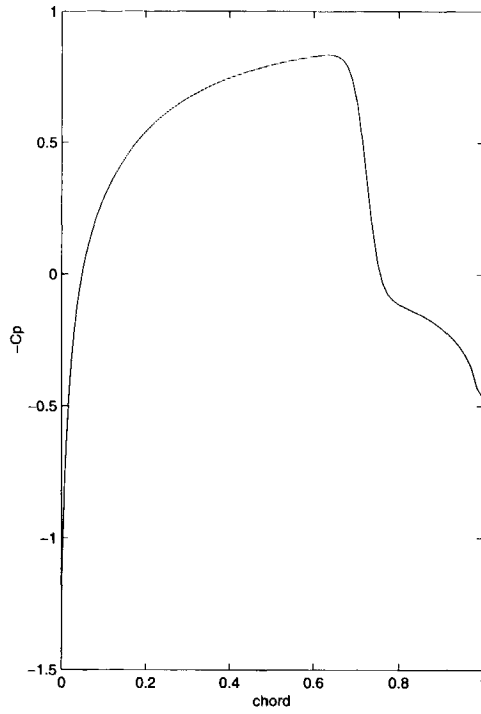


Figure 12.17: Dimensionless pressure distribution on NACA0012 airfoil, $M = 0.85$, $\alpha = 0^\circ$.



Chapter 13

A conservative Mach-uniform scheme for ideal magnetohydrodynamics

13.1 Introduction

Starting from the conservative pressure correction scheme for the Euler equations of Chapter 12 the extension to the equations of ideal magnetohydrodynamics is straightforward. We describe this extension and results for the Riemann testcases described in Chapter 11. Furthermore results are presented for two classic two-dimensional testcases: the *rotor problem* and the *Orzag-Tangh vortex* (see e.g. [90]).

13.2 A conservative pressure-correction method for MHD flows

The contributions of the magnetic energy and the work done by the magnetic pressure is included in the formulation of the pressure correction equation. Because the magnetic field is solved for in advance of the total energy, the former is available at the new time level. The pressure correction equation for magnetohydrodynamic flow reads:

$$M_{\text{ref}}^2 \left\{ \frac{\delta p}{\delta t} + \frac{(\gamma - 1) \left(\rho^{n+1} |\mathbf{u}^* - \frac{\delta t}{\rho} \nabla \delta p|^2 - \rho^n |\mathbf{u}^n|^2 + |\mathbf{B}^{n+1}|^2 - |\mathbf{B}^n|^2 \right)}{2\delta t} + \right. \quad (13.1)$$
$$\left. \left[\left(\gamma(p^n + \delta p) + \frac{\gamma - 1}{2} (\rho^{n+1} |\mathbf{u}^*|^2 + |\mathbf{B}^{n+1}|^2) \right) \left(u_{\alpha}^* - \frac{\delta t}{\rho} \delta p_{,\alpha} \right) + (\gamma - 1) (\Lambda_{\alpha\beta} u_{\beta}^n) \right]_{,\alpha} \right\}$$
$$+ \left(u_{\alpha}^* - \frac{\delta t}{\rho} \delta p_{,\alpha} \right)_{,\alpha} = 0,$$

where we used the same scaling as in (11.78) and

$$\Lambda_{\alpha\beta} = B_\alpha B_\beta \tag{13.2}$$

Pressure and momentum are updated in the same way as for(11.78):

$$p^{n+1} = p^n + \delta p, \tag{13.3}$$

$$m_\alpha^{n+1} = m_\alpha^* - \delta t \delta p_{,\alpha}. \tag{13.4}$$

13.3 Numerical results

As in the case of the Euler equations, the staggered scheme does not produce solutions to *standard* magnetohydrodynamic problems with accuracy and efficiency superior to collocated schemes. We intend to show that for standard testcases the staggered scheme has accuracy comparable to collocated schemes. Furthermore its Mach-uniform properties make it more versatile than collocated schemes.

Unfortunately there are no experimental results available to compare with. Standard testcases are of academic nature. This is because the conditions, in which the assumptions of MHD flow are valid, are very difficult to realize on a laboratory scale. In astrophysical flow the weakness of the magnetic field is compensated by the vastness of the length scale of the phenomena.

Riemann problems

In Figs. 13.1–13.2 we present results for both Riemann problems discussed in Sect. 11.5. It is clear that the conservative Mach uniform scheme converges to the correct weak solution.

The rotor problem

This test case is used to qualitatively judge the behavior of different schemes in [90], with emphasis on their ability to retain solenoidality of the discrete magnetic field. It consists of a dense rotating disk of fluid, surrounded by much less dense fluid at rest. The centripetal acceleration of the plasma in the spinning disk is altered by the magnetic forces. The initial condition is as follows: thermal pressure and magnetic field are uniform:

$$p = p_0, \quad B_x = B_{x0}, \quad B_y = 0, \tag{13.5}$$

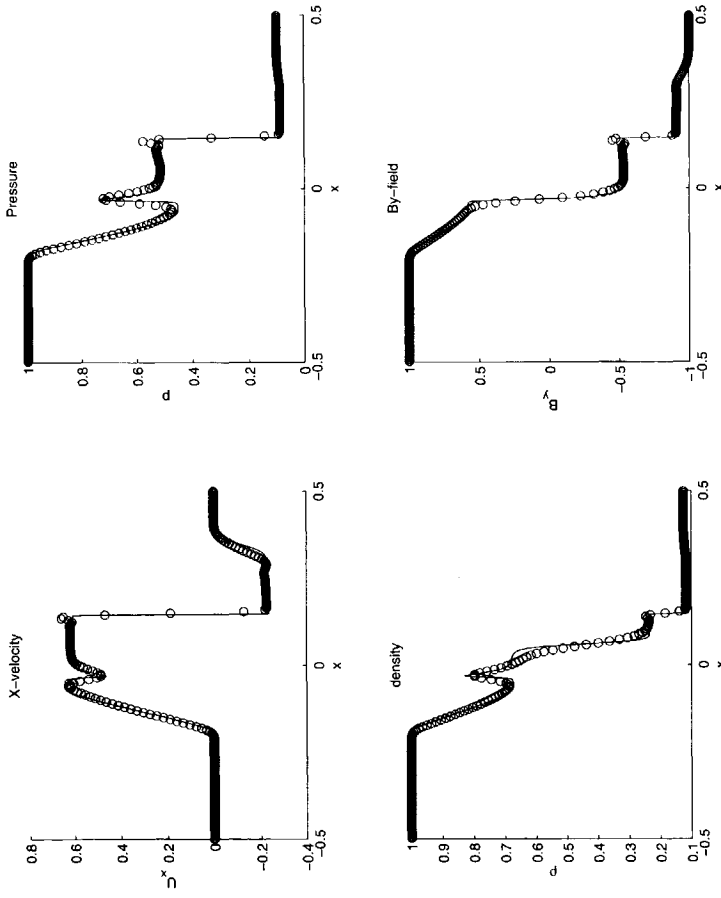


Figure 13.1: The Riemann problem of Brio and Wu, Mach-uniform scheme, 200 cells, $\lambda = 0.05$, $t_{\text{end}} = 0.1$.

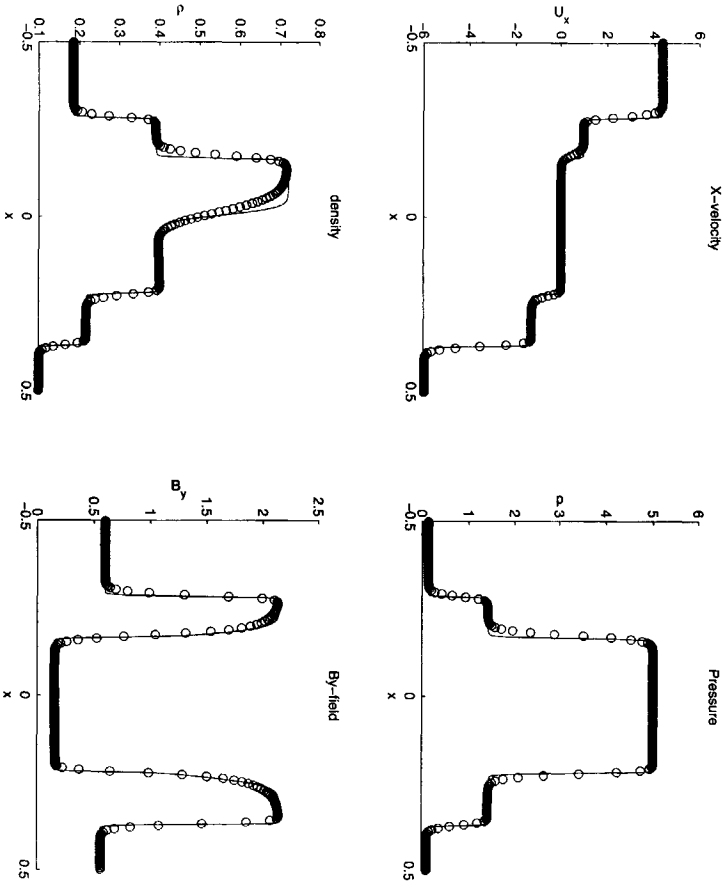


Figure 13.2: The Riemann problem of Dai and Woodward, Mach-uniform scheme, 200 cells, $\lambda = 0.05$, $t_{\text{end}} = 0.14$.

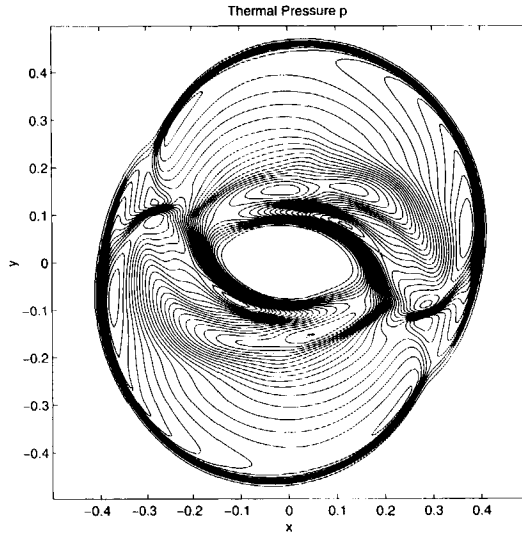


Figure 13.3: Thermal pressure p for the rotor problem. 200×200 cells, $t_{\text{end}} = 0.15$.

while the velocity is given by:

$$\left. \begin{aligned} u_x &= -u_0 (y - 0.5) / r_0 \\ u_y &= u_0 (x - 0.5) / r_0 \end{aligned} \right\} |r < r_0, \quad \left. \begin{aligned} u_x &= -f u_0 (y - 0.5) / r_0 \\ u_y &= f u_0 (x - 0.5) / r_0 \end{aligned} \right\} |r_0 < r < r_1, \quad (13.6)$$

$$\left. \begin{aligned} u_x &= 0 \\ u_y &= 0 \end{aligned} \right\} |r_1 < r,$$

where

$$r = \sqrt{x^2 + y^2}, \quad f = (r_1 - r) / (r_1 - r_0) \quad (13.7)$$

and we chose

$$v_0 = 2, \quad p_0 = 1, \quad r_0 = 0.1, \quad r_1 = 0.115, \quad B_{x0} = 5, \quad (13.8)$$

which corresponds to the *first rotor problem* in [90]. The computational domain is the unit square $-0.5 \leq x, y \leq 0.5$. Results are shown in Figs. 13.3 13.3. Taking into account the first order accuracy of the scheme, the correspondence with results presented in [90] is quite good. However, the characteristic based schemes are better in retaining the cylindrical shape of the inner part of the disk, compared to the dimensionally split staggered scheme.

The value of $(\nabla \cdot \mathbf{B})_{\text{max}} = 2.5 \cdot 10^{-14}$, as guaranteed by the constrained transport method. The large numerical diffusion of the first order upwind scheme causes loss of point symmetry of the solution.

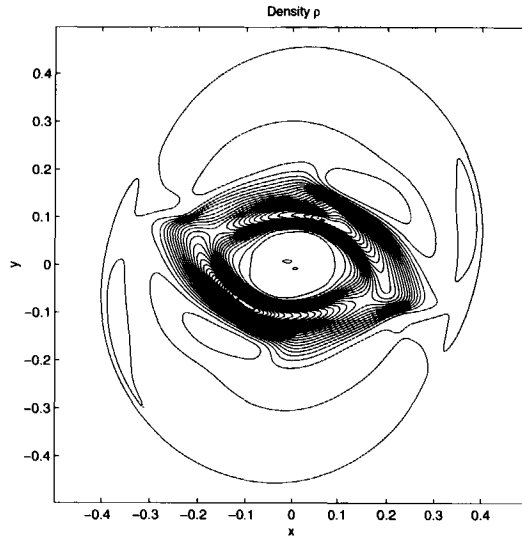


Figure 13.4: Density ρ for the rotor problem, 200×200 cells, $t_{\text{end}} = 0.15$.

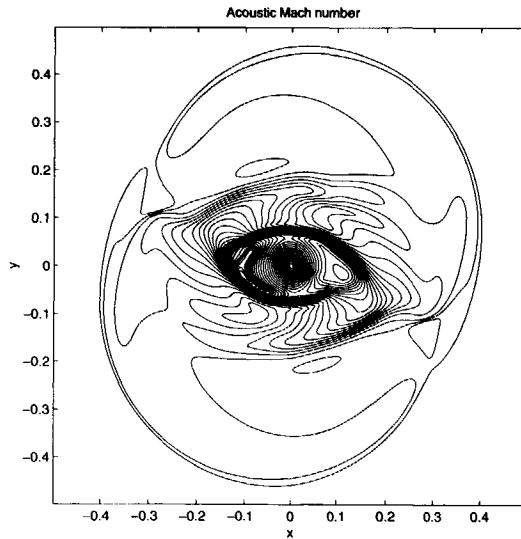


Figure 13.5: Mach number for the rotor problem, 200×200 cells, $t_{\text{end}} = 0.15$.

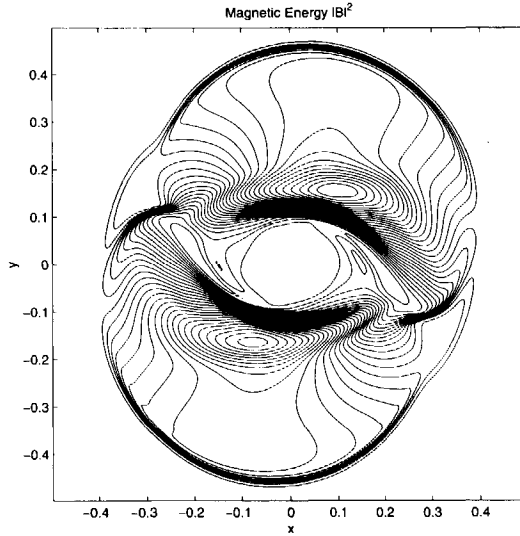


Figure 13.6: Magnetic energy $|B|^2$ for the rotor problem, 400×400 cells, $t_{\text{end}} = 0.15$.

The Orzag-Tang vortex

The Orzag-Tang vortex is another popular test case for two dimensional MHD flow, that has been studied for different initial Mach numbers. Different schemes are judged by comparing the resolution of the shockwaves and their ability to retain solenoidality of the discrete magnetic field. To test standard gasdynamic schemes the initial pressure field is chosen to have an initial Mach number of order 1. In [16] results are presented for initial Mach numbers $0 - 0.6$, obtained with a spectral code, to study the effect of compressibility on the solution. The initial condition for the problem is a velocity vortex superimposed by a magnetic vortex [60] given by:

$$\begin{aligned} u_x &= -\sin(y + \pi) & B_x &= -\sin(y + \pi) & \rho &= 25/9 \\ u_y &= \sin(x + \pi) & B_y &= \sin(2(x + \pi)) & p, \gamma &= 5/3 \end{aligned} \quad (13.9)$$

where we have used a scaling length $L_{\text{ref}} = 2\pi$, compared with the initial conditions described in [90]. The configuration is strongly unstable, and the resulting waves will form a complicated structure. The value of $(\nabla \cdot \mathbf{B})_{\text{max}} = 4.8 \cdot 10^{-15}$, as guaranteed by the constrained transport method.

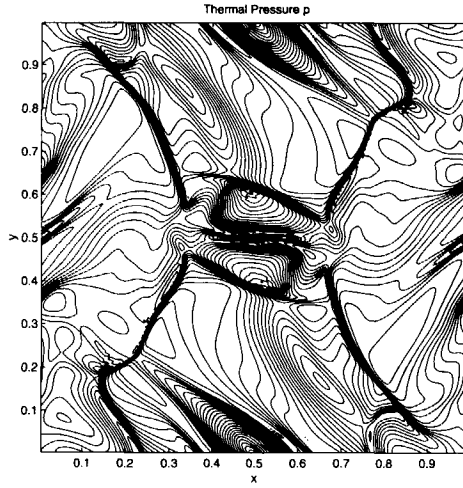


Figure 13.7: Thermal pressure p for the Orzag-Tang vortex, 200×200 cells, $t_{\text{end}} = 3.14$.

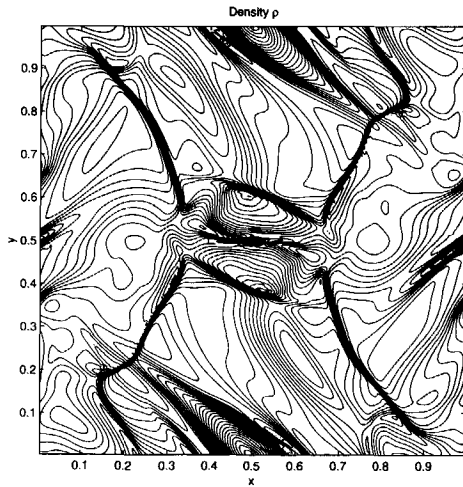


Figure 13.8: Density ρ for the Orzag-Tang vortex, 200×200 cells, $t_{\text{end}} = 3.14$.

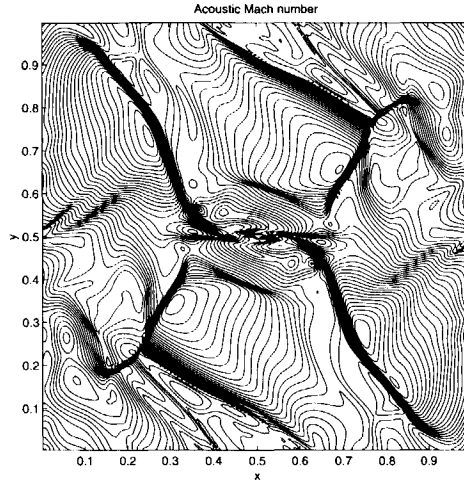


Figure 13.9: Mach number for the Orzag-Tang vortex, 200×200 cells, $t_{\text{end}} = 3.14$.

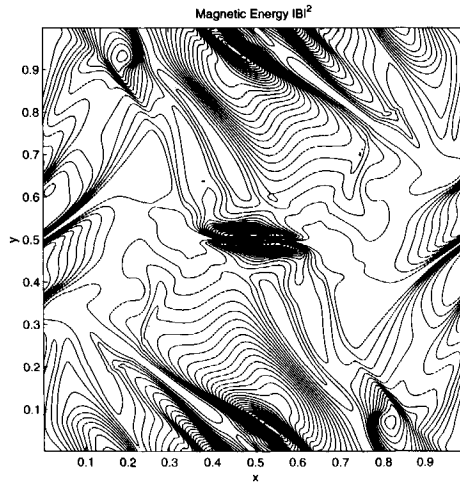


Figure 13.10: Magnetic energy $|B|^2$ for the Orzag-Tang vortex, 200×200 cells, $t_{\text{end}} = 3.14$.

13.4 Discussion

We have presented a potentially Mach uniform scheme for the equations of ideal magnetohydrodynamics for the case $\beta \gg 1$. However, many more testcases are needed to confirm the Mach uniform behavior. Furthermore, to have Mach-uniform behavior in the regimes $\beta \approx 1$ and $\beta \ll 1$ the induction equation and magnetic pressures have to be discretised implicitly. Finally, to have a fair comparison with other schemes for ideal magnetohydrodynamics the method has to be extended to second order spatial accuracy, but this can be achieved in a straightforward way using the MUSCL-approach for the inertia terms.

Bibliography

- [1] H. Abbot and A. E. von Doenhoff. *Theory of Wing Sections*. Dover Publications, New York, 1959.
- [2] R.W. Bain. *Steam tables 1964: physical properties of water and steam 0-800 C 0-1000 bars*. Edinburgh HMSO, 1964.
- [3] D.S. Balsara and D.S. Spicer. A staggered mesh algorithm using high order godunov fluxes to ensure solenoidal magnetic fields in magnetohydrodynamic simulations. *J. Comp. Phys.*, 149:270–292, 1999.
- [4] D.S. Balsara and D.S. Spicer. A staggered mesh algorithm using high order Godunov fluxes to ensure solenoidal magnetic fields in magnetohydrodynamic simulations. *J. Comp. Phys.*, 149:270–292, 1999.
- [5] G.K. Batchelor. *An Introduction to Fluid Dynamics*. Cambridge University Press, Cambridge, UK, 1967.
- [6] A. Bhattacharjee, C.S. Ng, and S.R. Spangler. Weakly compressible magnetohydrodynamic turbulence in the solar wind and the interstellar medium. *The Astrophysical Journal*, 494:409–418, 1998.
- [7] H. Bijl and P. Wesseling. A unified method for computing incompressible and compressible flows in boundary-fitted coordinates. *J. Comp. Phys.*, 141:153–173, 1998.
- [8] J.U. Brackbill and D.C. Barnes. The effect of nonzero $\nabla \cdot \mathbf{B}$ on the numerical solution of the magnetohydrodynamic equations. *Journal of Computational Physics*, 35:426, 1980.
- [9] R.P. Brent. *Algorithms for Minimization without Derivatives*. Prentice-Hall series in automatic computation. Prentice-Hall, Inc, Englewood Cliffs, N.J., 1973.
- [10] M. Brio and C.C. Wu. An upwind differencing scheme for the equations of ideal magnetohydrodynamics. *J. Comp. Phys.*, 75:400–422, 1988.
- [11] P.E.O. Buelow. Private Communication, 1997.

- [12] T. Chang and L. Hsiao. *The Riemann problem and interaction of waves in gas dynamics*. Pitman monographs and surveys in pure and applied mathematics. Longman Scientific and Technical, Harlow, England, 1989.
- [13] Y. Chen and S.D. Heister. A numerical treatment for attached cavitation. *Journal of Fluids Engineering*, 116:613–618, 1994.
- [14] Y. Chen and S.D. Heister. Two-phase modeling of cavitated flows. *Computers and Fluids*, 24(7):799–809, 1995.
- [15] P. Cooper. Analysis of single and two phase flows in turbopump inducers. *Journal of Engineering for Power*, October 1967.
- [16] R.B. Dahlburg and J.M. Picone. Evolution of the orszag-tang vortex system in a compressible medium. i. initial average subsonic flow. *The Physics of Fluids B*, 1:2153–2171, 1989.
- [17] W. Dai and P.R. Woodward. A simple Riemann solver and high-order Godunov schemes for hyperbolic systems of conservation laws. *J. Comp. Phys.*, 121:51–65, 1995.
- [18] W. Dai and P.R. Woodward. On the divergence-free condition and conservation laws in numerical simulations for supersonic magnetohydrodynamics. *The Astrophysical Journal*, 494:317–335, 1998.
- [19] D.F. de Lange. *Observation and Modelling of cloud formation behind a sheet cavity*. PhD thesis, Universiteit Twente, Enschede, The Netherlands, 1996.
- [20] Y. Delannoy. *Modélisation d'écoulements instationnaires et cavitants*. PhD thesis, INPG Grenoble, 1989.
- [21] Y. Delannoy and J.L. Kueny. Two phase flow approach in unsteady cavitation modelling. In O. Furuya, editor, *Cavitation and Multiphase Flow Forum, Toronto, Ontario, Canada, June 4-7, 1990*, FED-98, pages 153–158, New York, 1990. ASME.
- [22] I. Demirdžić, Z. Lilek, and M. Perić. A collocated finite volume method for predicting flows at all speeds. *Int. J. Num. Meth. in Fluids*, 16:1029–1050, 1993.
- [23] M. Deshpande, J. Feng, and C.L. Merkle. Nonlinear Euler analysis of 2-d cavity flow. In O. Furuya, editor, *Cavitation and Multiphase Flow Forum, Los Angeles, California, US, June 21-26, 1990*, FED-135, pages 213–219, New York, 1992. ASME.
- [24] L. Dieval and M. Arnaud. Numerical modeling of unsteady cavitating flows by a VOF method. In J.M. Michel and H. Kato, editors, *Third International Symposium on Cavitation, April 7-10, 1998, Grenoble*, volume 2, pages 243–248, 1998.

- [25] J.R. Edwards, R.K. Franklin, and M.-S. Liou. Low-diffusion flux-splitting methods for real fluid flows at all speeds. Preprint, 1999.
- [26] S. Eidelman, P. Colella, and R.P. Shreeve. Application of the Godunov method and its second-order extension to cascade flow modelling. *AIAA J.*, 22:1609–1615, 1984.
- [27] C.R. Evans and J.F. Hawley. Simulation of magnetohydrodynamic flows: A constrained transport method. *The Astrophysical Journal*, 332:659–677, September 1988.
- [28] R.A. Furness and S.P. Hutton. Experimental and theoretical studies of two dimensional fixed type cavities. *Journal of Fluids Engineering*, pages 515–522, 1975.
- [29] P.H. Gaskell and K.C. Lau. Curvature-compensated convective transport: SMART, a new boundedness-preserving transport algorithm. *Int. J. Num. Meth. in Fluids*, 8:617–641, 1988.
- [30] E. Godlewski and P.-A. Raviart. *Numerical Approximation of Hyperbolic Systems of Conservation Laws*. Springer, New York, 1996.
- [31] W. Hansen. Theorie zur Errechnung des Wasserstandes und der Strömungen in Randmeeren nebst Anwendungen. *Tellus*, 8:289–300, 1956.
- [32] F.H. Harlow and A.A. Amsden. Numerical calculation of almost incompressible flow. *J. Comp. Phys.*, 3:80–93, 1968.
- [33] F.H. Harlow and A.A. Amsden. Numerical calculation of almost incompressible flows. *J. Comp. Phys.*, 3:80–93, 1968.
- [34] F.H. Harlow and A.A. Amsden. A numerical fluid dynamics calculation method for all flow speeds. *J. Comp. Phys.*, 8:197–213, 1971.
- [35] F.H. Harlow and J.E. Welch. Numerical calculation of time-dependent viscous incompressible flow of fluid with a free surface. *The Physics of Fluids*, 8:2182–2189, 1965.
- [36] H.W.M. Hocijmakers, M.E. Janssens, and W. Kwan. Numerical simulation of sheet cavitation. In J.M. Michel and H. Kato, editors, *Third International Symposium on Cavitation, April 7–10, 1998, Grenoble*, volume 2, pages 257–262, 1998.
- [37] W.H. Isay. *Kavitation*. Schiffahrts-Verlag Hansa, Hamburg, 1989.
- [38] R. I. Issa. Solution of the implicitly discretised fluid flow equations by operator splitting. *J. Comp. Phys.*, 62:40–65, 1986.
- [39] R. I. Issa, A. D. Gosman, and A. P. Watkins. The computation of compressible and incompressible flows by a non-iterative implicit scheme. *J. Comp. Phys.*, 62:66–82, 1986.

- [40] R.I. Issa. Solution of the implicitly discretised fluid flow equations by operator-splitting. *J. Comp. Phys.*, 62:40–65, 1986.
- [41] R.I. Issa and M.H. Javareshkian. Pressure-based compressible calculation method utilizing total variation diminishing schemes. *AIAA Journal*, 36(9):1652–1657, September 1998.
- [42] J.K. Jakobsen. On the mechanism of head breakdown in cavitating inducers. *Journal of Basic Engineering*, pages 291–305, 1964.
- [43] M. Janssens. Calculations of unsteady attached cavitation. Master's thesis, Delft University of Technology, 1996.
- [44] John D. Anderson Jr. *Modern Compressible Flow, with historical perspective*. McGraw-Hill Series in Aeronautical and Aerospace Engineering. McGraw-Hill, New York, 1990.
- [45] K.C. Karki and S.V. Patankar. Pressure based calculation procedure for viscous flows at all speed in arbitrary configurations. *AIAA J.*, 27:1167–1174, 1989.
- [46] P.K. Khosla and S.G. Rubin. A diagonally dominant second-order accurate implicit scheme. *Computers and Fluids*, 2:207–209, 1974.
- [47] S.A. Kinnas and N.E. Fine. A numerical nonlinear analysis of the flow around two- and three-dimensional partially cavitating hydrofoils. *Journal of Fluid Mechanics*, 254:151–181, 1993.
- [48] R. Klein. Semi-implicit extension of a Godunov-type scheme based on low Mach number asymptotics 1: one-dimensional flow. *J. Comp. Phys.*, 121:213–237, 1995.
- [49] M.H. Kobayashi and J.C.F. Pereira. Characteristic-based pressure correction at all speeds. *AIAA journal*, 34(2):272–280, February 1996.
- [50] A. Kubota, H. Kato, and H. Yamaguchi. A new modelling of cavitating flows: A numerical study of unsteady cavitation on a hydrofoil section. *Journal of Fluid Mechanics*, 240:59–96, 1992.
- [51] A. Kubota, H. Kato, H. Yamaguchi, and M. Manda. Unsteady structure measurement of cloud cavitation on a foil section using conditional sampling technique. *Journal of Fluids Engineering*, 111:204–210, 1989.
- [52] R.F. Kunz, D.A. Boger, T.S. Chyczewski, D.R. Stinebring, and H.J. Gibeling. Multi-phase CFD analysis of natural and ventilated cavitation about submerged bodies. In P. A. Pfund, Y. Matsumoto, and H. Hayami, editors, *Proceedings of FEDSM'99 3rd ASME/JSME Joint Fluids Engineering Conference, San Francisco, California, US, July 18-23, 1999*, New York, 1999. ASME. CDROM, 9 pages.

- [53] C.B. Lancy. *Computational Gasdynamics*. Cambridge University Press, Cambridge, UK, 1998.
- [54] S.R. Lantz and Y. Fan. Anelastic magnetohydrodynamic equations for modeling solar and stellar convection zones. *The Astrophysical Journal*, 121:247–264, March 1999.
- [55] K. Lanzenberger. *Numerische und analytische Ansätze zur Simulation kavitierender Strömungen*. PhD thesis, Fakultät für Maschinenbau, Universität Karlsruhe, 1995.
- [56] P. Lax and B. Wendroff. Systems of conservation laws. *Comm. Pure and Appl. Math.*, 13:217–237, 1960.
- [57] P.D. Lax. Weak solutions of nonlinear hyperbolic equations and their numerical approximation. *Comm. Pure and Appl. Math.*, 7:159–193, 1954.
- [58] C.S. Lee. *Prediction of steady and unsteady performance of marine propellers with or without cavitation by numerical lifting surface theory*. PhD thesis, MIT, 1979.
- [59] R.J. LeVeque. *Numerical Methods for Conservation Laws*. Birkhäuser, Basel, 1992.
- [60] P. Londrillo and L. Del Zanna. High-order upwind schemes for multidimensional magnetohydrodynamics. *The Astrophysical Journal*, 530:508–524, 2000.
- [61] P.A. Lush and P.I. Peters. Visualisation of the cavitating flow in a venturi-type duct using high speed cine photography, AIRH. In *Operating problems of pump stations and power plants*, 1982.
- [62] R. Menikoff and B.J. Plohr. The Riemann problem for fluid flow of real materials. *Reviews of Modern Physics*, 61(1):75–130, January 1989.
- [63] C.L. Merkle, J. Feng, and P.E.O. Buelow. Computational modelling of the dynamics of sheet cavitation. In J.M. Michel and H. Kato, editors, *Third International Symposium on Cavitation, April 7–10, 1998, Grenoble*, volume 2, pages 307–311, 1998.
- [64] S. Osher and F. Solomon. Upwind difference schemes for hyperbolic systems of conservation laws. *Math. Comp.*, 38:339–374, 1982.
- [65] S. Osher and F. Solomon. Upwind difference schemes for hyperbolic systems of conservation laws. *Math. Comp.*, 38:339–374, 1982.
- [66] S.V. Patankar. *Numerical heat transfer and fluid flow*. Hemisphere, Washington, 1980.
- [67] S.V. Patankar. *Numerical Heat Transfer and Fluid Flow*. McGraw-Hill, New York, 1980.

- [68] K.G. Powell. An approximate Riemann solver for magnetohydrodynamics. ICASE Report 94-24, NASA Langley Research Center, Hampton, Virginia, 1994.
- [69] J.-L. Reboud and Y. Delannoy. Two-phase flow modelling of unsteady cavitation. In *The second International Symposium on Cavitation*, pages 39-44, April 1994.
- [70] J.-L. Reboud, B. Stutz, and O. Coutier. Two-phase flow structure of cavitation: Experiment and modelling of unsteady effects. In J.M. Michel and H. Kato, editors, *Third International Symposium on Cavitation, April 7-10, 1998, Grenoble*, volume 2, pages 203-208, 1998.
- [71] P. Reynier, P. Wesseling, L. Maraffa, and D. Giordano. Numerical investigation on liquid hydrazine behavior during venting into space. In E. Oñate, G. Bugeda, and B. Suárez, editors, *Proceedings European Congress on Computational Methods in Applied Sciences and Engineering, ECCOMAS 2000, Barcelona, September 11-14, 2000*, Barcelona, 2000. CIMNE. <http://ta.twi.tudelft.nl/users/wesseling/pub.html>.
- [72] C.M. Rhie and W.L. Chow. A numerical study of the turbulent flow past an isolated airfoil with trailing edge separation. *AIAA Journal*, 21:291-305, 1983.
- [73] A. Rizzi and H. Viviand, editors. *Numerical Methods for the Computation of Inviscid Transonic Flows with Shock Waves*, Braunschweig, Wiesbaden, 1981. Vieweg. Notes on Numerical Fluid Mechanics Vol. 3.
- [74] R. Saurel, J.-P. Cocchi, and P.B. Butler. A numerical study of cavitation in the wake of a hypervelocity underwater projectile. *Journal of Propulsion and Power*, 15(4):513-522, March-April 1999.
- [75] D.P. Schmidt, C.J. Rutland, and M.L. Corradini. A fully compressible, two dimensional model of small, high speed, cavitating nozzles. *Atomization and Sprays*, 9(3):255-276, May-June 1999.
- [76] G.H. Schnerr, S. Adam, K. Lanzenberger, and R. Schultz. Multiphase flows, condensation and cavitation problems. In *Computational Fluid Dynamics Review*, pages 245-249. John Wiley Ltd., Chichester, 1995.
- [77] R. Schulz. *Entwicklung eines numerischen Verfahren zur Simulation von Wolkenkavitation*. PhD thesis, Fakultät für Maschinenbau, Universität Karlsruhe, 1995.
- [78] Y.T. Shen and P.E. Dimotakis. The influence of surface cavitation on hydrodynamic forces. In *Proceedings of the 22nd American Towing Tank Conference, St. John's, Aug. 1989*, pages 44-53. Institute for Marine Dynamics of the National Research Council, Canada, 1989.
- [79] B.R. Shin and T. Ikohagi. A numerical study of unsteady cavitating flows. In J.M. Michel and H. Kato, editors, *Third International Symposium on Cavitation, April 7-10, 1998, Grenoble*, volume 2, pages 301-306, 1998.

- [80] Chi-Wang Shu. Total-variation-diminishing time discretisations. *SIAM J. Sci. Stat. Comput.*, 9(6):1073–1084, november 1988.
- [81] A. Sielecki. An energy-conserving difference scheme for the storm surge equations. *Mon. Weather Rev.*, 96:150–156, 1968.
- [82] W.G. Smyzak, J.M. Solomon, and A.E. Berger. Numerical simulations of cavitation inception. In *International Symposium on Cavitation CAV'95, Deauville, France*, pages 399–406, 1995.
- [83] G.A. Sod. A survey of several finite difference methods for systems of nonlinear conservation laws. *J. Comp. Phys.*, 27:1–31, 1978.
- [84] B.P. Sommeijer, P.J. van der Houwen, and J. Kok. Time integration of three-dimensional numerical transport models. *Appl. Num. Math.*, 16:201–225, 1994.
- [85] C. Song and J. He. Numerical simulation of cavitating flows by single-phase flow approach. In J.M. Michel and H. Kato, editors, *Third International Symposium on Cavitation, April 7–10, 1998, Grenoble*, volume 2, pages 295–300, 1998.
- [86] J.M. Stone and M.L. Norman. ZEUS-2D: A radiation magnetohydrodynamics code for astrophysical flows in two space dimensions. i. The hydrodynamic algorithms and tests. *The Astrophysical Journal Supplement Series*, 80:753–790, 1992.
- [87] J.M. Stone and M.L. Norman. ZEUS-2D: A radiation magnetohydrodynamics code for astrophysical flows in two space dimensions. i. The magnetohydrodynamic algorithms and tests. *The Astrophysical Journal Supplement Series*, 80:791–818, 1992.
- [88] B. Stutz and J.-L. Reboud. Two-phase flow structure of sheet cavitation. *Phys. Fluids*, 9(12):3678–3686, december 1997.
- [89] N. Takasugi, H. Kato, and H. Yamaguchi. Study on cavitating flow around a finite span hydrofoil. In *Cavitation and Multiphase Flow, Washington, June 20–24, 1993*, FED-153, pages 177–182, New York, 1993. ASME.
- [90] G. Tóth. The $\nabla \cdot b = 0$ constraint in shock-capturing magnetohydrodynamics. *J. Comp. Phys.*, 161(2):605–652, 2000.
- [91] I. Toumi, A. Kumbaro, and H. Paillère. Approximate Riemann solvers and flux vector splitting schemes for two-phase flow. In H. Deconinck, editor, *30th Computational Fluid Dynamics*, Lecture Series 1999-03. von Karman Institute for Fluid Dynamics, Brussels, March 1999.
- [92] D.R. van der Heul, C. Vuik, and P. Wesseling. Stability analysis of segregated solution methods for compressible flow. *App. Num. Math.*, 2001. To appear.

- [93] J.J.I.M. van Kan. A second-order accurate pressure correction method for viscous incompressible flow. *SIAM J. Sci. Stat. Comp.*, 7:870–891, 1986.
- [94] J.J.I.M. van Kan, C. Vuik, and P. Wesseling. Fast pressure calculation for 2d and 3d time dependent incompressible flows. *Numerical Linear Algebra with Applications*, 7:429–447, 2000.
- [95] B. van Leer. Towards the ultimate conservative difference scheme. V. A second-order sequel to Godunov’s method. *J. Comp. Phys.*, 32:101–136, 1979.
- [96] B. van Leer. On the relation between the upwind-differencing schemes of Godunov, Enquist-Osher and Roe. *SIAM J. Sci. Stat. Comp.*, 5:1–20, 1984.
- [97] Y. Ventikos and G. Tzabiras. A numerical study of the steady and unsteady cavitation phenomenon around hydrofoils. In *International Symposium on Cavitation CAV’95, Deauville, France*, pages 441–448, 1995.
- [98] Y. Ventikos and G. Tzabiras. A numerical method for the simulation of steady and unsteady cavitating flows. *Computers and Fluids*, 29:63–88, 2000.
- [99] C. Vuik. Solution of the discretized incompressible Navier-Stokes equations with the GMRES method. *Int. J. Num. Meth. in Fluids*, 16:507–523, 1993.
- [100] C. Vuik. Fast iterative solvers for the discretized incompressible Navier-Stokes equations. *Int. J. Num. Meth. in Fluids*, 22:195–210, 1996.
- [101] C. Vuik and J. Frank. A parallel block preconditioner accelerated by coarse grid correction. In M. Bubak, H. Afsarmanesh, R. Williams, and B. Hertzberger, editors, *High-Performance Computing and Networking, Proceeding of the 8th International Conference, HPCN Europe 2000, Amsterdam, The Netherlands, May 8-10, 2000*, Lecture Notes in Computer Science 1823, pages 99–108, Berlin, 2000. Springer.
- [102] B. Wendroff. The Riemann problem for materials with non-convex equations of state I: Isentropic flow. *Journal of Mathematical Analysis and Applications*, 38:454–466, 1972.
- [103] P. Wesseling. von neumann stability conditions for the convection-diffusion equation. *IMA journal of Numerical Analysis*, 16:583–598, 1996.
- [104] P. Wesseling. Non-convex hyperbolic systems. In H. Deconinck, editor, *30th Computational Fluid Dynamics*, Lecture Series 1999-03. von Karman Institute for Fluid Dynamics, Brussels, March 1999.
- [105] P. Wesseling. *Principles of Computational Fluid Dynamics*. Springer, Heidelberg, 2001.

- [106] P. Wesseling, A. Segal, and C.G.M. Kassels. Computing flows on general three-dimensional nonsmooth staggered grids. *J. Comp. Phys.*, 149:333–362, 1999.
- [107] P. Wesseling, A. Segal, C.G.M. Kassels, and H. Bijl. Computing flows on general two-dimensional nonsmooth staggered grids. *J. Eng. Math.*, 34:21–44, 1998.
- [108] P. Wesseling, D.R. van der Heul, and C. Vuik. Unified methods for computing compressible and incompressible flows. In E. Oñate, G. Bugeda, and B. Suárez, editors, *Proceedings European Congress on Computational Methods in Applied Sciences and Engineering, ECCOMAS 2000, Barcelona, September 11-14, 2000*, Barcelona, 2000. CIMNE. <http://ta.twi.tudelft.nl/users/wesseling/pub.html>.
- [109] P. Wesseling, D.R. van der Heul, and C. Vuik. Uniformly effective numerical methods for hyperbolic systems. In M. Deville and R. Owens, editors, *Proceedings of the 16th IMACS World Congress 2000, Lausanne, August 2000*, New Brunswick, 2000. Rutgers University. <http://ta.twi.tudelft.nl/users/wesseling/pub.html>.
- [110] H. Yamaguchi and H. Kato. On application of nonlinear cavity flow theory to thick foil sections. In *Second International Symposium on Cavitation*, pages 167–174. Mechanical Engineering Publications Limited, 1983.
- [111] H. Yamaguchi, M. Tanaka, and H. Kato. A numerical study on mechanism of vortex generation downstream of a sheet cavity on a two-dimensional hydrofoil. In *Cavitation and Multiphase Flow Forum, Portland, Oregon, June 23-27, 1991*, FED-109, pages 27–34, New York, 1991. ASME.
- [112] G.P. Zank and W.H. Matthaeus. The equations of nearly incompressible fluids.i. hydrodynamics, turbulence and waves. *The Physics of Fluids A*, 3:69–82, 1991.
- [113] G.P. Zank and W.H. Matthaeus. The equations of reduced magneto-hydrodynamics. *Journal of Plasma Physics*, 48:85–100, 1992.
- [114] G.P. Zank and W.H. Matthaeus. The equations of nearly incompressible fluids.ii. Magneto-hydrodynamics, turbulence and waves. *The Physics of Fluids A*, 5:257–273, 1993.
- [115] Y. Zhang, S. Gopalan, and J. Katz. On the flow structure and vorticity production due to sheet cavitation. In *Proceedings of FEDSM '98, 1998 ASME Fluids Engineering Division Summer Meeting, June 21-25, 1998, Washington DC*. ASME, 1999.
- [116] M. Zijlema. On the construction of a third-order accurate monotone convection scheme with application to turbulent flow in general coordinates. *Int. J. Num. Meth. in Fluids*, 22:619–641, 1996.



Appendix A

Some remarks on spatial discretisation on a staggered grid in general coordinates

A.1 Introduction

Discretization of the Navier-Stokes equations on a staggered grid in general coordinates is extensively discussed in [105, 106, 107]. However, in these publications emphasis is on discretisation with central schemes. In the case of the Euler equations an upwind scheme is used to introduce artificial viscosity to ensure that numerical solutions converge to weak solutions that satisfy the entropy condition. Here we consider one detail of the discretisation of the compressible Euler equations: the inertia term in the momentum equation. The momentum equation in coordinate invariant form is given by:

$$\frac{1}{\rho} \frac{\partial \mathbf{u}}{\partial t} + \frac{1}{\sqrt{g}} \frac{\partial}{\partial \xi^\gamma} (\mathbf{u} V^\gamma) = -\frac{1}{\sqrt{g}} \frac{\partial}{\partial \xi^\beta} (\sqrt{g} a_\alpha^{(\beta)} p) \quad (\text{A.1})$$

where

Integration of the momentum equation over the shifted control volume $\Omega_{j+\epsilon 1}$ depicted in Fig. A.1 leads for the inertia terms to:

$$\int_{j+\epsilon 1} \frac{1}{\sqrt{g}} \frac{\partial}{\partial \xi^\alpha} (\mathbf{u} V^\alpha) d\Omega. \quad (\text{A.2})$$

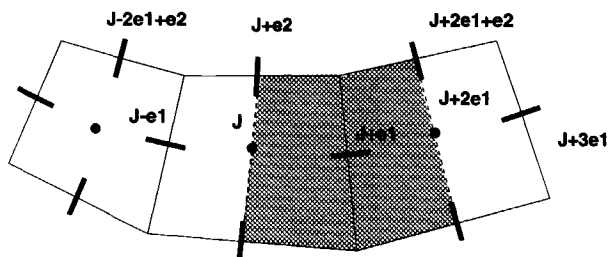


Figure A.1: The control volume for the contravariant velocity V^1 .

The integral consists of two parts:

$$\mathbf{I}_{11} = \int_{j+e1} \frac{1}{\sqrt{g}} \frac{\partial}{\partial \xi^1} (\mathbf{u} V^1) d\xi^1 d\xi^2 = \int_{\xi_{j_2-\frac{1}{2}}^2}^{\xi_{j_2+\frac{1}{2}}^2} (\mathbf{u} V^1) \Big|_{j_1}^{j_1+1}, \quad (\text{A.3})$$

$$\mathbf{I}_{12} = \int_{j+e1} \frac{1}{\sqrt{g}} \frac{\partial}{\partial \xi^2} (\mathbf{u} V^2) d\xi^1 d\xi^2 = \int_{\xi_{j_1-\frac{1}{2}}^2}^{\xi_{j_1+\frac{1}{2}}^2} (\mathbf{u} V^2) \Big|_{j_1}^{j_1+1}. \quad (\text{A.4})$$

The integrals are approximated by the midpoint rule:

$$\mathbf{I}_{11} \approx \Delta \xi^2 (\mathbf{u} V^1) \Big|_j^{j+2e1}, \quad (\text{A.5})$$

$$\mathbf{I}_{12} \approx \Delta \xi^1 (\mathbf{u} V^2) \Big|_{j+e1-e2}^{j+e1+e2}. \quad (\text{A.6})$$

To form an equation for the contravariant momentum flux component V_{j+e1}^1 the integrals are premultiplied by $\mathbf{a}_{j+e1}^{(1)}$. In both cases we have to approximate $\mathbf{a}_{j+e1}^{(1)} (\mathbf{u} V^\alpha)$ in the integration points. We will not discuss the derivation of the momentum equation for the contravariant flux component V_{j+e1}^2 because its treatment is completely analogous.

Two different upwind schemes for the convective term in the momentum equation were discussed in [7]:

- *partial upwind*, where the *convective flux* V^α is centrally interpolated and the *convected velocity* \mathbf{u} is upwind interpolated.
- *full upwind*, where both the *convective flux* V^α and the *convected velocity* \mathbf{u} are upwind interpolated.

Fig.A.2 and Fig.A.3 show results for partial upwind and full upwind respectively, for a Riemann problem, with initial condition $u_{\text{left}} = 1$, $u_{\text{right}} = 0.5$ for the inviscid Burgers equation on a regular mesh with 40×7 cells. Only the full upwind scheme gives a monotone solution. For the Euler equations the partial upwind scheme will give more crisp resolution

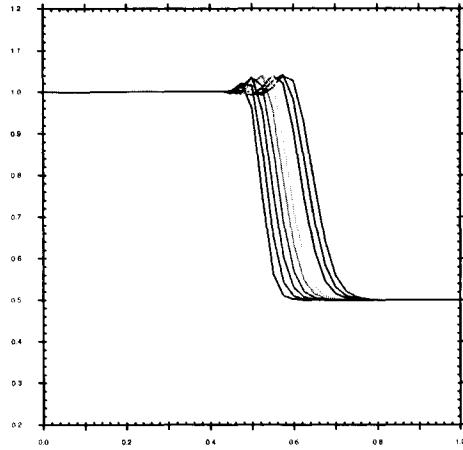


Figure A.2: Velocity at the center line, partial upwind discretisation on regular mesh.

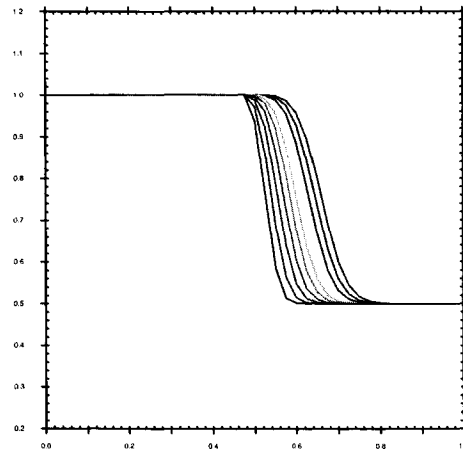


Figure A.3: Velocity at the center line, full upwind discretisation on regular mesh.

of shocks than the full upwind scheme. However, linear stability of the full upwind scheme is better than for the partial upwind scheme (Chapter 8). Because stability of the scheme is our main concern in this application we use the full upwind scheme in all numerical experiments both in one and two space dimensions.

Discretisation in general coordinates is done following the approach of [105, 106, 107]. First the vector equation is integrated over a control volume, before the equation is projected in the contravariant direction. This avoids the discretisation of the Christoffel symbols, which leads to loss of accuracy on nonsmooth grids.

We will first discuss an improved discretisation of the convective flux for the full upwind scheme in general coordinates. Next the approach of [107, 105, 106] is extended for a higher order limited κ -scheme for the *convected velocity*.

A.2 Improved discretisation of the convective flux for full upwind scheme.

On nonsmooth grids the direct one-sided interpolation of the contravariant velocity in the full upwind scheme provides an inaccurate approximation of the contravariant velocity at the cell face, because the variation in geometric quantities is not taken into account. A more accurate interpolation to the different integration points is described below.

We will consider the approximation in the integration point $j + 2e_1$:

- Partial upwind discretisation:

$$\mathbf{a}_{j+e_1}^{(1)} \mathbf{u}_{j+2e_1} V_{j+2e_1}^1 = \frac{1}{2} \mathbf{a}_{j+e_1}^{(1)} \cdot \mathbf{u}_{j+e_1} (V_{j+e_1}^1 + V_{j+3e_1}^1), \quad (\text{A.7})$$

- Full upwind discretisation:

$$\mathbf{a}_{j+e_1}^{(1)} \mathbf{u}_{j+2e_1} V_{j+2e_1}^1 = \mathbf{a}_{j+e_1}^{(1)} \cdot \mathbf{u}_{j+e_1} (-\mathbf{a}_{(2),j+2e_1} \otimes \mathbf{u}_{j+e_1}), \quad (\text{A.8})$$

where:

$$\mathbf{u}_{j+e_1} = \frac{1}{\sqrt{g_{j+e_1}}} (\mathbf{a}_{(1)} V^1 + \mathbf{a}_{(2)} V^2)_{j+e_1}, \quad (\text{A.9})$$

and we have used:

$$V_{j+e_1}^2 = \frac{1}{4} (V_{j+e_2}^2 + V_{j-e_2}^2 + V_{j+2e_1+e_2}^2 + V_{j+2e_1-e_2}^2), \quad (\text{A.10})$$

$$\mathbf{a}_{(1)j+e_1} = \frac{1}{4} (\mathbf{a}_{(1)j+e_2} + \mathbf{a}_{(1)j-e_2} + \mathbf{a}_{(1)j+2e_1+e_2} + \mathbf{a}_{(1)j+2e_1-e_2}). \quad (\text{A.11})$$



Figure A.4: Irregular mesh to test the improved upwind scheme.

Note: the previously used implementation of the full upwind discretisation is given by:

$$\mathbf{a}_{j+e1}^{(1)} \mathbf{u}_{j+2e1} V_{j+2e1}^1 = \mathbf{a}_{j+e1}^{(1)} \cdot \mathbf{u}_{j+e1} V_{j+e1}^1, \quad (\text{A.12})$$

which gives large errors on nonsmooth grids. Computation of the flux for the integration point j can be done analogously.

The approximation in the integration point $j + e1 + e2$ is as follows:

$$\mathbf{a}_{j+e1}^{(1)} \mathbf{u}_{j+e1+e2} V_{j+e1+e2}^2 = \frac{1}{2} \mathbf{a}_{j+e1}^{(1)} \cdot \mathbf{u}_{j+e1} (V_{j+e2}^2 + V_{j+2e1+e2}^2), \quad (\text{A.13})$$

where:

$$\mathbf{u}_{j+e1} = \frac{1}{\sqrt{g}_{j+e1}} (\mathbf{a}_{(1)} V^1 + \mathbf{a}_{(2)} V^2)_{j+e1}, \quad (\text{A.14})$$

and we have used:

$$V_{j+e1}^2 = \frac{1}{4} (V_{j+e2}^2 + V_{j-e2}^2 + V_{j+2e1+e2}^2 + V_{j+2e1-e2}^2), \quad (\text{A.15})$$

$$\mathbf{a}_{(1)j+e1} = \frac{1}{4} (\mathbf{a}_{(1)j+e2} + \mathbf{a}_{(1)j-e2} + \mathbf{a}_{(1)j+2e1+e2} + \mathbf{a}_{(1)j+2e1-e2}). \quad (\text{A.16})$$

Computation of the flux for the integration point $j + e1 - e2$ can be done analogously.

We compare the original and the improved discretisation of the convective flux for the inviscid Burgers equation on the nonsmooth mesh of Fig. A.4, with 40×7 cells, $-0.5 \leq x \leq 0.5$, $0 \leq y \leq 0.02$. The initial condition is chosen as $u_{\text{left}}=1, u_{\text{right}}=0.5$. The solutions for time $t = i\Delta t, i = 1 \dots 10$ are shown for the original and improved discretisation in Figs. A.5 and A.6 respectively.

A.3 A higher order limited κ -scheme in general coordinates

In the case of a higher order upwind discretisation the variables are interpolated with a limited κ -scheme to the integration points. We will consider a V^1 cell, where we have to approximate the fluxes in the four integration points $j, j + 2e1, j + e1 - e2$ and $j + e1 + e2$.

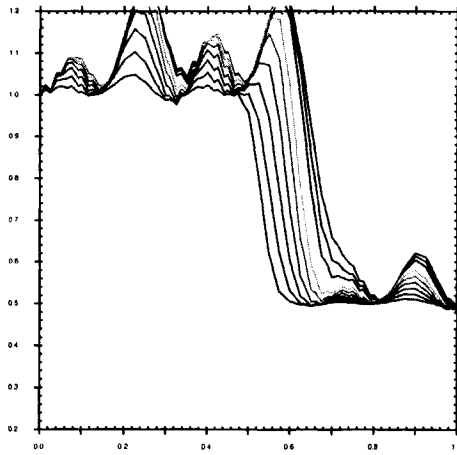


Figure A.5: Velocity at the center line, original fully upwind discretisation on the mesh of Fig. A.4.

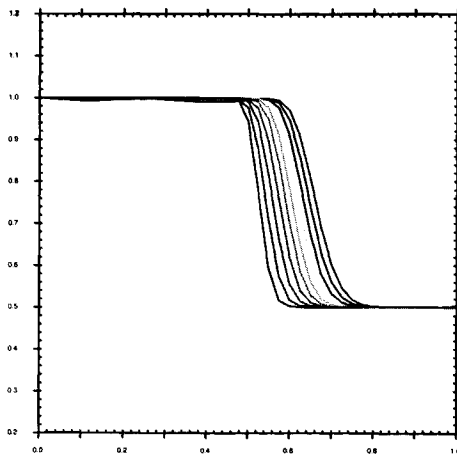


Figure A.6: Velocity at the center line, improved fully upwind discretisation on the mesh of Fig. A.4.

The base vectors $\mathbf{a}^{(\alpha)}$ and $\mathbf{a}_{(\alpha)}$ are defined in Appendix C.

In integration point $j + 2e1$ we have to approximate:

$$\mathbf{a}_{j+e1}^{(1)} \cdot \mathbf{u}_{j+2e1} V_{j+2e1}^1. \quad (\text{A.17})$$

This is done by defining:

$$\tilde{V}_{j+e1}^{-1} = \mathbf{u}_{j+e1} \cdot \mathbf{a}_{j+e1}^{(1)}, \quad (\text{A.18})$$

$$\tilde{V}_{j-e1}^{-1} = \mathbf{u}_{j-e1} \cdot \mathbf{a}_{j+e1}^{(1)}, \quad (\text{A.19})$$

$$\tilde{V}_{j+3e1}^{-1} = \mathbf{u}_{j+3e1} \cdot \mathbf{a}_{j+e1}^{(1)}, \quad (\text{A.20})$$

$$\mathbf{a}_{j+e1}^{(1)} \cdot \mathbf{u}_{j+2e1} = \tilde{V}_{j+2e1}^{-1} = \tilde{V}_{j+e1}^{-1} + \Psi(r_{j+e1}) \left(\tilde{V}_{j+e1}^{-1} - \tilde{V}_{j-e1}^{-1} \right), \quad (\text{A.21})$$

$$r_{j+e1} = \frac{\tilde{V}_{j+3e1}^{-1} - \tilde{V}_{j+e1}^{-1}}{\tilde{V}_{j+e1}^{-1} - \tilde{V}_{j-e1}^{-1}}, \quad (\text{A.22})$$

$$\Psi(r) = \frac{1}{2} (r + |r|) \frac{r + 3}{(1 + r)^2}, \quad (\text{A.23})$$

where $\Psi(r)$ is the ISNAS-limiter of [116]. It was found that interpolation of the components of the Cartesian velocity, instead of the projected velocity does not give substantially different results.

The convective flux is discretised in the following way:

- Partial upwind discretisation

$$V_{j+2e1}^1 = \frac{1}{2} (V_{j+e1}^1 + V_{j+3e1}^1). \quad (\text{A.24})$$

- Full upwind discretisation

Here we have to make a higher order upwind interpolation to the integration point for V_{j+2e1}^1 . This is done in the following way:

$$\hat{V}_{j+e1}^1 = \mathbf{u}_{j+e1} \otimes \mathbf{a}_{(2)j+2e1}, \quad (\text{A.25})$$

$$\hat{V}_{j-e1}^1 = \mathbf{u}_{j-e1} \otimes \mathbf{a}_{(2)j+2e1}, \quad (\text{A.26})$$

$$\hat{V}_{j+3e1}^1 = \mathbf{u}_{j+3e1} \otimes \mathbf{a}_{(2)j+2e1}, \quad (\text{A.27})$$

$$V_{j+2e1}^1 = \hat{V}_{j+2e1}^1 = \hat{V}_{j+e1}^1 + \Psi(r_{j+e1}) \left(\hat{V}_{j+e1}^1 - \hat{V}_{j-e1}^1 \right), \quad (\text{A.28})$$

$$r_{j+e1} = \frac{\hat{V}_{j+3e1}^1 - \hat{V}_{j+e1}^1}{\hat{V}_{j+e1}^1 - \hat{V}_{j-e1}^1}. \quad (\text{A.29})$$

Construction of the flux for the integration point j can be done in an analogous way.

In integration point $j + e1 + e2$ we have to approximate:

$$\mathbf{a}_{j+e1}^{(1)} \cdot \mathbf{u}_{j+e1+e2} V_{j+e1+e2}^2. \quad (\text{A.30})$$

This is done by defining:

$$\tilde{V}_{j+e1}^1 = \mathbf{u}_{j+e1} \cdot \mathbf{a}_{j+e1}^{(1)} = \frac{V_{j+e1}^1}{\sqrt{g_{j+e1}}}, \quad (\text{A.31})$$

$$\tilde{V}_{j+e1-2e2}^1 = \mathbf{u}_{j+e1-2e2} \cdot \mathbf{a}_{j+e1}^{(1)}, \quad (\text{A.32})$$

$$\tilde{V}_{j+e1+2e2}^1 = \mathbf{u}_{j+e1+2e2} \cdot \mathbf{a}_{j+e1}^{(1)}, \quad (\text{A.33})$$

$$\mathbf{a}_{j+e1}^{(1)} \cdot \mathbf{u}_{j+e1+e2} = \tilde{V}_{j+e1+e2}^1 = \tilde{V}_{j+e1}^1 + \Psi(r_{j+e1+e2}) \left(\tilde{V}_{j+e1}^1 - \tilde{V}_{j+e1-2e2}^1 \right), \quad (\text{A.34})$$

$$r_{j+e1+e2} = \frac{\tilde{V}_{j+e1+2e2}^1 - \tilde{V}_{j+e1}^1}{\tilde{V}_{j+e1}^1 - \tilde{V}_{j+e1-2e2}^1}, \quad (\text{A.35})$$

$$V_{j+e1+e2}^2 = \frac{1}{2} (V_{j+e2}^2 + V_{j+2e1+e2}^2). \quad (\text{A.36})$$

Construction of the flux for the integration point $j + e1 - e2$ can be done in an analogous way. We have applied the higher order ISNAS-scheme to compute the solution to the Riemann problem described in Sect. A.2. The timestep is chosen $\delta t = 0.002$. Fig. A.7 shows the solution for the classic discretisation in general coordinates using Christoffel symbols, whereas Fig. A.8 shows results for the present discretisation.

A.4 Conclusions

Two different upwind discretisations for the convective term of the momentum equation are discussed. Only the *full upwind* scheme gives monotone solutions for the inviscid Burgers equation and will be shown to have better stability properties than the *partial upwind* scheme.

An improved discretisation of the first order full upwind scheme in general coordinates is discussed and the extension of the full upwind scheme to a limited higher order κ -scheme.

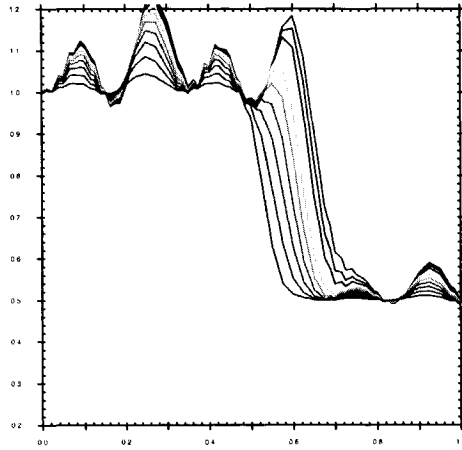


Figure A.7: Velocity at the center line, classic higher order upwind discretisation on the mesh of Fig. A.4.

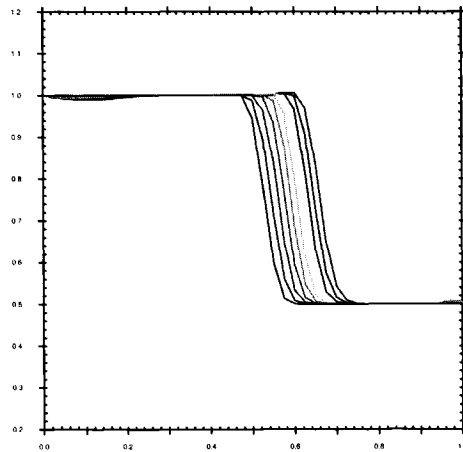


Figure A.8: Velocity at the center line, improved higher order upwind discretisation on the mesh of Fig. A.4.



Appendix B

Two pressure correction schemes

SIMPLE type iterative pressure correction for implicitly discretised momentum equation

With a SIMPLE type solution method, the actual discretisation becomes:

$$\frac{m_{j+\frac{1}{2}}^{n+1} - m_{j+\frac{1}{2}}^n}{\delta t} + (u^{n+1} m^{n+1})|_{j+\frac{1}{2}}^{j+\frac{1}{2}} = -p^{n+1}|_j^{j+1}, \quad (\text{B.1})$$

$$\frac{\rho(p^{n+1}) - \rho(p^n)}{\delta t} + (\zeta m)^{n+1}|_{j-\frac{1}{2}}^{j+\frac{1}{2}} = 0. \quad (\text{B.2})$$

Note that now the convective term is taken fully implicit. To eliminate all errors due to linearisation and segregation of the system in an attempt to solve the target discretisation accurately, we have to use an iterative method. Although very costly, this provides a means to check the suitability of a target discretisation.

For brevity we will discuss the case without the density upwind bias, and assume that the resulting pressure correction equation can be linearized. In practice the nonlinear pressure correction equations are solved by the algorithm discussed in Sect. 7.6.1.

The system (B.1),(B.2) is solved by a sequence of pressure correction steps. Each iterative step commences with the implicit calculation of a tentative momentum field $m^{*(k+1)}$, using the pressure and velocity from the previous iteration:

$$\frac{m_{j+\frac{1}{2}}^{*(k+1)} - m_{j+\frac{1}{2}}^n}{\delta t} + \frac{1}{\delta x} (u^{(k)} m^{*(k+1)})|_{j-\frac{1}{2}}^{j+\frac{1}{2}} = -\frac{1}{\delta x} p^{(k)}|_j^{j+1}. \quad (\text{B.3})$$

Similar to the single step solution procedure, the momentum correction is postulated as

$$\frac{m_{j+\frac{1}{2}}^{(k+1)} - m_{j+\frac{1}{2}}^{*(k+1)}}{\delta t} = -\frac{1}{\delta x} (p^{(k+1)} - p^{(k)})|_j^{j+1}, \quad (\text{B.4})$$

and this is substituted in the mass conservation equation to obtain:

$$\frac{\rho(p_j^{(k+1)}) - \rho(p_j^n)}{\delta t} - \frac{1}{\delta x} \left(\frac{\delta t}{\delta x} (p^{(k+1)} - p^{(k)}) \Big|_{l=-\frac{1}{2}}^{l+\frac{1}{2}} \right) \Big|_{l=j-\frac{1}{2}}^{l=j+\frac{1}{2}} = -\frac{1}{\delta x} m^{*(k+1)} \Big|_{j+\frac{1}{2}}^{j+\frac{1}{2}}. \quad (\text{B.5})$$

Now subtract the term $\rho(p^{(k)})/\delta t$ left and right to obtain:

$$\begin{aligned} \frac{\rho(p_j^{(k+1)}) - \rho(p_j^{(k)})}{\delta t} - \frac{1}{\delta x} \left(\frac{\delta t}{\delta x} (p^{(k+1)} - p^{(k)}) \Big|_{l=-\frac{1}{2}}^{l+\frac{1}{2}} \right) \Big|_{l=j-\frac{1}{2}}^{l=j+\frac{1}{2}} = \\ -\frac{1}{\delta x} m^{*(k+1)} \Big|_{j+\frac{1}{2}}^{j+\frac{1}{2}} - \frac{\rho(p_j^{(k)}) - \rho(p_j^n)}{\delta t}. \end{aligned} \quad (\text{B.6})$$

The iterative pressure correction method to solve this equation is given by:

$$p_j^{(k+1)} - p_j^{(k)} = \delta p_j^{(k)}, \quad (\text{B.7})$$

$$\begin{aligned} \frac{d\rho}{dp} \Big|_{p=p_j^{(k)}} \frac{\delta p_j^{(k)}}{\delta t} - \frac{1}{\delta x} \left(\frac{\delta t}{\delta x} (\delta p^{(k)}) \Big|_{l=-\frac{1}{2}}^{l+\frac{1}{2}} \right) \Big|_{l=j-\frac{1}{2}}^{l=j+\frac{1}{2}} = \\ -\frac{1}{\delta x} m^{*(k+1)} \Big|_{j-\frac{1}{2}}^{j+\frac{1}{2}} - \frac{\rho(p^{(k)}) - \rho(p^n)}{\delta t}. \end{aligned} \quad (\text{B.8})$$

Finally, we put

$$m_{j+\frac{1}{2}}^{(k+1)} = m_{j+\frac{1}{2}}^{(k)} - \frac{\delta t}{\delta x} \delta p^{(k)} \Big|_j^{j+1},$$

and

$$u_{j+\frac{1}{2}}^{(k+1)} = \frac{m_{j+\frac{1}{2}}^{(k+1)}}{\rho(\frac{1}{2}(p_j^{(k+1)} + p_{j+1}^{(k+1)}))}.$$

The sequence is started with the values of the previous timestep. Upon convergence the right-hand side of the iterative pressure correction will vanish as will the pressure correction itself. This means that the tentative momentum field already fullfills the continuity constraint and no further projection is needed. Both the pressure and momentum update are underrelaxed. According to [66], this is essential to avoid divergence. This is confirmed by numerical experiments. To avoid a strongly nonsolenoidal tentative momentum field, it is underrelaxed in the following way. The fully discretised momentum equation can be

expressed as the following linear system:

$$Am^{*(k+1)} = b, \quad (\text{B.9})$$

$$A_{ii}m_i^{*(k+1)} = - \sum_{j=1, j \neq i}^n A_{ij}m_j^{*(k+1)} + b_i, \quad (\text{B.10})$$

$$m_i^{*(k+1)} = \frac{- \sum_{j=1, j \neq i}^n A_{ij}m_j^{*(k+1)} + b_i}{A_{ii}}, \quad (\text{B.11})$$

$$m_i^{*(k+1)} = m_i^{(k)} + \frac{- \sum_{j=1, j \neq i}^n A_{ij}m_j^{*(k+1)} + b_i}{A_{ii}} - m_i^{(k)}. \quad (\text{B.12})$$

Now the increment in the momentum is underrelaxed with a factor α :

$$m_i^{*(k+1)} = m_i^{(k)} + \alpha \left(\frac{- \sum_{j=1, j \neq i}^n A_{ij}m_j^{*(k+1)} + b_i}{A_{ii}} - m_i^{(k)} \right), \quad (\text{B.13})$$

$$\frac{A_{ii}}{\alpha} m_i^{*(k+1)} = \frac{A_{ii}}{\alpha} (1 - \alpha) m_i^{(k)} - \sum_{j=1, j \neq i}^n A_{ij}m_j^{*(k+1)} + b_i. \quad (\text{B.14})$$

This leads to the following modified system

$$A'm^{*(k+1)} = b', \quad (\text{B.15})$$

$$A'_{ij} = A_{ij}, i \neq j \quad ; \quad A'_{ij} = \frac{A_{ij}}{\alpha}, i = j, \quad (\text{B.16})$$

$$b'_i = b_i + \frac{A_{ii}}{\alpha} (1 - \alpha) m_i^{(k)}, \quad (\text{B.17})$$

where α is chosen between 0.5 and 1. The pressure correction is underrelaxed in the following way:

$$p^{(k+1)} = p^{(k)} + \beta \delta p^{(k)}, \quad (\text{B.18})$$

where β is chosen in the same range as α . Because the nonlinear pressure correction has to be solved in each iteration, this modified SIMPLE method is very expensive.

Compressible pressure correction for explicit momentum equation

A different way to circumvent the errors induced by the linearisation and segregation of the equations is to change the target scheme, by using an explicit discretisation of the convective terms in the momentum equation. The system will then be what is called

semi-implicit. Now the target discretisation is:

$$\frac{m_{j+\frac{1}{2}}^{n+1} - m_{j+\frac{1}{2}}^n}{\delta t} + \frac{1}{\delta x} (u^n m^n)_{j+\frac{1}{2}}^{j+\frac{1}{2}} = -\frac{1}{\delta x} p^{n+1}|_j^{j+1}, \quad (\text{B.19})$$

$$\frac{\rho(p^{n+1}) - \rho(p^n)}{\delta t} + Dm^{n+1} = 0. \quad (\text{B.20})$$

The semi-implicit system is solved in the same way as discussed in Section 7.6.1. First a tentative momentum field is calculated:

$$\frac{m_{j+\frac{1}{2}}^* - m_{j+\frac{1}{2}}^n}{\delta t} + \frac{1}{\delta x} (u^n m^n)_{j-\frac{1}{2}}^{j+\frac{1}{2}} = -\frac{1}{\delta x} p^n|_j^{j+1}. \quad (\text{B.21})$$

The pressure correction equation can now be obtained by subtracting the equation for the tentative momentum field from the target momentum equation which gives:

$$\frac{m_{j+\frac{1}{2}}^{n+1} - m_{j+\frac{1}{2}}^*}{\delta t} = -\frac{1}{\delta x} (p^{n+1} - p^n)|_j^{j+1}. \quad (\text{B.22})$$

The pressure correction equation is the same as in the implicit case. Note that the derivation of the pressure correction equation is *exact* so that the resolved scheme is identical to the target scheme. This scheme has to satisfy a more severe restriction on the timestep than its implicit counterpart. Because the additional cost of the solution of the implicit momentum equation is negligible with respect to the cost of the solution of the nonlinear pressure correction equation, this semi-implicit scheme is not very efficient.

Appendix C

Conservative pressure correction solution algorithm in general coordinates

To compute flows in general domains the equations are brought in coordinate invariant form, using tensor notation:

$$\frac{\partial \rho}{\partial t} + (\rho U)_{,\alpha}^{\alpha} = 0, \quad (\text{C.1})$$

$$\frac{(\rho U)^{\alpha}}{\delta t} + (\rho U^{\alpha} U^{\beta})_{,\beta} = - (g^{\alpha\beta} p)_{,\beta}, \quad (\text{C.2})$$

$$M_r^2 (\gamma - 1) \left(\frac{1}{\gamma - 1} \frac{\partial p}{\partial t} + \frac{\frac{1}{2} \rho |\mathbf{u}|^2}{\delta t} + \right. \quad (\text{C.3})$$

$$\left. \left(\frac{\gamma}{\gamma - 1} U^{\alpha} p + U^{\alpha} \left(\frac{1}{2} \rho |\mathbf{u}|^2 \right) \right)_{,\alpha} \right) + U_{,\alpha}^{\alpha} = 0,$$

where $|\mathbf{u}|^2 = g_{\alpha\beta} U^{\alpha} U^{\beta}$, and $(\rho U)^{\alpha} = \mathbf{a}^{(\alpha)} \cdot (\rho \mathbf{u})$ are the contravariant momentum components, and where the contravariant metric tensor and base vectors are defined as:

$$g^{\alpha\beta} = \mathbf{a}^{(\alpha)} \cdot \mathbf{a}^{(\beta)}, \quad \mathbf{a}^{(\alpha)} = \frac{\partial \xi^{\alpha}}{\partial \mathbf{x}}, \quad (\text{C.4})$$

and similarly the covariant metric tensor and base vectors are defined as:

$$g_{\alpha\beta} = \mathbf{a}_{(\alpha)} \cdot \mathbf{a}_{(\beta)}, \quad \mathbf{a}_{(\alpha)} = \frac{\partial \mathbf{x}}{\partial \xi^{\alpha}}. \quad (\text{C.5})$$

The coordinate invariant pressure correction algorithm takes the following form:
First the mass conservation equation is solved:

$$\frac{\rho^{n+1} - \rho^n}{\delta t} + (\rho^{n+1} U^\alpha n)_{,\alpha} = 0. \quad (\text{C.6})$$

Next a prediction of the momentum field $m^{\alpha*}$ is computed from:

$$\frac{(m^\alpha)^* - m^n}{\delta t} + (m^{\alpha*} U^\beta n)_{,\beta} = - (g^{\alpha\beta} p^n)_{,\beta}. \quad (\text{C.7})$$

The following pressure correction is postulated:

$$\frac{U^\alpha n^{+1} - U^\alpha *}{\delta t} = - \frac{1}{\rho^{n+1}} (g^{\alpha\beta} (p^{n+1} - p^n))_{,\beta}. \quad (\text{C.8})$$

The postulate is substituted in the energy equation and taking the kinetic energy at the tentative * level, one obtains the following pressure correction equation:

$$\begin{aligned} M_r^2 (\gamma - 1) \left[\frac{1}{\gamma - 1} \frac{\delta p}{\delta t} + \frac{\rho^{n+1} |\mathbf{u}^* - \frac{\delta t}{\rho^{n+1}} \nabla \delta p|^2 - |\mathbf{u}^n|^2}{2\delta t} + \right. \\ \left. \left((U^\alpha * - \delta t (g^{\alpha\beta} \delta p)_{,\beta}) \left(\frac{\gamma}{\gamma - 1} (p^n + \delta p) + \frac{1}{2} \rho^{n+1} |\mathbf{u}^n|^2 \right) \right)_{,\alpha} \right] \\ + (U^\alpha * - \delta t (g^{\alpha\beta} \delta p)_{,\beta})_{,\alpha} = 0. \end{aligned} \quad (\text{C.9})$$

For details on spatial discretisation in general coordinates we refer to [105, 106, 107].

Summary

This thesis is divided into two parts. In the first part the development of a staggered scheme for the equations of the Homogeneous Equilibrium Model (HEM) is discussed. The HEM is a simple model to describe two-phase liquid/vapor flow and is used to model unsteady sheet cavitation. The second part is devoted to the formulation of a staggered discretisation of the equations of ideal magnetohydrodynamics, that model the dynamics of an inviscid plasma under the influence of a magnetic field.

We discuss physical aspects of cavitation. An overview is given of cavitation models. The HEM turns out to be the most generally applicable model, with modest assumptions. We review Delannoy's classic method, the first successful application of the HEM to compute cavitation, because it forms the starting point of our method.

We analyze the nonconvex equation of state of the HEM and discuss the Riemann problem for a general nonconvex equation of state. Solutions of two Riemann problems are used as testcases for the numerical scheme.

The choice of a suitable time integration method is clarified by distinguishing between the *target*, the *actual* and the *resolved* discretisation. Although a straightforward extension of our staggered scheme for the Euler equations produces results for Riemann problem test cases with accuracy comparable to a standard colocated scheme, this scheme has to satisfy a severe stability restriction on the timestep when applied to the computation of cavitation. Our aim is to formulate a noniterative solution procedure, with stability properties for high Mach number flow, comparable to the iterative SIMPLE method used by Delannoy. To gain insight in the stability properties of segregated solution procedures, we turn to von Neumann stability analysis. The simplicity of linear analysis allows inclusion of details of the segregated solution procedure. This analysis reveals a strong dependence of the maximum allowable dimensionless timestep on the Mach number. It explains the severe restriction on the time step of the original method for the high Mach number flow encountered in cavitation simulations and leads the way to a time integration method with more uniformity of the stability properties in the Mach number. We use this time-stepping method to compute a number of applications.

In the second part we consider the equations of ideal magnetohydrodynamics. A key aspect of numerical simulation of magnetohydrodynamics is retaining solenoidality of the discrete magnetic field. Furthermore, in some astrophysical applications the plasma flow is weakly compressible, but with physically important density variations. A staggered scheme retains the solenoidality of the discrete magnetic field to machine precision and

its efficiency and accuracy in the low Mach number limit. This makes it very suitable for computing weakly compressible MHD flow.

The straightforward extension of a Mach-uniform method for the Euler equations produces inaccurate approximations to weak solutions, because of lack of conservation of the discretisation. For the Euler equations the deviations are very small. But for the equations of ideal MHD they become unacceptable. We construct a conservative Mach-uniform pressure correction method for the Euler equations, that produces more accurate approximations to weak solutions.

Next, extension of the method to ideal MHD is discussed. Two staggered arrangements of the magnetic field are considered. The new method's ability to produce accurate results for a number of classic Riemann problems and for a two-dimensional test case is shown.

Duncan Roy van der Heul

Samenvatting

Dit proefschrift bevat twee delen. In het eerste deel wordt de ontwikkeling van een *gestaggered* schema voor de discretisatie van de vergelijkingen van het Homogeneous Equilibrium Model (HEM) besproken. Het HEM is een eenvoudig model voor de beschrijving van vloeistof/damp twee-fasen stromingen en wordt gebruikt voor de modellering van instationaire vliecavitatie. Het tweede deel is gewijd aan de formulering van een gestaggerde discretisatie van de vergelijkingen van de ideale magnetohydrodynamica, welke de dynamica van een niet visceus plasma onder de invloed van een magnetisch veld beschrijven.

We bespreken fysische aspecten van cavitatie. Een overzicht van cavitatiemodellen wordt gegeven. Het HEM blijkt het meest algemeen toepasbare model te zijn, met bescheiden aannames. Wij nemen de methode van Delannoy, de eerste succesvolle toepassing van het HEM voor de berekening van cavitatie, opnieuw in ogenschouw, omdat ze de basis vormt van onze methode.

We analyseren de niet-convexe toestandsvergelijking van het HEM en bespreken tweeëdimensionale gelijkvormighheids oplossingen voor een algemene niet-convexe toestandsvergelijking. De geconstrueerde oplossingen zijn gebruikt als test gevallen voor het discretisatieschema.

De keuze van een passende tijdsintegratiemethode wordt verhelderd door onderscheid te maken tussen de *target*, de *actual* en de *resolved* discretisation. Hoewel een directe uitbreiding van ons gestaggerde schema voor de vergelijkingen van Euler resultaten produceert voor de èèdimensionale testgevallen met een nauwkeurigheid die vergelijkbaar is met een standaard gecollocerd schema, moet dit schema voldoen aan een sterke stabiliteitsbeperking van de tijdstap wanneer het wordt toegepast voor de berekening van cavitatie.

Ons doel is om een niet-iteratief tijdstap algoritme te formuleren, met stabiliteitseigenschappen vergelijkbaar met die van het SIMPLE algoritme, dat wordt gebruikt door Delannoy. Om inzicht te verkrijgen in de stabiliteits-eigenschappen van ontkoppelde oplosmethoden maken we gebruik van analyse volgens de methode van von Neumann. De eenvoud van lineaire analyse laat toe dat details van de ontkoppelde oplosmethodiek kunnen worden meegenomen. De analyse laat zien dat er een sterke afhankelijkheid bestaat tussen de maximum toelaatbare dimensieloze tijdstap en het getal van Mach. Ze verklaart de sterke stabiliteitsbeperking van de tijdstap van de oorspronkelijke methode voor de sterk samendrukbare stroming in de cavitatie simulaties en wijst de weg naar een tijdstapmethode met meer uniformiteit in de stabiliteitseigenschappen in het getal van Mach.

We gebruiken deze tijdstapmethode voor het berekenen van een aantal praktisch relevante caverende stromingen.

In het tweede deel bekijken we de vergelijkingen van ideale magnetohydrodynamica (MHD). Een belangrijk aspect van numerieke simulatie van magnetohydrodynamica is het behouden van de solenoidaliteit van het discrete magnetische veld. Daar komt nog bij dat in sommige astrofysische toepassingen de plasma stroming zwak compressibel is, maar fysisch relevante dichtheidsvariatics heeft. Een gestaggered schema behoudt de solenoidaliteit van het discrete magnetische veld tot machine nauwkeurigheid en efficiency en hoge nauwkeurigheid in de limiet naar nul van het getal van Mach. Dit maakt het schema bijzonder geschikt voor de berekening van zwak compressibele MHD stromingen.

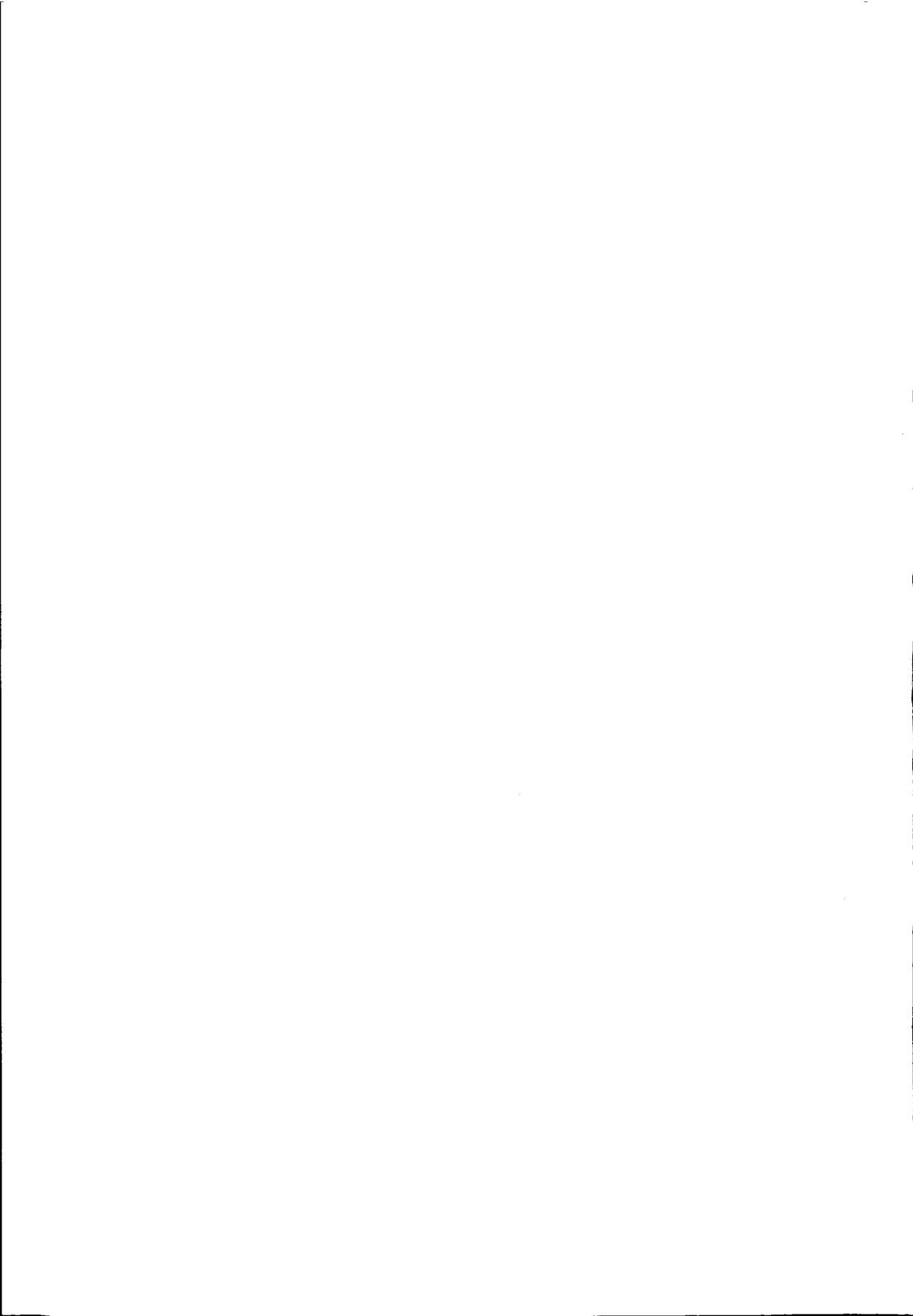
Een rechtstreekse uitbreiding van een niet conservatieve Mach-uniforme methode voor de vergelijkingen van Euler produceert onnauwkeurige benaderingen van zwakke oplossingen. Voor de vergelijkingen van Euler zijn de afwijkingen zeer klein, maar voor de vergelijkingen van ideale MHD zijn ze onaanvaardbaar groot. We construeren een conservatieve Mach-uniforme druk correctie methode voor de Euler vergelijkingen, die meer nauwkeurige benaderingen van zwakke oplossingen produceert.

Vervolgens bespreken wij de uitbreiding van de methode voor ideale MHD. Twee verschillende gestaggerde plaatsingen van het magnetische veld worden overwogen. Het gestaggerde schema geeft nauwkeurige resultaten voor een aantal klassieke Riemann problemen en voor een twee-dimensionaal testgeval.

Duncan Roy van der Heul

Curriculum Vitae

- 2001-present National Aerospace Laboratory, Department of Computational Fluid Dynamics, Amsterdam, The Netherlands, research scientist.
- 1997-2001 Delft University of Technology, The Netherlands, PhD-student in Numerical Analysis, supported by the Netherlands Organisation for Scientific Research (NWO), subject: *Computation of time-dependent weakly compressible flow*, thesis advisor: Prof.dr.ir. P. Wesseling, Department of Applied Mathematical Analysis, Faculty of Information Technology and Systems.
- 1991-1997 Delft University of Technology, The Netherlands, Master's degree in Naval Architecture, subject: Computational Ship Hydrodynamics, first graduate of class of 1991.
- 1986-1991 Stedelijk Gymnasium Leiden, The Netherlands, secondary school, VWO (8 subjects), prize from German ambassador for best grade in German.



List of Publications

- Journal papers

- D.R. van der Heul, C. Vuik, P. Wesseling, A staggered scheme for hyperbolic conservation laws applied to unsteady sheet cavitation, *Computing and Visualisation in Science*, 2:63-68, 1999.
- D.R. van der Heul, C. Vuik, P. Wesseling, Stability analysis for segregated solution methods for compressible flow, *Applied Numerical Mathematics*, 38:257-274, 2001.
Report 00-06, Department of Applied Mathematical Analysis, Delft University of Technology, Delft, The Netherlands, 2000.
http://ta.twi.tudelft.nl/Ftp/TWA_Reports
- D.R. van der Heul, C. Vuik, P. Wesseling, Efficient computation of flow with cavitation with compressible pressure correction, Accepted for publication to *International Journal for Numerical Methods in Fluids*.
Report 00-11, Department of Applied Mathematical Analysis, Delft University of Technology, Delft, The Netherlands, 2000.
http://ta.twi.tudelft.nl/Ftp/TWA_Reports
- D.R. van der Heul, C. Vuik, P. Wesseling, A conservative pressure correction method for flow at all speeds, Accepted for publication in *Computers & Fluids*.
Report 01-04, Department of Applied Mathematical Analysis, Delft University of Technology, Delft, The Netherlands, 2001.
http://ta.twi.tudelft.nl/Ftp/TWA_Reports/
- D.R. van der Heul, C. Vuik, P. Wesseling, A conservative pressure correction method for the Euler and ideal MHD equations at all speeds. Accepted for publication in *International Journal for Numerical Methods in Fluids*.
- P. Wesseling, D.R. van der Heul, Uniformly effective numerical methods for hyperbolic systems, *Computing*, 66:249-267, 2000.

- Conference Proceedings

- D.R. van der Heul, P. Wesseling, A staggered scheme for hyperbolic conservation laws. Pp.730-735 in: K.D. Papailiou, D. Tsahalis, J. Périaux, C. Hirsch, M.

- Pandolfi (eds.): Computational Fluid Dynamics '98, Vol. 2 Wiley, Chichester, 1998
- D. R. van der Heul, P. Wesseling, A staggered scheme for hyperbolic conservation laws applied to computation of flow with cavitation. In: E. Toro (ed.) Godunov Methods: Theory and Applications. Edited Review. Kluwer/Plenum Academic Publishers. To appear April 2001.
 - D.R. van der Heul, C. Vuik, P. Wesseling, Efficient Computation of Flow with Cavitation by Compressible Pressure Correction. In: H. Paillère (ed.): AMIF-ESF Workshop Computing Methods for Two-Phase Flow, Aussois, Jan. 2000 CDROM, CEA, Saclay, 2000, 6 pages.
 - D.R. van der Heul, C. Vuik, P. Wesseling Efficient computation of flow with cavitation by compressible pressure correction. In: E. Oñate, G. Bugeda, B. Suárez: ECCOMAS 2000, Proceedings of the European Congress on Computational Methods in Applied Sciences and Engineering, Barcelona, Sept. 2000 CDROM, ISBN 84-89925-70-4, CIMNE, Barcelona, 2000. 11 pages.
 - D.R. van der Heul, C. Vuik, P. Wesseling, A conservative pressure correction method for the Euler and ideal MHD equations at all speeds. To appear in: Proceedings ICFD Conference on Numerical Methods for Fluid Dynamics, Oxford, March 2001.
 - P. Wesseling, D.R. van der Heul, C. Vuik Uniformly effective numerical methods for hyperbolic systems. In: M. Deville and R. Owens (eds.): Proceedings of the 16th IMACS World Congress 2000. Lausanne, August 2000. CDROM ISBN 3-9522075-1-9, Rutgers University, New Brunswick, 2000. 6 pages.
 - P. Wesseling, D.R. van der Heul, C. Vuik Unified methods for computing compressible and incompressible flows. In: E. Oñate, G. Bugeda, B. Suárez (eds.): ECCOMAS 2000, Proceedings of the European Congress on Computational Methods in Applied Sciences and Engineering, Barcelona, Sept. 2000 CDROM, ISBN 84-89925-70-4, CIMNE, Barcelona, 2000. 23 pages.











